**RADIATION**
INCORPORATED

# FINAL REPORT
## (Fourth Quarter)

# INVESTIGATION OF USES OF
# HOLOGRAPHIC OPTICAL ELEMENTS

Period:

1 June 1972 to 31 May 1973

FINAL REPORT
(Fourth Quarter)

INVESTIGATION OF USES OF
HOLOGRAPHIC OPTICAL ELEMENTS

NASA Contract No. NAS 8-28949

DCN 1-2-40-231201F

Prepared For:

National Aeronautics and Space Administration
George C. Marshall Space Flight Center
Marshall Space Flight Center, Alabama 35812

Prepared By:

Harris Electro-Optics Center
of Radiation
P.O. Box 1084
Ann Arbor, Michigan 48106

## FOREWORD

This report was prepared by the Harris Electro-Optics Center of
Radiation, a Division of Harris Intertype Corporation, and covers the
work performed between 1 June 1972 and 31 May 1973 on Contract NAS 8-28949
with the NASA Space Flight Center, Huntsville, Alabama. The effort is
monitored by E. J. Reinbolt. The contractor's report number is 8204-Q-4.

The principal investigators for this program are R. G. Zech (for the Harris
Electro-Optics Center) and J. Latta (for the Environmental Research Institute
of Michigan). Contributors to this report are J. C. Dwyer, R. Fairchild,
and L. M. Ralston. The program manager is R. G. Zech. This report was
prepared under the direction of A. Kozma and A. Vander Lugt.

**HARRIS ELECTRO-OPTICS CENTER**

**RADIATION**

a DIVISION OF HARRIS INTERTYPE CORPORATION

## TABLE OF CONTENTS

# 1
# INTRODUCTION

This is the final report for the program entitled "Investigation of Uses of Holographic Optical Elements". It is a joint effort between the Harris Electro-Optics Center and the Environmental Research Institute of Michigan. The main objectives of the program are to develop a better understanding of single and multiple element holographic optical systems, to conduct an experimental investigation of single and multiple holographic optical systems to determine whether their performance is in agreement with the predictions of computer-based analysis, and to evaluate the recording and reconstruction parameters of various hologram recording materials in terms of their potential for the fabrication of holographic optical elements. To realize these objectives an extensive theoretical and experimental program was planned and completed.

Section 2 discusses in detail the analytical work performed for the analysis of single holographic optical elements. Multielement design work was reported in previous quarterly reports. Section 3 summarizes experimental work for both single and multiple element holographic optics. There is a consistent relationship between analysis and experiment that is strongly emphasized in Sections 2 and 3. Finally, in Section 4 the properties, the methods of preparation and processing, and the hologram parameters for various candidate light-sensitive materials are given, together with supporting experimental data.

In Appendix A we summarize analytical and experimental data for single element holographic optics with photographs and tables. The chromatic and Seidel aberration profiles are given for three different geometries and for a number of different recording materials. Nearly 150 experimental conditions were investigated and documented. Appendix B discusses some practical applications of holographic optics.

The data in this report represent a thorough study of the aberrations and imaging properties of holographic optical elements. Principle milestones include (1) the indepth experimental investigation of single holographic optical elements, (2) the verification of the accuracy of the theoretical computer-based description of hologram behavior, (3) the computer-generation of interferograms that are characteristic of a prescribed aberrated imaging condition, (4) the experimental verification of wavelength optimization, (5) the experimental determination of the space bandwidth product of single holographic optical elements as a function of bending and field angle, and (6) the first experimental study of the aberration properties of holographic optical elements constructed in very thick (750 $\mu$m) recording media.

Our investigation of the properties and uses of holographic optical elements was comprehensive. It provides not only quantitative data about the imaging and aberration properties of single and multiple holographic optical elements, but also verifies the accuracy of theoretical models and demonstrates the practical utility of computer-aided design. We believe that the present effort has provided a solid basis for the future development of holographic optics.

Based on the positive results of this program, we recommend that it be continued with emphasis on the following objectives:

1.  A more detailed experimental evaluation of the imaging properties of multicomponent holographic elements,

2.  The optimization of fabrication techniques for both transmissive and reflective holographic optical elements.

3.  A delineation of the problems related to the construction of synthetic holographic optical elements.

2

# ANALYTICAL INVESTIGATION

## 2.1 Introduction

In this section we discuss the results of a theoretical study of the properties of single holographic optical elements. An important objective of this study was to correlate the experimental measurement of wavefront aberrations with results derived from a computer model that is based on ray tracing. The wavefront aberrations were determined by an experimental interferometric technique proposed by Kubota and Ose.[1] In both the theoretical analysis and the experimental measurements, many different parameters were varied. We present in this section a detailed discussion of the methods used to realize the theoretical results with the computer analysis. Only a sample of the representative results in the form of computer plots and numerical tables are given here. A complete summary of the results are included in Appendix A.

## 2.2 Ray Tracing Analysis of Hologram Geometries

In our discussion of the computer analysis we will be concerned with the influence of "bending" on the performance of the hologram.[2] That is, the focal length of the hologram will be kept constant while the radial distances of the object and reference beams, $R_o$ and $R_R$, respectively, are varied. This is in direct analogy with the concept of lens bending where the curvatures of the lens surfaces of a simple lens are varied and the focal length is kept constant.

The basic geometry used for the hologram construction is shown in Figure 2-1. The subscripts 0 and R denote object and reference beams, respectively. The hologram lies in the x,y plane; i.e., normal to the paper, with an object beam angle of $\alpha_0$ and radial distance from the center
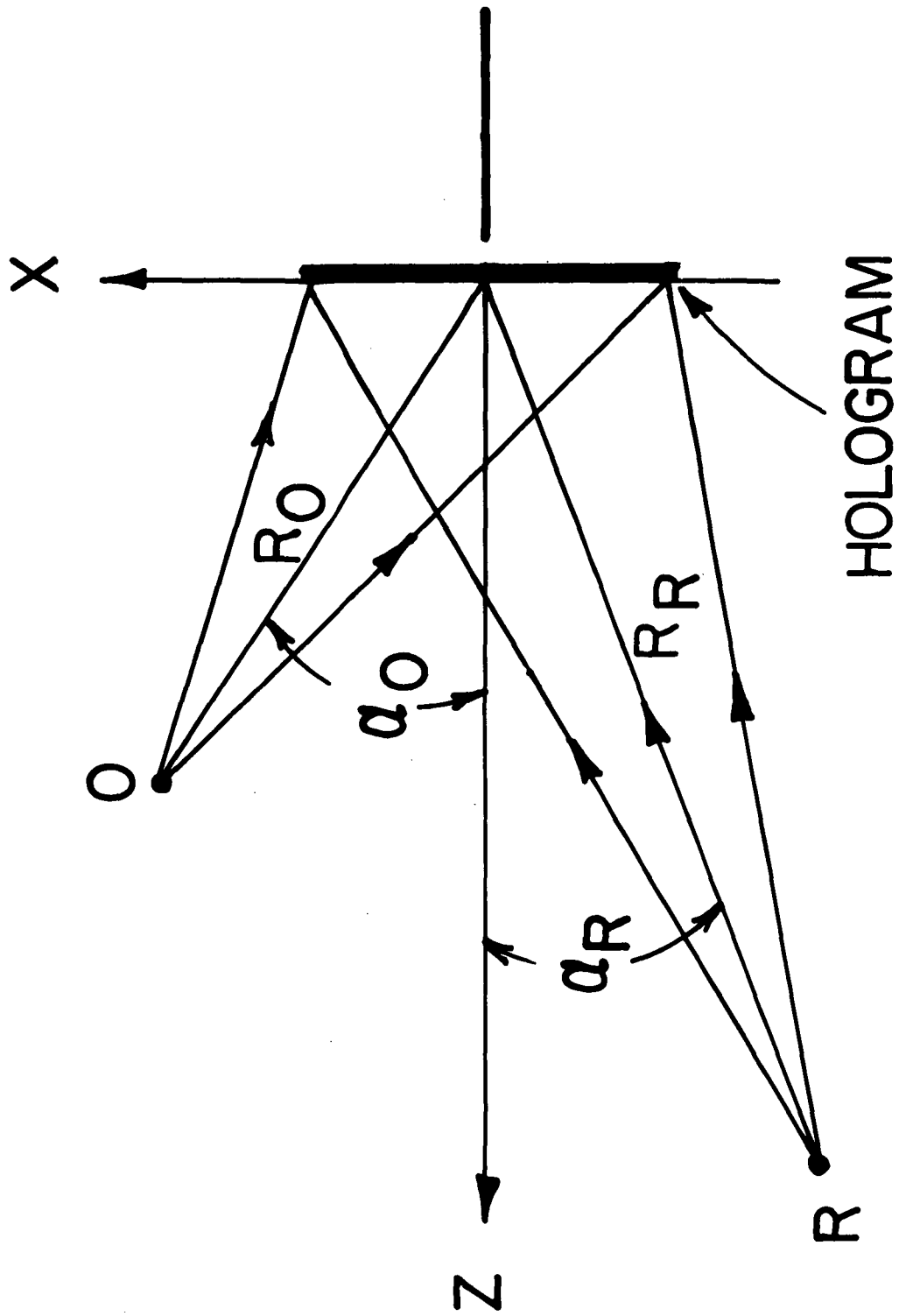
FIGURE 2-1.  Basic construction geometry for the ray tracing analysis of holographic optical elements.

4

of the hologram to the point source of $R_0$. Similar parameters, $\alpha_R$ and $R_R$, describe the location of the reference beam point source. The Q-factor describes the relative bending of the hologram and is defined by the equation

$$Q = \frac{R_R + R_0}{R_R - R_0}$$

Consider holograms with Q-factors of 1, 2, and 4. The values of $R_0$ and $R_R$ are listed below for a fixed focal length f of 400 mm.

| Q | $R_0$(mm) | $R_R$(mm) |
|---|-----------|-----------|
| 1 | 400 | $\infty$ |
| 2 | 267 | 800 |
| 4 | 160 | 267 |

To determine the properties of the hologram as a function of the Q-factor, we will consider several values of Q and the aberrations present in the image. The angles we used for this investigation are for all Q-factors given by $\alpha_0 = -15°$, $\alpha_R = +15°$, and $\alpha_C = +15°$. In each case the hologram is reconstructed with a plane wave, $R_C \to \infty$, and for $\alpha_C = +15°$. The hologram diameter is 45 mm and thus f/8.9. The construction wavelength is $\lambda_0 = 4825\text{Å}$ and the reconstruction wavelengths are $\lambda_C = 4680\text{Å}$, $4762\text{Å}$, $4825\text{Å}$, $5682\text{Å}$, and $6471\text{Å}$.

The aberrations to be considered for each Q-factor are $\Delta_A$, $\Delta_C$, and $\Delta_G$. These aberrations are, respectively, the total wavefront deviations due to astigmatism, coma, and the total of all aberrations. In the case of astigmatism, the aberration value given is at the edge of the aperture, i.e., the maximum value of the aberration for a given fan of rays when the focus is along an orthogonal set of rays. In other words, the astigmatism given would be that measured in the sagittal plane when the focus is in the tangential plane. The coma is also given by its maximum value at the edge of the aperture.

HARRIS ELECTRO-OPTICS CENTER

The total aberration, $|\Delta_G|$, is the maximum to minimum deviation of the total wavefront due to all aberrations.

Shown in Figure 2-2 is a plot of the astigmatism $|\Delta_A|$ as a function of wavelength for each Q. We note that this aberration is zero at the hologram construction wavelength. In addition, the astigmatism is independent of Q. The situation is more complex for coma as is shown in Figure 2-3. There are zero values of coma for Q = 1 and 2, but not for Q = 4. The zero value is to be expected at Q = 1, because at $\lambda_C$ = 4825$\overset{o}{A}$ the reconstruction geometry exactly duplicates the construction geometry; i.e., $R_C = R_R \to \infty$. The two aberrations of astigmatism and coma are dominant in forming the image, but are not the only ones present. For this reason, the value of $|\Delta_G|$ as shown in Figure 2-4 will not exactly correspond to the sum of $|\Delta_A|$ and $|\Delta_C|$.

The trends in $|\Delta_G|$ as a function of $\lambda_C$ are, however, quite evident. That is, with Q = 1, for $\lambda_C = \lambda_0$ the aberrations are zero as expected. In no other geometries does this happen for $R_C \to \infty$. For Q = 2, the aberrations are small around $\lambda_C = \lambda_0$ but increase rapidly as $\lambda_C$ increases. This is expected from Figure 2-2 where astigmatism is the dominant aberration for increasing $\lambda_C$. The aberrations are quite large for Q = 4 and change only a small amount as $\lambda_C$ is varied. In this example, we see the interaction of coma with astigmatism to cause large wavefront deviations.

From these three figures it is not obvious that aberration balancing can take place when a wavelength shift is present. We noted that only at one point did $|\Delta_G|$ reach or approach zero. The reason for this is that the reconstructions are all at $\alpha_C = \alpha_R$; i.e., at the angle of construction. Astigmatism, for example, can be varied by modifying the reconstruction angle; in fact, aberrations can generally be modified and reduced by using a reconstruction beam at a location different from that used for construction. This was verified experimentally (see Section 3 and Appendix A). With this in mind, the techniques used for aberration balancing and reducing the fringes present on the hologram become evident. The methods used to balance aberrations with holograms over a large wavelength shift range may, of course,
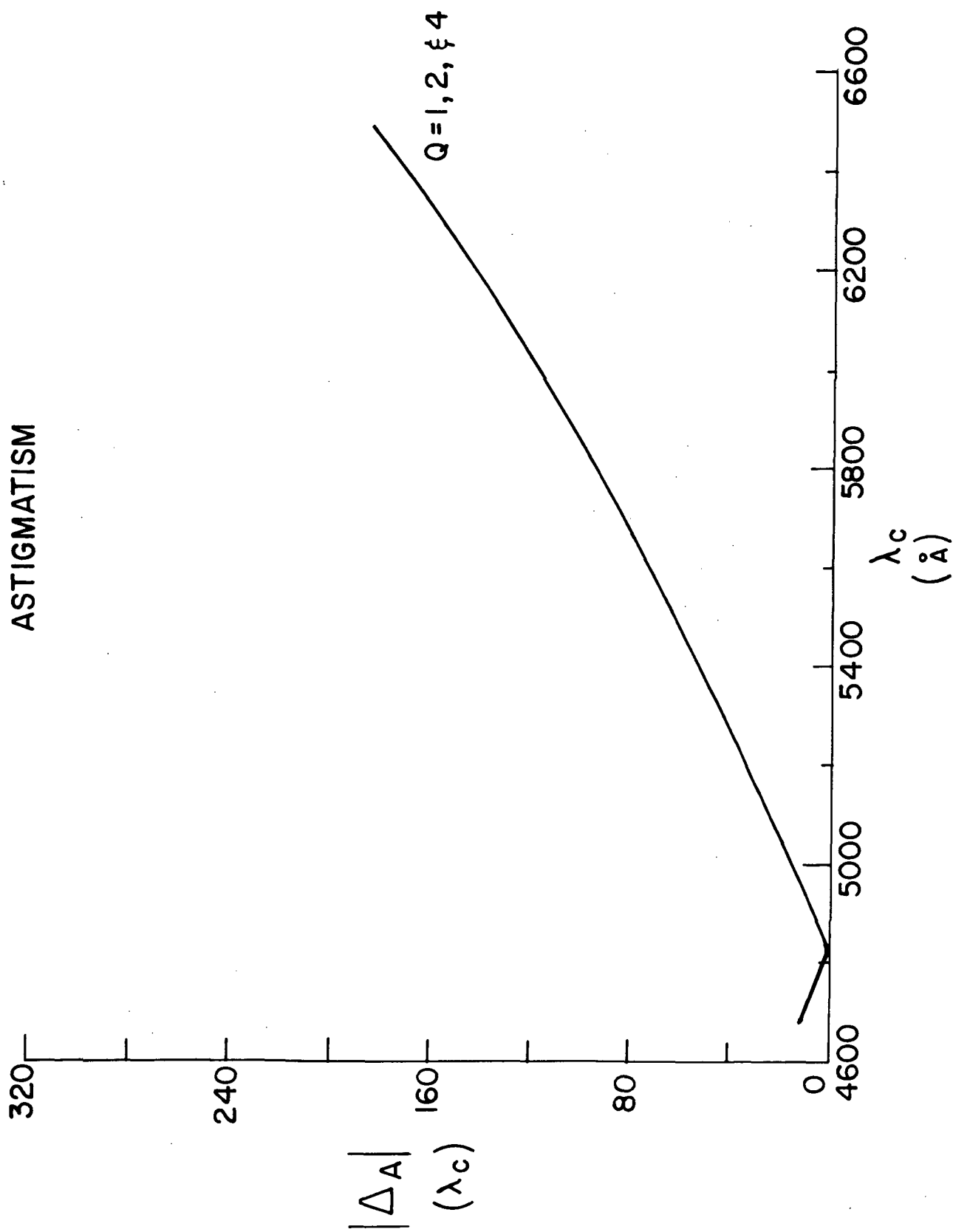
ASTIGMATISM



FIGURE 2-2. Astigmatism for a single holographic element with Q-factors of 1, 2, and 4 vs wavelength of reconstruction.
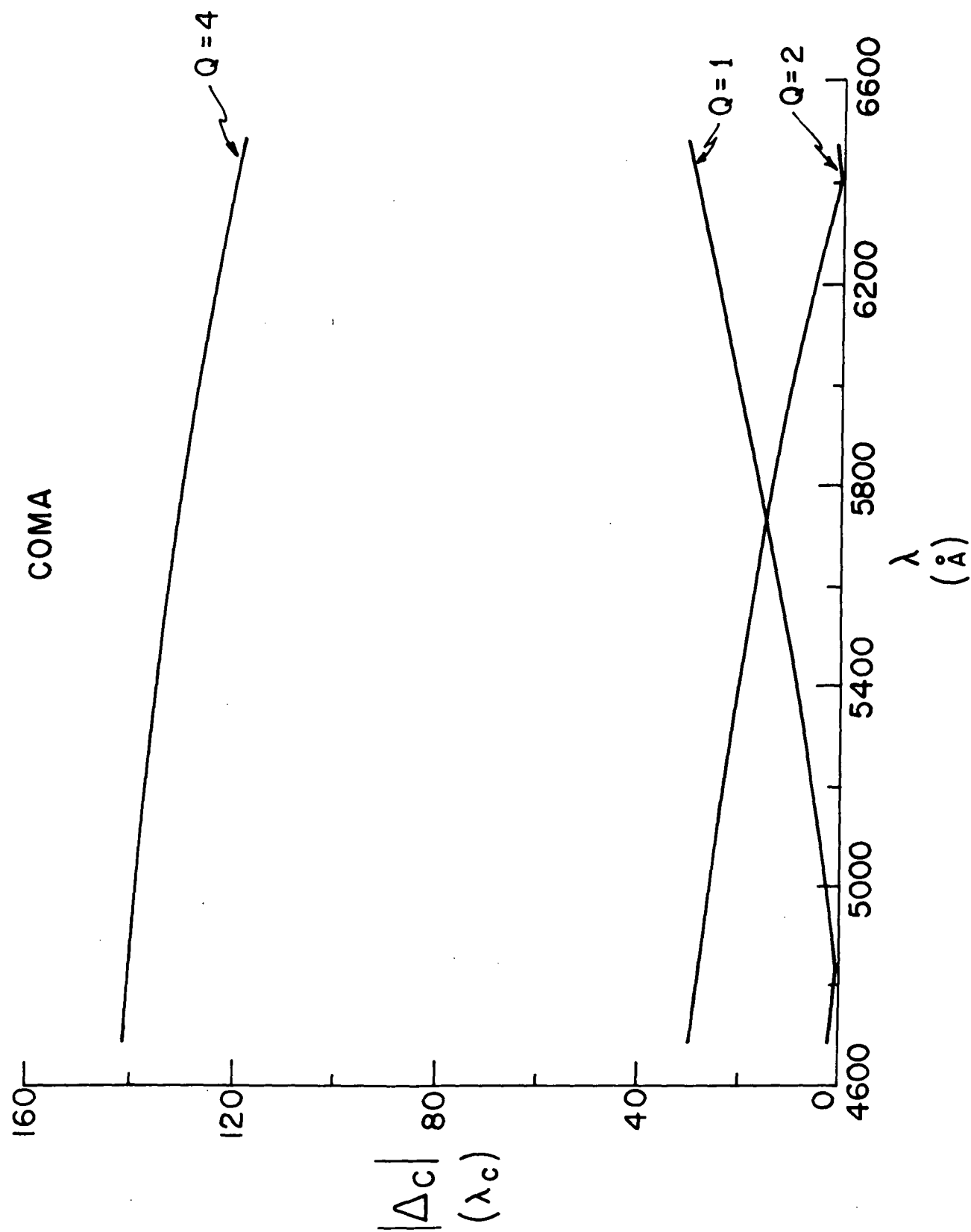
7

FIGURE 2-3. Coma for a single holographic element with Q-factors of 1, 2, and 4 vs wavelength of reconstruction.
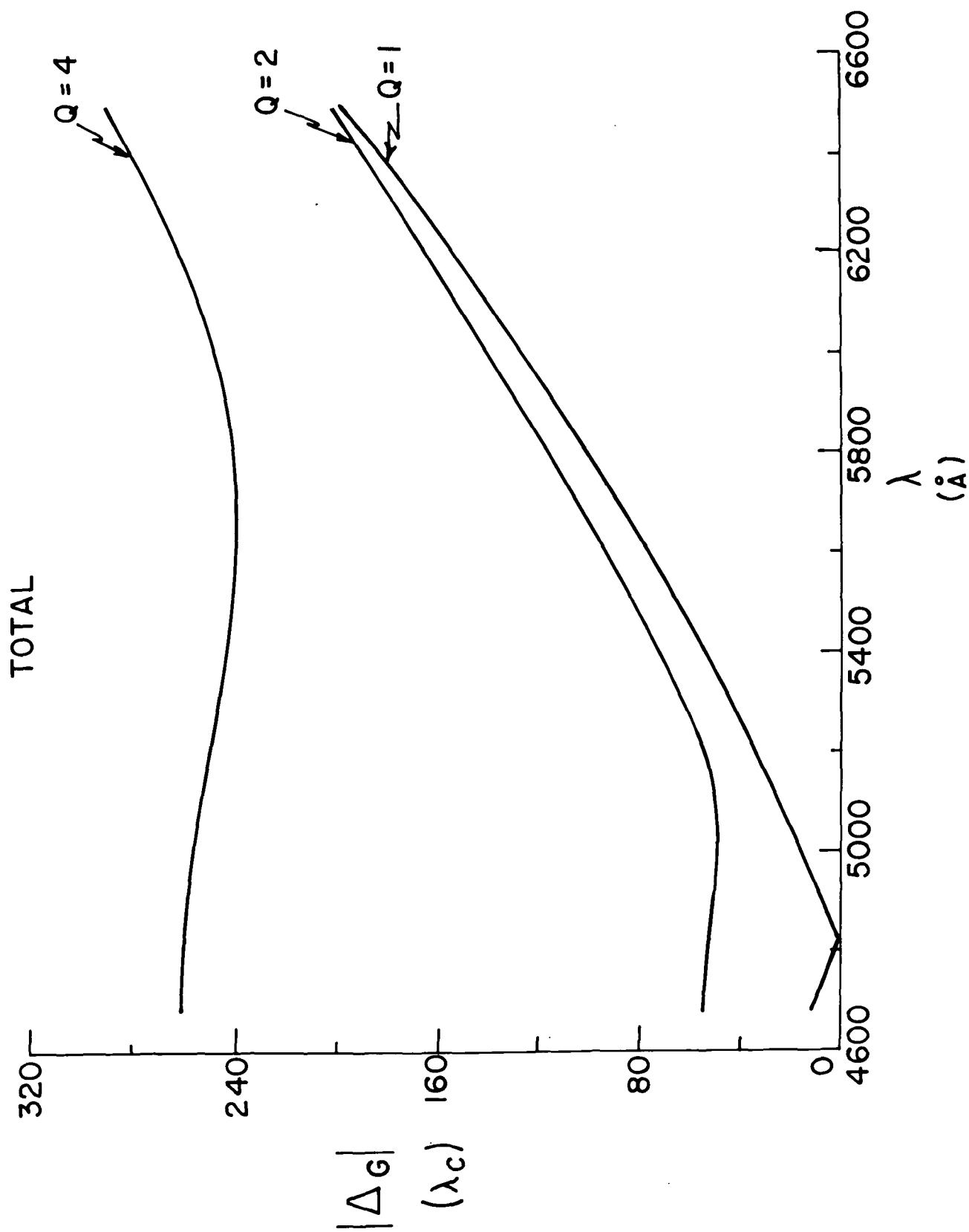
8

FIGURE 2-4. Total wavefront aberrations for a single holographic element with Q-factors of 1, 2, and 4 vs wavelength of reconstruction.

9

encompass more than a simple change in $\alpha_C$. Correspondingly, the technique used to simulate the hologram reconstruction will be more complex.

## 2.3 Computer Analysis of Hologram Interferometer

The hologram interferometer to determine the wavefront aberrations present in a holographic element is constructed in two parts. First, the element must be constructed in a geometry corresponding to that shown in Figure 2-1. In the second step the hologram is reconstructed as illustrated in Figure 2-5. In this case, the hologram is being reconstructed by beam C at an angle $\alpha_C$ with a radial distance to the center of the hologram $R_C$. Once this beam has propagated through the hologram, it becomes the image beam I. It is important to differentiate between I and IR, the image reference. The image beam I is diverging and, if the focus of I is the same as IR and there were no aberrations in I, the hologram surface would have no interference fringes. At the hologram surface we are comparing an ideal spherical wavefront coming from the point IR with the image wavefront I diverging from the hologram. Parameters that can be varied in reconstruction include the point source position IR and C and the wavelength $\lambda_C$. Note the variations in the point source positions include x, y, z or in the notation used in the computer program $\alpha$, $\beta$ and R. The angle $\beta$ is simply that angle formed by the projection of the radial line R onto the yz plane; that is, it is the angle between this projection and the xz plane.

A block diagram of the computer program used to simulate the geometries shown in Figure 2-1 and 2-5 is illustrated in Figure 2-6. The basic kernel of these programs is the hologram ray tracing routines that have been discussed earlier.[3] These programs normally analyze a hologram that has been constructed in a specific geometry and then reconstructed with a beam C. The image location and properties are then determined from the rays that
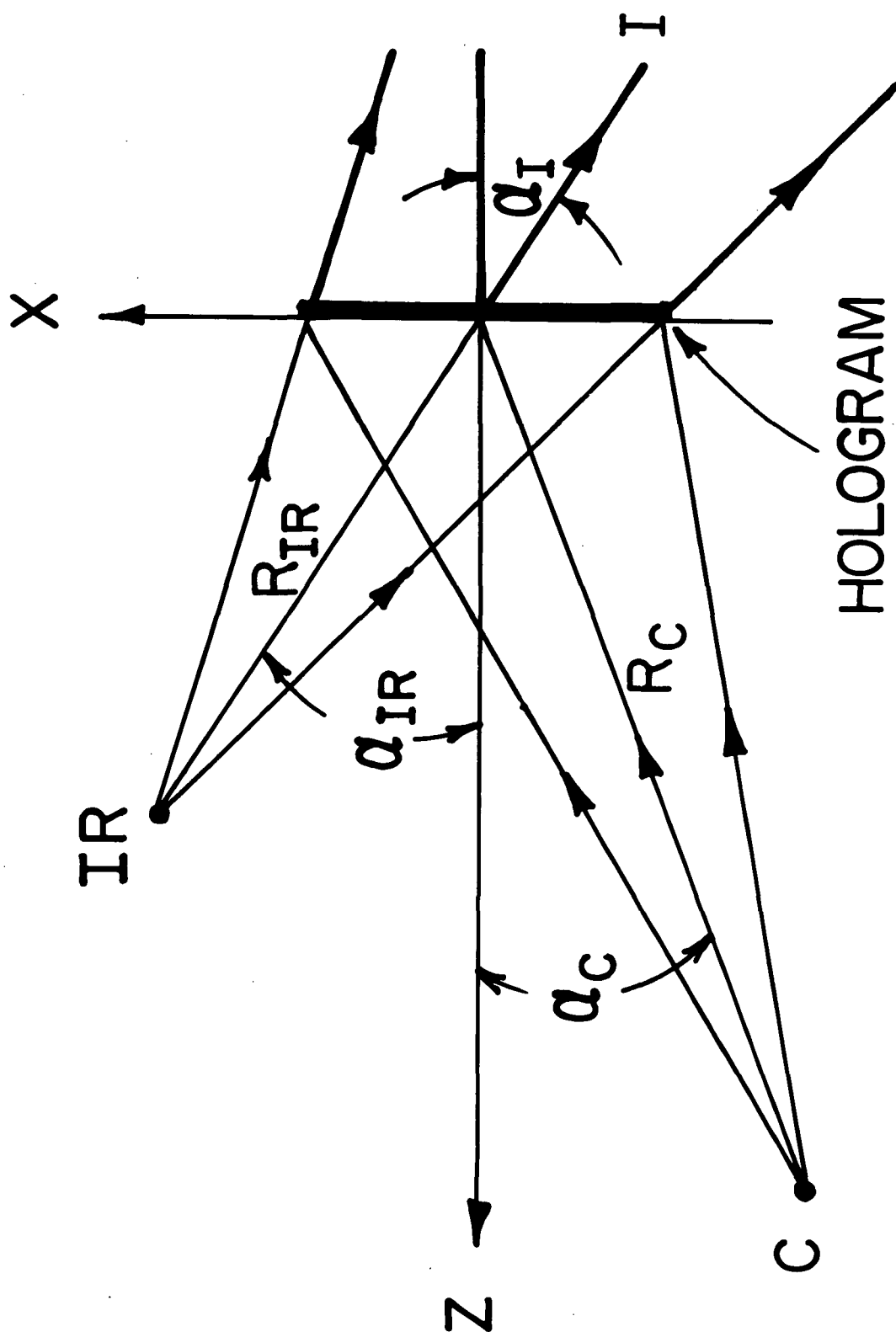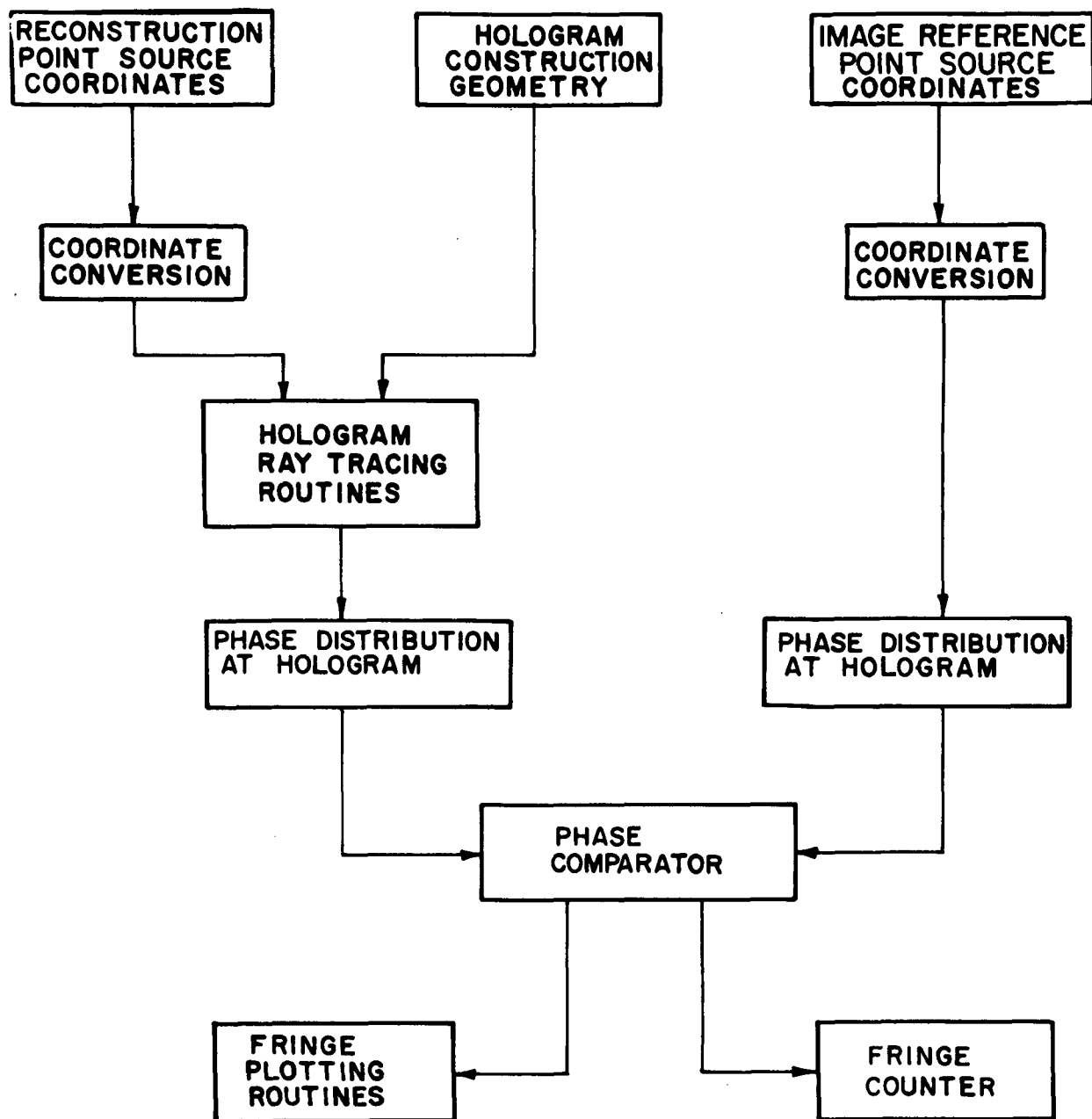
FIGURE 2-5. Basic reconstruction geometry for the holographic interferometer to test the wavelength aberrations of a single holographic element.

INTERFERENCE FRINGE ANALYSIS PROGRAM

FIGURE 2-6. Block diagram of the interference fringe analysis program.

exit from the hologram. In the analysis to determine the interference fringes on the hologram surface, a determination of the hologram image location is not necessary. This is simply a reflection of the fact that the interference fringes are localized on the hologram surface, and our interest is therefore confined to the phase distribution at this surface. To be able to simulate the interference fringes on the hologram surface, it is necessary to introduce an image reference point source in the same sense that it was used to construct the fringes in our experimental measurements. This path in the block diagram is shown on the right side of Figure 2-6. Note that in the case of both the reconstruction and image reference beams that a coordinate conversion takes place to transform the coordinates given in the experimental data to the system used by the computer programs. The output from the ray tracing programs for both the image from the hologram and the image reference beam is a phase record on the hologram surface. These two phase histories are then compared by difference operations from which the fringe data is accumulated. The programs may operate in two independent modes to either generate fringe data along fans of rays or an array of rays to generate fringe plots with the computer. A fringe occurs when a positive or negative integer multiple is passed through in the phase comparison data.

As a result of our initial analysis of the experimental data used to generate the interference fringes, very small errors could cause noticable changes in the fringe patterns displayed by the computer. This does not necessarily reflect gross errors in either the theoretical model or experimental measurements, but are simply a result of the sensitivity of the measurement technique. To at least null out these errors, it is necessary to make slight modifications to the coordinate data supplied by the experiments. It should be pointed out that the variables that can be varied by the computer program must correspond to the same set that were varied in the experiments. For example, if the reconstruction angle $\alpha_c$ is changed from the ideal reconstruction point source angle in the experiments, that same variable should be

13

the only one which can be changed when seeking to match both the experimental and theoretical interference fringes. In some cases the number of variables can be as large as six. It should be quite obvious that the task of correlating computer generated interference fringes with experimental results can be tedious. To simplify this task, we chose to incorporate the interference fringe analysis program into an optimization program that would do the correlation automatically.

Shown in Figure 2-7 is a block diagram of the computer programs used to optimize the fringe patterns. The initial input, as can be seen at the left of the figure, includes the initial hologram data which describes the hologram construction and reconstruction geometry. In addition, a variable selection list is supplied to the optimization control program. This list is used to specify variables of the hologram geometry that may vary and the ranges they may cover. A number of search techniques are available in the optimization control program, but since we know that the input data is close to the correct geometry, a multi-variant direct search developed by R. Hooke and T. A. Jeeves[4] was used exclusively. The "frng" merit function was used by the direct search in evaluating the success of the search process. In general, the merit function is written to numerically evaluate a particular goal set by the optimization program. In the case of the fringe analysis, the merit function was written to reflect the square root of the sum of the squares of the differences of the calculated fringe counts and the experimental fringe counts. Expressing this in the form of an equation,

$$FCT = \left[ (C1_E - C1_A)^2 + (C2_E - C2_A)^2 + (C3_E - C3_A)^2 + (C4_E - C4_A)^2 \right]^{1/2}$$

where

$C1_E$, $C2_E$, $C3_E$ and $C4_E$ are the experimental fringe counts taken from the photographs

$C1_A$, $C2_A$, $C3_A$ and $C4_A$ are the analytical fringe counts computed by the ray tracing programs.

HARRIS ELECTRO-OPTICS CENTER

INPUT                                    OUTPUT

```
┌──────────────┐          ┌──────────────┐
│  VARIABLE    │────────▶ │ OPTIMIZATION │
│  SELECTION   │          │   CONTROL    │
└──────────────┘          │   PROGRAM    │
                          └──────┬───────┘
                                 │
                                 ▼
                          ┌──────────────┐
                          │    DIRECT     │──────────┐
                          │   SEARCH      │          │
                          └──────┬────────┘          │
                                 │                   │
                                 ▼                   │
┌──────────────┐          ┌──────────────┐          │    ┌──────────────┐
│   INITIAL    │          │   FRINGE     │          │    │  OPTIMIZED   │
│  HOLOGRAM    │────────▶ │  ANALYSIS    │──────────┼──▶ │  HOLOGRAM    │
│    DATA      │          │  PROGRAM     │          │    │    DATA      │
└──────────────┘          └──────┬───────┘          │    └──────┬───────┘
                                 │                   │           │
                                 ▼                   │           ▼
                          ┌──────────────┐          │    ┌──────────────┐
                          │    "FRNG"    │          │    │   FRINGE     │
                          │    MERIT     │──────────┘    │  PLOTTING    │
                          │  FUNCTION    │               │  PROGRAMS    │
                          └──────────────┘               └──────┬───────┘
                                                                │
                                                                ▼
                                                         ┌──────────────┐
                                                         │  COMPUTER    │
                                                         │  GENERATED   │
                                                         │   FRINGE     │
                                                         │   PLOTS      │
                                                         └──────────────┘
```
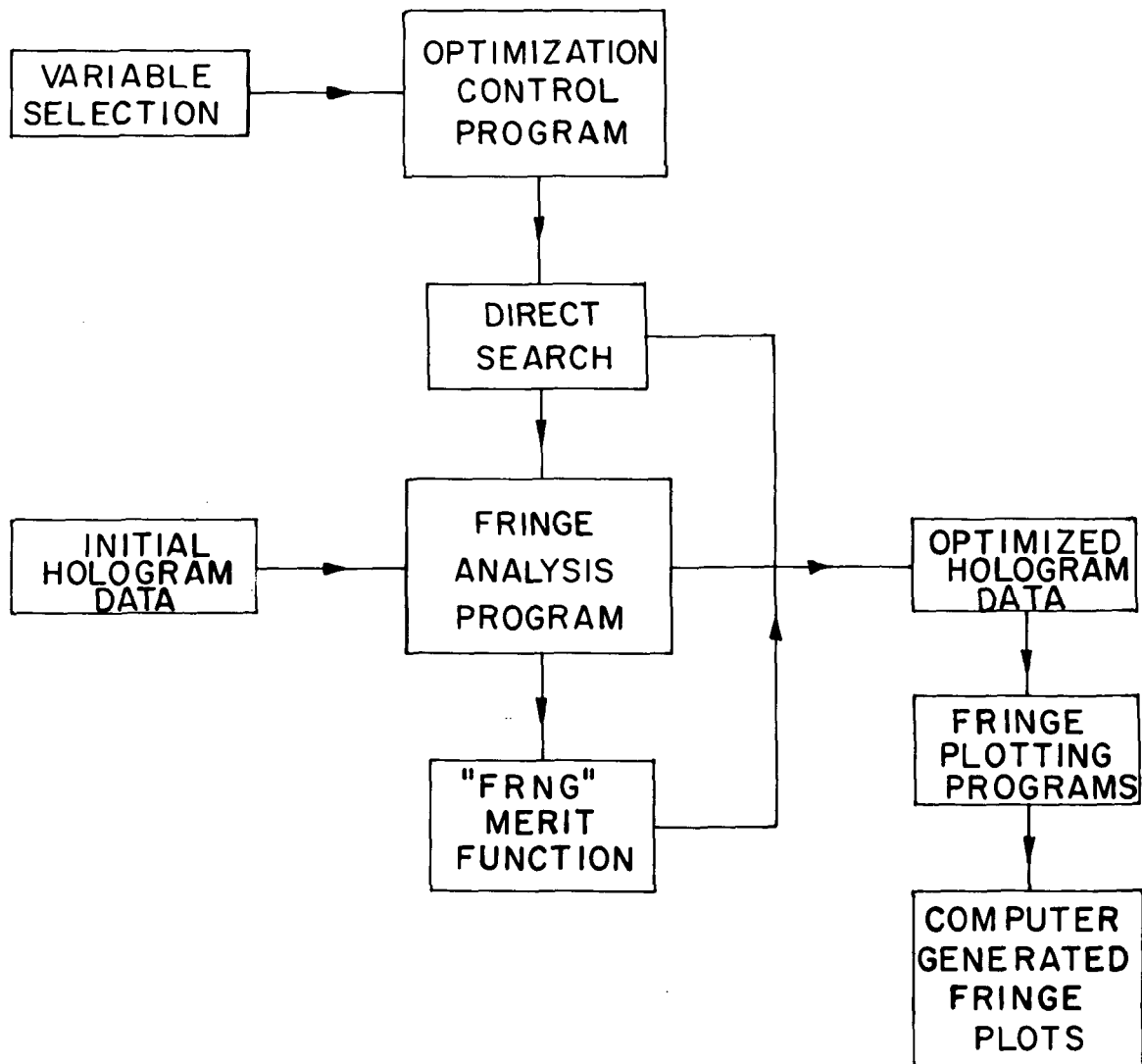
FIGURE 2-7.  Block diagram of the program to optimize the interference
             fringes on a holographic element.

15

It can be seen that as the analytical fringe counts $C1_A$, $C2_A$, $C3_A$ and $C4_A$ approach the same values as their respective experimental fringe counts $C1_E$, $C2_E$, $C3_E$ and $C4_E$, the value of FCT approaches zero. If the experimental fringe counts are all set at zero, the actual fringe counts are minimized, simulating the condition of aberration balancing. The merit function FCT is calculated at each iteration of the optimization process and passed back to the direct search from the merit function. When the direct search is satisfied that the merit function has a minimum value (to within a predetermined tolerance value), the optimization process is stopped and the modified hologram geometry is printed out. This new geometry is then used to computer generate a fringe plot.

## 2.4 Theoretical Data

Shown in Figures 2-8 through 2-12 are the computer-generated fringe plots corresponding to the photographs in Figures 3-5 to 3-9 of Section 3. The particular conditions and parameters used to realize these fringes experimentally is discussed in Section 3.

Consider first Figure 2-8 and Figure 3-5 (theory vs experiment). In general, the agreement is quite good. Not all of the fringes are shown in plots (b) and (c) because we elected to plot only 25 fringes in order to decrease the necessary computer time spent in calculating the fringes. We note that part (d) of the figure does not exactly agree with the experimental fringe picture. It was our experience that when the fringe count was near one $\lambda_c$ that it was quite difficult to exactly locate the fringe on the plot. This should not be viewed as a shortcoming because under these conditions we are working with one wavelength or less of wavefront aberration.

In comparing Figure 2-9 with Figure 3-6 we again observe close agreement between the theory and experiment; the same comments apply to the other figures except that the situation is somewhat different when coma is the dominant
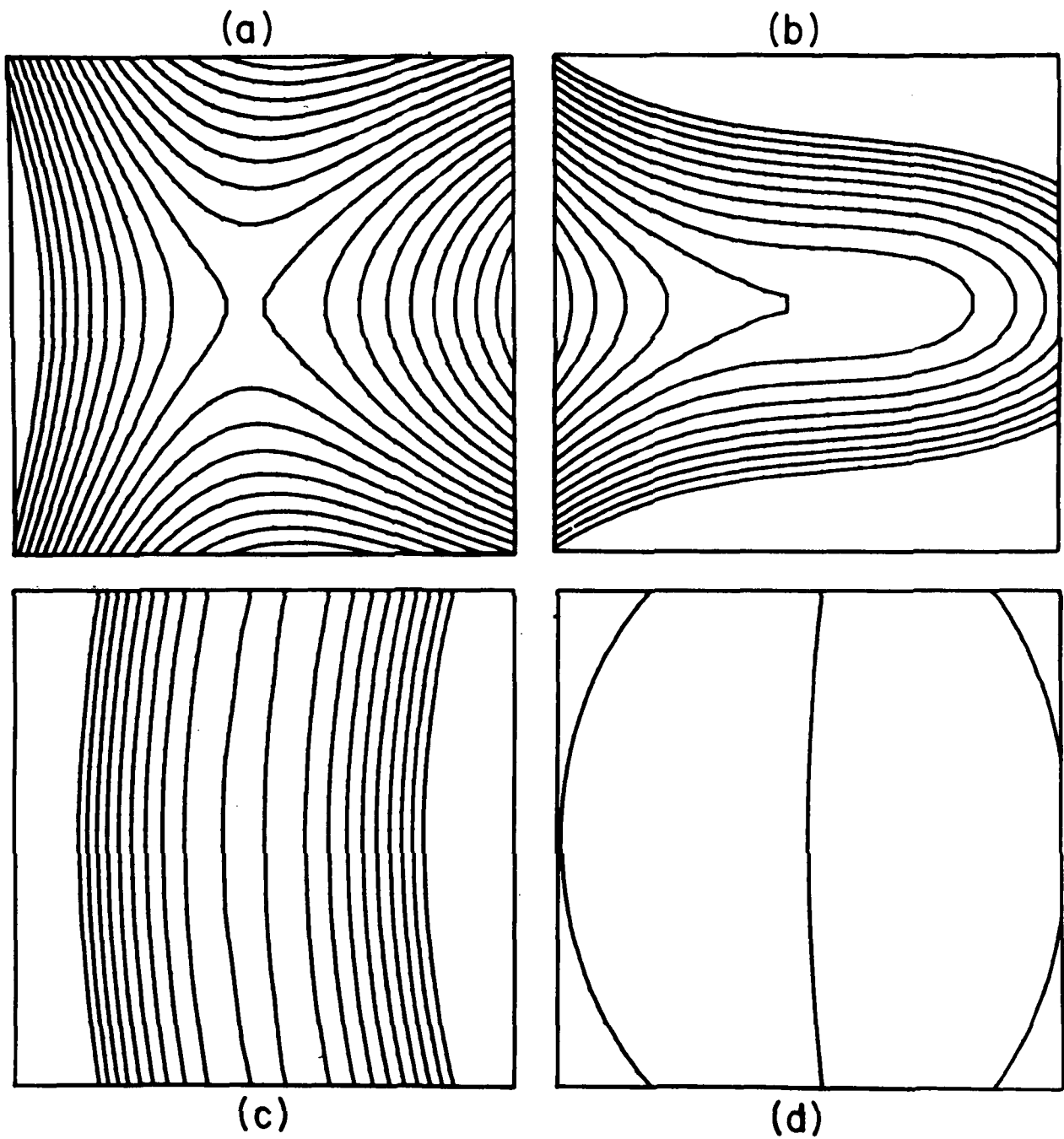
FIGURE 2-8. Theoretical analysis of chromatic aberration ($\lambda_c$ = 476.5 nm): (a) circle of least confusion, (b) tangential focus, (c) sagittal focus, and (d) wavelength optimization.
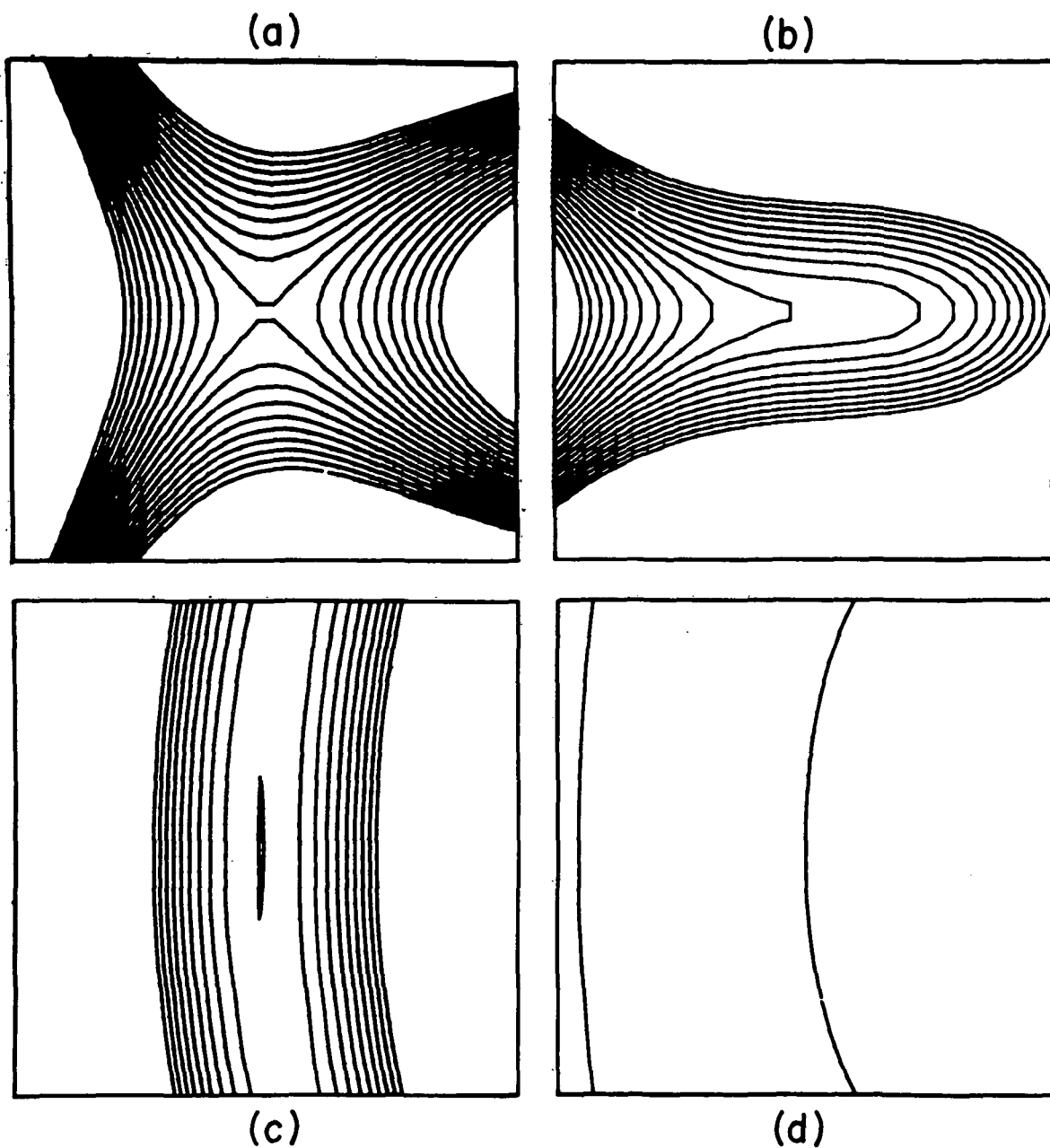
FIGURE 2-9.   Theoretical analysis of chromatic aberration ($\lambda_c$ = 514.5 nm):
(a) circle of least confusion, (b) tangential focus, (c) sagittal
focus, and (d) wavelength optimization.
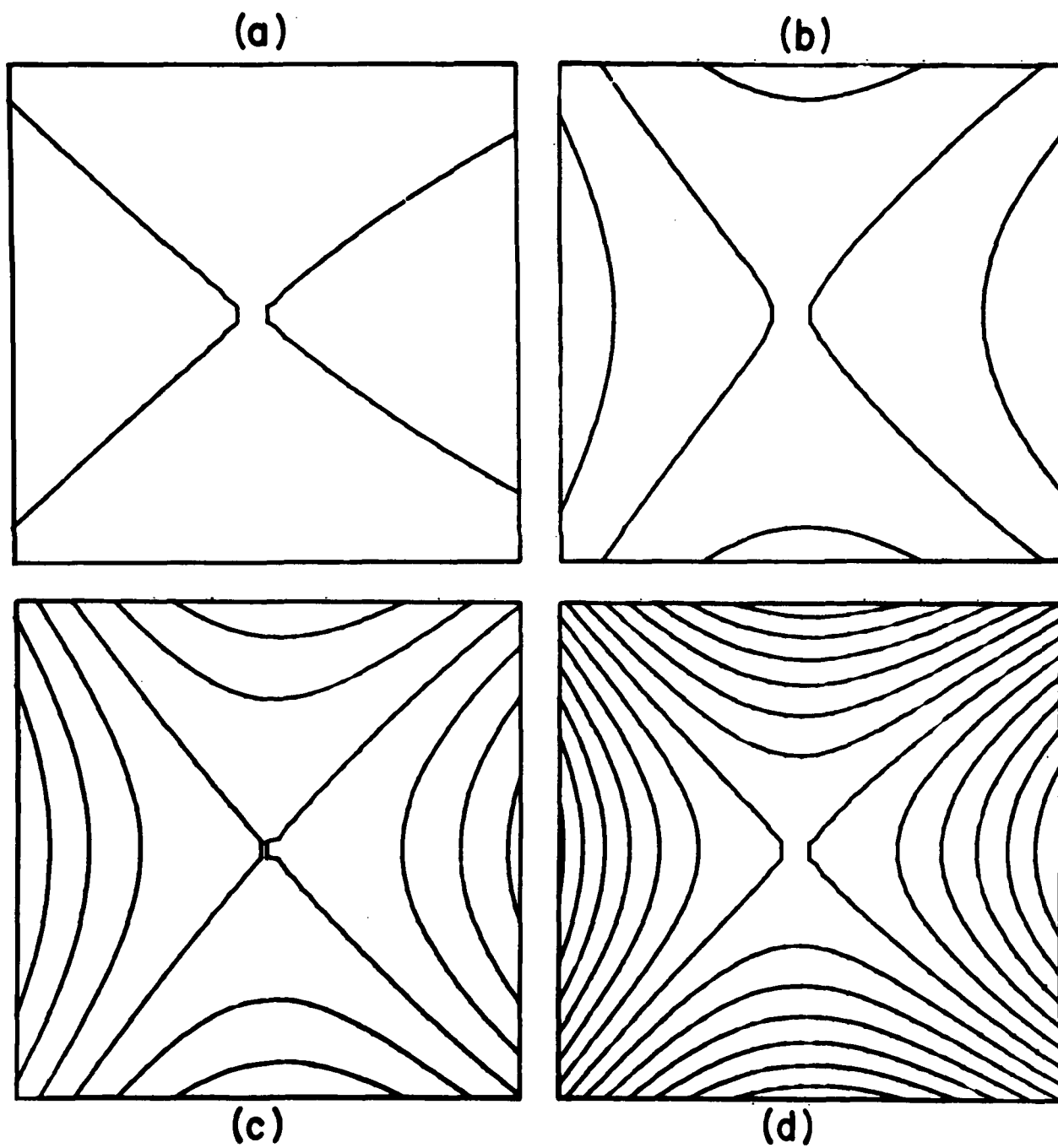
FIGURE 2-10. Theoretical analysis of Seidel aberrations ($x_0 - z_0$ plane): (a) $\Delta x_0 = 0.1$ mm, (b) $\Delta x_0 = 0.2$ mm, (c) $\Delta x_0 = 0.4$ mm, and (d) $\Delta x_0 = 0.8$ mm.
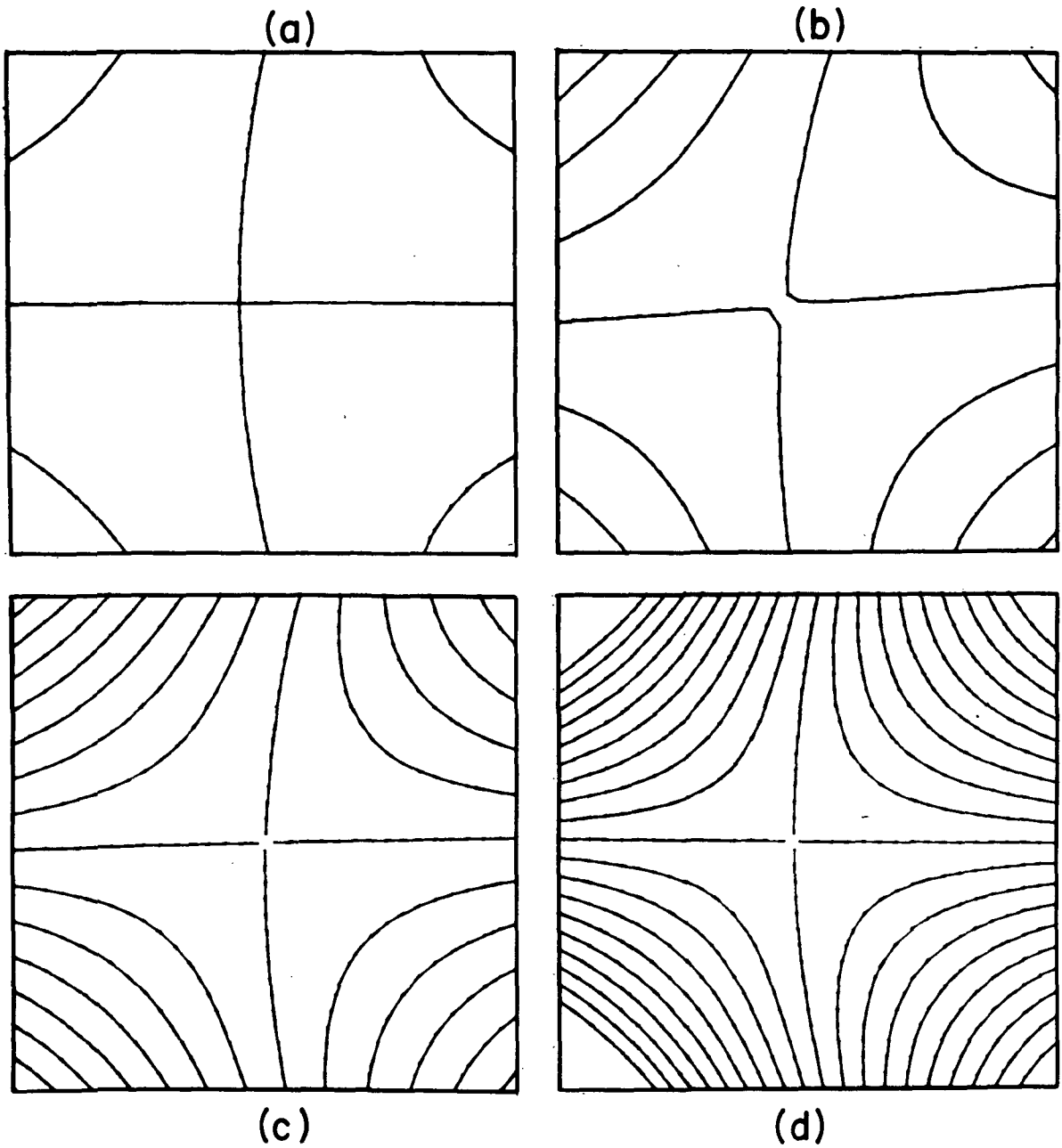
FIGURE 2-11. Theoretical analysis of Seidel aberrations ($y_0 - z_0$ plane):
(a) $\Delta y_0 = 0.1$ mm, (b) $\Delta y_0 = 0.2$ mm, (c) $\Delta y_0 = 0.4$ mm, and
(d) $\Delta y_0 = 0.8$ mm.
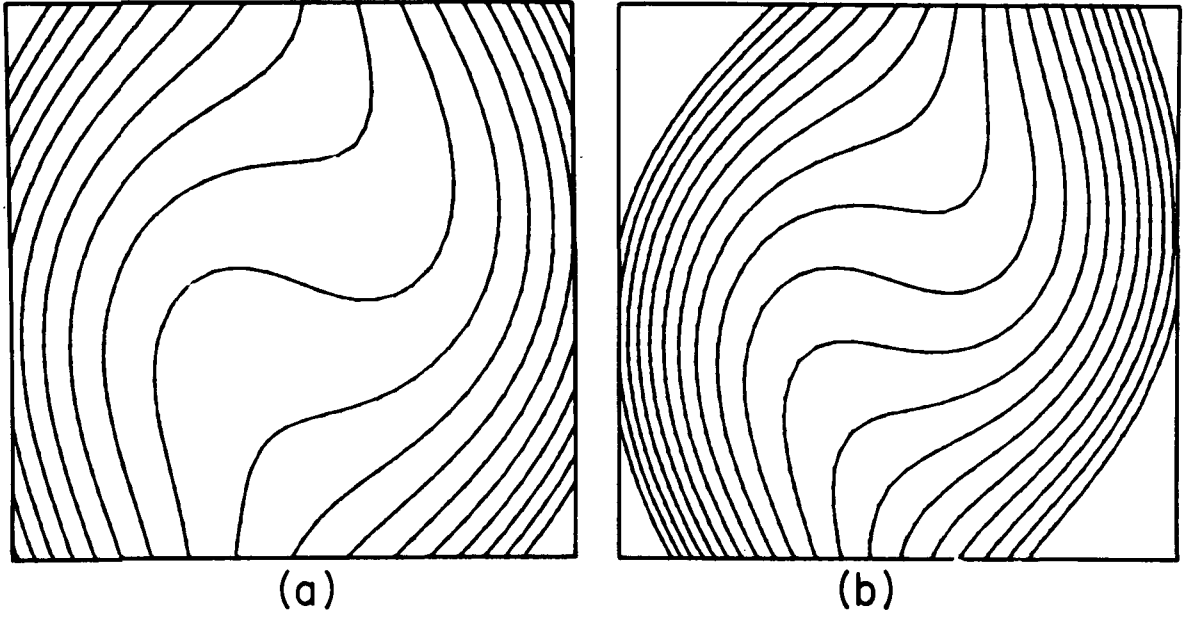
FIGURE 2-12. Theoretical analysis of Seidel aberrations (axial):
(a) $\Delta z_o$ = 2.5 mm and (b) $\Delta z_o$ = 4.5 mm.

21

aberration, as shown in Figure 2-12. The fringe pattern is quite curved, but not enough so that it folds back upon itself as in Figure 3-9 of Section 3. We should point out here that what is being observed is a limitation of the particular fringe merit function that was constructed. This merit function used as an input the total number of fringes that were counted from the center of the hologram along the +x, +y, -x, and -y axes. However, there was no mechanism included in the count of the fringes to allow a particular fringe to occur more than once. Thus, with respect to the fringes shown in Figure 3-9, a more appropriate merit function might include an intermediate fringe count located at the center of the fringe circles. This relatively small difference between the experimental results and the fringe plots does not infer any basic shortcoming in the analysis technique.

The aberrations present in geometries shown in Figures 2- through 2-12 are listed in Table 2-1. The table illustrates numerically several important factors that are shown in the computer plots. In both Figures 2-8 and 2-9, the wavelength optimization point (d) shows a significant reduction in aberrations and specifically the astigmatism and coma. Also in Figures 2-8 and 2-9, the aberrations do not change significantly when the focus moves to the circle of least confusion, tangential and sagittal foci. Figure 2-12 is the only case where coma is the dominant aberration, while in Figures 2-8 and 2-9 this aberration is small relative to astigmatism.

## 2.5 Summary and Conclusions

The results presented here establish a rather high level of confidence in ability of the computer-based models to accurately predict the results of the analysis of a single holographic element. It is also apparent that holographic elements are not unlike simple lenses in that they can exhibit large aberrations. Thus, it is only reasonable to expect that high levels of optical performance from holographic systems will only be realized through multielement systems.

**HARRIS ELECTRO-OPTICS CENTER**

TABLE 2-1

The Wavefront Aberrations Present in the Interferograms
Shown in Figures 2-8 to 2-12

| FIGURE | ABERRATIONS* | | | |
|---|---|---|---|---|
| | SPHERICAL | COMA | ASTIGMATISM | TOTAL |
| 8(a) | 0.23 | 8.2 | 20.1 | 20.8 |
| 8(b) | 0.23 | 8.2 | 20.0 | 23.8 |
| 8(c) | 0.23 | 8.2 | 20.2 | 19.3 |
| 8(d) | 0.24 | 1.6 | 0.14 | 0.6 |
| 9(a) | 0.75 | 19.9 | 48.6 | 53.7 |
| 9(b) | 0.75 | 19.9 | 48.6 | 58.0 |
| 9(c) | 0.75 | 19.9 | 48.6 | 48.5 |
| 9(d) | 0.45 | 2.0 | 0.15 | 0.75 |
| 10(a) | 0.009 | 0.28 | 1.6 | 1.6 |
| 10(b) | 0.012 | 0.69 | 3.3 | 3.2 |
| 10(c) | 0.024 | 1.4 | 6.7 | 6.7 |
| 10(d) | 0.06 | 2.5 | 13.3 | 12.9 |
| 11(a) | 0.01 | 0.35 | 1.8 | 1.7 |
| 11(b) | 0.02 | 0.63 | 3.3 | 3.1 |
| 11(c) | 0.04 | 1.3 | 6.7 | 7.3 |
| 11(d) | 0.08 | 2.6 | 13.5 | 13.5 |
| 12(a) | 0.99 | 10.6 | 0.59 | 8.9 |
| 12(b) | 1.8 | 19.5 | 0.93 | 16.9 |

*All aberrations expressed in terms of the reconstruction
wavelength $\lambda_c$.

HARRIS ELECTRO-OPTICS CENTER

## 2.6 Recommendations

This research has gone in a number of significant ways beyond a simple analysis of the performance of holographic optics. As a result, we now have a much better perspective of the shortcomings and attributes of these elements. A major conclusion of this work is that multielement holographic optical systems are the next logical step. We recommend that this work be continued with the same close tracking of experimental efforts with analysis and design.

## 2.7 References

1. Kubota, T., and T. Ose, J. Opt. Soc. Am., 61, 1539, 1971.
2. Latta, J., Appl. Opt., 10, 599, 1971.
3. Latta, J., Appl. Opt., 11, 1686, 1972.
4. Hooke, R. and T. A. Jeeves, J. Acm., 8, 218, 1961.

# 3

# EXPERIMENTAL INVESTIGATION

In this section we report data obtained from an experimental study of the properties of single and multiple holographic optical elements. A main objective of the study was to measure, over a fixed hologram aperture, the aberrations generated by either a change in reconstruction wavelength or by a shift of object point position. To obtain these data we used the interferometric technique suggested by Kubota and Ose.[1] We determined both chromatic and Seidel aberrations for several geometries and for a number of planar and volume recording media. Another objective was to verify theoretical predictions, based on computer ray tracing analyses such as developed by Latta,[2] about the imaging and aberration behavior of holographic zone plates. Finally, a practical objective was to determine some of the imaging properties and characteristics of single and of multielement holographic optical systems.

## 3.1 Basic Concepts for the Single Element Aberration Study

The Kubota-Ose interference method provides a means for displaying the total wavefront aberration of single holographic optical elements. The technique compares a known object point source with its holographic replica. The interference pattern generated by the original object wavefront and its holographic reconstruction gives a quantitative measure of the total number of waves of aberration. For an ideal reconstruction, the interfering wavefronts agree in phase over the aperture of the hologram. As a consequence, we observe a dark field (the holographic process introduces a constant 180° phase shift). Any deviation from the ideal reconstruction produces an interference pattern. The method is analogous in many ways to the Twyman-Green interferometric approach for testing conventional optics.

An interference pattern with a minimum number of fringes can always be found for any reconstruction geometry. This is equivalent to defining a minimum blur circle (circle of least confusion) or a sagittal or tangetial focus. We emphasize, however, that without a priori knowledge, the interference pattern obtained from some aberrated imaging condition is not generally unique. Furthermore, it does not explicitly display the types of aberration that are present, but only the total number of waves of aberration.

### 3.2  Experimental Setup and Appartus

The optical configuration used for the experimental investigation is shown schematically in Figure 3-1. Figure 3-2 is a picture of the actual experimental arrangement. A Spectra Physics 165 ion laser was used as a coherent light source. Since both krypton and argon plasma tubes were available with this laser, several recording and reconstruction wavelengths were available. An electro-mechanical shutter with a 1 ms to 10 s range was used for turning the laser beam on and off, a convenience utilized both for hologram recording and the photographic exposure of interference patterns. A small portion of the laser beam was used for monitoring laser power and mode structure. The remainder of the laser beam was divided into a reference and a signal beam to form matched interferometer paths. Each path (see Figure 3-1) provided a spatially-filtered, collimated beam that was about 150 mm in diameter. Note that the collimators are mounted on x-z translation stages. This permitted not only precise collimation, but also correction for chromatic defocus when the laser reconstruction wavelength was changed.

To form point sources we used two well-corrected 60 mm, f/2.4 achromatic lenses. The lenses were mounted on x-y-z Line Tool micropositioners that have a resolution of 2.5 μm on each axis. A rail and platform provided support for the micropositioner and allowed the position of a point source to be set with an accuracy of about 1 mm. Final settings were made with the micropositioners.
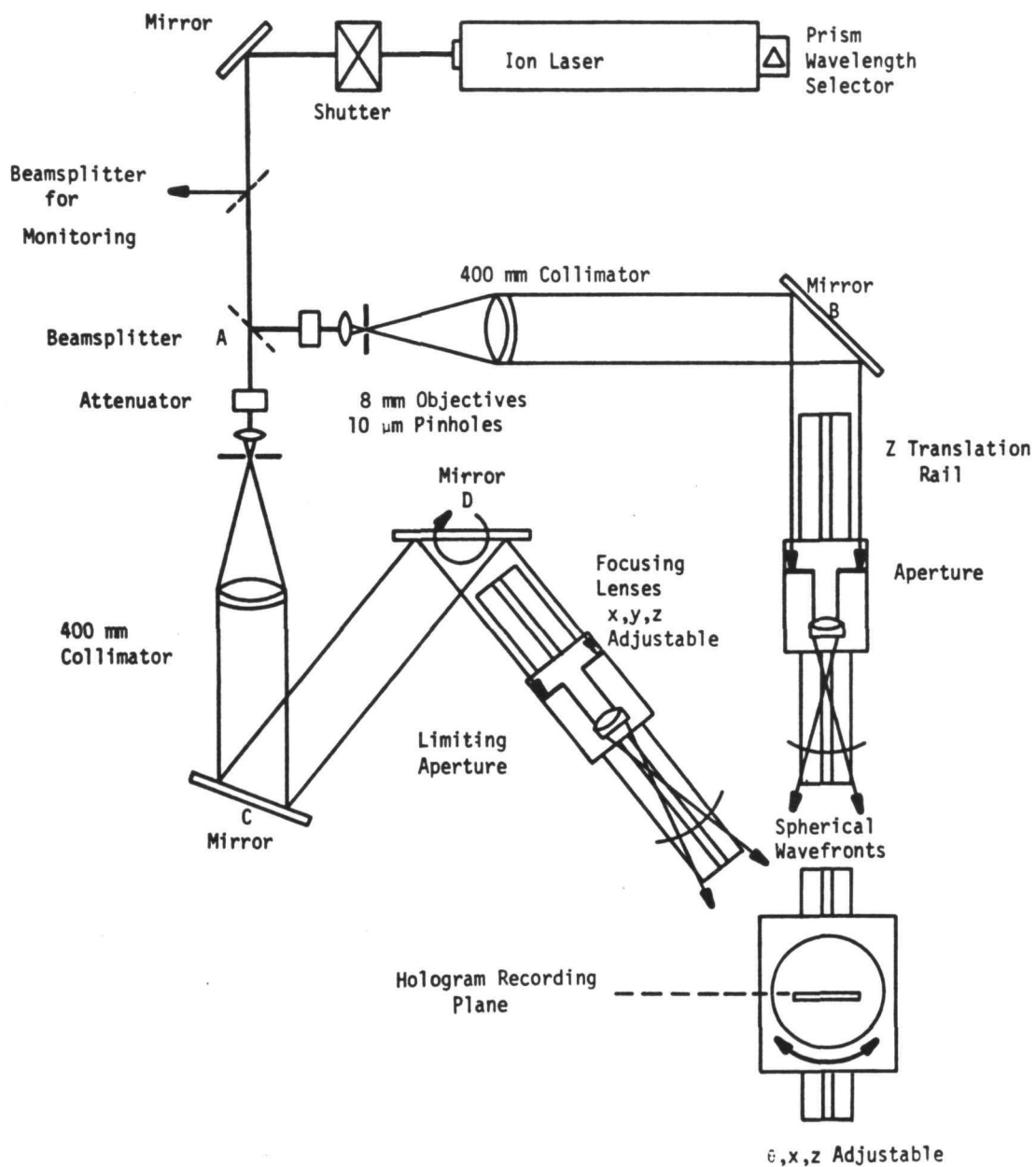
FIGURE 3-1. Schematic diagram of the experimental setup used for the aberration investigation.
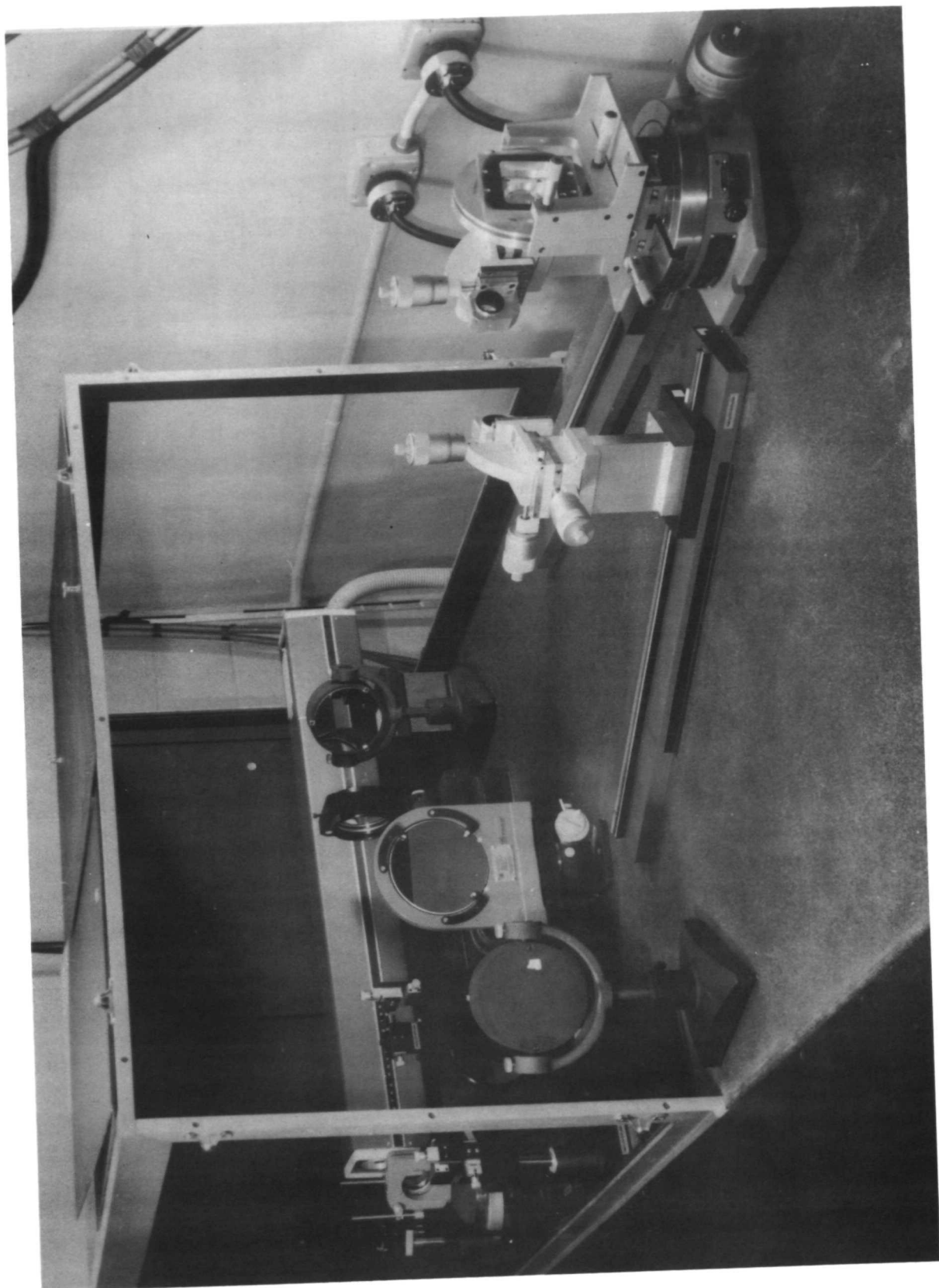
FIGURE 3-2. Photograph of the experimental setup.

The hologram plateholder was designed to provide both translational and rotational degrees of freedom. The plateholder accepts 50 mm x 50 mm plates with a clear aperture of 45 mm diameter. We attached the plateholder to a Lansing gimbaled mount that in turn was placed on top of x-z Lansing translation stages. The entire assembly was mounted on a Troyke rotary table. A platform and rail were available for course z-translation.

The recording material was held in the plateholder by means of three thumb screws. Repeatability of position was obtained by resting the recording material substrate on three pins. This permitted the removal of the exposed recording material for chemical processing and subsequent replacement with good precision. We were able to consistently obtain the zero fringe, dark field initial condition without difficulty.

The average angle between the reference and object beams $<\theta>$ was fixed at 29.°5. The plateholder was oriented so that the average fringe vector $<\bar{K}>$ was parallel to the hologram surface; we abbreviate this fact by saying that $<\bar{K}>$ = split bisector. By means of changes in the radial distances of the reference and object points, we varied the bending factor Q of the holographic optical elements while maintaining the focal length f = 400 mm constant. The bending factors used were Q = 1, 2, and 4. The clear aperture of the holographic optical element was 1.75 inches (44.5 mm) in diameter. For the photographs of interferograms shown in Appendix A, the diameters are shown as 2.5 inches (63.5 mm) to enable better interpretation of the interference patterns.

## 3.3 Experimental Procedure

The procedure followed for obtaining experimental data started with the selection of a recording geometry and wavelength. The hologram recording material was carefully placed in the precision holder, exposed, and removed for chemical processing. Without disturbing the experimental setup, the processed plate was repositioned in the plateholder to obtain the zero fringe condition; i.e., the interference between the real object point and the reconstructed holographic object point was made to consist of a single dark

fringe over the entire hologram aperture. After completing this task, we proceeded with the measurement of chromatic and Seidel aberrations.

To determine chromatic aberrations, the reconstruction wavelength was changed and the signal and reference beams carefully recollimated. The position of the reconstruction point was left fixed, but the position of the object point was adjusted to coincide with the new position of the reconstructed image point. This adjustment was necessary to compensate for first order aberrations (defocus and lateral shift) which greatly exceed the chromatic aberrations.

Because of the chromatic aberrations, the reconstructed image point was not "diffraction-limited". In general, the adjustment of the object point was made to produce some equivalent focal condition, e.g., the circle of least confusion, of the reconstructed image point. A photograph was made of the interference pattern generated by the adjusted object and reconstructed image waves. The interference pattern was characteristic of some combination of chromatic aberrations. A photograph was taken 25 centimeters behind the hologram plane without imaging. However, the interference pattern at this plane agrees point for point with the pattern at the hologram plane; that is, the fringes are localized in the hologram plane.

Photographs were taken for a number of different wavelengths, and also for the case where the reconstruction point was moved. The reconstruction point was moved to accomplish aberration balancing. By this we mean that reconstruction and object point positions were found that yielded a minimum fringe interference pattern within the hologram aperture.

For Seidel aberration measurements we first made the reconstruction and construction wavelengths equal. Then the experimental setup was carefully returned to its initial state. The criterion for this was a completely dark field within the hologram aperture. By displacing the reconstruction point source in a plane transverse to the radial line joining the hologram center, we generated various Seidel aberrations. This is equivalent to "mapping" the

HARRIS ELECTRO-OPTICS CENTER

angular field of the holographic optical element. We also investigated the effect of radial displacements. As in the case of the chromatic aberration study, photographs were made of the interference pattern corresponding to each reconstruction pertubation.

### 3.4 Coordinate Systems and Definitions

Figure 3-3 describes the geometry and coordinate systems applicable for all experimental data. Note that the reference and object point coordinate systems are right-handed and use the radial distances $R_R$ and $R_0$ to define the z-axes. These coordinate systems were selected to coincide with the axes of the precision micropositioners.

In our investigation of chromatic aberrations, we photographed fringe patterns corresponding to residual aberrations at the "circle of least confusion" and at the tangential and the sagittal foci. As with conventional lenses, the image of a point formed by a holographic optical element is a line at either the tangential or sagittal focus. The meaning of "circle of least confusion" also remains the same. However, there is some modification to the meaning of the terms tangential and sagittal planes. Figure 3-4 defines these planes for the virtual image mode of hologram reconstruction.

Throughout this section (and in Appendix A) various symbols, abbreviations, and parameters are used on graphs and in tables. For convenience we have compiled a list of these quantities. They are as follows:

$(x_h, y_h, 0)$ = hologram origin

$(x_0, y_0, z_0)$ = object point position

$(x_R, y_R, z_R)$ = reference point position

$(x_I, y_I, z_I)$ = image point position

$(x_c, y_c, z_c)$ = reconstruction point position

$\lambda_0$ = recording wavelength

$\lambda_c$ = reconstruction wavelength

**HARRIS ELECTRO-OPTICS CENTER**
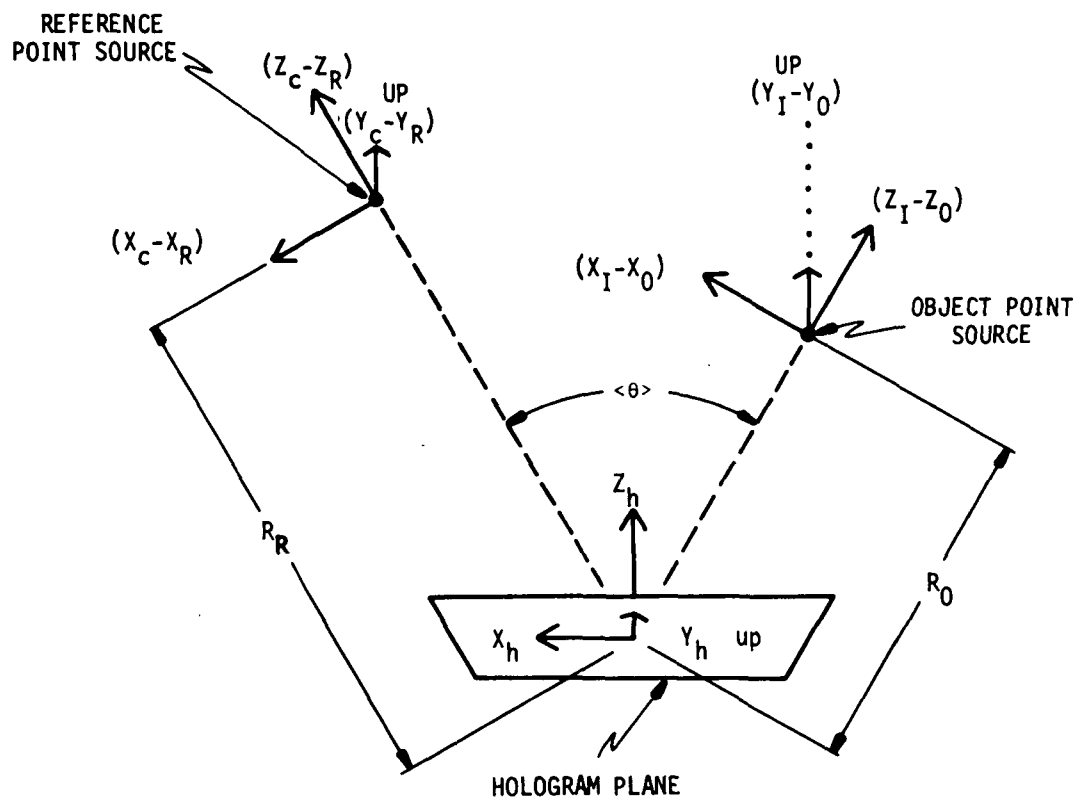
FIGURE 3-3. Top view of the hologram recording and reconstruction geometry together with coordinate systems.

FOLDED SAGGITAL PLANE

HOLOGRAM

CHIEF RAY

$R_C$

$O$

$R_O$

$R_I$

$R_R$

IMAGE TANGENTIAL PLANE

OPTICAL AXIS

OBJECT TANGENTIAL PLANE
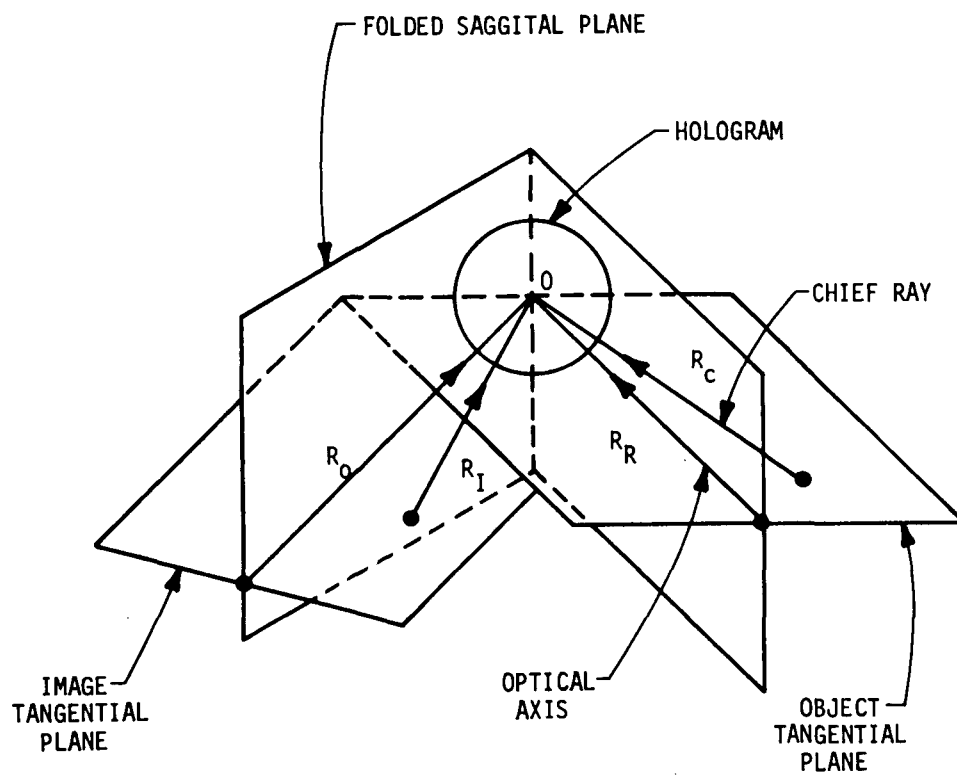
FIGURE 3-4. The tangential and sagittal planes associated with a single holographic optical element in the virtual image reconstruction mode.

$$\Delta x_i = x_I - x_o$$

$$\Delta y_i = y_I - y_o$$

$$\Delta z_i = z_I - z_o$$

$$\Delta x_c = x_c - x_R$$

$$\Delta y_c = y_c - y_R$$

$$\Delta z_c = z_c - z_R$$

$\Delta\alpha_c, \Delta\beta_c$ = angular motions relative to the hologram plane of the recon-
struction beam (plane waves only)

$$Q = (R_R + R_o)/(R_R - R_o)$$

$\Delta_x$ = number of waves of aberration along the $x_h$ axis

$\Delta_y$ = number of waves of aberration along the $y_h$ axis

$|\Delta_G|$ = total aberration, wavelengths

$|\Delta_G|_c$ = total chromatic aberration, wavelengths

$|\Delta_G|_s$ = total Seidel aberrations, wavelengths

SBP = space bandwidth product

### 3.5 Experimental Data for Single Holographic
Optical Elements

We have already noted that several recording geometries were selected
for the single element aberration study. In addition, we also selected a
number of promising recording materials for evaluation. The materials were
Kodak HR plates (amplitude and phase), dichromated gelatin, and cellulose
acetate butyrate.[3] Further information about these materials can be found
in Section 4.

Our experimental data is summarized with both photographs and tables in
Appendix A. Each photograph is an interferogram that corresponds to some form
and amount of aberration for a given experimental condition. The tables give
in quantitative form the geometry associated with each aberration condition,
the type of aberration, and the number of waves of aberration.

HARRIS ELECTRO-OPTICS CENTER

The experimental data is arranged in seven groups. Groups 1 to 4 contain data for holographic optical elements recorded on Kodak HR plates (unbleached). Group 1 concentrates on chromatic aberration while Group 2 considers only Seidel aberrations; both cases are for $Q = 4$. Groups 3 and 4 contain data for both chromatic and Seidel aberrations for $Q = 1$ and 2, respectively. Groups 5 to 7 summarize data for various phase recording materials. A Q value of 4 was used for these groups, and both chromatic and Seidel aberration data were collected.

We present experimental data relevant to each group in Appendix A. The format is (1) an explanatory introduction, (2) a table of recording and reconstruction parameters, together with an experimental count of total waves of aberration (3) a table listing type and number of waves of aberration for each experimental condition listed in (2) obtained by computer analysis, and (4) a series of photographs of interference patterns together with their computer generated verifications. The data in Appendix A summarizes both analytical and experimental work reported in previous quarterly reports.

As an aid to interpreting some of the experimental data in Appendix A, we briefly describe in this section one of the data groups. We selected the data from Group 5 as being representative of the aberration properties of single holographic optical elements. These data were previously discussed in Section 2-4.

Thus, in Figures 3-5 through 3-9, the interferometric aberration profile of a bleached Kodak High Resolution emulsion is given for construction parameters $R_o = 160$ mm and $R_R = 267$ mm, a recording wavelength $\lambda_o$ of 488 nm, and a clear aperture of 45 mm. The focal length f of the holographic optical element was 400 mm with a bending factor Q of 4.

Figures 3-5 and 3-6 illustrate aberrations introduced by wavelength shifts corresponding to reconstruction wavelengths $\lambda_c$ of 476.5 nm and 514.5 nm. We photographed the interference patterns for conditions equivalent to the circle of least confusion, the tangential focus, and the sagittal focus; these results are shown in photographs (a), (b) and (c) of Figures 3-5 and
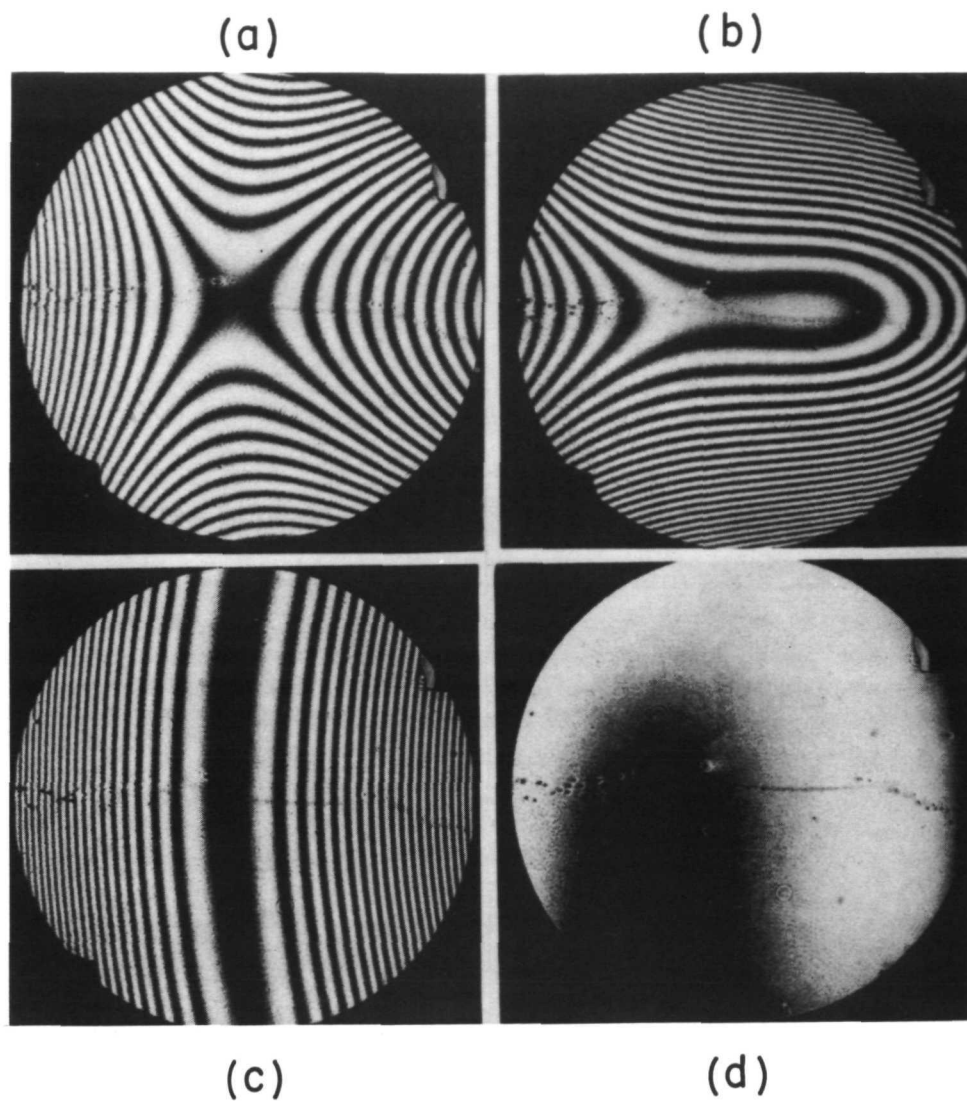
FIGURE 3-5. Chromatic aberration ($\lambda_c$ = 476.5 nm): (a) circle of least confusion, (b) tangential focus, (c) sagittal focus, and (d) wavelength optimization. Note that the total number of waves of aberration in (a), (b), and (c) are equal. The principal aberration is astigmatism.

36
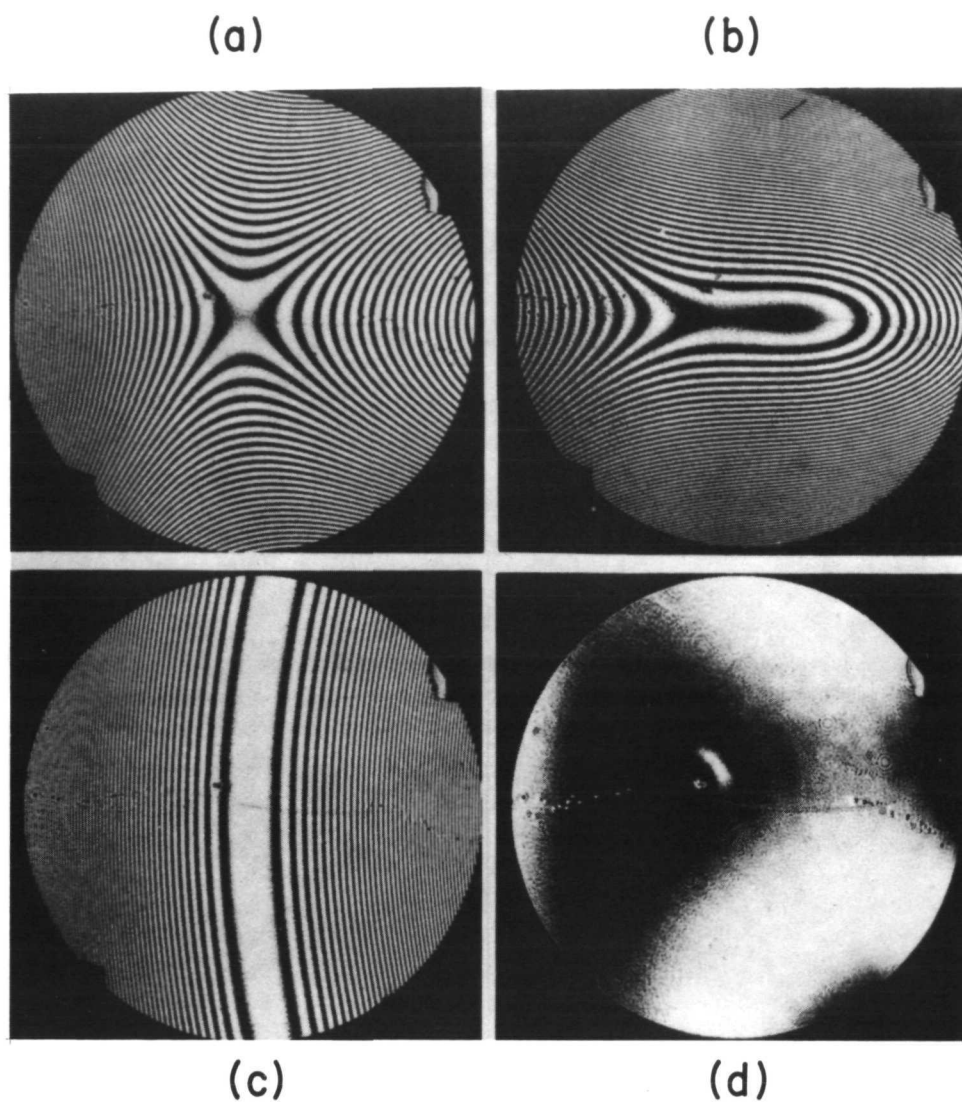
FIGURE 3-6. Chromatic aberration ($\lambda_c$ = 514.5 nm): (a) circle of least confusion, (b) tangential focus, (c) sagittal focus, and (d) wavelength optimization. Note that the total number of waves of aberration in (a), (b), and (c) are equal. The principal aberration is astigmatism.

37
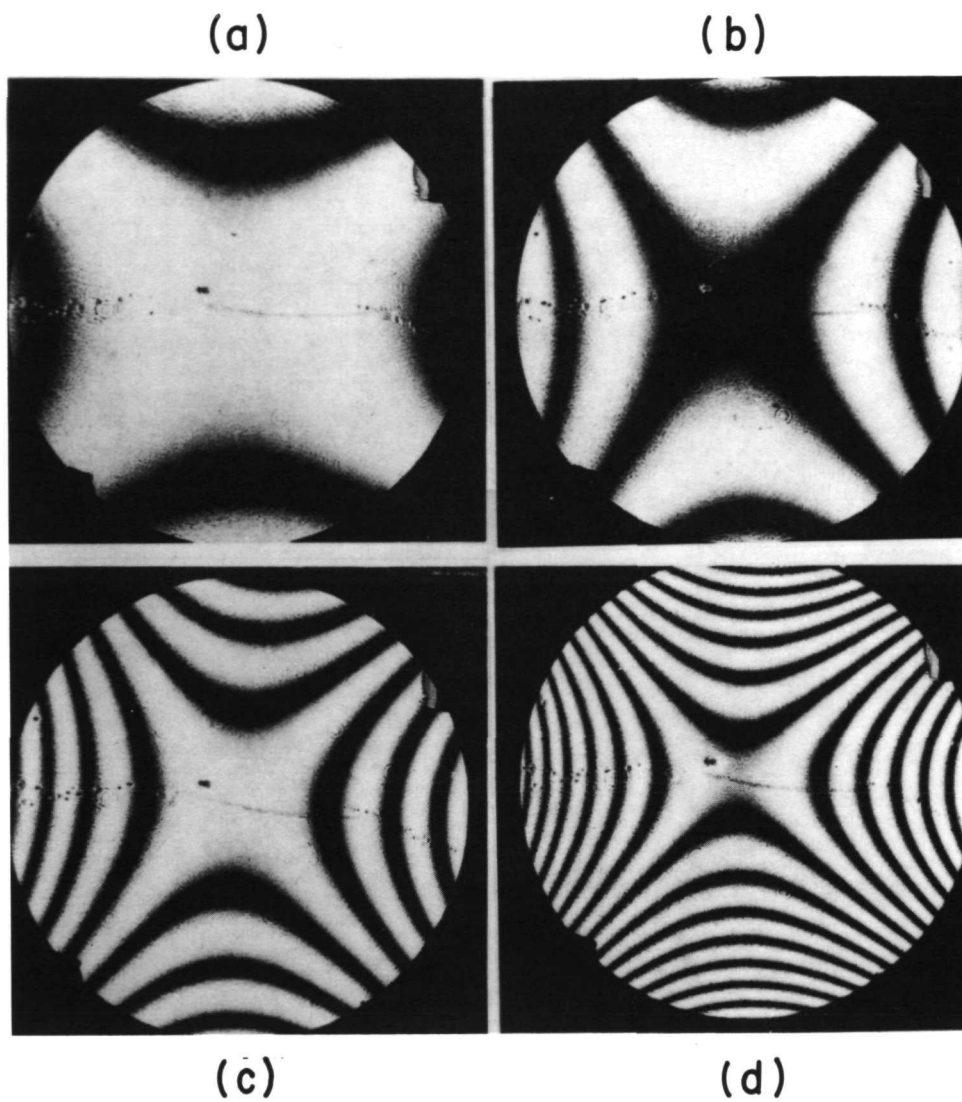
FIGURE 3-7. Seidel aberrations ($x_o$-$z_o$ plane): (a) $\Delta x_o$ = 0.1 mm, (b) $\Delta x_o$ = 0.2 mm, (c) $\Delta x_o$ = 0.4 mm, and (d) $\Delta x_o$ = 0.8 mm. The principal aberration is astigmatism.

FIGURE 3-8.  Seidel aberrations ($y_0$-$z_0$ plane):  (a) $\Delta y_0$ = 0.1 mm,
(b) $\Delta y_0$ = 0.2 mm, (c) $\Delta y_0$ = 0.4 mm, and (d) $\Delta y_0$ = 0.8 mm.
The principal aberration is astigmatism.

**(a)**                    **(b)**

FIGURE 3-9.  Seidel aberrations (axial):  (a) $\Delta z_0$ = 2.5 mm and
(b) $\Delta z_0$ = 4.5 mm.  The primary aberration for this
case is coma rather than astigmatism.

and 3-6. Photograph (d) in Figures 3-5 and 3-6 represents a condition of wavelength optimization. That is, the spatial location of an object point that results in an aberration-free image for the condition $\lambda_c \neq \lambda_o$. Although this possibility has been predicted by analysis, this appears to be the first experimental confirmation.

Figures 3-7 and 3-8 show total waves of Seidel aberrations as a function of the semiangular fields in the $x_o$-$z_o$ and $y_o$-$z_o$ planes. The interferograms were photographed for a condition equivalent to the circle of least confusion. The minimum angle was 0.635 mrad in photograph (a) and doubled for each suceeding photograph as shown in (b), (c), and (d) of Figures 3-7 and 3-8. This is roughly equivalent to imaging an object about 2 mm in diameter for the largest angle.

Figure 3-9 shows the number of waves of aberration generated by translating the object point axially; that is, along the optical axis of the hologram. The interferogram represents one of two equivalent conditions of minimum fringe count. The translation distances were 2.5 mm for (a) and 4.5 mm for (b).

## 3.6 Graphical Data

In the preceding section and in Appendix A extensive photographic and tabular data obtained by interferometric means are given that describe the chromatic and Seidel aberrations of single holograhic optical elements for three different geometries and a number of different recording materials. In this section we summarize with relevant curves the most important aspects of the experimental research. Our selection of data for graphical display was in a large measure influenced by the requirements of the analytical investigation and by the need to demonstrate the practical aspects of holographic optics.

Figure 3-10 shows chromatic aberration in wavelengths as a function of reconstruction wavelength $\lambda_c$ with Q as a parameter. The solid curves are for wavelengths of aberration counted along the hologram x-axis; the dashed curves are for wavelengths of aberration along the hologram y-axis. The magnitude of the chromatic aberrations will be rather large for spectral components of an object more than about ±10 nm on either side of the recording wavelength $\lambda_0$. Of course, we showed that object points exist that reduce chromatic aberration significantly. However, this is true only for a single object point; multielement holographic optical systems are required for achromatization.

A locus of focus plot is given in Figure 3-11. That is, we have plotted the change in effective focal length of the holographic optical element as a function of wavelength with Q as a parameter. To obtain the change in foci we used the relationship

$$\Delta f = \left(\frac{f}{R_c}\right)^2 \Delta R_c ,$$

where f is the nominal Gaussian focal length given by

$$\frac{1}{f} = \mu\left(\frac{1}{R_R} - \frac{1}{R_0}\right)$$

Note that our experimental values are different from the values predicted by the paraxial formula

$$\Delta f = \left(\frac{1-\mu}{\mu}\right) f$$

This is because the Gaussian focus is not influenced by chromatic aberrations or bending factor. Table 3-1 illustrates the differences.
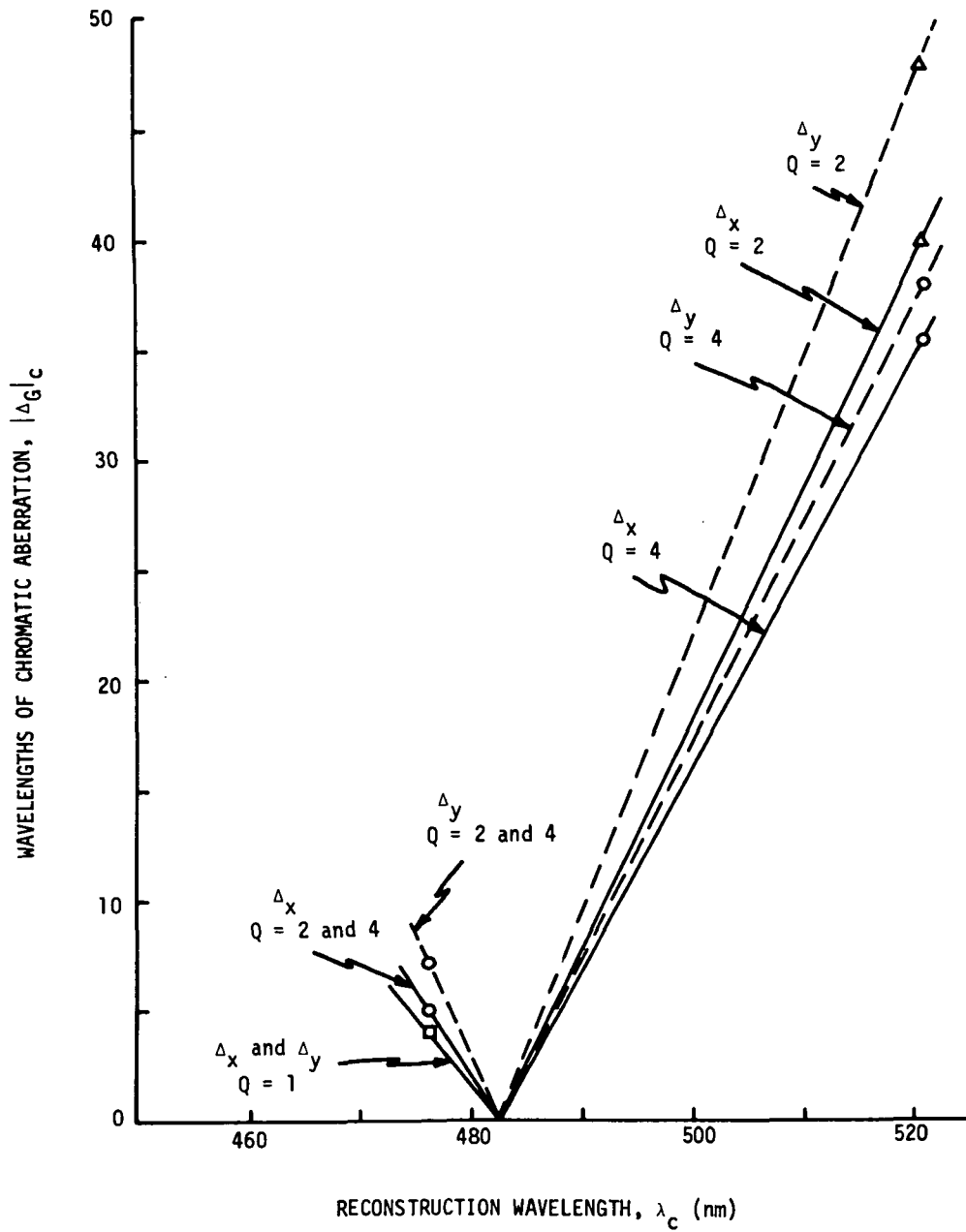
FIGURE 3-10. Chromatic aberration as a function of wavelength with Q as a parameter.
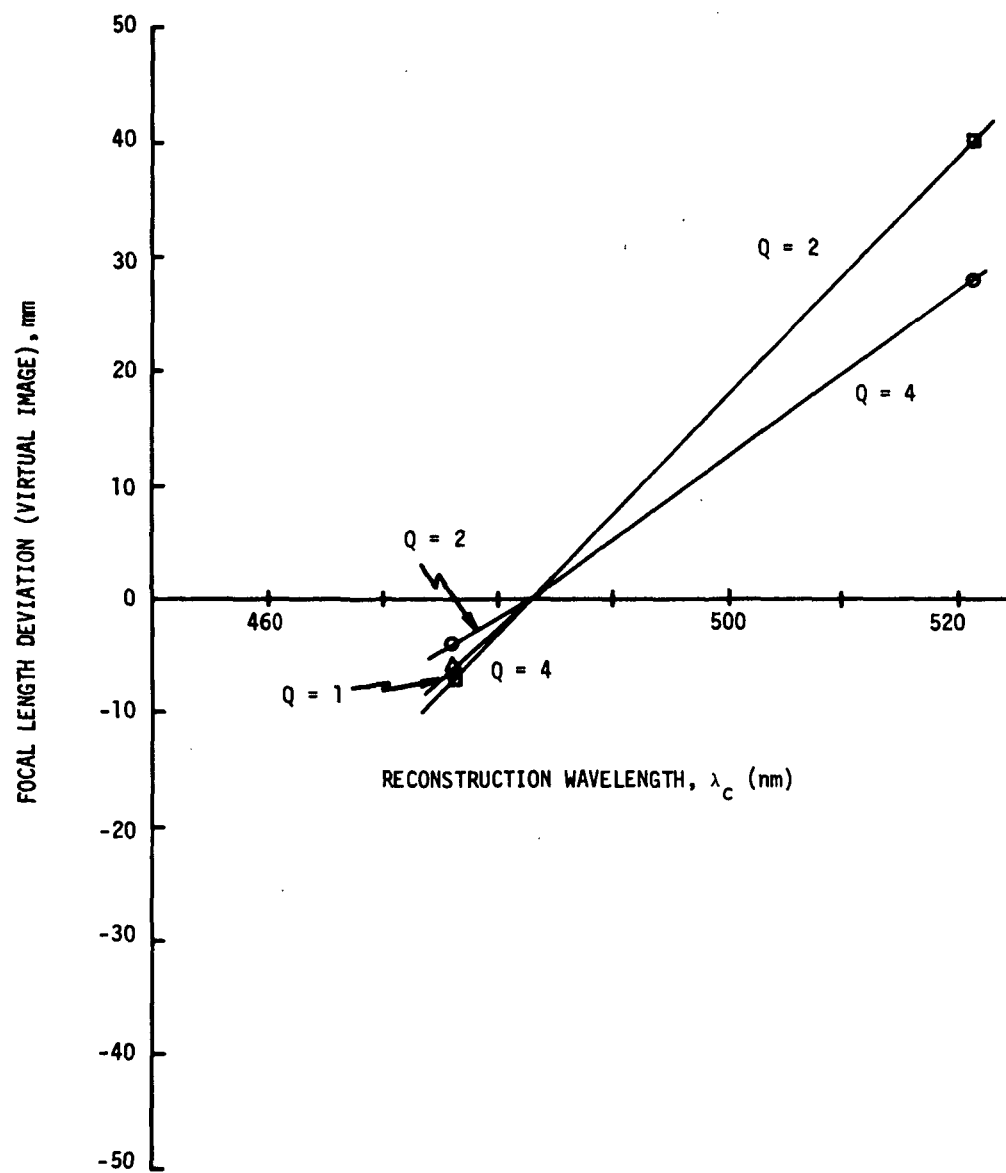
FIGURE 3-11.  Locus of focus plot with Q as a parameter.

TABLE 3-I

FOCAL LENGTH VS WAVELENGTH

| $\lambda_c$ (nm) | Q | $\Delta f$ (Gaussian) | $\Delta f$ (experimental) |
|---|---|---|---|
| 476.2 | 1 | - 5.31 mm | - 5.8 mm |
| 476.2 | 2 | - 5.31 mm | - 6.6 mm |
| 476.2 | 4 | - 5.31 mm | - 4.2 mm |
| 520.8 | 1 | + 29.9 mm | * |
| 520.8 | 2 | + 29.9 mm | + 40.2 mm |
| 520.8 | 4 | + 29.9 mm | + 28.7 mm |

* Data not available

For the case of Seidel aberrations we restrict our attention to the x-direction along the hologram aperture. Figure 3-12 shows total Seidel aberrations in wavelengths as a function of field angle $\Delta\alpha$ with Q as a parameter. The amount of aberration increases fairly rapidly with increasing field angle and is greatest for Q = 4, as expected from a classical point of view.[4] For a plano-convex lens the equivalent bending factor is Q = 1 and, for our geometric arrangement, this approximately satisfies the conditions necessary to minimize spherical aberration and to reduce coma to zero. For increasing values of Q, the Seidel aberrations in general tend to increase.

We have generally thought of holographic optical elements in terms of their imaging properties. From the point of view of communication theory, the information transmission properties of the holographic optical elements are also of interest. A quantitative measure of the imaging quality of a holographic optical element is given by its number of degrees of freedom or space bandwidth product (SBP). Figure 3-13 shows SBP (three dimensional) as a function of field angle with Q as a parameter. The curves are straight lines with unit slope on a log-log graph. The experimental data thus predict a linear relationship between SBP and field angle. This is in good agreement with the fact that the principle aberration is astigmatism.

We computed each SBP from experimental data. In review, the SBP is defined as the ratio of the area of the signal space to the area of a diffraction-limited spot. Mathematically, we have that

$$SBP = \frac{A_s}{\Delta A}$$

where $A_s = (f\Delta\alpha)^2$

$A = (1.22 \; \lambda f/D)^2$ and

D and f are the hologram exit pupil diameter and focal length, respectively.

**HARRIS ELECTRO-OPTICS CENTER**
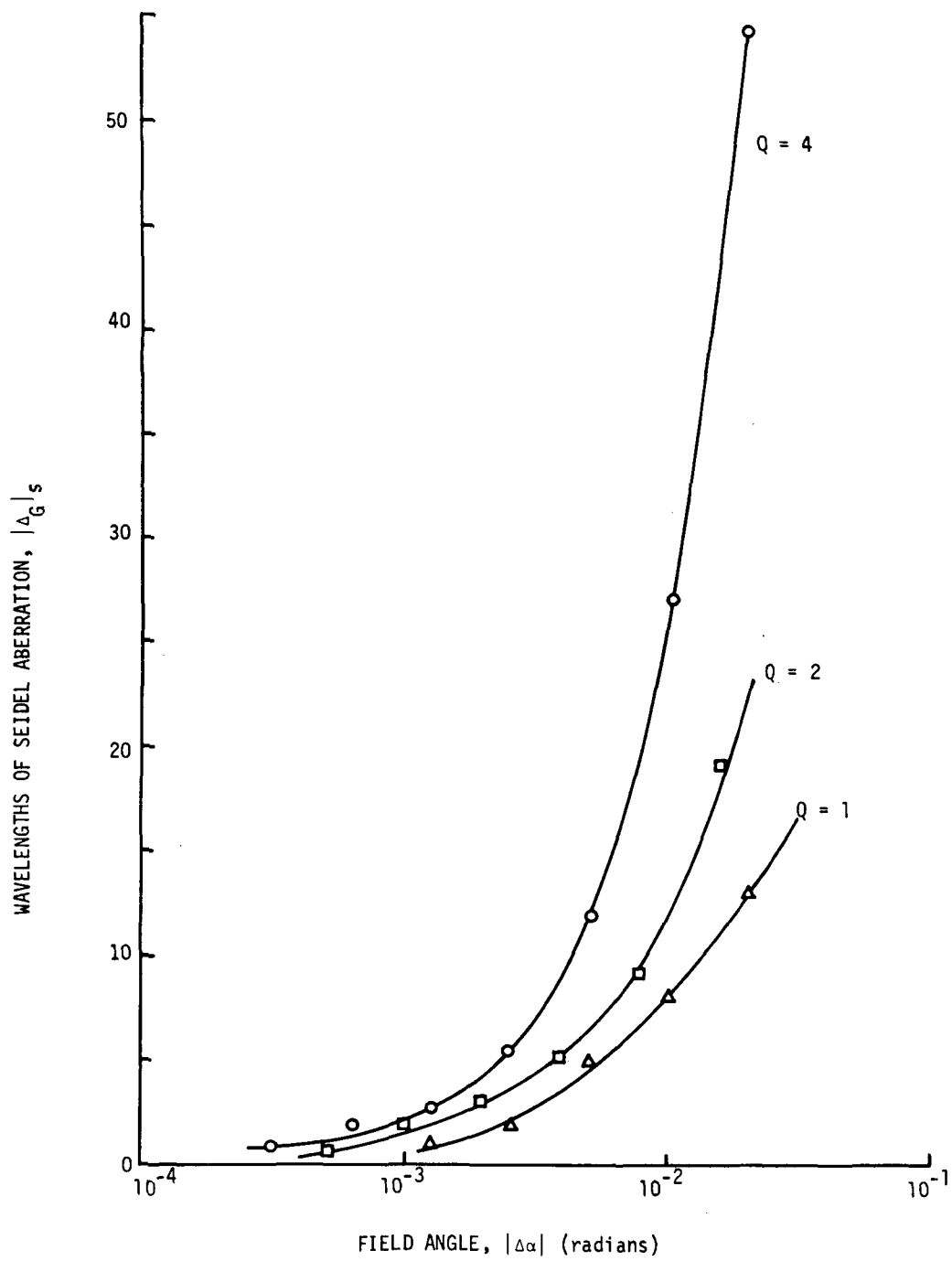
FIGURE 3-12. Seidel aberrations as a function of field angle.
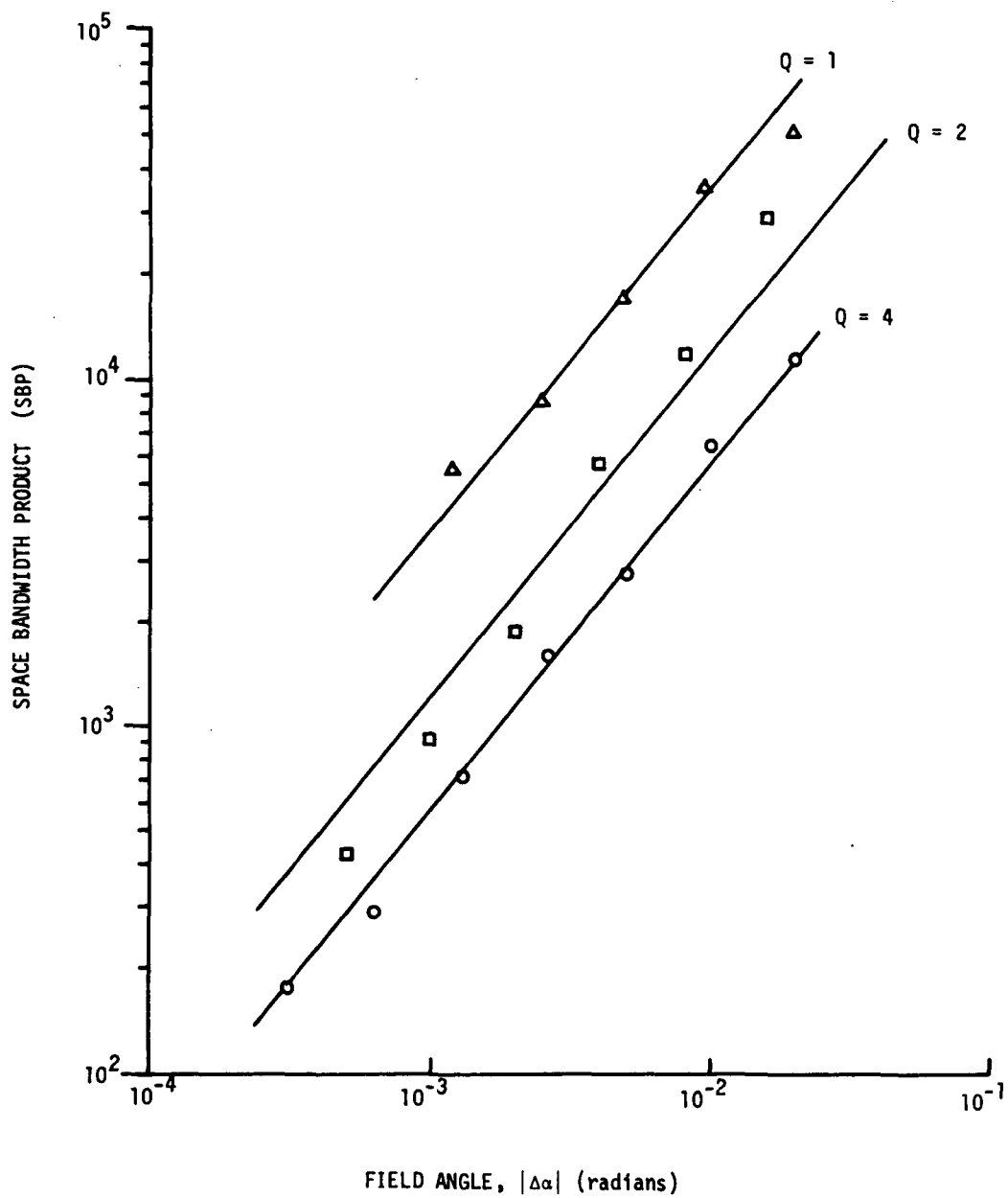
FIGURE 3-13. Space bandwidth product as a function of field angle with Q as a parameter.

This equation becomes

$$SBP = \frac{2}{3}\left(\frac{\Delta\alpha D}{\lambda}\right)^2$$

We chose $\lambda_c = \lambda_0$, and $\Delta\alpha$ is the independent variable.

The magnitude of D is determined by the maximum number of waves of aberration allowed in the holographic optical element exit pupil. To measure D we determined the diameter that most closely matched the area in the hologram aperture that corresponded to one full wave of aberration. Then, in accordance with the Rayleigh $\lambda/4$ criterion, we divided each diameter by two. In other words, D is taken to be twice the radial distance from the hologram origin to the first circle of constant $\lambda/4$ phase shift.

### 3.7 Single and Multielement Experimental Investigation

During the fourth quarter the imaging properties of single and multiple holographic optical elements were studied. Simple one and two element designs that have well known conventional lens counterparts were constructed for the study. This study supplements previous experimental work that concentrated on aberrations as measured in the exit pupil of the hologram. We show the effect of aberrations on the image of point objects and a 1951 Air Force resolution target. Our objectives were to show that holographic optical elements can be used in a manner similar to conventional optics, and to determine the similarities and the differences in the imaging properties of holographic optical elements and conventional optics.

### 3.7.1 Classical Imaging Experiments with a Single Holographic Optical Element. — A holographic optical element was recorded using the geometry shown in Figure 3-14. The reference beam was collimated and incident at an angle of 30° with respect to the hologram normal. The signal beam was a spherical wave expanding from a point 400 mm in front of the hologram.
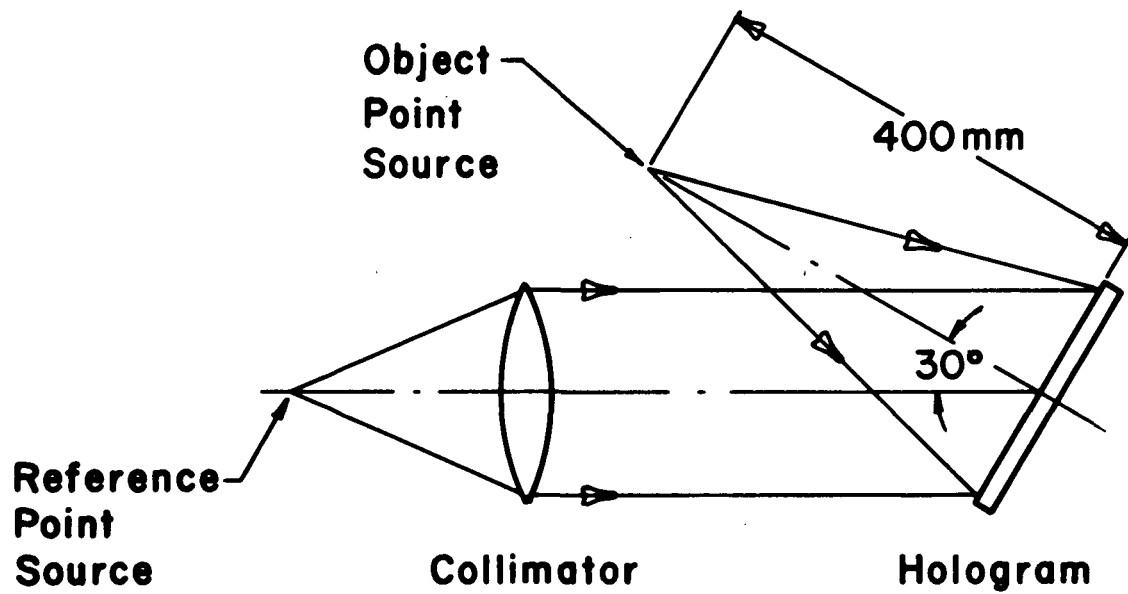
FIGURE 3-14. Recording geometry for holographic optical element construction.

Hence, the focal length f was 400 mm and the bending factor Q was 1. The hologram was recorded on a Kodak High Resolution emulsion and subsequently bleached to produce a high quality and efficient holographic optical element. The clear aperture was 45 mm; thus, the holographic optical element was nominally an f/9 system.

The geometry shown in Figure 3-15 was used for reconstruction and imaging. This configuration corresponds to using the holographic optical element as a telescope objective, but in reverse. The analysis of the imagery obtained is, however, equivalent to the case of a telescope; i.e., the case where the object and image planes are reversed. By using a rapidly spinning diffuser behind an Air Force resolution target, incoherent illumination was produced and thus, the limiting resolution is twice that obtained by using a plane wave to illuminate the target. An adjustable aperture was placed directly in front of the holographic optical element so that a study of image resolution and quality could be made as a function of f-number. The image rays from a point on the target, that unaltered would form an image at infinity, were brought to focus with a well-corrected lens. The aerial image was enlarged with a microscope objective and photographs were taken.

A problem was noted in the course of this experiment. Initially the image of a single point source through the holographic optical element was examined and found to be badly aberrated as shown in Figure 3-16. The cause of the aberrated point focus was due to lack of flatness of the glass substrate of the photographic emulsion. The holographic optical element produced a diffraction-limited point image only when apertured down to f/32 or smaller. This will have to be taken into account when interpreting the results for the present study. In future studies of potential applications such as large aperture holographic optical elements, specially prepared substrates having the appropriate optical quality will be required.

Laser
Beam

Spinning Diffuser

Air Force Resolution
Target

Adjustable Aperture

Magnified
Image

Microscope
Objective

Hologram

Converging
Lens
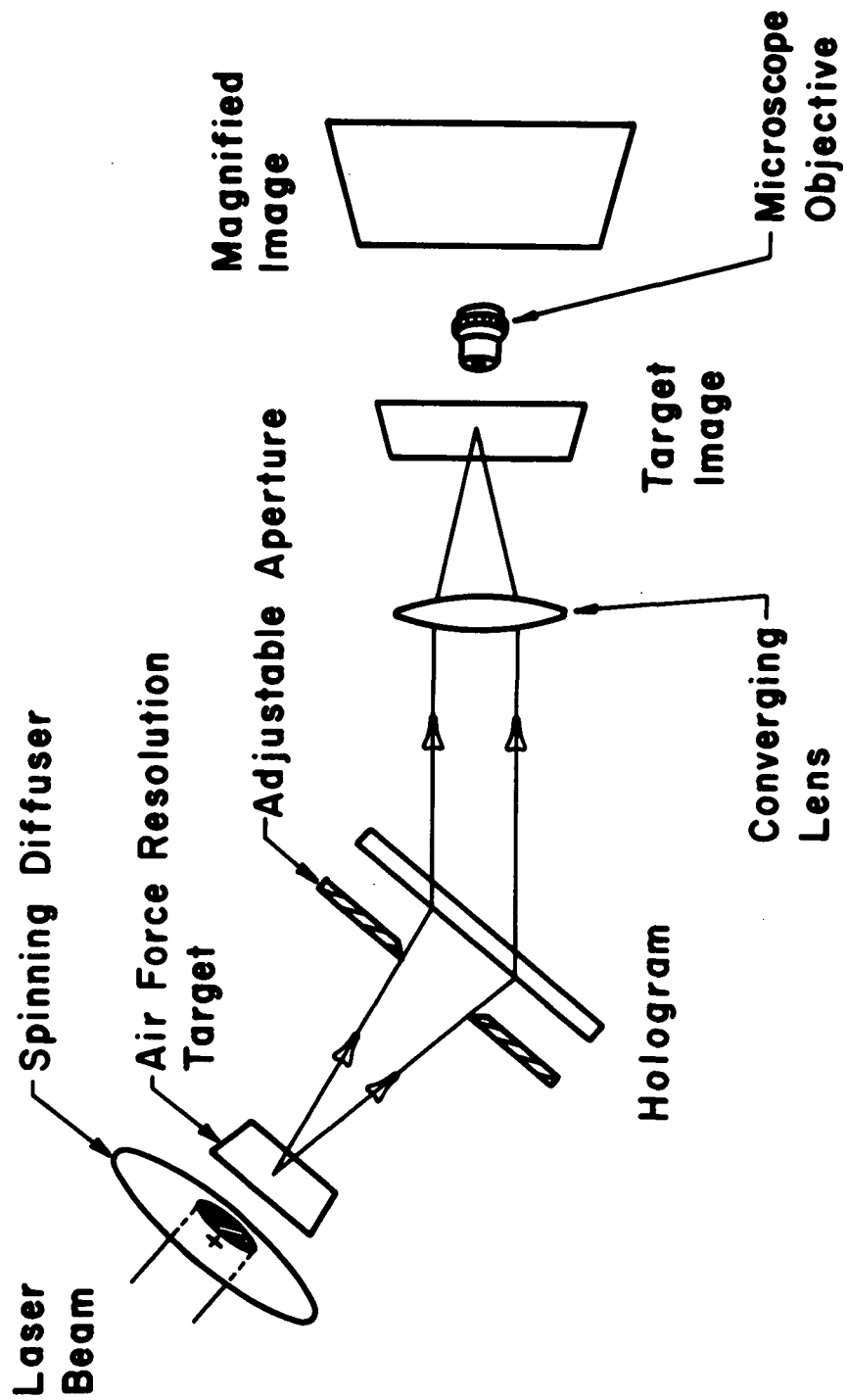
Target
Image

FIGURE 3-15. Reconstruction and imaging geometry.

FIGURE 3-16.  Point image aberrations caused by
the holographic optical element
substrate.

Figure 3-17 shows photographs of the image of the Air Force resolution target for various f-numbers and for the reconstruction wavelength $\lambda_c$ equal to the recording wavelength $\lambda_o$. The resolution data from these photographs are summarized in Table 3-II. Table 3-II also shows for comparison calculated results as a function of f-number. There is reasonably good agreement between the observed and calculated resolution up to f/32. For apertures larger than f/32, the observed resolution actually decreases due to the aberrations introduced by the substrate, as explained before.

Figure 3-18 shows some results for imaging with a reconstruction wavelength different than the recording wavelength. The position of the image of the target shifted in going from 488 nm to 514.5 nm. This shift in position had previously been called a first order aberration. It is also apparent from the photographs that there are third order aberrations that reduce image resolution. At f/64 the image is diffraction-limited just as for the previous case where $\lambda_c = \lambda_o$. But at f/32 and larger apertures, there is a considerable loss of image resolution. Table 3-III summarizes the results of Figure 3-18 and should be compared with Table 3-II.

Figure 3-18 illustrates degradation of image resolution in the presence of chromatic aberrations. As pointed out in earlier work, however, an optimization is possible at the new wavelength that will eliminate these aberrations. It is necessary to move the object position to accomplish this optimization. Figure 3-19 shows a series of photographs again for $\lambda_c' \neq \lambda_o$, but with the optimization performed to provide the best visual image. It can be seen that the resolution at all f-numbers has been almost completely restored. Table 3-IV is the summary of the data in Figure 3-19 and should be compared with Table 3-II and Table 3-III.

3.7.2 Classical Imaging Experiments with Multielement Holographic Optics. — For the experimental study of imaging by multielement holographic optics, a 4X telescope design was selected for evaluation. The telescope design incorporates two holograms operating in the reflective mode. The holograms were recorded on Shipley AZ1350 photoresist. The evaluation of
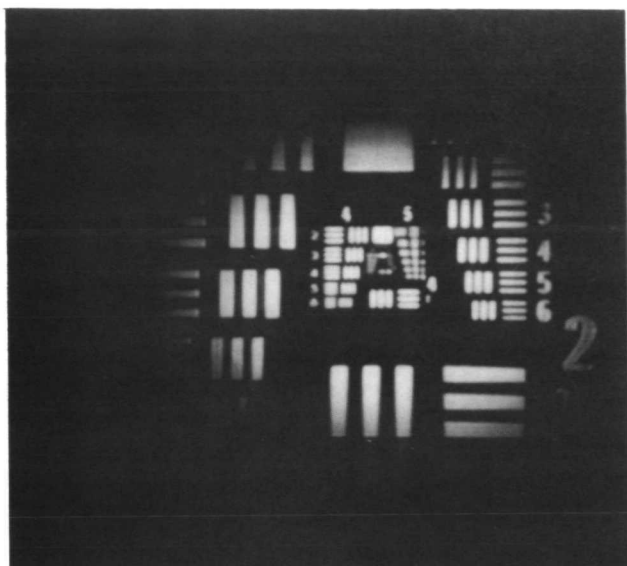
(a) f/64
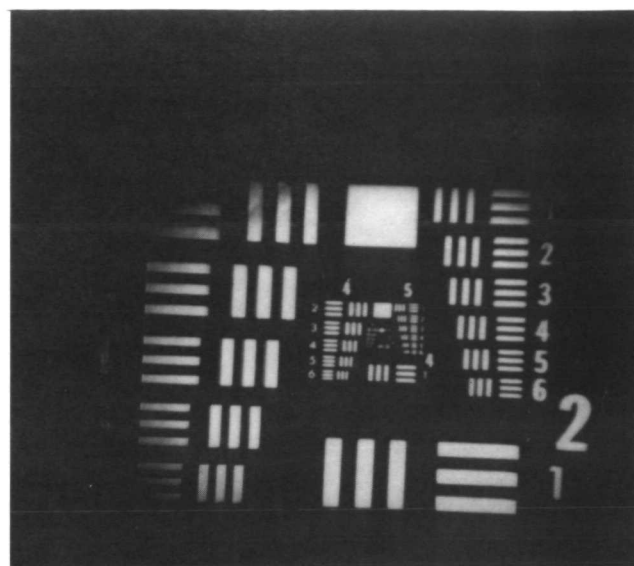
(b) f/32
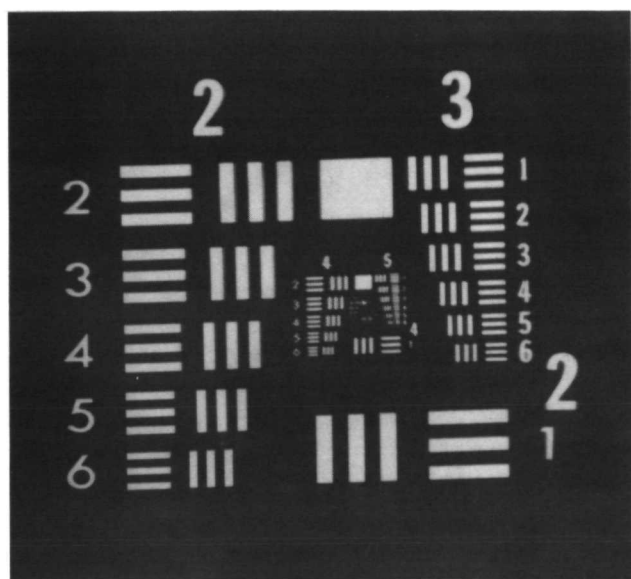
(c) f/16
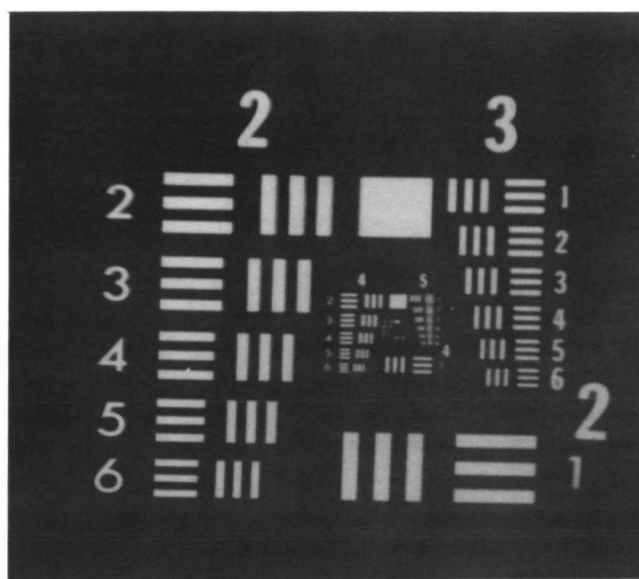
(d) f/10

FIGURE 3-17. Single holographic optical element imaging of a standard Air Force resolution target as a function of f/number with $\lambda_c = \lambda_o$

55
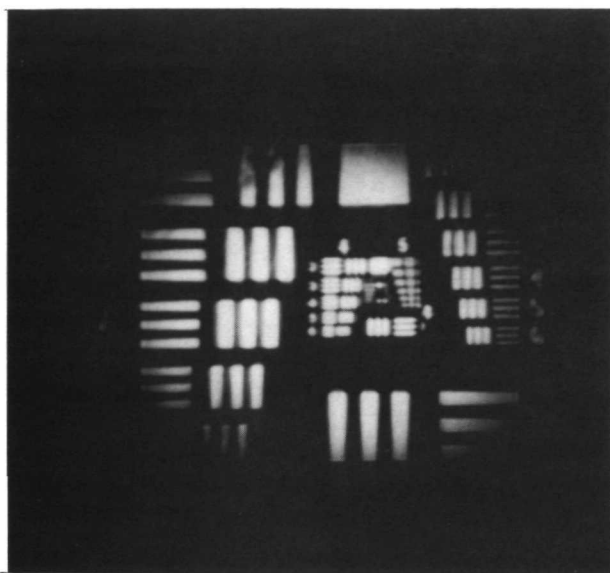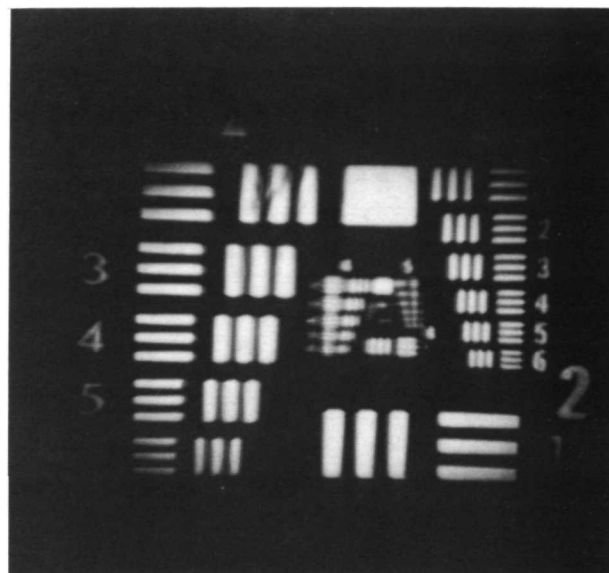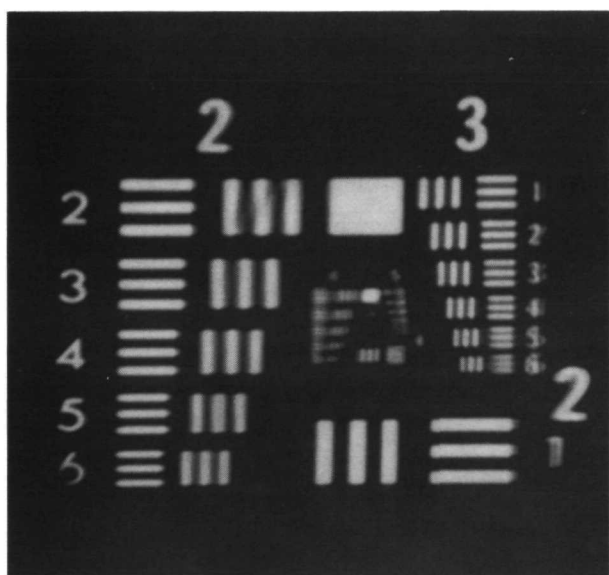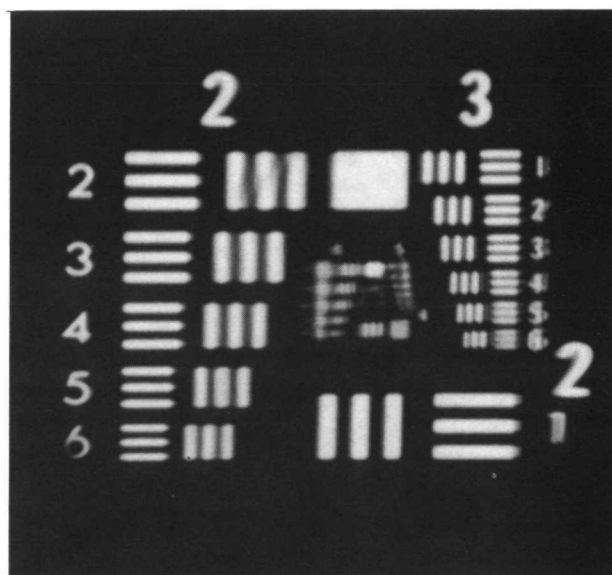
(a) f/64                        (b) f/32

(c) f/16                        (d) f/10

FIGURE 3-18. Single holographic optical element imaging of a standard Air Force resolution target as a function of f/number with $\lambda_c \neq \lambda_o$ and without compensation
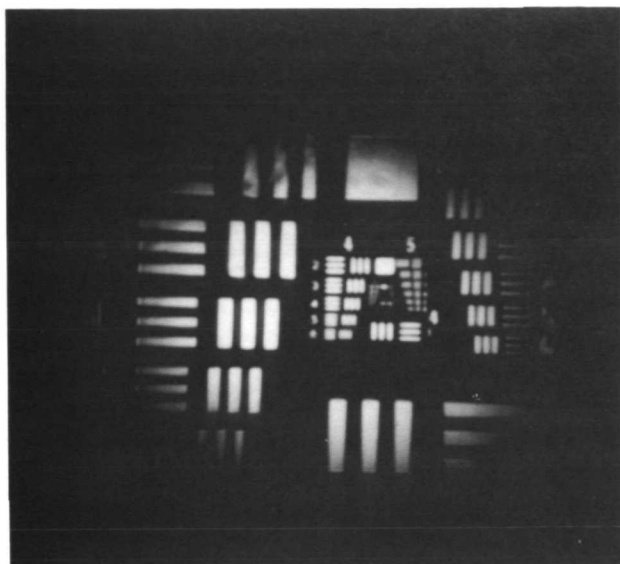
(a) f/64
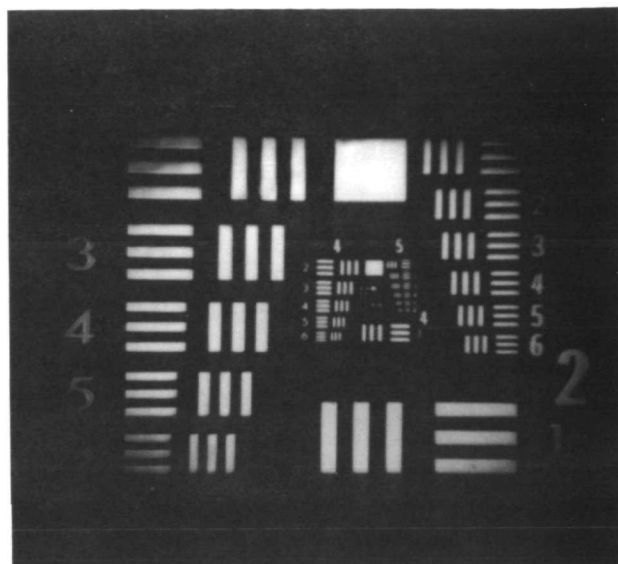
(b) f/32
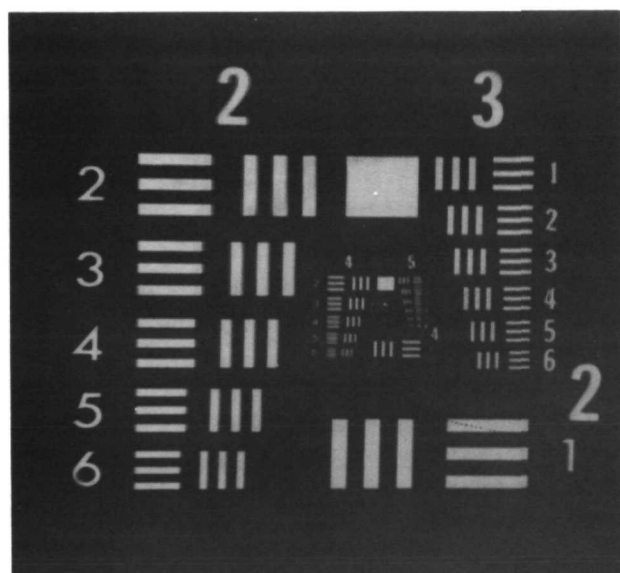
(c) f/16
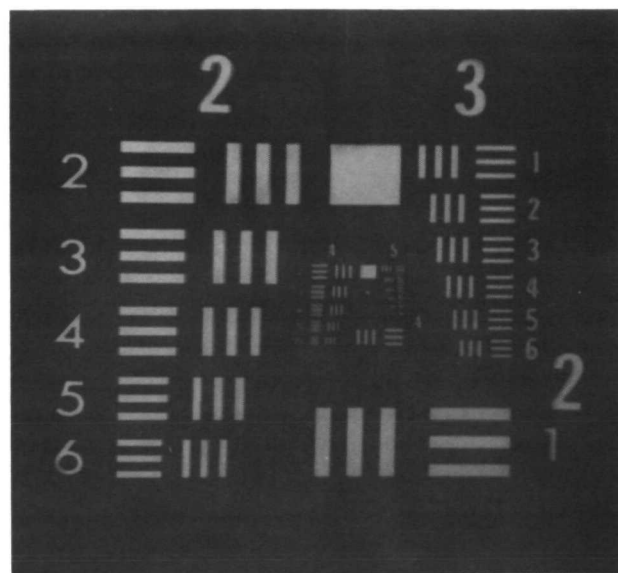
(d) f/10

FIGURE 3-19. Single holographic optical element imaging of a standard Air Force resolution target as a function of f/number with $\lambda_c \neq \lambda_o$ and with wavelength optimization

TABLE 3-II.  Calculated and observed image resolution as a function of aperture for a single holographic optical element with $\lambda_c = \lambda_o$.

| | Calculated | | Observed | |
|---|---|---|---|---|
| f/No. | Diffraction Limited Resolution ($\ell$/mm) = | Group-Element | Group-Element = | Limiting Resolution ($\ell$/mm) |
| 64 | 26 | 4-5 | 4-4 | 23 |
| 32 | 52 | 5-5 | 5-3 | 40 |
| 16 | 104 | 6-5 | 5-1 | 32 |
| 9 | 186 | 7-4 | 4-6 | 29 |

TABLE 3-III.  Calculated and observed image resolution as a function of aperture for a single holographic optical element with $\lambda_c \neq \lambda_o$.

| | Calculated | | Observed | |
|---|---|---|---|---|
| f/No. | Diffraction Limited Resolution ($\ell$/mm = | Group Element | Group-Element = | Limiting Resolution ($\ell$/mm) |
| 64 | 26 | 4-5 | 4-3 | 20 |
| 32 | 52 | 5-5 | 4-1 | 16 |
| 16 | 104 | 6-5 | 3-6 | 14 |
| 9 | 186 | 7-4 | 3-6 | 14 |

TABLE 3-IV.  Calculated and observed image resolution of a holographic optical element with $\lambda_c \neq \lambda_o$ and the image optimized by refocus and lateral shift of the object position.

| | Calculated | | Observed | |
|---|---|---|---|---|
| f/No. | Diffraction Limited Resolution ($\ell$/mm) = | Group-Element | Group-Element = | Limiting Resolution ($\ell$/mm) |
| 64 | 26 | 4-5 | 4-4 | 23 |
| 32 | 52 | 5-5 | 5-3 | 40 |
| 16 | 104 | 6-5 | 4-5 | 25 |
| 9 | 186 | 7-4 | 4-5 | 25 |

the telescope design included (1) a study of angular resolution as measured for point images (star simulation) both on and off-axis and (2) imaging with wavelengths different than the recording wavelength. A standard 1951 Air Force resolution target was also imaged through the telescope.

Both hologram elements for the telescope were recorded in the experimental geometry shown in Figure 3-20. The 457.9 nm line of an argon laser was used to expose the photoresist. The reference beam was collimated and was incident at an angle of 45° with respect to the hologram normal. The signal beam was a spherical wave diverging from a point that was centered on the hologram at a distance $R_s$. For the telescope objective $R_s$ was 16 cm, while for the eyepiece $R_s$ was 4 cm. This gave the individual elements 16 cm and 4 cm focal lengths, respectively, and the telescope combination a 4X angular magnification. The use of divergent rather than convergent signal beams greatly facilitates the construction of these elements because we are no longer constrained by the availability of large aperture converging lenses or by the difficulty of keeping these optical components out of the path of the reference beam.

The photoresist was spin-coated onto 2 x 2 inch glass substrates with a Plat-General model 102F photoresist spinner. Filtered resist solution was first puddled onto the stationary plates. The plates were then rapidly accelerated to 1600 rpm. This provided uniform coatings of 0.8 µm thickness. The plates were dried and then vacuum baked for 20 minutes at 100°C. The plates required an exposure of 200 mJ/cm$^2$ at 457.9 nm. Finally, the plates were processed for 20 seconds at 70°F in Shipley AZ303 developer diluted with four parts of distilled water to one part of developer. This combination of coating, exposure, and processing parameters provided good reconstruction parameters for hologram readout in the reflective mode.

To construct the telescope, we aligned the two holograms as shown in Figure 3-21. In arriving at the configuration shown in Figure 3-21, the eye piece was rotated 180° about the x-axis and then translated 20 cm in the negative z-direction. The objective was rotated 180° about the z-axis before
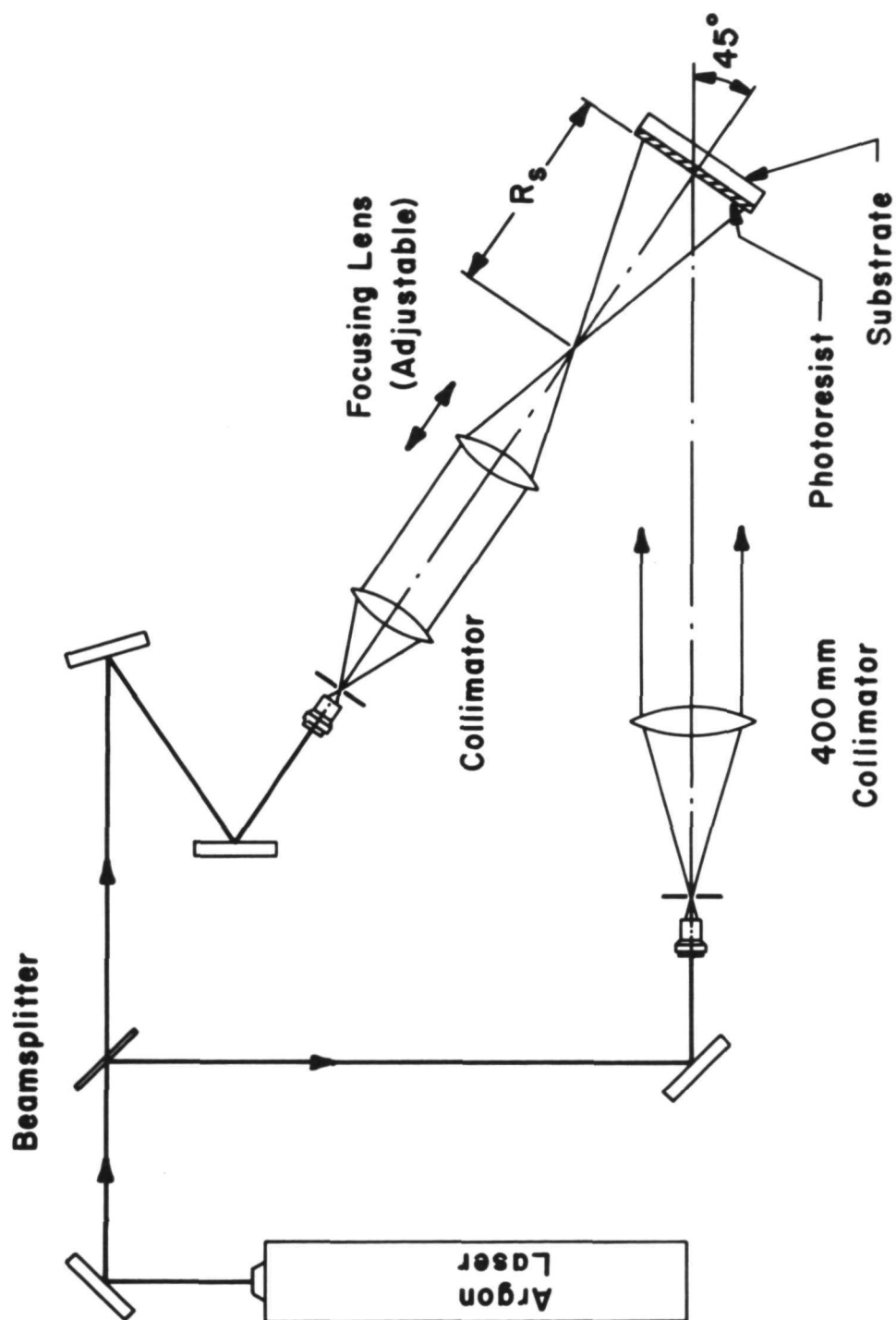
FIGURE 3-20. Construction geometry for the 4X holographic optical element telescope.
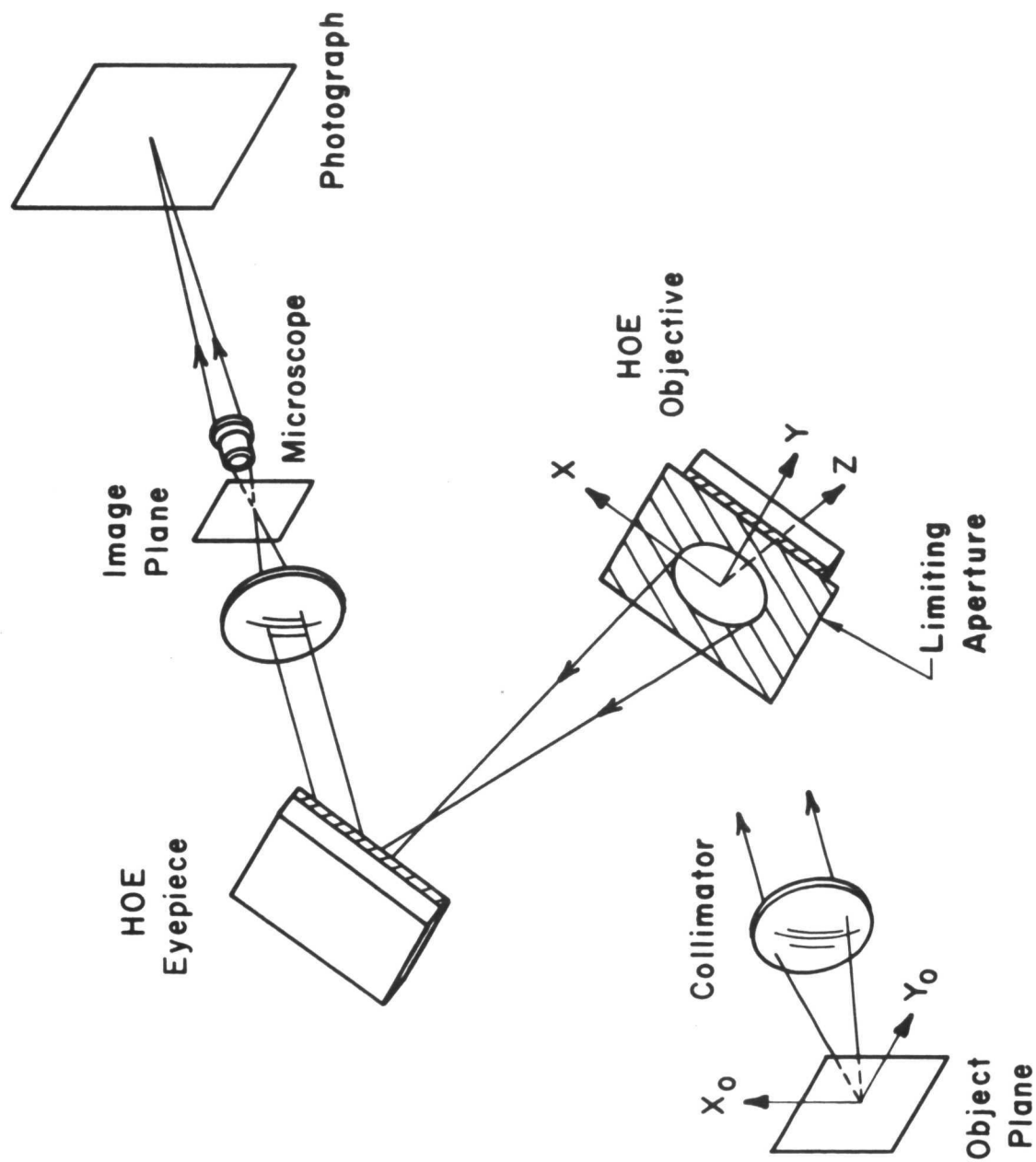
FIGURE 3-21. Geometry for testing the 4X holographic optical element telescope.

61

repositioning. This reorientation and realignment must be made very precisely in order for the two holograms to be correctly aligned, and to provide a diffraction-limited system. The objective converged the incoming plane wave to a real point focus 4 cm in front of the eye piece; the eyepiece recollimated the beam. An eliptically shaped aperture was placed immediately in front of the telescope objective to limit the size of the incoming plane wave. This aperture presented a circular crossection to the incoming wave. The eyepiece was left unapertured. The object plane, which must effectively be at an infinite distance from the telescope, is located at the back focal plane of the reference beam collimator. In order to examine the image from the telescope, a lens was used to focus the rays from the eyepiece (this is normally done by the eye). Finally, the image was magnified by a microscope objective and refocused on a second image plane for photographing.

The resolving power of the telescope is measured in terms of the smallest angular separation between two plane waves incident on the objective that are brought to focus as "resolved" Airy discs. This is, of course, just the well-known Rayleigh criterion. With the telescope apertured to f/8, Figure 3-22a shows that a focused point is not diffraction-limited. The reason for this is the lack of perfect substrate flatness, as explained for the case of single element imaging. At f/16 the telescope becomes diffraction limited, as shown in Figure 3-22b. The photograph in Figure 3-22b was purposely overexposed to show the second and third maxima of the Airy disc. At f/16 the angular resolution of the telescope, as given by the Rayleigh criterion, is $5.6 \times 10^{-2}$ milliradians. Figure 3-22c shows two point images separated by approximately this angle. The small intensity dip between the two point images is clearly evident. The two point sources of Figure 3-22c were made mutually incoherent by exposing the film to each point sequentially. Figure 3-22d shows two well-resolved point images whose angular separation is nominally twice the Rayleigh criterion.

(a) Substrate aberration at f/8
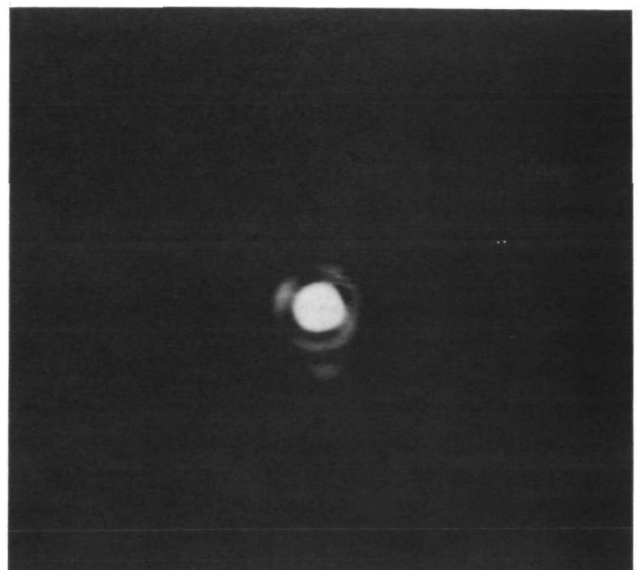


(b) Diffraction-limited spot at f/16
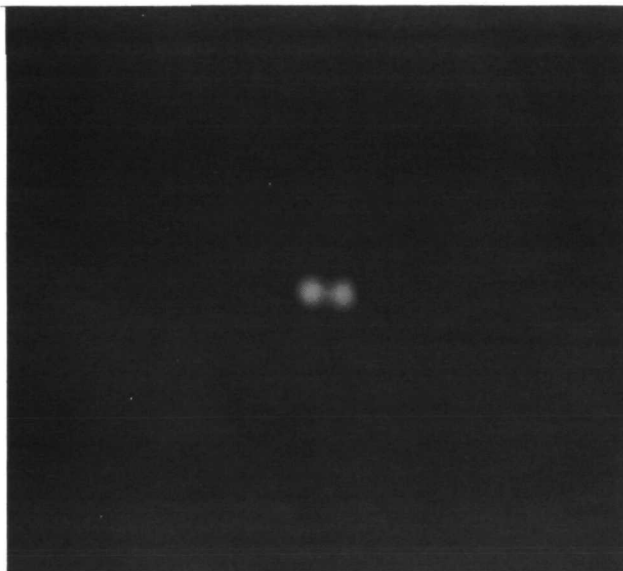


(c) Rayleigh-resolved point sources



(d) Double Rayleigh-resolved point sources

FIGURE 3-22.   Point images formed with a 4X reflective holographic optical element telescope with $\lambda_c = \lambda_o$.

In Figure 3-23a the point source was moved off-axis by one half degree in the $x_0$ direction. The image is still very nearly diffraction-limited. In Figure 3-23b the angular field was increased to one degree and in Figure 3-23c to two degrees. Not until an off-axis angle of two degrees does the image become badly aberrated. The dominant aberration present is astigmatism. Figure 3-23c shows the 2° field at the circle of least confusion while Figure 3-23d gives the same data for the tangential focus. When the point source is moved two degrees off axis in the $y_0$ direction the image remains nearly diffraction-limited as seen in Figure 3-23e.

Figure 3-24a shows the image of a point source on axis, but at a reconstruction wavelength different than the construction wavelength. The wavelength difference $\Delta\lambda_c$ was 7.9 nm. The image is badly aberrated as expected. Note that there is a scale difference between Figure 3-24 and previous figures. In Figure 3-24b the limiting aperture was closed down until a diffraction-limited image was obtained; this occured at f/80 and thus, there is a five fold loss in angular resolution due to chromatic aberrations.

Figure 3-25 is the diffraction-limited image of a 1951 Air Force resolution target. The illumination of the target was incoherent (obtained by means of a spinning diffuser). An angular scale is included in the photograph because the target group and element numbers can be misinterpretted. Group 5 element 4, which is the last group resolved, again corresponds to $5.6 \times 10^{-2}$ milliradian angular resolution. The result obtained for coherent illumination is shown in Figure 3-26.

These results show that a multielement holographic optical telescope acts in many respects as its counterpart made from conventional optical elements. The holographic optical element system differs, however, in at least two significant respects. The holographic optical element systems are not usually centered and thus, off-axis imaging will not generally be the same in different directions. We saw an example where aberrations from the objective and eyepiece cancelled in one direction rather dramatically, but not in the orthogonal direction. Secondly, without achromatization, first order chromatic aberrations will limit the utility of the telescope to quasimonochromatic light.
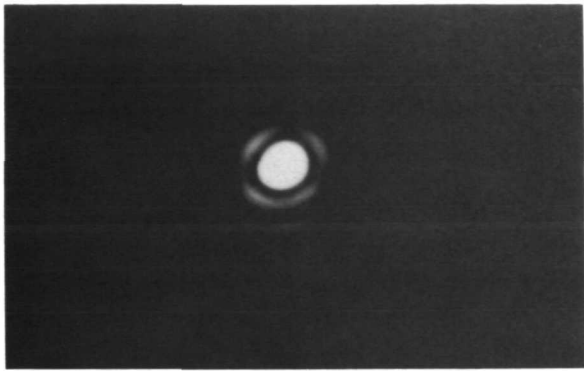
(a) $x_0 - z_0$ plane, 1/2° field
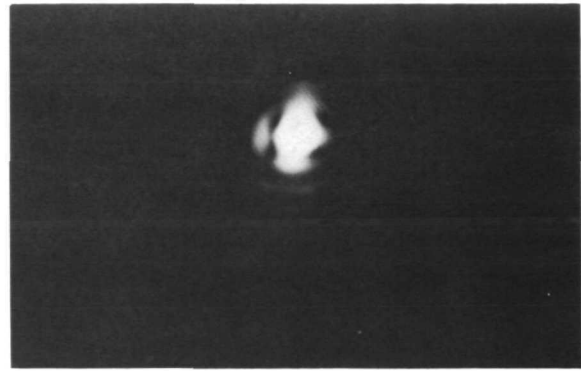
(b) $x_0 - z_0$ plane, 1° field
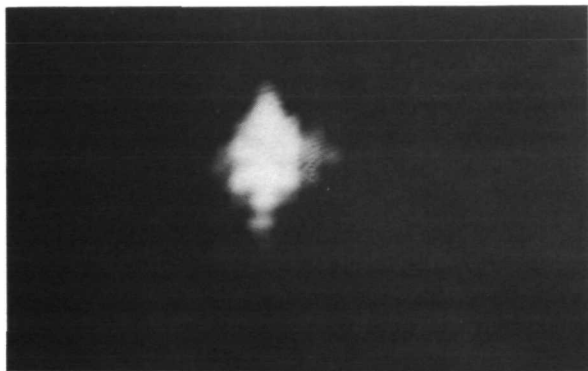
(c) $x_0 - z_0$ plane, 2° field (circle of least confusion)
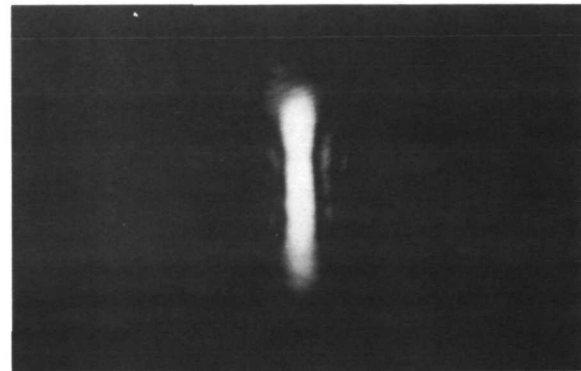
(d) $x_0 - z_0$ plane, 2° field (tangential focus)
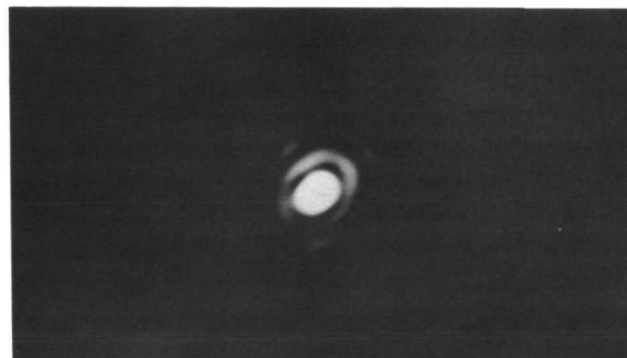
(e) $y_0 - z_0$ plane, 2° field

FIGURE 3-23. Seidel aberrations for a 4X reflective holographic optical element telescope with $\lambda_c = \lambda_o$.
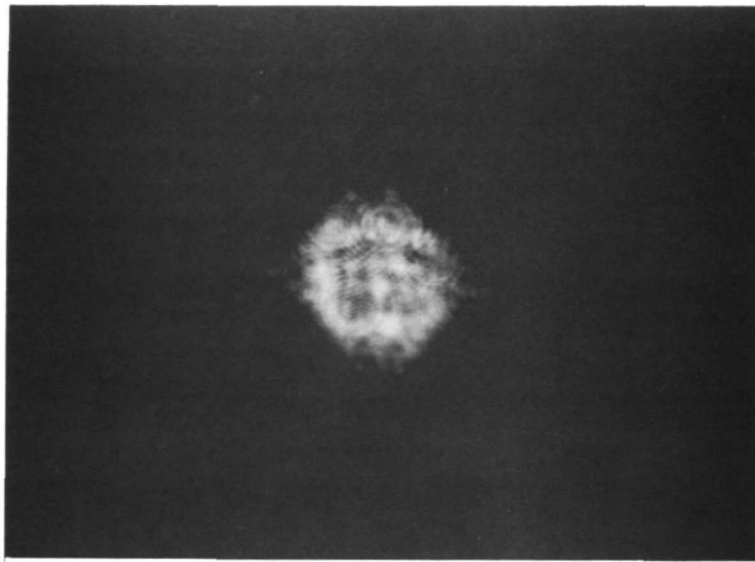
(a) Full Aperture, $\Delta\lambda$ = 7.9 nm
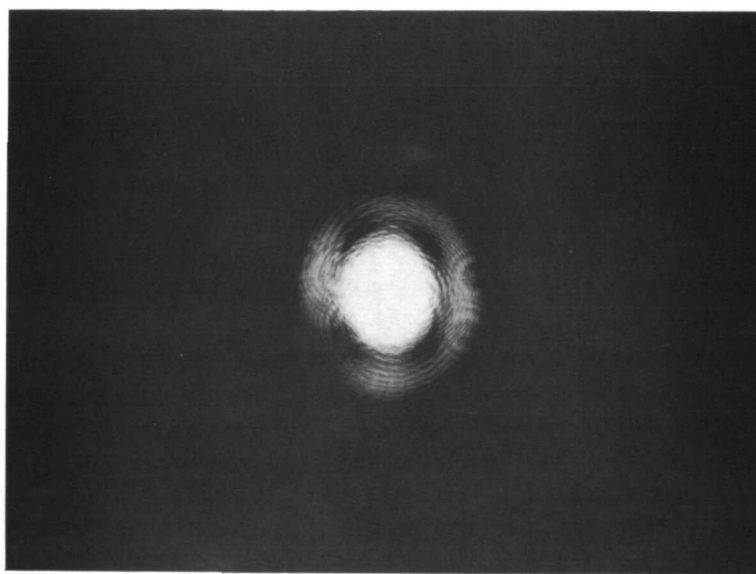


(b) Reduced Aperture (f/80), $\Delta\lambda$ = 7.9 nm

FIGURE 3-24.   Chromatic aberrations of a point
              imaged through a 4X reflective holo-
              graphic optical element telescope.
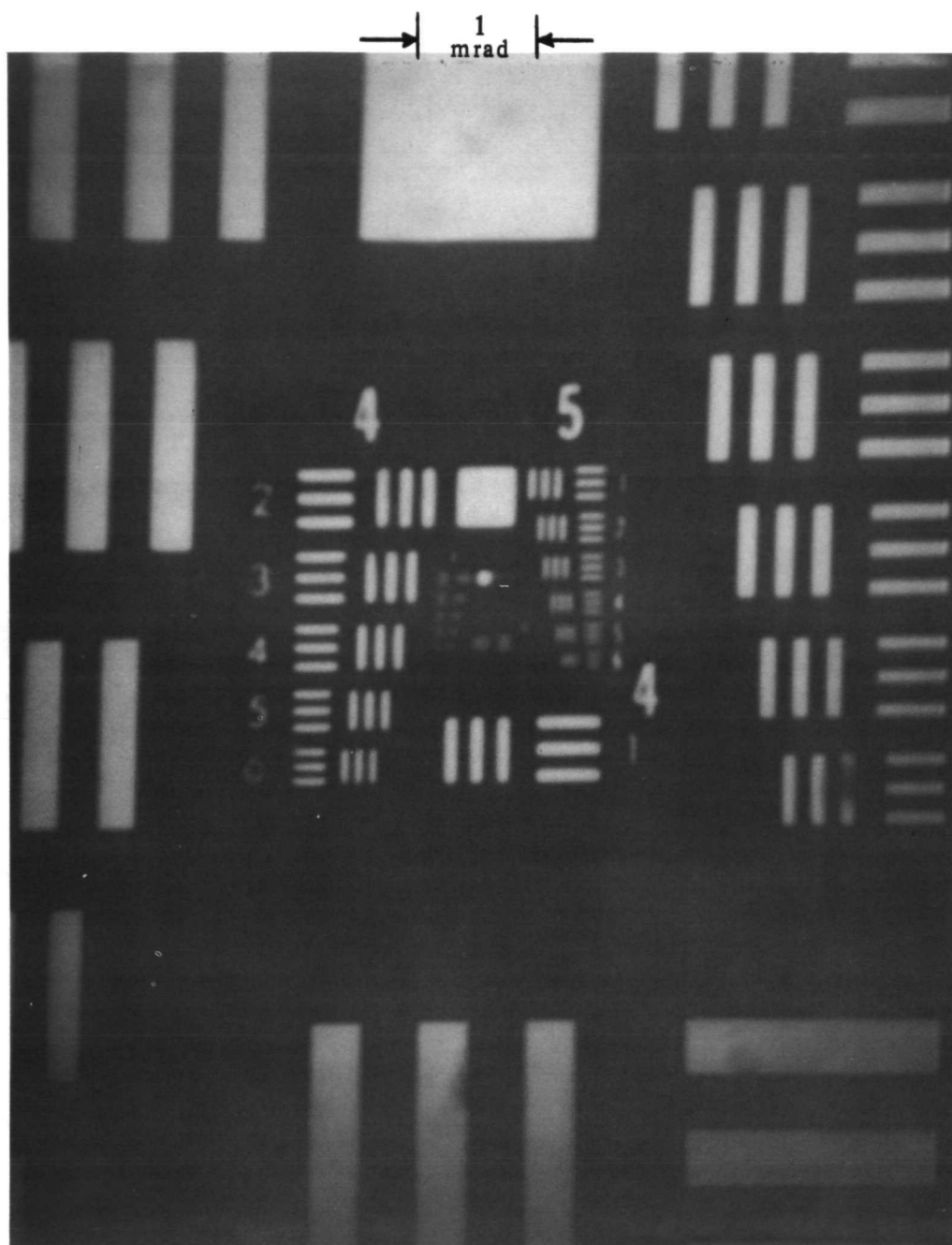
FIGURE 3-25.   Image of 1951 Air Force
resolution target illuminated
with spatially incoherent
laser light.
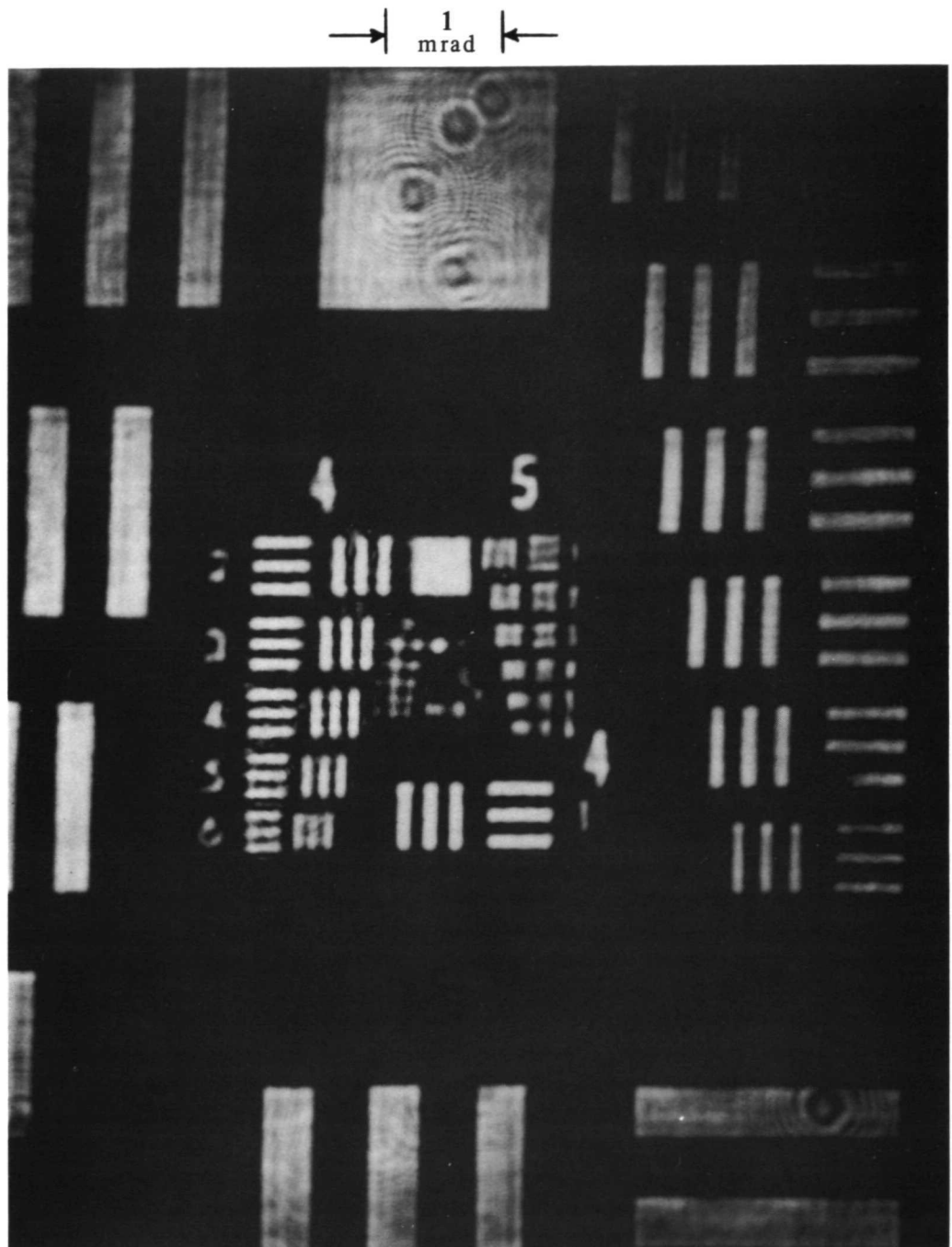
FIGURE 3-26. Image of 1951 Air Force resolution target illuminated with coherent light.

## 3.8 Summary and Conclusions

We have performed an extensive experimental study of the aberration and imaging properties of holographic optical elements. Using an interferometric method, we have measured total waves of chromatic and Seidel aberration for single element holographic optics. Three different geometries were used, corresponding to bending factors $Q$ of 1, 2, and 4. In addition, we recorded the holographic optical elements on a number of different light-sensitive materials. A large amount of useful data in photographic, tabular, and graphical form is available from the study. To complement the results of our interferometric evaluation, we performed classical imaging experiments to study the effects of aberration on image resolution. Finally, we constructed a 4X reflective telescope and investigated its imaging properties.

We have found that the aberration properties of a single holographic optical element are similar in many ways to those of a simple thin lens. A major difference is the dominance of astigmatism in the lateral paraxial field and for achromatic objects. The reason for this is the off-axis nature of the holographic zone plate. As a high-quality imaging device, it appears from our experimental data that single holographic optical elements are of limited utility. Nevertheless, good performance can be expected for relatively simple applications such as a monochromatic collimation. However, the data presented in this paper emphasize the need for two or more holographic optical elements in order to obtain high-quality imaging performance over wide fields or for chromatic objects.

Our study of multielement holographic optical systems is of a qualitative nature. The main objective was a preliminary study of the problems associated with the design, fabrication, alignment, and testing of multielement holographic optical systems. As in the case of the single holographic optical element, we found that the 4X holographic telescope selected for evaluation behaved in most respects as its conventional counterpart. But perhaps more importantly,

the aberration limits of the computer-aid design discussed in previous reports were verified. Thus, it appears that gains in performance can be obtained with two or more element holographic optical systems.

## 3.9 Recommendations

The depth of the single element investigation was sufficient to verify the accuracy of computer-based analytical models and design procedures. Further effort in the area would be of limited utility. However, considerable experimental and analytical work remains in the area of multielement holographic optical systems. Specific areas for further investigation should include a thorough study of imaging properties and characteristics, fabrication problems (especially metallic and dielectric overcoating), alignment techniques, and testing procedures for multielement holographic optical systems.

## 3.10 References

1. T. Kubota and T. Ose, J. Opt. Soc. Am., <u>61</u> 1539 (1971).

2. John Latta, Ph.D. Thesis, University of Kansas, December (1970).

3. R. G. Zech, "Hologram Recording in Thick Light-Sensitive Polymers," San Francisco meeting of the Opt. Soc. Am., October (1972).

4. F. Jenkins and H. White, <u>Fundamentals of Optics</u>, McGraw-Hill, 3rd Ed. (1957), pp. 130-145.

4

## CANDIDATE RECORDING MATERIALS

The practical utility of holographic optical elements will be determined in part by the availability of suitable light-sensitive recording materials. The prominent place accorded recording media in our overall investigation is due to the following consideration. A holographic optical element can be modeled as an ideal holographic phase structure in series with a random phase mask. The holographic phase structure in the absence of geometrical peturbations or wavelength shift, will provide a perfect diffraction-limited image. The random phase mask represents the inherent defects of the substrate and the light-sensitive layer. Poor surface flatness, orange peel, ripple, reticulation, and embedded artifacts are the primary defects. Their overall effect is to generate aberrations and scatter noise that degrade image contrast, resolution, and signal/noise ratio. Thus, recording materials of the highest optical quality must be used for the construction of holographic optical elements in order to achieve optimum imaging performance.

The most important holographic parameters of the light-sensitive medium are diffraction efficiency, signal/noise ratio, resolving power, and exposure sensitivity. By diffraction efficiency (DE) we mean the ratio of diffracted power to incident power minus reflected power. Signal/noise ratio (SNR) is defined as the ratio of average signal power to average noise power as measured from the reconstructed real image of a diffuse target with an opaque center. For SNR measurements the beam ratio K is chosen to be much greater than unity so that nonlinear noise is minimized. In this way only random noise due to scattering centers and artifacts influence the value of SNR. This technique is mainly useful for comparing various recording media in a consistent manner. Resolving power is a measure of the finest spatial detail the recording medium can record. The materials selected for evaluation all have very high resolving power. Some of the recording media

can in fact resolve spatial frequencies as high as 6000 cycles/mm. High resolving power is required to obtain good efficiency, especially for large offset angles. Finally, exposure sensitivity, which is a measure of the energy/unit area required to produce either maximum diffraction efficiency or signal/noise ratio, is important for a number of practical reasons. The fabrication of high quality holographic optical elements requires uniform construction beams. Due to the nonuniform intensity profile of most laser beams, the construction beams must be expanded to about twice the element size. This reduces usable laser power by a factor of four. The problem is compounded as the size of the element increases. Also, the single frequency power available from most lasers is less than a few hundred milliwatts. The combination of these two factors results in exposure times that can be as long as 10 hours for a moderate size (25 cm diameter) element. Hence, exposure sensitivity is a foremost consideration.

## 4.1 Testing Procedure

The testing of light-sensitive materials to determine holographic parameters is relatively straightforward. Our procedure consists of four steps: (1) optimization of preparation, (2) hologram recording and playback parameters measurement, (3) optimization of processing, (4) and stabilization. Steps (1) and (3) depend on the particular recording medium while step (2) is identical for each material. Step (4) usually includes the cementing of a glass coverplate over the light-sensitive layer. We found that a lens bond (Summers Laboratory, type M62) was best suited for this purpose.

Diffraction efficiency data are obtained by recording a series of plane wave gratings with different exposure levels. After processing, incident, reflected, transmitted, and diffracted powers are measured. These data are also used to specify exposure sensitivity. For signal/noise ratio measurements we record Fresnel holograms of a ground glass diffuser with an opaque center for a series of average exposures. By means of a scanning photomultiplier, a log amplifier, and chart recorder we obtained for each hologram a direct

display of SNR in dB units. As we have mentioned, this type of experiment provides comparitive data. Its relevance to holographic optical elements is established by the fact that undesirable or anomalous materials behavior is usually of a similar type. Hence, a relative measure is obtained of complex degradation phenomena.

In the following section we discuss the recording media that were evaluated. Details of how each material was prepared and processed are given, together with experimental data.

## 4.2 Experimental Data

There are a large number of candidate recording media to consider for holographic optical element applications. We selected photoresists, dichromated gelatin, photographic emulsions, iron oxide, and photodegradable plastics. Our choices were motivated by the ready availability of high quality materials and by a priori knowledge about the level of holographic reconstruction parameters to be expected from these materials. For each material we determined diffraction efficiency, signal/noise ratio, and exposure sensitivity. Because each material has its own unique properties and characteristics, there is some variation of the recording parameters. Generally, a K-ratio of 10 or 20 was used together with a spatial carrier frequency $(v_c)$ of 1000 $\ell$/mm; the information packing density (IPD) was maintained fixed for all materials at $5 \times 10^6$ bits/cm$^2$.

4.2.1 Horizons Research Incorporated LHS7 Photoresist. — A new and useful hologram recording material has been developed by Horizons Research Incorporated of Cleveland, Ohio. It has a number of interesting properties; for example, (1) it is dry-working; i.e., it does not require solvent development, (2) it has peak exposure sensitivity near the 488 nm line of an argon laser, and (3) it has hologram reconstruction parameters comparable to those obtained with the best photographic emulsions.

To prepare exposure samples we used dip coating. The plates were dipped in a clean box at a temperature of 20°C and a relative humidity of 30%. The substrate was a 50 mm x 75 mm glass microslide (Corning #2947). By means of trial and error we settled on a 2.5 mm/sec pullout rate. This gave a dry coating thickness of 0.9 μm. Faster pullout rates which gave thicker coatings were tried, but proved unsatisfactory because the dried layer had poor surface quality (the surface crazed). Slower pullout rates which yielded thinner coatings were also tried, but it was found that hologram reconstruction parameters for these samples were reduced in value.

The details of the coating procedure, which can be done under strong red safelight, are as follows:

1) The glass substrate was cleaned and was backed with a removable, self-adhesive layer.

2) The glass substrate was slowly dipped into the photoresist solution and allowed to remain for 30 seconds.

3) The coated substrate was withdrawn from the solution at a rate of 2.5 mm/second.

4) The coated substrate was positioned about 5 mm above the photoresist solution and dried in the solvent vapors for 2 minutes.

5) The dried coating was removed from the clean box and the self-adhesive backing layer peeled off.

The above procedure gave coatings of excellent surface quality. They were placed in a light-tight box and exposed as soon as possible.

Processing requires only a stream of heated air. After exposure, the photoresist was developed and fixed in a calibrated black box designed for this purpose at a temperature of 160°C for 90 seconds. This renders the photoresist insensitive to further exposure. A small amount of sensitizer dye remains after heat processing, but this can be readily photobleached with the reconstruction beam.

HARRIS ELECTRO-OPTICS CENTER

Standard testing procedures were used to evaluate the Horizons Research photoresist recording material. An argon laser operating at 488 nm was used for both recording and readout. Plane wave gratings were used to investigate diffraction efficiency (DE) performance, resolving power, and exposure sensitivity. The ground glass with opaque center input signal was used to determine signal-to-noise ratio (SNR) as a function of exposure, reference-to-signal-beam ratio K, and spatial carrier frequency $\nu_c$ for a resolution-limited information packing density of $5 \times 10^6$ bits/cm$^2$. Figure 4-1 shows percent diffraction efficiency as a function of exposure with spatial frequency $\nu$ as a parameter. Signal/noise ratio data are summarized in Figure 4-2 where we have graphed maximum SNR and associated DE as a function of K-ratio with carrier frequency $\nu_c$ as a parameter. These data indicate that the photoresist is a well-qualified holographic recording material. More details can be found in the Third Quarterly.

4.2.2  <u>Shipley AZ1350 Photoresist.</u> — Shipley AZ1350 photoresist is a high-quality recording material widely used in the fabrication of micro-electronics. It is characterized by a very high resolving power (on the order of 1500 lines/mm) determined by the measurement of holographic grating efficiency. Exposure sensitivity is quite low for visible light, but increases rapidly for blue-near UV wavelengths. Maximum sensitivity occurs at around 350 nm. At 488 nm more than 5J/cm$^2$ are required to reach maximum diffraction efficiency; corresponding values are about 300 mJ/cm$^2$ at 457.9 nm and 20 mJ/cm$^2$ at 441.6 nm. For our experimental investigation we used the 457.9 nm line of an argon laser.
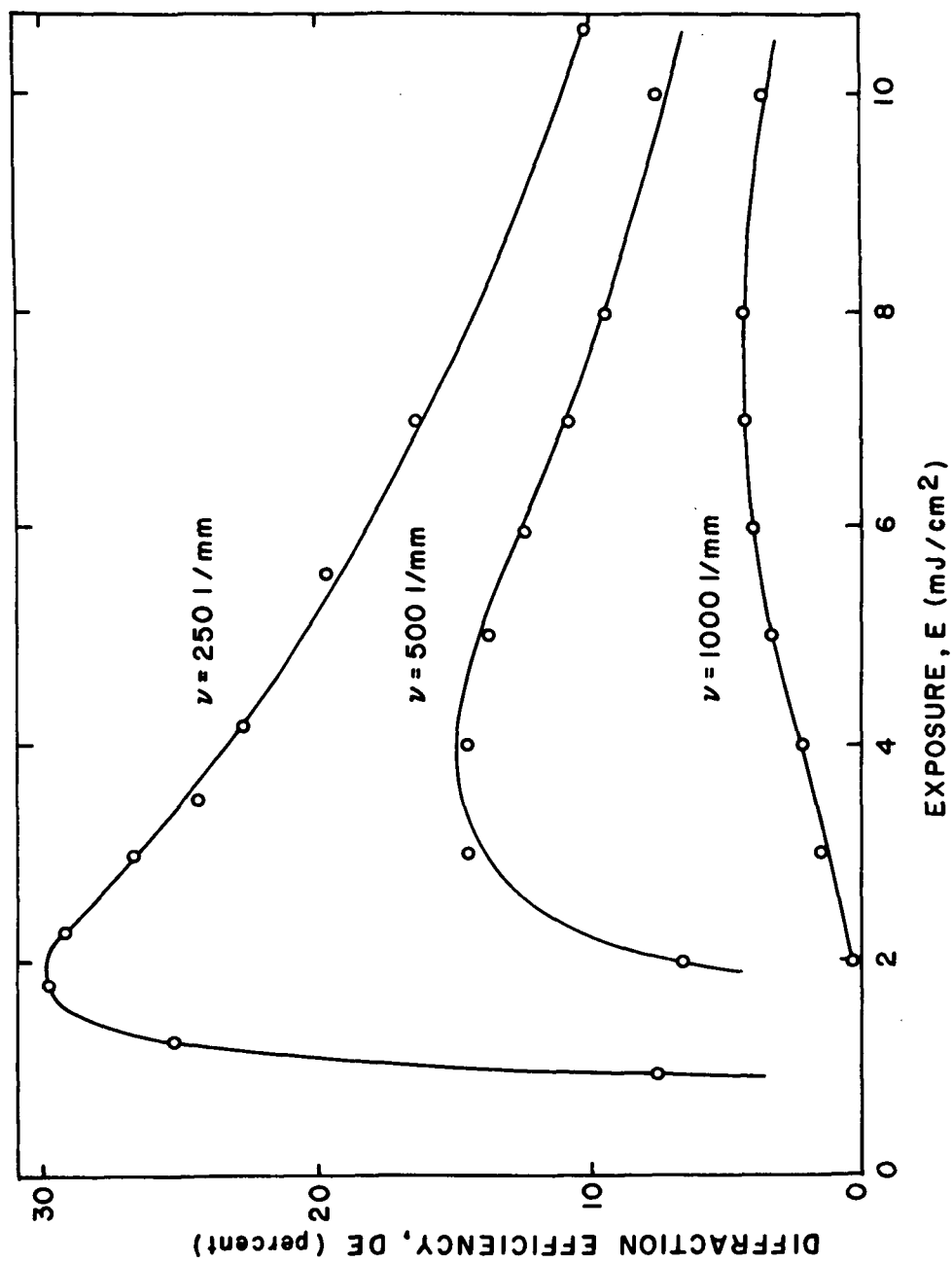
FIGURE 4-1. Diffraction efficiency as a function of exposure with spatial frequency $\nu$ as a parameter.
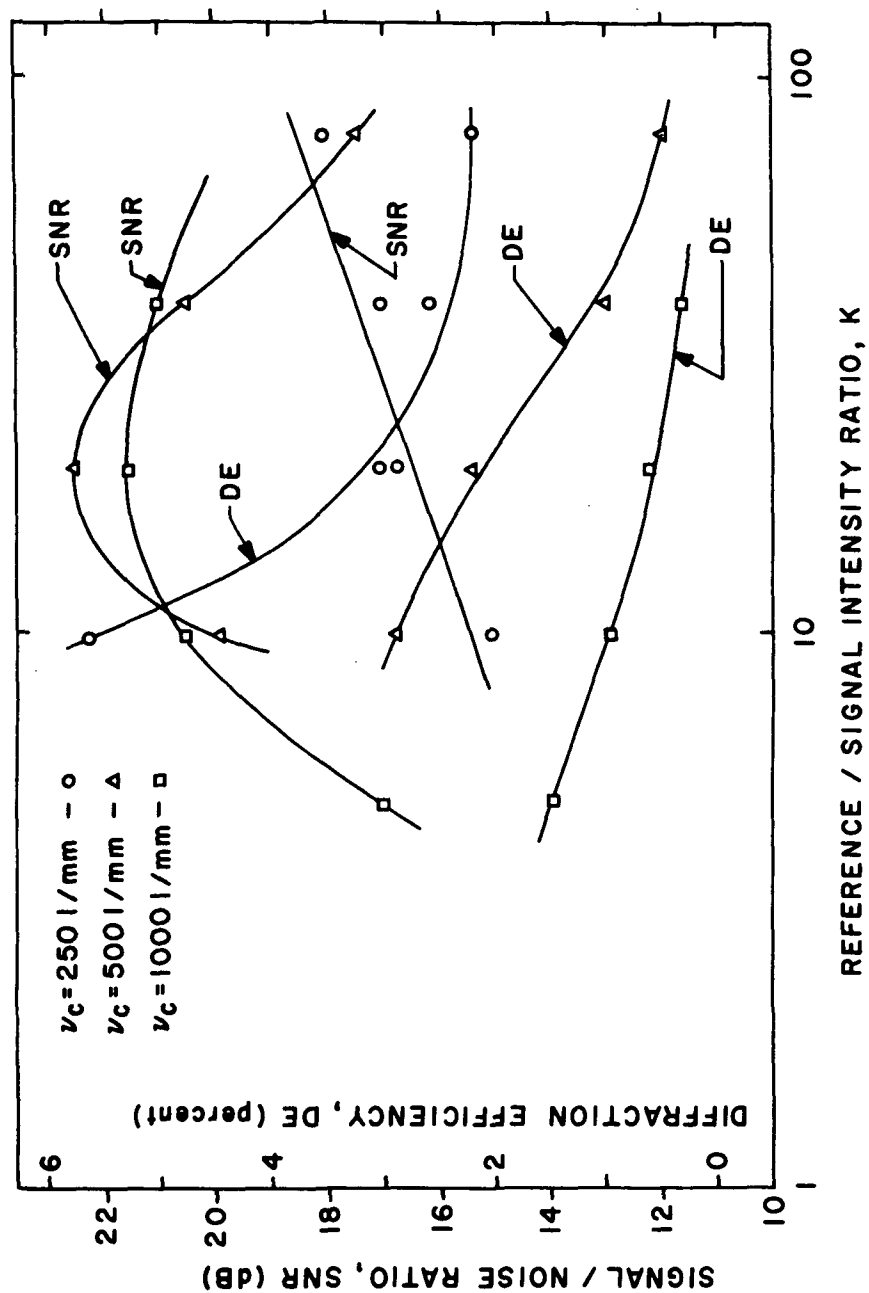
FIGURE 4-2: Maximum Signal/Noise Ratio and Diffraction Efficiency as a function of reference/signal ratio K with spatial frequency $\nu$ as a parameter.

Because we were interested in both efficiency and cosmetic quality, we tried both spinning and dip-coating glass substrates to provide exposure samples. All samples were vacuum baked for 20 minutes at 100°C after coating. Dry coating thickness was on the order of 1 μm. In addition, a number of developers were tried including type 1350 and type 303 (with various dilution ratios).

After performing a number of preliminary tests, a number of problem areas became evident. First, although we were consistently able to obtain maximum efficiencies of greater than 20% for gratings, it was observed that signal-to-noise ratio data was poor. Part of the problem was due to back reflections; this produced a course grating structure that was minimized with an antireflection coating. For spin-coated plates strong scatter noise propagated in the direction of the reconstructed signal. The orientation and shape of the signal area illuminated by the scatter noise depended on the location of the hologram on the sample. We hypothesize that this problem is related to the spinning technique of coating. A possible explanation is that spinning causes the radial alignment of solid particles. The dip coating technique described in the previous section eliminated this anomaly. Finally, we discovered that post baking for one hour at 100°C improved cosmetic quality to some extent.

Although we tried a number of different methods to optimize sample preparation, exposure, and development, we did not find a combination of these parameters that provided both high efficiency and good cosmetic quality (measured in terms of signal-to-noise ratio). We are presently trying to determine whether this is an inherent property of the photoresist or preparation and processing faults.

4.2.3 <u>Dichromated Gelatin.</u> — Dichromated gelatin plates were prepared according to the method of Chang.[1] The development procedure was similar to that described by Lin.[2] Gelatin layers were obtained by fixing out the silver halide from Kodak 649F plates. Our procedures are summarized in Table 4-I. Figure 4-3 shows some typical experimental results. We have normalized

TABLE 4-I

DICHROMATED GELATIN PREPARATION AND PROCESSING

Preparation*

1. Fix in Part A of Kodak Rapid Fixer - 10 minutes.

2. Wash with running water at 90°F for 15 minutes.
   — Start at 70°F and raise temperature at 2.5°F per minute to 90°F.

3. Stand in air 1 minute.

4. Rinse in distilled water with 2 drops per liter of Photo-Flo 600 for 30 seconds.

5. Dry completely in room environment.

6. Soak in room temperature water for 2 minutes.

7. Harden in both Part A and Part B of Rapid Fixer for 10 minutes.

8. Wash for 15 minutes at 70°F in running water.

9. Rinse in Photo-Flo solution for 30 seconds.

10. Dry overnight at room temperature.

11. Soak plates for 5 minutes in 5% ammonium dichromate solution with 2 drops per liter of Photo-Flo 600.

12. Wipe ammonium dichromate off glass side of plates.

13. Dry at room temperature.


*Start with 649F plates.


Development

1. Develop in a 0.5% solution of ammonium dichromate for 5 minutes.

2. Bath in Kodak Rapid Fixer for 5 minutes.

3. Water rinse for 10 minutes.

4. Soak in a 50/50 solution of water and isopropyl alcohol for 3 minutes.

5. Soak in 100% isopropyl alcohol for 3 minutes

6. Free air dry.
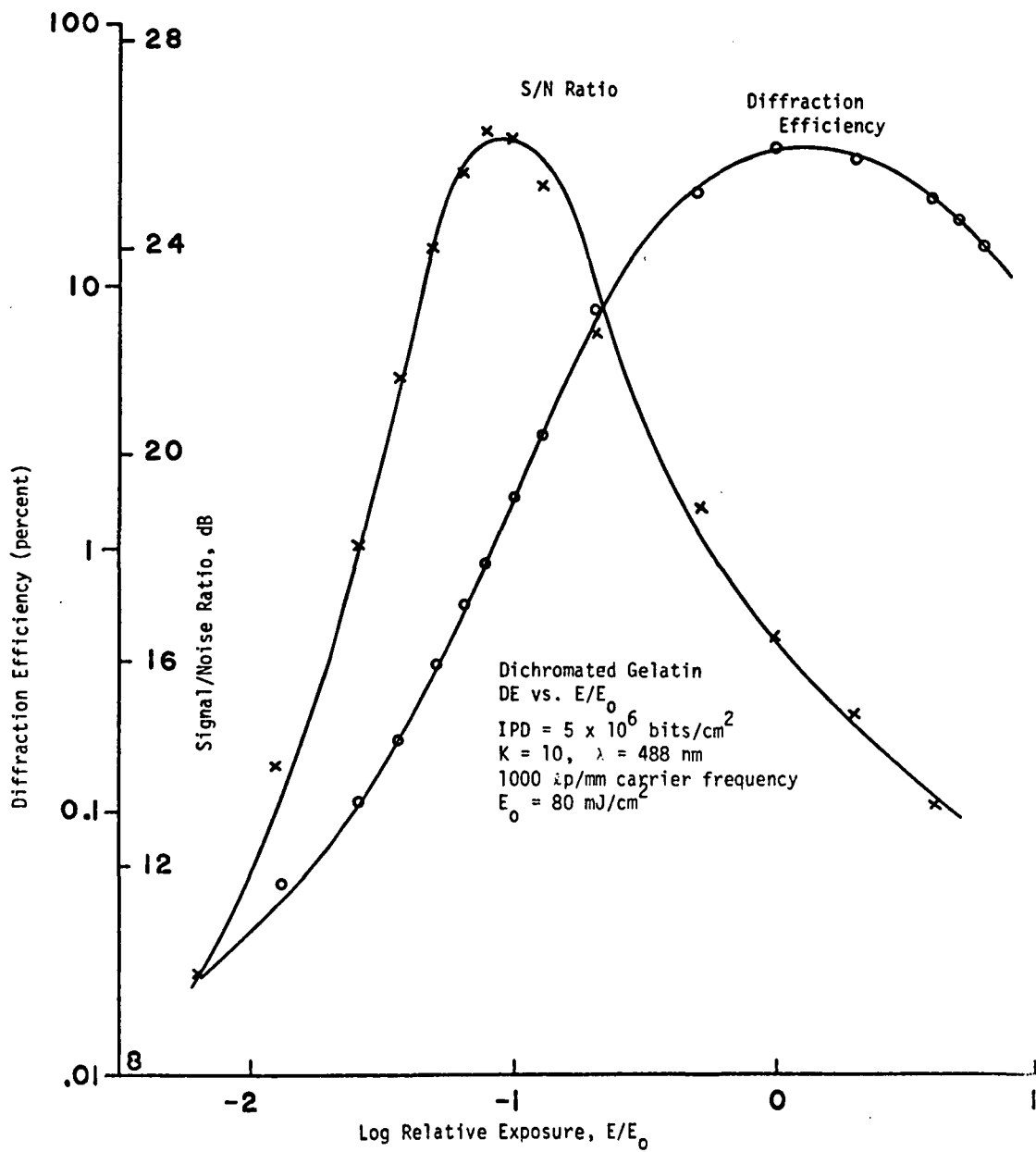
FIGURE 4-3. Hologram reconstruction parameters for dichromated gelatin.

exposure with respect to maximum diffraction efficiency which was 34%. Maximum SNR was 27 dB for a packing density of $5 \times 10^6$ bits/cm$^2$ and for K = 10 and $\nu_c$ = 1000 $\ell$/mm. Note that maximum SNR is obtained for an exposure almost ten times less than that required for maximum diffraction efficiency. In related experimental work we obtained maximum diffraction efficiencies of 90% and 75% for a plane wave grating and a zone plate, respectively. Surface quality was good and scatter noise low.

4.2.4 Bleached Photographic Emulsions. — We have evaluated both Kodak 649F and High Resolution plates. These are basically the same emulsions. The differences are in spectral sensitization and coating thickness. Kodak 649F is panchromatic and 17 μm thick while HRP is orthochromatic and 6 μm thick. Both have resolving power in excess of 3000 cycles/mm. After exposure and development, we bleached the emulsion to form phase holograms. Our processing procedures are summarized in Table 4-II. Figures 4-4 and 4-5 show results obtained for 649F at 633 nm and HRP at 488 nm. Exposure is again normalized with respect to maximum diffraction efficiency. The recording parameters were K = 10 and $\nu_c$ = 1000 $\ell$/mm while the packing density was $5 \times 10^6$ bits/cm$^2$. From these data it appears that HRP is somewhat better than 649F. Maximum diffraction efficiencies and SNR were 15.5% and 19% and 20 dB and 21 dB, respectively. As is typical of phase holograms, maximum SNR is obtained for exposures much less than required for maximum efficiency. The falloff of SNR at high efficiencies is significant in the case of silver halide emulsions because of scattering. In related work we obtained 40% efficiency for a plane wave grating and 20% efficiency for a zone plate. Surface quality was good but some scatter noise was noticable.

4.2.5 <u>Iron Oxide</u>. — Iron oxide plates were prepared by thermally decomposing iron pentacarbonyl, $Fe(CO)_5$, on glass substrates to a depth of about 0.4 μm. The iron oxide, $Fe_2O_3$, was then overcoated by spinning with a 1 μm layer of Shipley AZ1350 photoresist. Prior to exposure the plates were baked for 30 minutes at 100°C. After exposure the plates were (1) developed

HARRIS ELECTRO-OPTICS CENTER

TABLE 4-II
CHEMICAL PROCESSING OF PHOTOGRAPHIC EMULSION

<u>649F and HR Plates</u>

1. Develop: D19, 5 minutes

2. Stop: Kodak Indicator, 20 seconds

3. Fix: Kodak Rapid Fixer, 10 minutes

4. Rinse: 30 minutes

[a]5. Bleach: 10 minutes

6. Rinse: 5 minutes

[b]7. Clear: 5 minutes

8. Rinse: 10 minutes

[c]9. 50/50 Dry: 5 minutes

[d]10. 100 Dry: 3 minutes

11. Free Air Dry: 30 minutes


— Keep all bath temperatures at 70°F —

---

[a]<u>Bleach</u> - (a) To 500 ml of distilled $H_2O$ add 25g $FeCl_3$ and mix, (b) Now add 25g $CuBr_2$ and stir, (c) Carefully add 10 ml of concentrated $H_2SO_4$ while stirring slowly, (d) Note color of solution - if a brilliant emerald green add enough distilled $H_2O$ to make 1000 ml of solution - if not the right color add up to 10 ml more of $H_2SO_4$ and then add distilled $H_2O$ to make 1000 ml of solution, (e) Filter through paper towel, (f) Use bleach only once, i.e., do not return used bleach solution to original container.

[b]<u>Clear</u> - Part A: 5g/1000 ml distilled $H_2O$ of potassium permanganate Part B: To 500 ml of distilled $H_2O$ add 50 g KBr and mix. Then carefully mix in 10 ml of concentrated $H_2SO_4$. Add distilled water to make 1000 ml. Just before using add one part of A to 10 parts of B. Use only once.

[c]<u>50/50 Dry</u> - This means a mixture of one part distilled water and one part methanol.

[d]<u>100 Dry</u> - This means pure methanol.
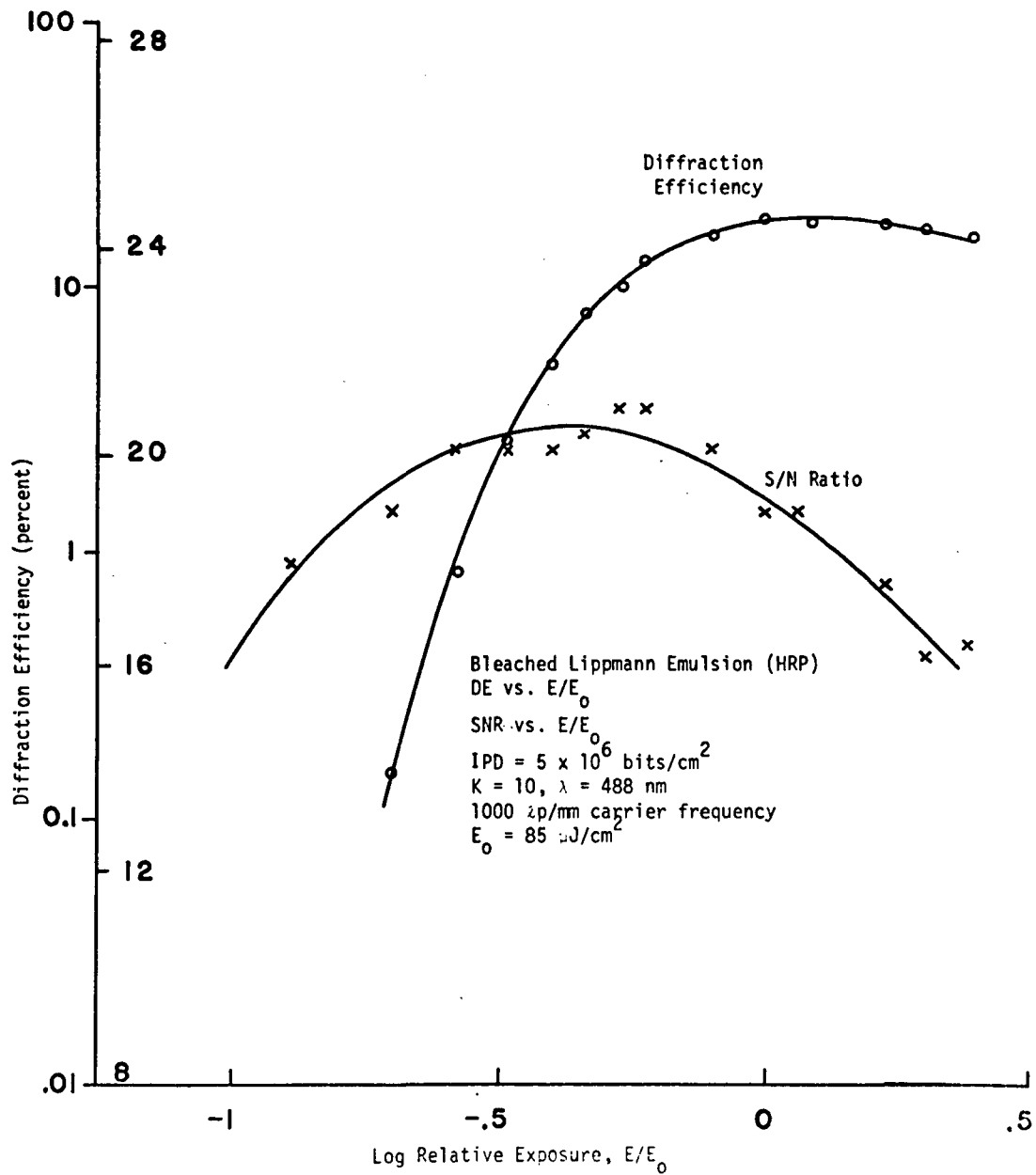
FIGURE 4-4. Hologram reconstruction parameters for Kodak HRP.
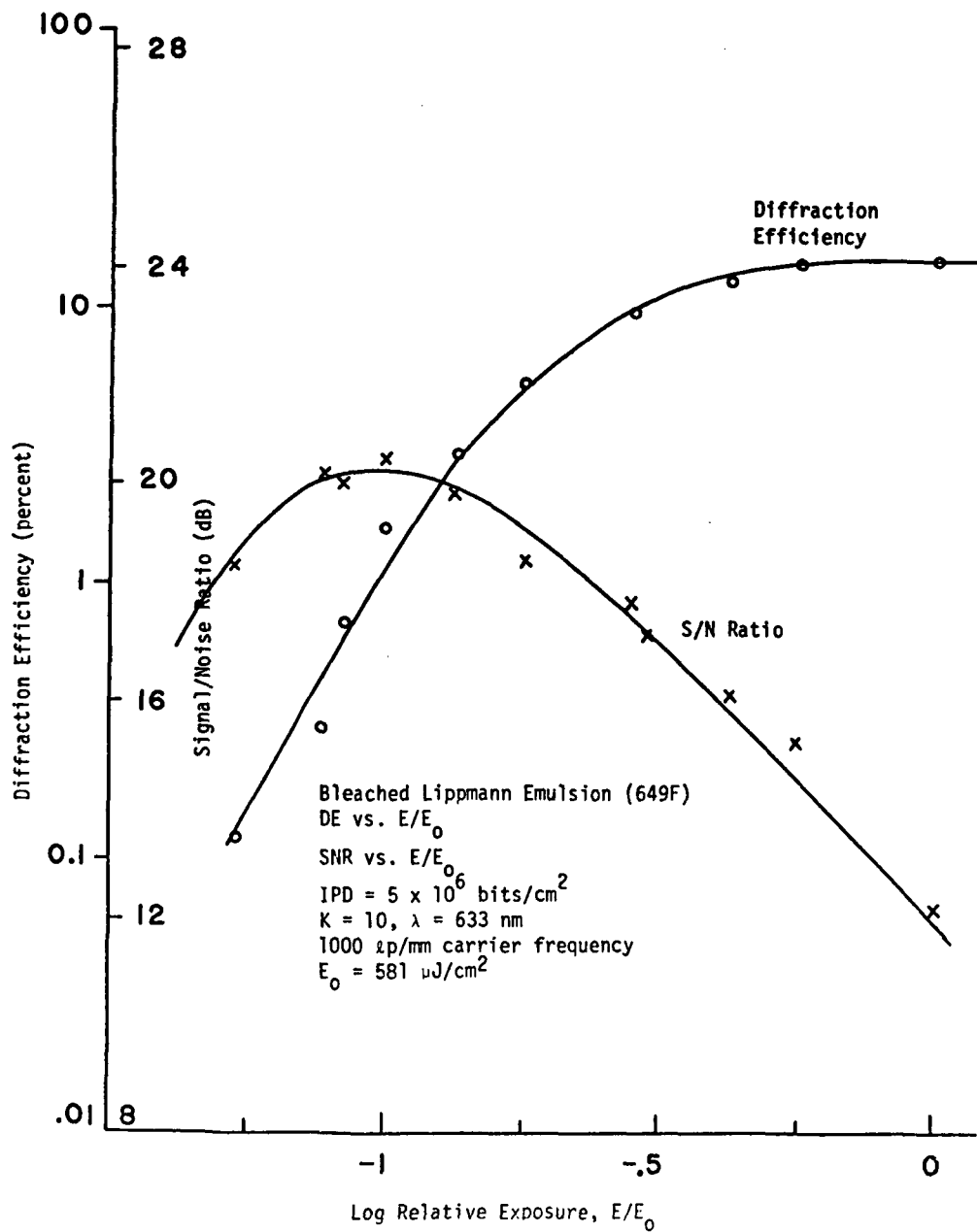
FIGURE 4-5. Hologram reconstruction parameters for Kodak 649F.

The figure shows two curves plotted against Log Relative Exposure, $E/E_o$ (horizontal axis ranging from about -1 to 0). The left vertical axis shows Diffraction Efficiency (percent) on a logarithmic scale from .01 to 100, and the inner axis shows Signal/Noise Ratio (dB) from 8 to 28.

Labels on the curves: "Diffraction Efficiency" and "S/N Ratio".

Text box within figure:
Bleached Lippmann Emulsion (649F)
DE vs. $E/E_o$
SNR vs. $E/E_o$
IPD = 5 x $10^6$ bits/$cm^2$
K = 10, $\lambda$ = 633 nm
1000 $\ell$p/mm carrier frequency
$E_o$ = 581 $\mu$J/$cm^2$

in Shipley AZ Developer for 60 seconds, (2) etched in a 10M solution of HCl, (3) washed with distilled water, (4) stripped with acetone, and (5) free-air dried. The end result is a modulated iron oxide layer on a glass substrate.

Typical experimental results are shown in Figures 4-6 and 4-7. For these data exposure was made at 457.9 nm and reconstruction at 632.8 nm. The reasons are that the photoresist is most sensitive at 457.9 nm and that iron oxide has very low absorption at 632.8 nm. Figure 4-6 shows diffraction efficiency as a function of exposure for plane wave gratings with K = 1 and $\nu$ = 570 cycles/mm and $\nu$ = 1600 cycles/mm. A maximum efficiency of 20% was achieved at $\nu$ = 1600 cycles/mm with an exposure of about 150 mJ/cm$^2$. The narrowing of the DE vs E curve for increasing spatial frequencies is an indication of the need for careful control of post exposure processing. Figure 4-7 shows SNR and DE as a function of exposure for the following recording parameters: K = 10, a carrier frequency of 570 cycles/mm, and a resolution-limited information packing density of 5 x 10$^6$ bits/cm$^2$. The maximum SNR was about 12 dB at a diffraction efficiency of 2%. This low value of SNR is attributable to the highly nonlinear nature of thin phase holograms.

Our experience with iron oxide recording materials indicates that it has a high degree of environmental stability, but relatively poor hologram reconstruction parameters. It is not clear, however, that preparation and processing have been optimized. Thus, for the present we conclude that iron oxide layers are marginally qualified for holographic optical element applications.

4.2.6 Thick Plastics. — We have investigated the holographic properties of poly (methy methacrylate) and cellulose acetate butyrate, abbreviated PMM and CAB, respectively. These materials were prepared in the laboratory by (1) dissolving either PMM or CAB in chloroform, (2) adding to the solution 0.05 grams of p-benzoquinone (PBQ) per gram of plastic, and (3) casting the sensitized plastic solution on a glass substrate.
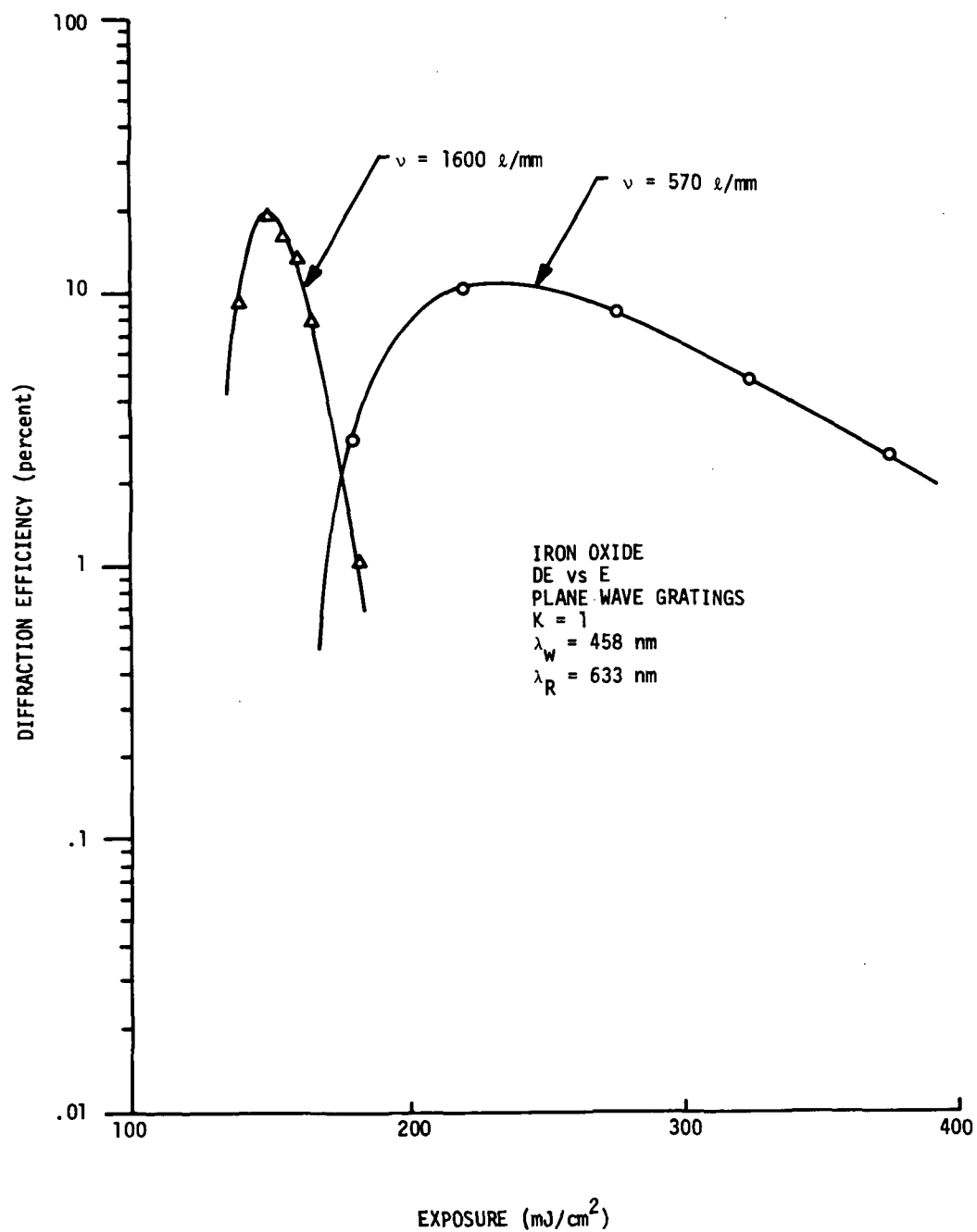
FIGURE 4-6. Diffraction efficiency for plane waves as a function of
exposure for iron oxide.
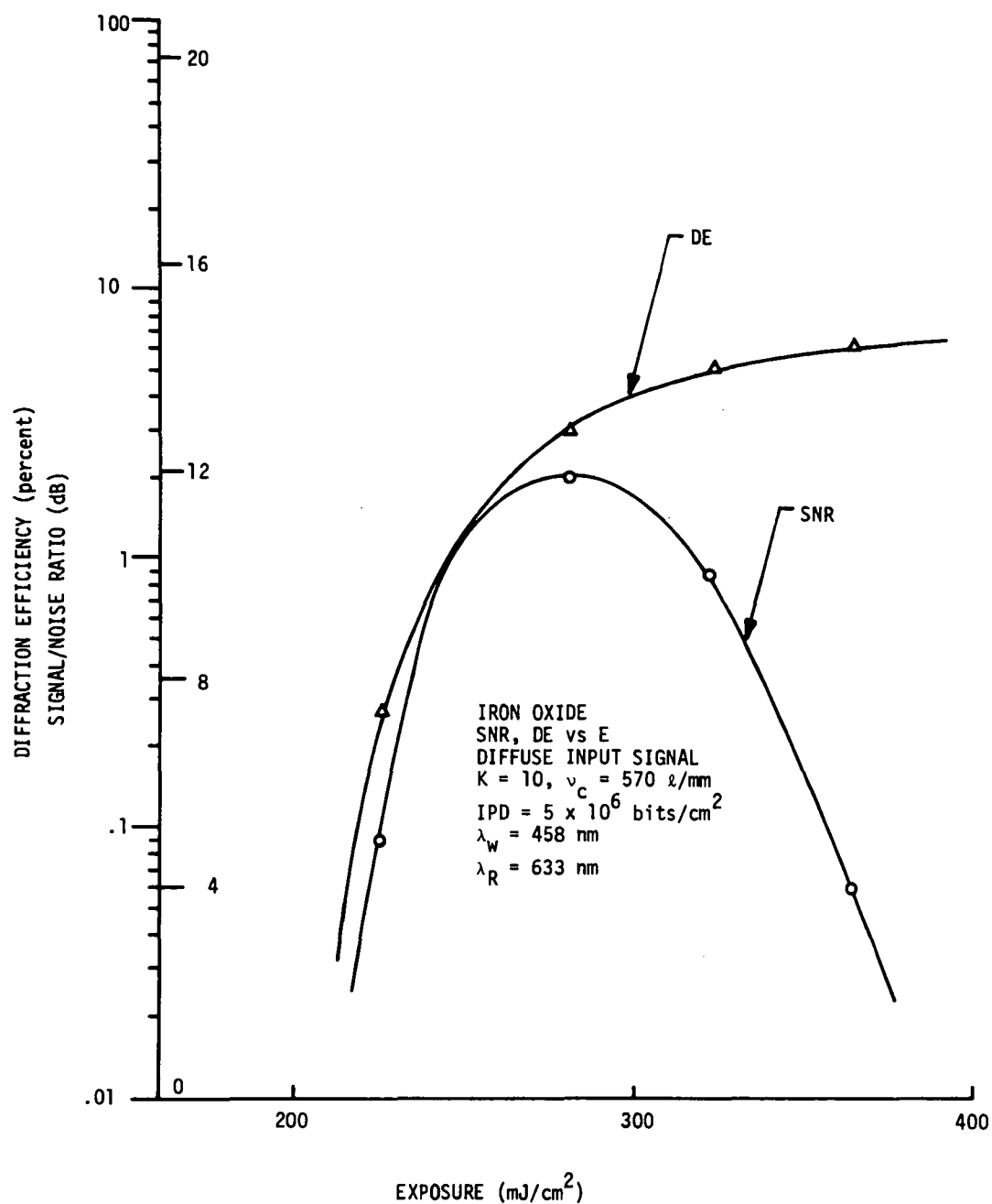
FIGURE 4-7. Signal/Noise ratio and diffraction efficiency as a function of exposure for iron oxide.

The preparation of thick plastic layers of good optical quality is difficult. Through trial and error experimentation we have found that the following procedure consistently produces good results:

1. Thoroughly clean a glass substrate.

2. Level the glass substrate.

3. Pour a measured amount of the light-sensitive solution on the substrate. Outline the perimeter of the substrate near the edges first. Then pour the remainder in the center. A guideline is 0.2 ml of solution/cm$^2$ of substrate area, assuming a solution viscosity of 2,000 cp.

4. Cover the cast layer with an inverted glass dish or equivalent. The cast layer must dry slowly in an atmosphere of its own solvent to avoid blushing.

5. Dry slowly for 24-48 hours.

6. Bake for two hours at 70°C. Start at room temperature and slowly raise the temperature to 70°C. Cool slowly. This procedure removes residual solvent and anneals the plastic layer.

Depending on the plastic concentration, pour casting yields layers ranging in thickness from 50-300 μm for PMM and CAB (17% butyrate). CAB (55% butyrate) is extremely soluble and layers 750 μm thick are easily prepared. Layers of PMM up to 2 mm thick can be cast using masking tape dams on the substrate to prevent overflow. CAB is too brittle to form layers this thick. Exploratory work indicates that injection molding may provide an alternative method for constructing thick layers.

Experimental results for selected samples of PMM and CAB are shown in Figures 4-8 and 4-9. Figure 4-8 gives DE as a function of exposure for a 100 μm and a 1 mm layer of PMM and a 250 μm layer of CAB. Although these materials have a low exposure sensitivity, maximum achievable efficiency is quite high; we have obtained (somewhat inconsistently) efficiencies on the order of 95 percent. Figure 4-9 shows SNR and DE for a 250 μm layer of CAB.

THICK PLASTICS
DE vs E
PLANE WAVE GRATINGS
K = 1, $\nu$ = 1,000 $\ell$/mm
$\lambda_W$ =$\lambda_R$ = 488 nm

○ - PMM, 100 μm Layer

△ - PMM, 1 mm Layer

□ - CAB, 250 μm Layer
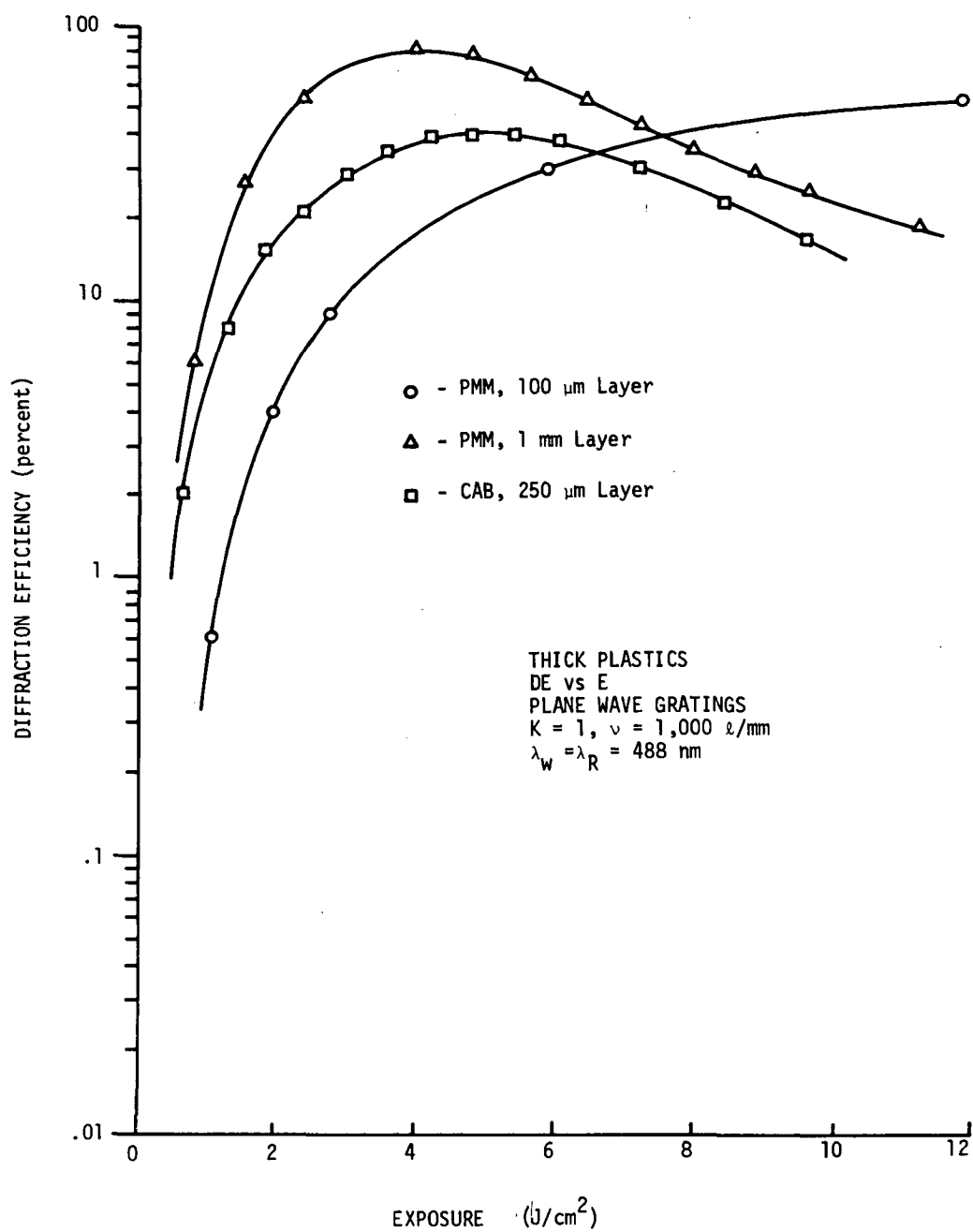
FIGURE 4-8. Diffraction efficiency for plane waves as a function of exposure for thick plastics.
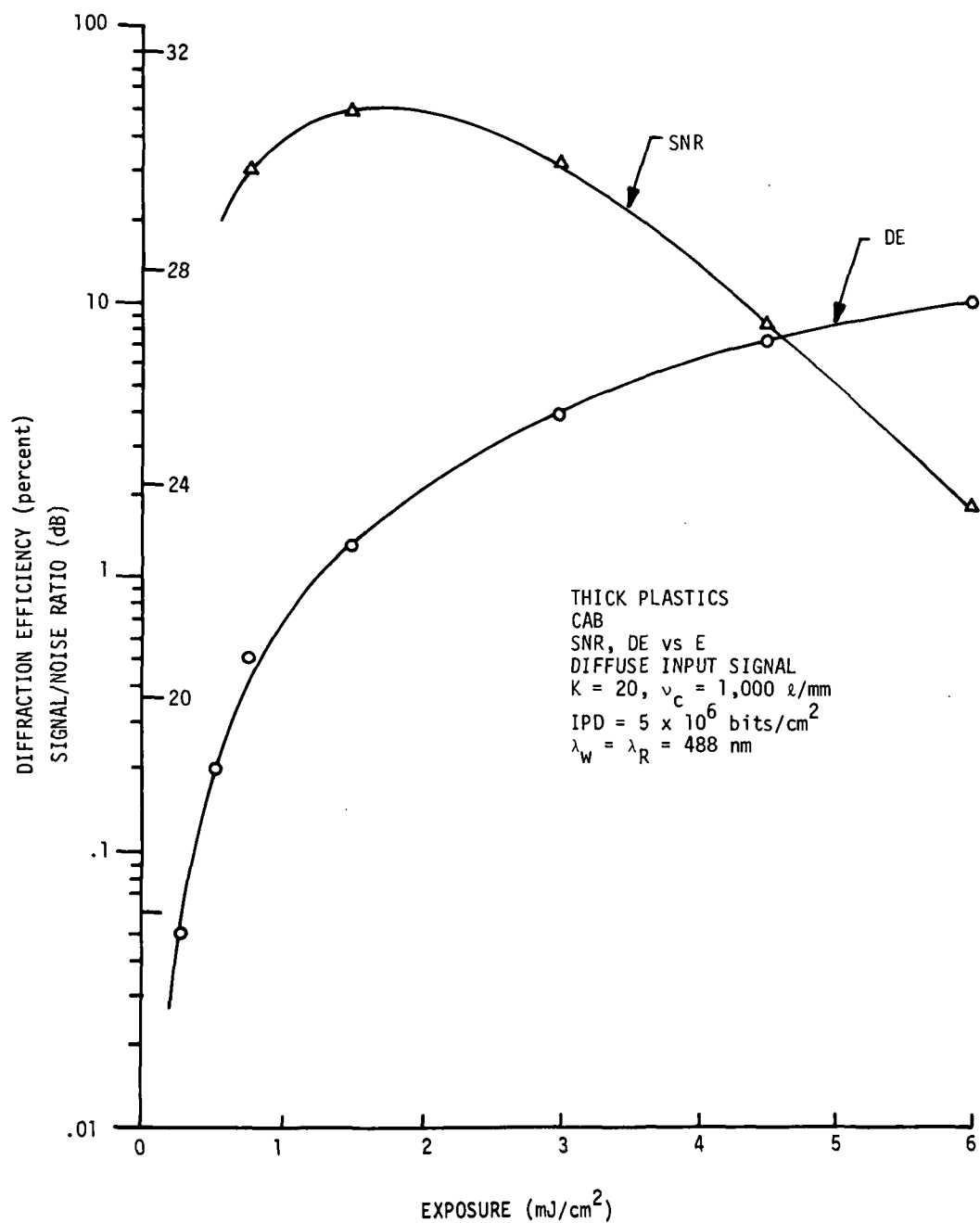
FIGURE 4-9. Signal/noise ratio and diffraction efficiency as a function of exposure for CAB.

The recording parameters were K = 20, a carrier frequency of 1000 cycles/mm, and a resolution-limited information packing density of $5 \times 10^6$ bits/cm$^2$. The maximum SNR measured was 31 dB with a corresponding DE of about 2%. This is the largest value of SNR we have ever measured.

## 4.3 Summary and Conclusions

We have evaluated a number of representative holographic recording media. Because of efficiency considerations, only phase materials were studied. In terms of holographic properties we can categorize these materials as planar (photoresists and iron oxide), intermediate (dichromated gelatin and bleached photographic emulsions), and volume (photodegradable plastics). The planar materials can achieve a maximum efficiency of about 34% and exhibit no Bragg sensitivity. The intermediate and volume materials can approach diffraction efficiencies of 100 percent. Bragg sensitivity increases with layer thickness for typical recording geometries. As we have shown, aberration behavior for planar and volume recording media appears to be similar. However, Bragg sensitivity limits the angular field and spectral range of holographic optical elements recorded in volume materials.

For experimental purposes any of the materials we investigated are suitable. Photographic emulsions (bleached or unbleached) are clearly the most convenient to use for determining the optical properties of holographic elements. Unfortunately, photographic emulsions have a number of properties that limit their utility. In particular, bleached photographic emulsions scatter a great amount of light at high efficiencies and, they are unstable to prolonged illumination even under controlled conditions. Many other light-sensitive materials suffer from similar deficiencies.

Thus, from a practical point of view, the choice of recording materials is limited. For constructing holographic optical elements, we feel that two types of material should be considered: (1) Photoresists - These materials

HARRIS ELECTRO-OPTICS CENTER

are well suited for the fabrication of reflective elements. They are readily aluminized and can also be dielectric-coated for ultraviolet and infrared applications, and (2) Dichromated Gelatin - In terms of efficiency and cosmetic quality, no other materials are competitive. Although gelatin can be adversley effected by high relative humidity and bacteria and tends to change dimensionally after processing (a swelling effect), these problems can be solved by postprocessing and overcoating, e.g., with a glass coverplate.

## 4.4 Recommendations

We recommend that the physical, chemical, and holographic properties of photoresists and dichromated gelatin be further studied. The goal of the study should be the delineation of the technology required to produce high quality recording media. Specific areas of investigation should include preparation, processing, and stabilization optimization beyond presently available technology. In addition, vacuum coating methods for constructing reflective elements merit further study.

## 4.5 References

1. M. Chang, Appl. Opt., 10, 2550 (1971).
2. L. H. Lin, Appl. Opt., 8, 963 (1969).

# 5
# NEW TECHNOLOGY

After a thorough review of the work performed under this contract we find that no new innovation, discovery, improvement, or invention has resulted.

HARRIS ELECTRO-OPTICS CENTER

# 6
# FINANCIAL STATUS

A. Expenditures to Date:  $38,700

B. Funding Required for Completion:  $15,550

C. Problem Areas:  None.

HARRIS ELECTRO-OPTICS CENTER

**RADIATION**

A DIVISION OF HARRIS - INTERTYPE CORPORATION

<u>APPENDIX A</u>

Aberration Data for

Single Holographic Optical Elements

A.1 Introduction

A.2 Chromatic and Seidel Aberration Data as a Function of
Bending Factor Q:  Groups 1 to 4

A.3 Chromatic and Seidel Aberration Data for Phase Recording
Materials:  Groups 5 to 7.

HARRIS ELECTRO-OPTICS CENTER

RADIATION

A DIVISION OF HARRIS - INTERTYPE CORPORATION

## A.1

## Introduction

Appendix A is a summary of the experimental and analytical data generated by a joint study of the aberration properties of single holographic optical elements by the Harris Electro-Optics Center and the Environmental Research Institute of Michigan. The data are arranged in groups that reflect particular experimental objectives. For example, Group 1 is an in depth study of chromatic aberrations. Taken as a whole, this effort represents the most extensive and general investigation of the properties of holographic optical elements now available.

The data for each group are prefaced by an explanatory introduction. This is followed by a table containing recording and reconstruction parameters, geometrical data, and an experimental count of total waves of aberration. Note that each entry in the table corresponds to some experimental condition for which there is a photograph of an interferogram that represents an aberrated imaging condition. The next table is a computer printout of the geometrical data contained in the previous table. The numbers differ in general by at most one part in one hundred. This represents a consistant attempt to reconcile the positional data of the experimental work as reported with the aberration data generated by the computer analysis. A main source of error was the measurement (experimental) of the initial radial distances of the point sources from the hologram recording plane. In the following table, the types and amounts of aberration obtained by computer analysis using optimized geometry are presented. Finally, photographs of interferograms corresponding to each experimental condition are shown, together with a computer-generated version of the interferogram on the facing page.

HARRIS ELECTRO-OPTICS CENTER

A.2

Chromatic and Seidel Aberration Data as a

Function of Bending Factor Q

Groups 1 to 4

(Krypton Laser Construction and Readout)

Group 1

Chromatic Aberrations

Kodak HR Plate

$Q = 4$

Group 1 contains data only for chromatic aberrations. For $\lambda_c$ = 476.2 nm, 520.8 nm, and 568.2 nm we photographed interference patterns corresponding to image aberrations at the circle of least confusinon, the tangential focus, and the sagittal focus (all photographs are arranged in this order; see for, example, NH101, 102 and 103). These data are shown in photographs NH101, 102 and 103, NH108, 109 and 110 and NH115, 116 and 117, respectively. For $\lambda_c$ = 568.2 nm the reconstruction point adjustment far exceeded the calibrated range of our micropositioner. Hence, we have no positional data for this case. Photographs NH104, 105 and 106 and NH111, 112 and 113 respectively, show the existance of object points that reduce residual aberrations by a factor of one half. Finally, for $\lambda_c$ = 476.2 nm and for $\lambda_c$ = 520.8 nm, object positions were located that essentially eliminate residual aberrations over the entire hologram aperture; these cases are illustrated in photographs NH107 and NH114.

HARRIS ELECTRO-OPTICS CENTER

## GROUP 1

Kodak HR Plate (Chromatic Aberrations)

$R_o$ = 6.32 in.    $\lambda_o$ = 482.5 nm    $\langle\theta\rangle$ = 29.°5

$R_R^o$ = 10.5 in.    Q = 4    $\langle\bar{K}\rangle$ = split bisector

All dimensions in inches

| Photo | $\Delta x_i$ | $\Delta y_i$ | $\Delta z_i$ | $\Delta x_c$ | $\Delta y_c$ | $\Delta z_c$ | $\lambda_c$ | $\Delta_x$ | $\Delta_y$ |
|---|---|---|---|---|---|---|---|---|---|
| 101 | 0 | 0 | 0 | -.0737 | 0 | -.0724 | 476.2 | 5 | 7 |
| 102 | 0 | 0 | 0 | -.0737 | 0 | -.0522 | 476.2 | 2 | 13 |
| 103 | 0 | 0 | 0 | -.0733 | 0 | -.0945 | 476.2 | 12 | 0 |
| 104 | .0250 | 0 | .0250 | -.0305 | 0 | -.0362 | 476.2 | 3 | 2 |
| 105 | .0250 | 0 | .0250 | -.0305 | 0 | -.0450 | 476.2 | 1 | 6 |
| 106 | .0250 | 0 | .0250 | -.0305 | 0 | -.0267 | 476.2 | 6 | 0 |
| 107 | .0177 | 0 | .0250 | -.0429 | 0 | -.0284 | 476.2 | .5 | 0 |
| 108 | 0 | 0 | 0 | .4683 | 0 | .4863 | 520.8 | 36 | 38 |
| 109 | 0 | 0 | 0 | .4640 | 0 | .3775 | 520.8 | 17 | 70 |
| 110 | 0 | 0 | 0 | .4728 | 0 | .6138 | 520.8 | 67 | 1 |
| 111 | -.0750 | 0 | -.0750 | .3293 | 0 | .3532 | 520.8 | 8 | 8 |
| 112 | -.0750 | 0 | -.0750 | .3290 | 0 | .3320 | 520.8 | 4 | 15 |
| 113 | -.0750 | 0 | -.0750 | .3302 | 0 | .3827 | 520.8 | 15 | 0 |
| 114 | -.0960 | 0 | -.0990 | .2907 | 0 | .3081 | 520.8 | .25 | 0 |
| 115 | - | - | - | - | - | - | 568.2 | - | - |
| 116 | - | - | - | - | - | - | 568.2 | - | - |
| 117 | - | - | - | - | - | - | 568.2 | - | - |

GROUP 1 OPTIMIZED   KODAK H.R. PLATE

RO = 6.3 IN.      AO = 14.7 DEG.      LAMO = 482.5 NM.
RR = 10.5 IN.     AR =-14.7 DEG.      Q = 4.0

| PHOTO | DXI | DYI | DZI | DXC | DYC | DZC | LAMC |
|-------|-----|-----|-----|-----|-----|-----|------|
| NH101 | 0.0 | 0.0 | 0.0 | -0.0715 | 0.0 | -0.0692 | 476.2 |
| NH102 | 0.0 | 0.0 | 0.0 | -0.0715 | 0.0 | -0.0498 | 476.2 |
| NH103 | 0.0 | 0.0 | 0.0 | -0.0711 | 0.0 | -0.0907 | 476.2 |
| NH104 | 0.0252 | 0.0 | 0.0251 | -0.0305 | 0.0 | -0.0309 | 476.2 |
| NH105 | 0.0252 | 0.0 | 0.0272 | -0.0305 | 0.0 | -0.0336 | 476.2 |
| NH106 | 0.0251 | 0.0 | 0.0183 | -0.0305 | 0.0 | -0.0404 | 476.2 |
| NH107 | 0.0176 | 0.0 | 0.0217 | -0.0429 | 0.0 | -0.0320 | 476.2 |
| NH108 | 0.0 | 0.0 | 0.0 | 0.4596 | 0.0 | 0.4419 | 520.8 |
| NH109 | 0.0 | 0.0 | 0.0 | 0.4560 | 0.0 | 0.3394 | 520.8 |
| NH110 | 0.0 | 0.0 | 0.0 | 0.4636 | 0.0 | 0.5619 | 520.8 |
| NH111 | -0.0735 | 0.0 | -0.0734 | 0.3259 | 0.0 | 0.3224 | 520.8 |
| NH112 | -0.0758 | 0.0 | -0.0611 | 0.3230 | 0.0 | 0.3398 | 520.8 |
| NH113 | -0.0758 | 0.0 | -0.0705 | 0.3232 | 0.0 | 0.3616 | 520.8 |
| NH114 | -0.0951 | 0.0 | -0.0929 | 0.2873 | 0.0 | 0.2948 | 520.8 |

GROUP 1 OPTIMIZED KODAK H.R. PLATE

| PHOTO | SPHERICAL | COMA | ABERRATIONS ASTIGMATISM | RMS | TOTAL |
|-------|-----------|------|-------------------------|-----|-------|
| NH101 | 0.23164 | 3.40698 | 6.89349 | 1.69262 | 7.68379 |
| NH102 | 0.16203 | 2.63865 | 7.48707 | 2.62516 | 7.79978 |
| NH103 | 0.30808 | 4.23348 | 6.95599 | 2.32134 | 6.75993 |
| NH104 | 0.05087 | 1.17103 | 3.64348 | 0.86883 | 3.65342 |
| NH105 | 0.05577 | 1.06618 | 3.62622 | 1.13413 | 3.58268 |
| NH106 | 0.06818 | 0.80371 | 3.65834 | 1.15536 | 3.59916 |
| NH107 | 0.07466 | 0.20714 | 0.50112 | 0.10497 | 0.43914 |
| NH108 | 1.45439 | 20.71803 | 39.94451 | 9.70514 | 45.16502 |
| NH109 | 1.14159 | 17.31966 | 40.40547 | 12.78231 | 48.44353 |
| NH110 | 1.80773 | 24.57319 | 39.35300 | 12.54419 | 40.55223 |
| NH111 | 0.85483 | 7.33747 | 9.67751 | 2.43249 | 10.42270 |
| NH112 | 0.90548 | 7.68979 | 8.81359 | 2.89860 | 11.30089 |
| NH113 | 0.97601 | 8.41958 | 8.69770 | 2.90439 | 9.79655 |
| NH114 | 0.69992 | 3.55962 | 0.51018 | 0.41080 | 1.42293 |
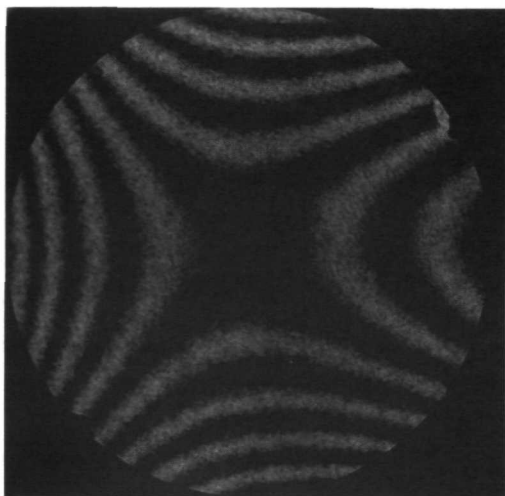
NH101
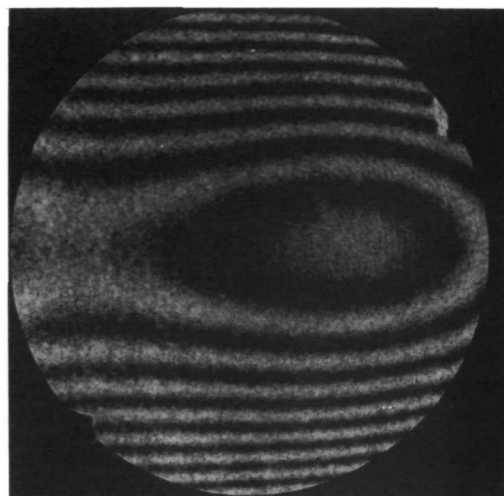
NH102
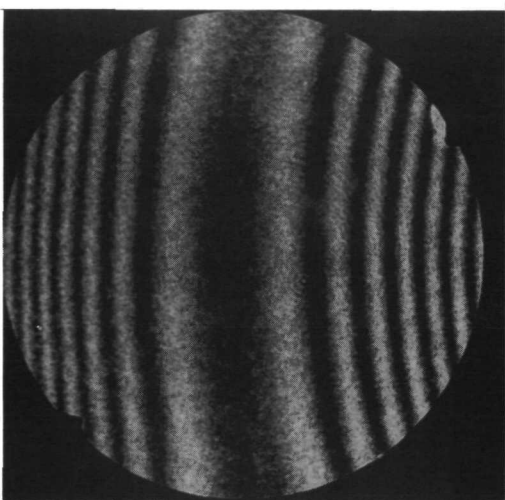
NH103
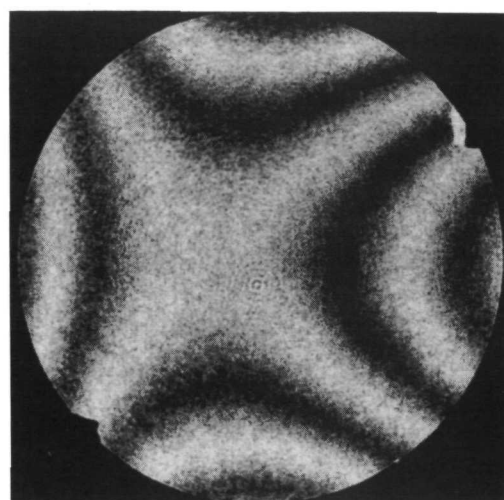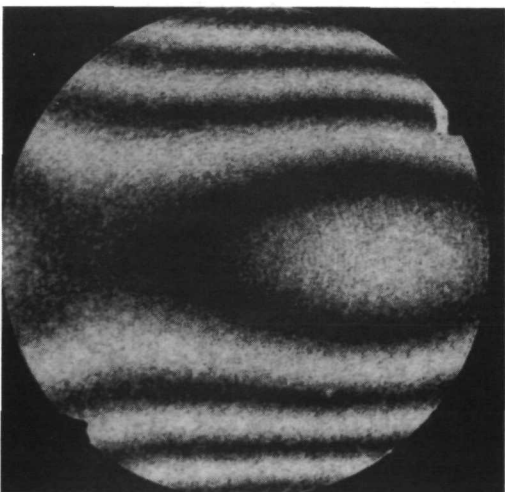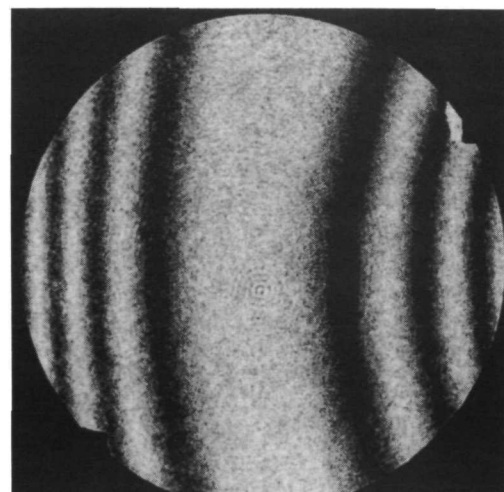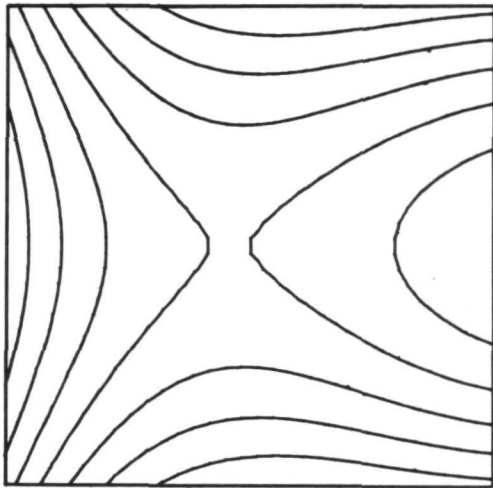
NH104

NH105

NH106

NH101
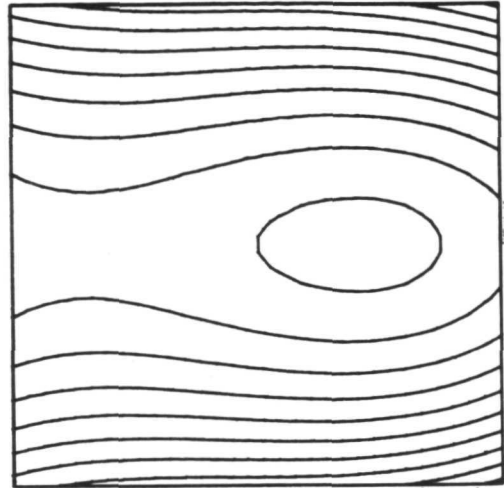


NH102
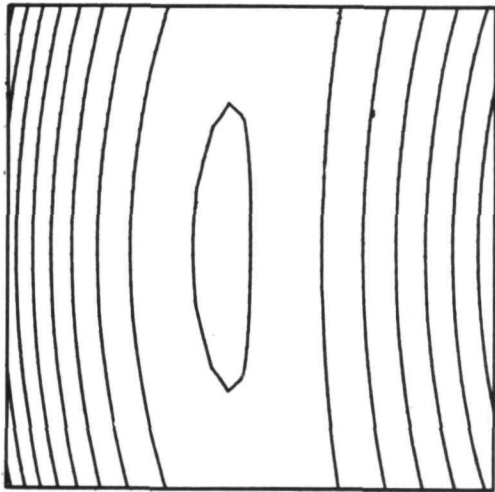


NH103
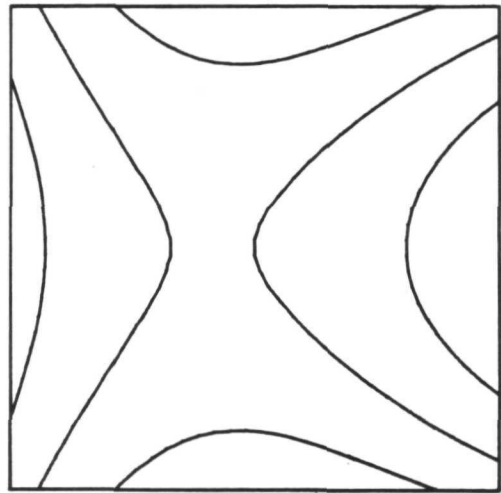


NH104
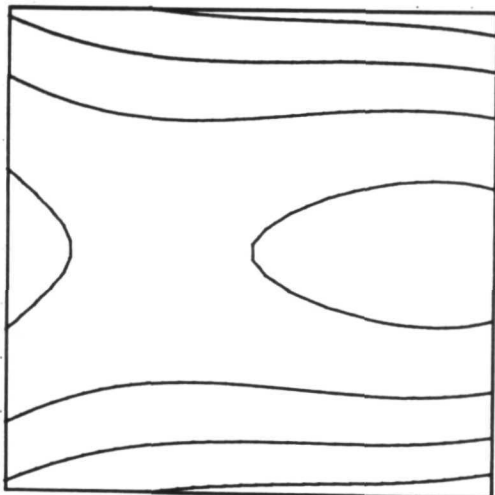


NH105
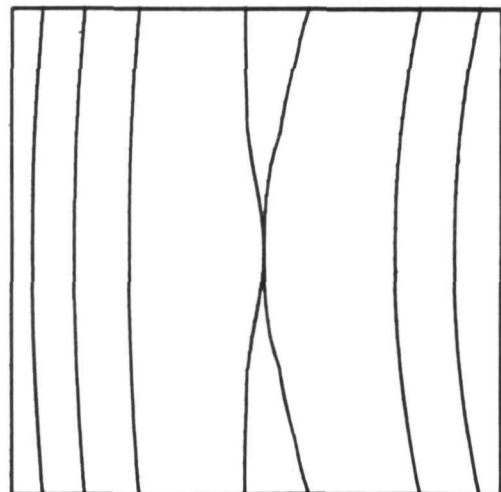


NH106
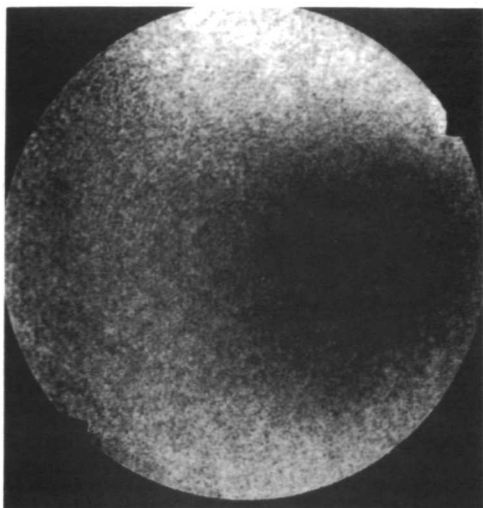
NH107
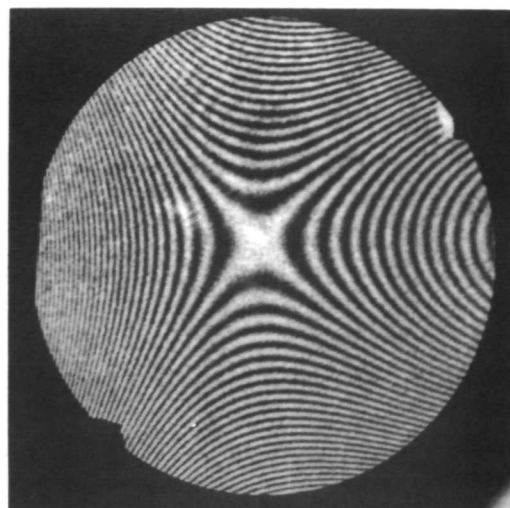


NH108
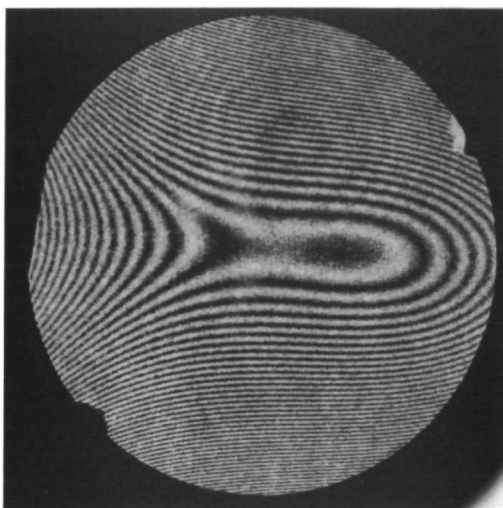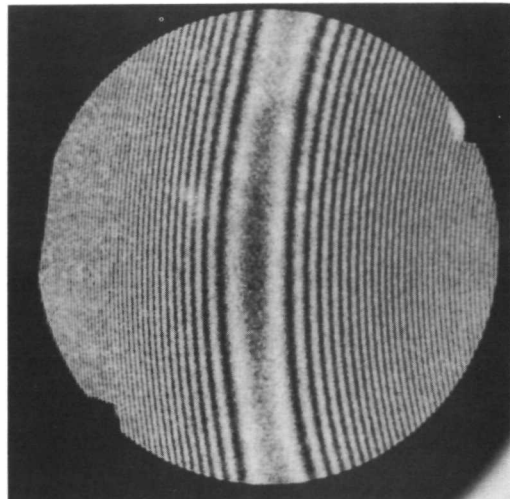


NH109



NH110



NH111



NH112

A-9

NHI07



NHI08



NHI09



NHII0



NHIII
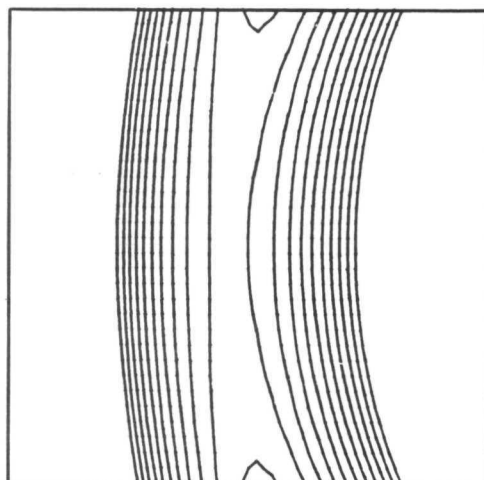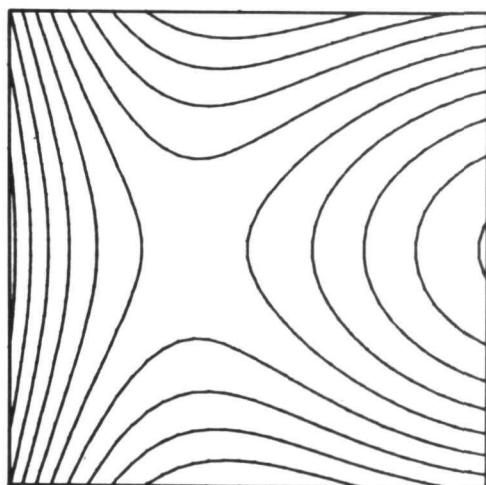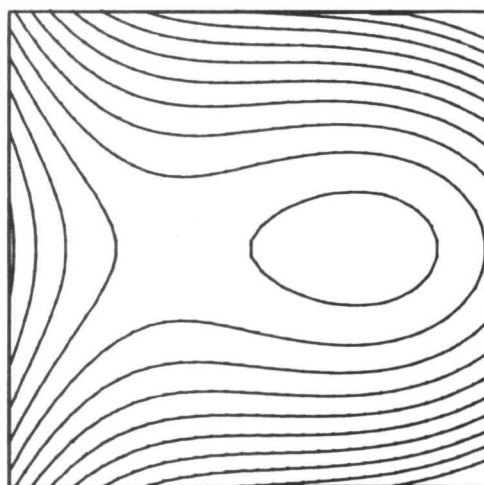


NHII2
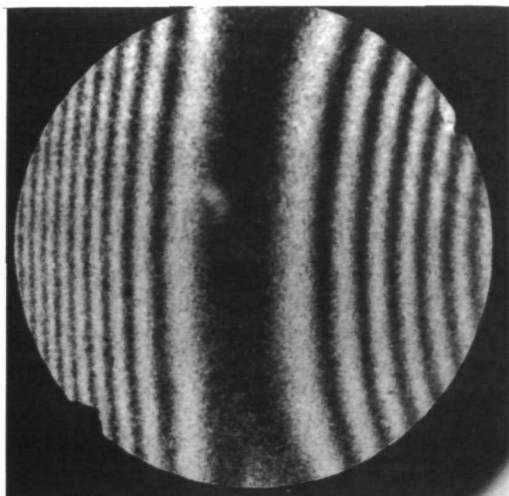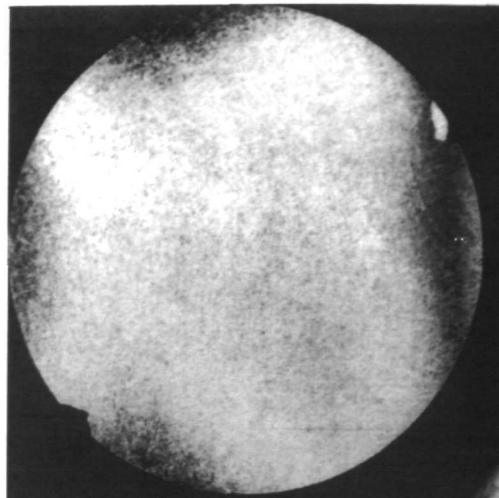
NH113

NH114

NH115
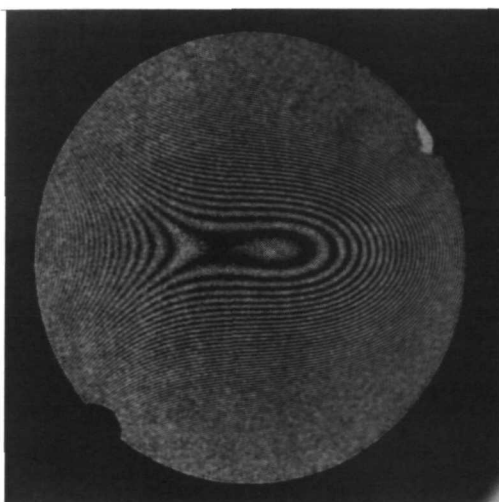
NH116
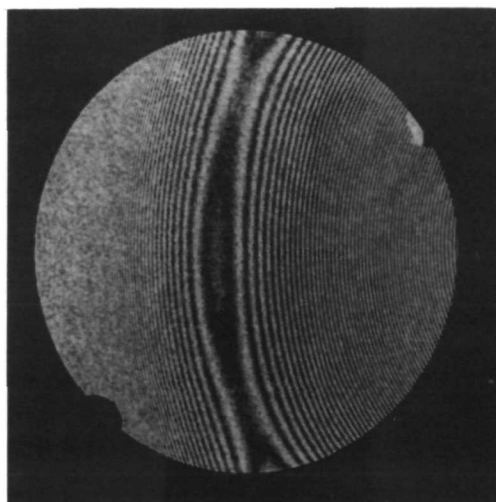
NH117

NHII3



NHII4
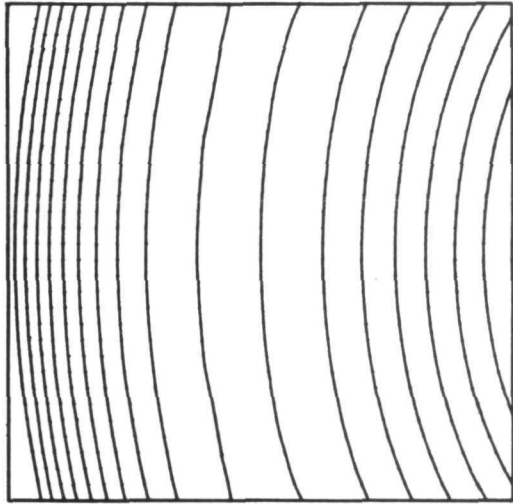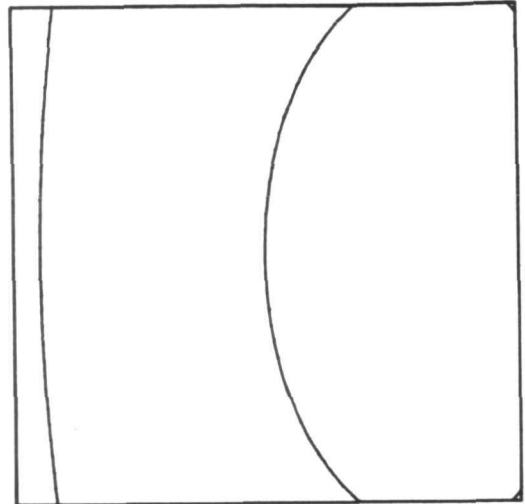
Group 2

Seidel Aberrations

Kodak HR Plate

$Q = 4$

The data in Group 2 concern only Seidel or third order monochromatic aberrations (this is a slight misnomer since our experimental data involve no approximations; however, third order aberrations dominate for the field angles involved in the present investigation). The angular field of the holographic optical elements both above and below the optical axis was explored in the $x_0 - z_0$ plane. The results of this study are shown in photographs NH118 to NH131. In a similar manner the positive $y_0 - z_0$ plane was investigated; the interferograms are shown in photographs NH132 to NH138. Photographs NH139 illustrates the zero order condition when the two wavefronts are midway through a random phase shift. Finally, the photographs numbered NH140 to NH145 were obtained by moving the object point longitudinally. Note that the interference patterns for this case are different than those obtained by exploring the transverse field. Moreover, the type of pattern shown in these photographs (which are selected on the basis of minimum fringe count) can be modified.

Note that we have chosen to show the aberration interferograms in this series of photographs only for the case of the circle of least confusion. This convention is followed for all succeeding data groups for Seidel aberrations.

HARRIS ELECTRO-OPTICS CENTER

## GROUP 2

Kodak HR Plate (Seidel Aberrations)
$R_o$ = 6.32 in.      $\lambda_o$ = 482.5 nm      $\langle\theta\rangle$ = 29.°5
$R_R^o$ = 10.5 in.    $Q^o$ = 4      $\langle\bar{K}\rangle$ = split bisector

| Photo | $\Delta x_i$ | $\Delta y_i$ | $\Delta z_i$ | $\Delta x_c$ | $\Delta y_c$ | $\Delta z_c$ | $\lambda_c$ | $\Delta_x$ | $\Delta_y$ |
|---|---|---|---|---|---|---|---|---|---|
| 118 | -.0020 | 0 | 0 | -.0034 | 0 | .0019 | 482.5 | 1 | 0 |
| 119 | -.0040 | 0 | 0 | -.0067 | 0 | .0039 | 482.5 | 2 | 2 |
| 120 | -.0080 | 0 | 0 | -.0135 | 0 | .0100 | 482.5 | 2 | 3 |
| 121 | -.0160 | 0 | 0 | -.0260 | 0 | .0176 | 482.5 | 6 | 6 |
| 122 | -.0320 | 0 | 0 | -.0541 | 0 | .0344 | 482.5 | 13 | 11 |
| 123 | -.0640 | 0 | 0 | -.1086 | 0 | .0685 | 482.5 | 27 | 22 |
| 124 | -.1280 | 0 | 0 | -.2186 | 0 | .1397 | 482.5 | 55 | 50 |
| 125 | .0020 | 0 | 0 | .0034 | 0 | -.0026 | 482.5 | 0 | .5 |
| 126 | .0040 | 0 | 0 | .0068 | 0 | -.0047 | 482.5 | 2 | 1 |
| 127 | .0080 | 0 | 0 | .0136 | 0 | -.0101 | 482.5 | 2.5 | 2 |
| 128 | .0160 | 0 | 0 | .0269 | 0 | -.0197 | 482.5 | 5.5 | 6.5 |
| 129 | .0320 | 0 | 0 | .0540 | 0 | -.0369 | 482.5 | 12 | 12 |
| 130 | .0640 | 0 | 0 | .1078 | 0 | -.0755 | 482.5 | 25 | 26 |
| 131 | .1280 | 0 | 0 | .2154 | 0 | -.1366 | 482.5 | 52 | 48 |
| 132 | 0 | .0020 | 0 | 0 | .0035 | 0 | 482.5 | 1 | 0 |
| 133 | 0 | .0040 | 0 | 0 | .0070 | 0 | 482.5 | 2 | 1 |
| 134 | 0 | .0080 | 0 | 0 | .0136 | 0 | 482.5 | 3 | 3 |
| 135 | 0 | .0160 | 0 | 0 | .0271 | 0 | 482.5 | 6 | 6 |
| 136 | 0 | .0320 | 0 | 0 | .0542 | 0 | 482.5 | 12 | 13 |
| 137 | 0 | .0640 | 0 | 0 | .1082 | 0 | 482.5 | 25 | 25 |
| 138 | 0 | .1280 | 0 | 0 | .2173 | 0 | 482.5 | 49 | 53 |
| 139 | 0 | 0 | 0 | 0 | 0 | 0 | 482.5 | .5 | 0 |
| 140 | 0 | 0 | -.0020 | 0 | 0 | -.0053 | 482.5 | 0 | 0 |
| 141 | 0 | 0 | -.0080 | 0 | 0 | -.0225 | 482.5 | 0 | 0 |
| 142 | 0 | 0 | -.0160 | 0 | 0 | -.0459 | 482.5 | 1.5 | 0 |
| 143 | 0 | 0 | -.0320 | 0 | 0 | -.0933 | 482.5 | 2.5 | .5 |
| 144 | 0 | 0 | -.0640 | 0 | 0 | -.1807 | 482.5 | 5 | 1 |
| 145 | 0 | 0 | -.1280 | 0 | 0 | -.3623 | 482.5 | 10 | 4 |

GROUP 2 OPTIMIZED   KODAK H.R. PLATE

RO = 6.3 IN.    AO = 14.7 DEG.      LAMO = 482.5 NM.
RR = 10.5 IN.   AR = -14.7 DEG.     Q = 4.0

| PHOTO | DXI | DYI | DZI | DXC | DYC | DZC | LAMC |
|-------|-----|-----|-----|-----|-----|-----|------|
| NH118 | -0.0021 | 0.0 | 0.0001 | -0.0034 | 0.0 | 0.0020 | 482.5 |
| NH119 | -0.0041 | 0.0 | 0.0012 | -0.0067 | 0.0 | 0.0066 | 482.5 |
| NH120 | -0.0082 | 0.0 | -0.0000 | -0.0135 | 0.0 | 0.0099 | 482.5 |
| NH121 | -0.0157 | 0.0 | -0.0000 | -0.0260 | 0.0 | 0.0162 | 482.5 |
| NH122 | -0.0326 | 0.0 | -0.0008 | -0.0541 | 0.0 | 0.0309 | 482.5 |
| NH123 | -0.0651 | 0.0 | -0.0001 | -0.1086 | 0.0 | 0.0670 | 482.5 |
| NH124 | -0.1257 | 0.0 | 0.0002 | -0.2106 | 0.0 | 0.1348 | 482.5 |
| NH125 | 0.0021 | 0.0 | -0.0000 | 0.0034 | 0.0 | -0.0023 | 482.5 |
| NH126 | 0.0041 | 0.0 | 0.0003 | 0.0068 | 0.0 | -0.0032 | 482.5 |
| NH127 | 0.0082 | 0.0 | -0.0000 | 0.0136 | 0.0 | -0.0091 | 482.5 |
| NH128 | 0.0163 | 0.0 | -0.0016 | 0.0269 | 0.0 | -0.0216 | 482.5 |
| NH129 | 0.0326 | 0.0 | -0.0000 | 0.0540 | 0.0 | -0.0359 | 482.5 |
| NH130 | 0.0652 | 0.0 | -0.0064 | 0.1076 | 0.0 | -0.0916 | 482.5 |
| NH131 | 0.1287 | 0.0 | -0.0033 | 0.2124 | 0.0 | -0.1419 | 482.5 |
| NH132 | 0.0 | -0.0000 | -0.0000 | 0.0 | 0.0001 | -0.0000 | 482.5 |
| NH133 | 0.0 | 0.0039 | -0.0004 | 0.0 | 0.0065 | -0.0026 | 482.5 |
| NH134 | 0.0 | 0.0079 | 0.0009 | 0.0 | 0.0131 | -0.0023 | 482.5 |
| NH135 | 0.0 | 0.0159 | -0.0000 | 0.0 | 0.0263 | 0.0017 | 482.5 |
| NH136 | 0.0 | 0.0324 | 0.0029 | 0.0 | 0.0537 | 0.0090 | 482.5 |
| NH137 | 0.0 | 0.0655 | 0.0037 | 0.0 | 0.1086 | 0.0136 | 482.5 |
| NH138 | 0.0 | 0.1316 | 0.0189 | 0.0 | 0.2194 | 0.0604 | 482.5 |
| NH139 | 0.0 | 0.0 | 0.0 | 0.0 | 0.0 | 0.0 | 482.5 |
| NH140 | 0.0 | 0.0 | -0.0020 | 0.0 | 0.0 | -0.0055 | 482.5 |
| NH141 | 0.0 | 0.0 | -0.0080 | 0.0 | 0.0 | -0.0218 | 482.5 |
| NH142 | 0.0 | 0.0 | -0.0160 | 0.0 | 0.0 | -0.0420 | 482.5 |
| NH143 | 0.0 | 0.0 | -0.0320 | 0.0 | 0.0 | -0.0862 | 482.5 |
| NH144 | 0.0 | 0.0 | -0.0640 | 0.0 | 0.0 | -0.1715 | 482.5 |
| NH145 | 0.0 | 0.0 | -0.1280 | 0.0 | 0.0 | -0.3518 | 482.5 |

GROUP 2 OPTIMIZED KODAK H.R. PLATE

| PHOTO | SPHERICAL | COMA | ABERRATIONS ASTIGMATISM | RMS | TOTAL |
|-------|-----------|------|--------------------------|-----|-------|
| NH118 | 0.00322 | 0.17987 | 0.86554 | 0.21077 | 0.87569 |
| NH119 | 0.01081 | 0.24994 | 1.70302 | 0.41566 | 1.72198 |
| NH120 | 0.01621 | 0.63197 | 3.42346 | 0.81820 | 3.30336 |
| NH121 | 0.02656 | 1.32584 | 6.59367 | 1.56314 | 6.34465 |
| NH122 | 0.05066 | 2.86755 | 13.72260 | 3.25351 | 13.26614 |
| NH123 | 0.10978 | 5.55947 | 27.53084 | 6.51606 | 27.76263 |
| NH124 | 0.22095 | 10.57491 | 53.31829 | 12.61820 | 54.77923 |
| NH125 | 0.00374 | 0.16805 | 0.86469 | 0.20605 | 0.85578 |
| NH126 | 0.00661 | 0.38544 | 1.72468 | 0.40932 | 1.69608 |
| NH127 | 0.01489 | 0.67125 | 3.45240 | 0.82029 | 3.35252 |
| NH128 | 0.03538 | 1.18985 | 6.83327 | 1.62111 | 6.59108 |
| NH129 | 0.05875 | 2.67130 | 13.71267 | 3.25088 | 13.72821 |
| NH130 | 0.15038 | 4.57830 | 27.43956 | 6.52250 | 27.49942 |
| NH131 | 0.23183 | 10.49979 | 54.06779 | 12.91078 | 56.67854 |
| NH132 | 0.00015 | 0.00254 | 0.02613 | 0.30330 | 1.00027 |
| NH133 | 0.01172 | 0.36048 | 1.60687 | 0.40070 | 1.57021 |
| NH134 | 0.01830 | 0.64509 | 3.25288 | 0.76675 | 3.18681 |
| NH135 | 0.03681 | 1.25473 | 6.53800 | 1.53726 | 6.39575 |
| NH136 | 0.07475 | 2.63466 | 13.35564 | 3.12513 | 13.39778 |
| NH137 | 0.15048 | 5.18251 | 26.95888 | 6.31098 | 27.12793 |
| NH138 | 0.29129 | 11.25888 | 54.04947 | 12.73957 | 59.01809 |
| NH139 | 0.0 | 0.0 | 0.0 | 0.0 | 0.0 |
| NH140 | 0.01919 | 0.20937 | 0.01248 | 0.03246 | 0.20989 |
| NH141 | 0.07653 | 0.83475 | 0.04927 | 0.12939 | 0.83673 |
| NH142 | 0.14771 | 1.61385 | 0.38021 | 0.30013 | 1.65435 |
| NH143 | 0.30579 | 3.33456 | 0.33836 | 0.53008 | 3.36016 |
| NH144 | 0.61726 | 6.70513 | 0.76295 | 1.07686 | 6.76839 |
| NH145 | 1.30796 | 14.09054 | 0.62069 | 2.20018 | 13.93269 |
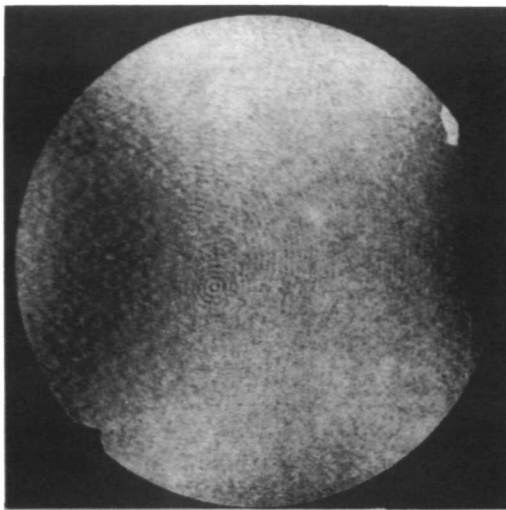
NH118
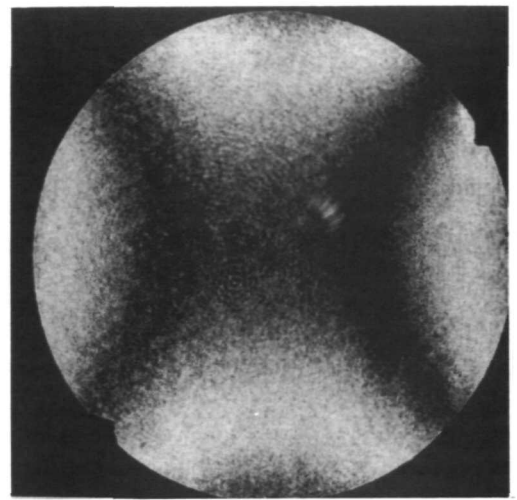

NH119
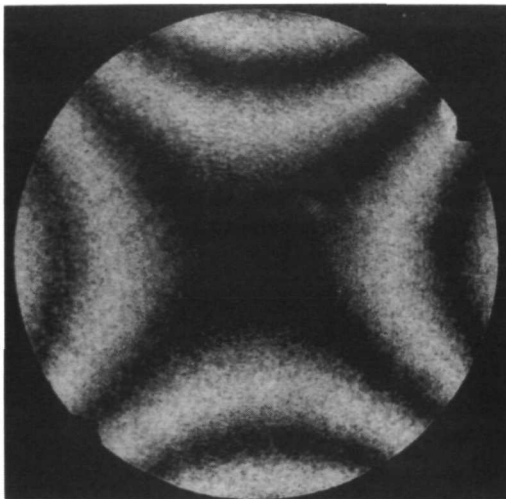

NH120
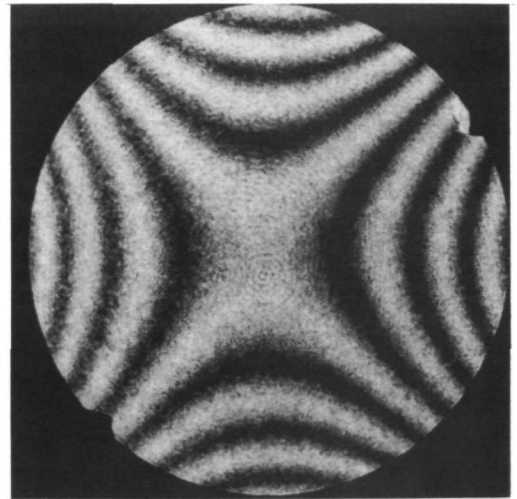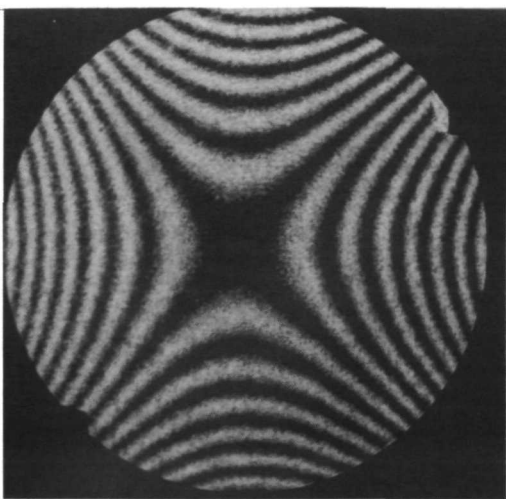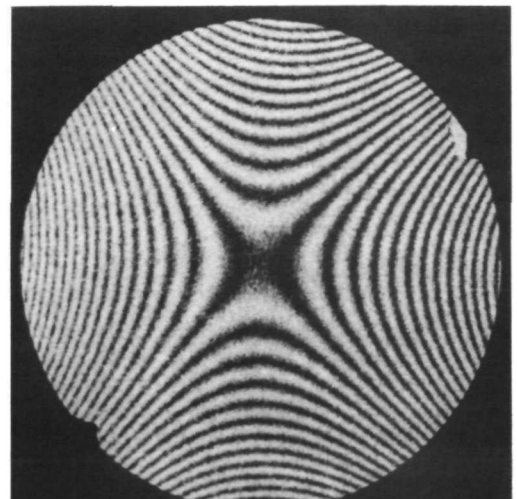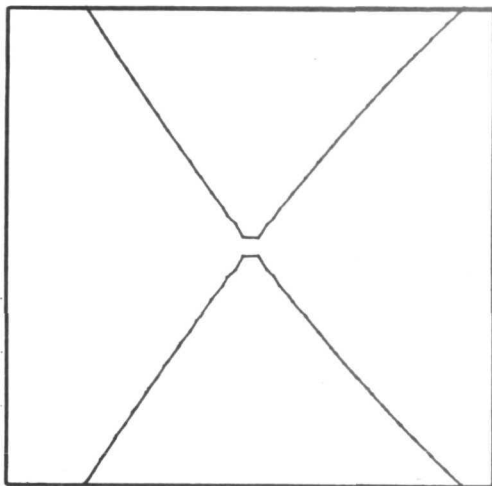

NH121


NH122


NH123

NH118
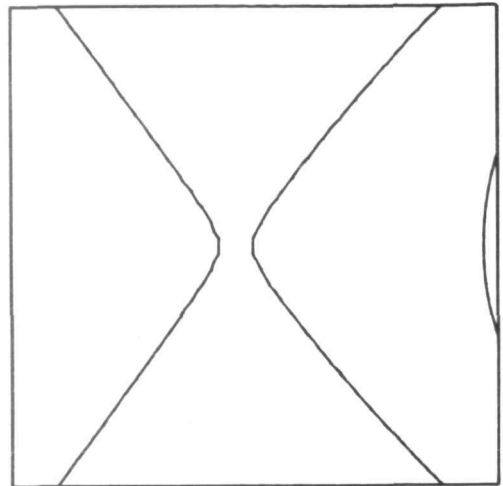


NH119
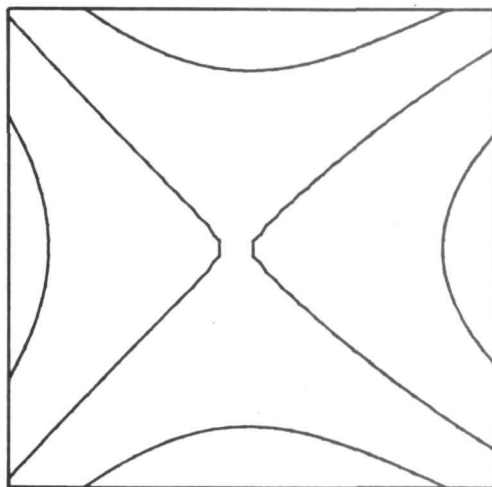


NH120
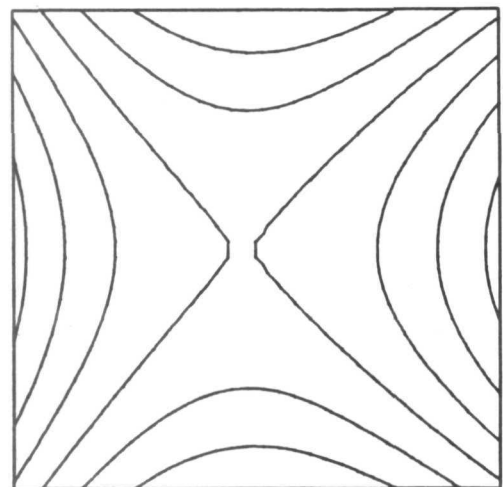


NH121
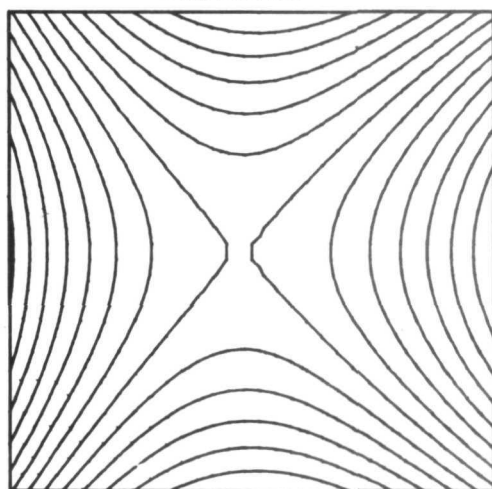


NH122
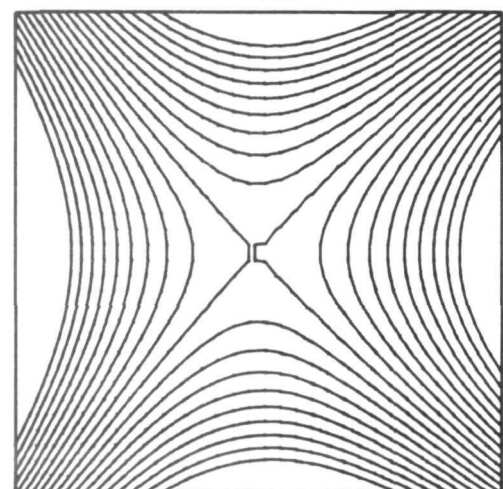


NH123
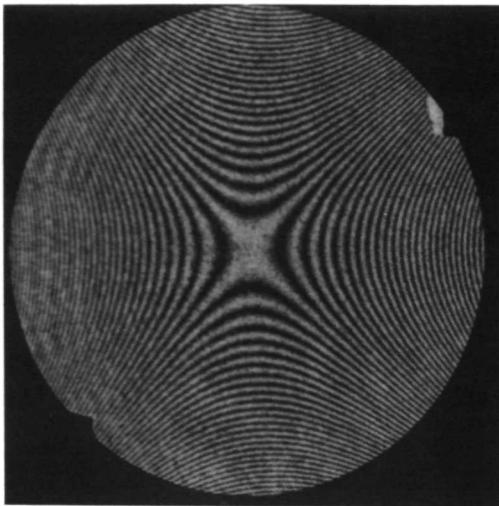
NH124
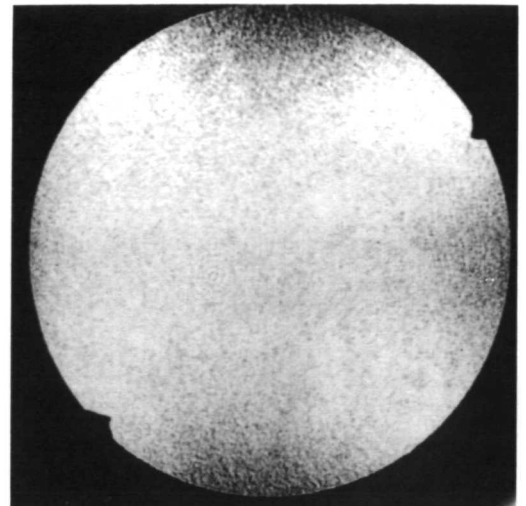


NH125
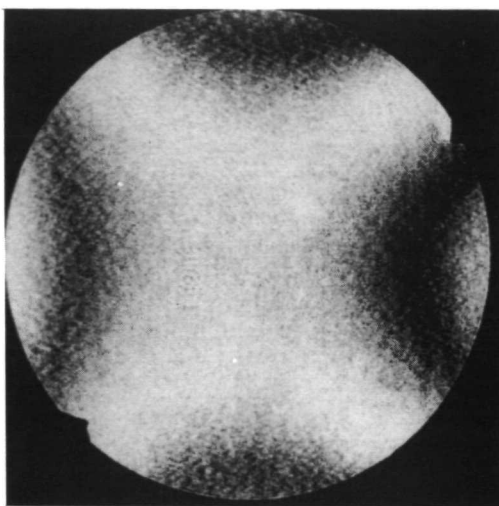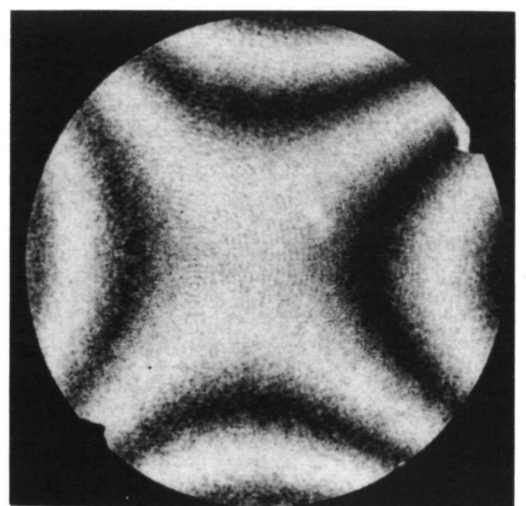


NH126



NH127



NH128



NH129

A-19

NHl24

NHl25

NHl26

NHl27

NHl28
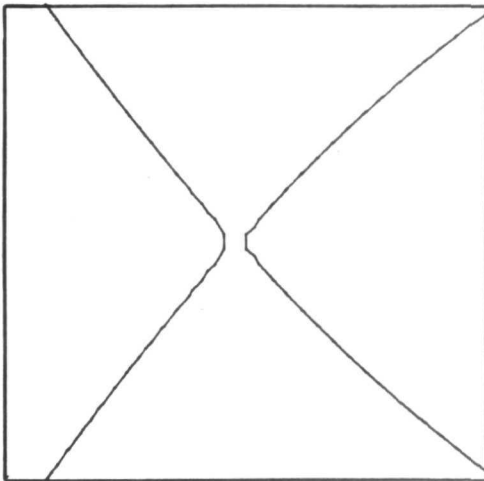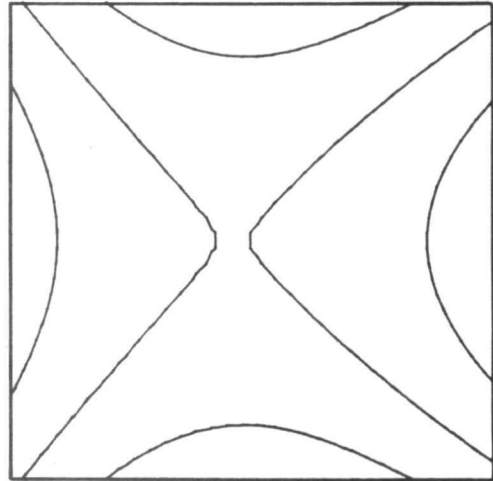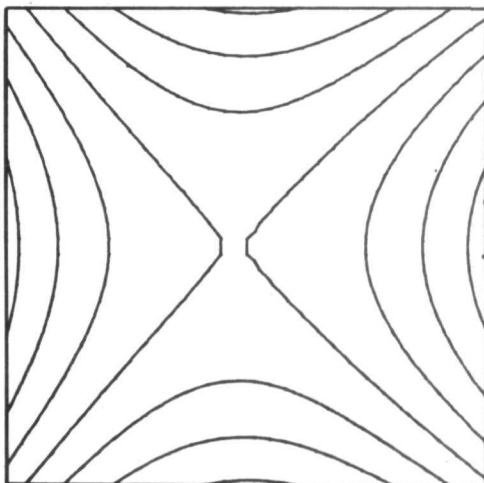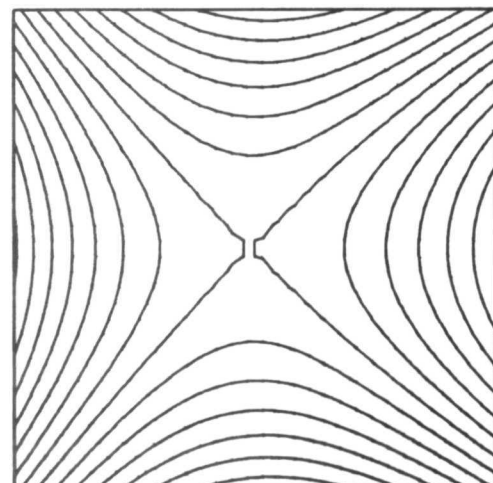
NHl29
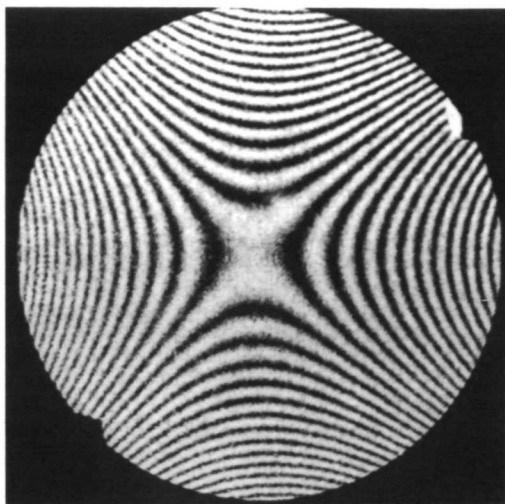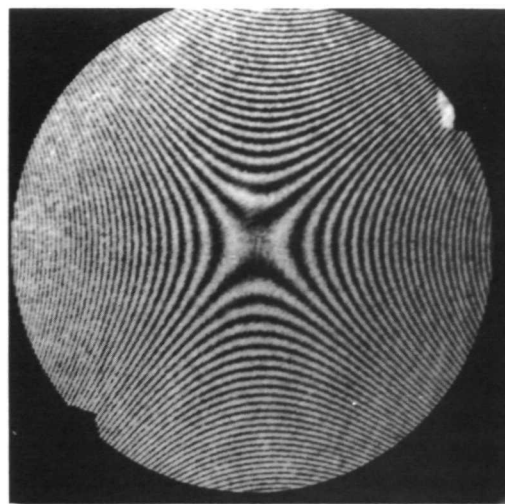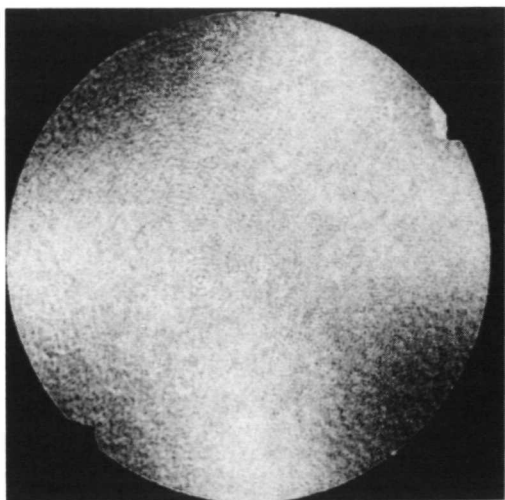
NH130



NH131



NH132
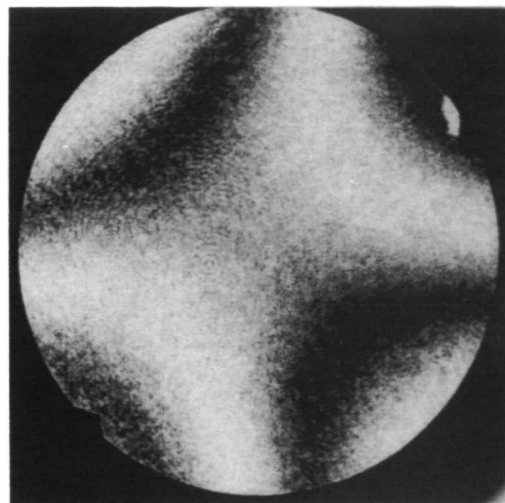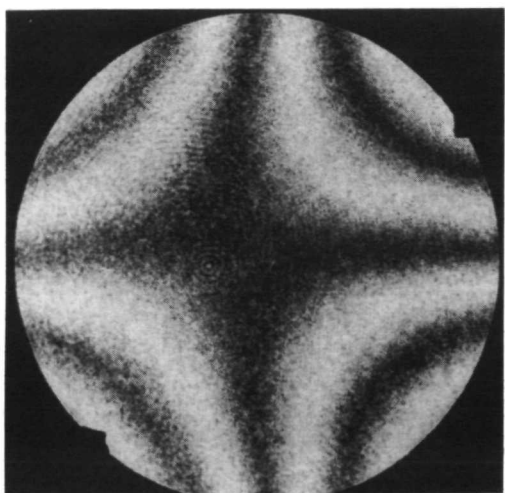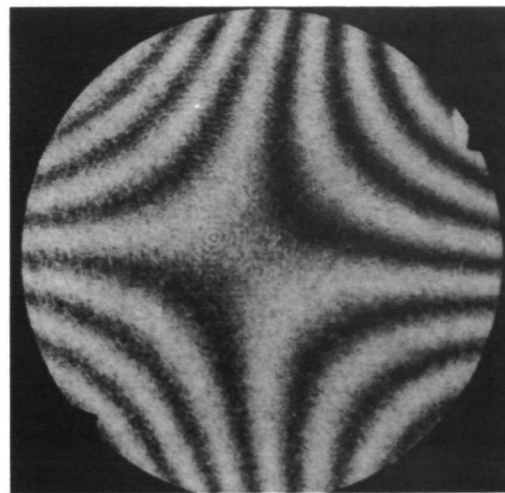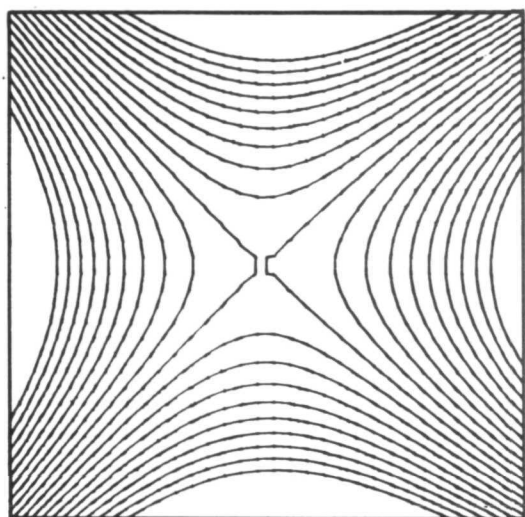


NH133



NH134



NH135

NH130
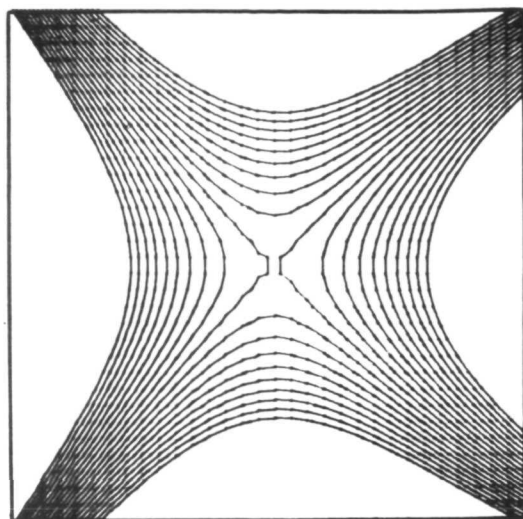


NH131
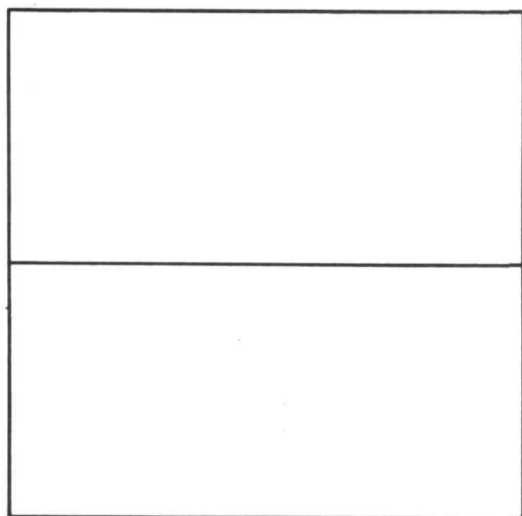


NH132
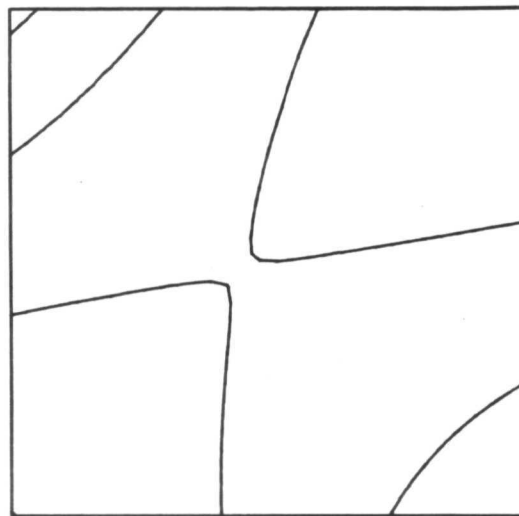


NH133
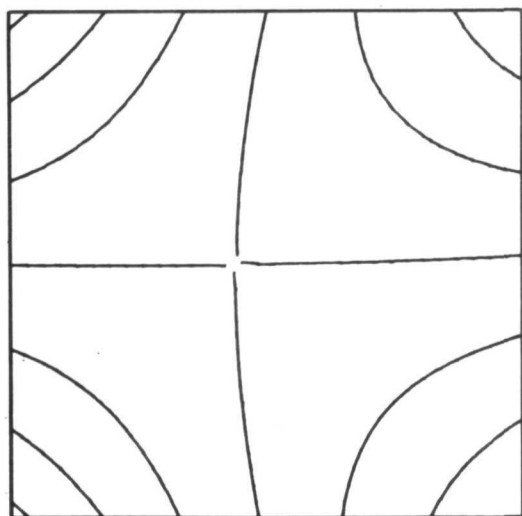


NH134
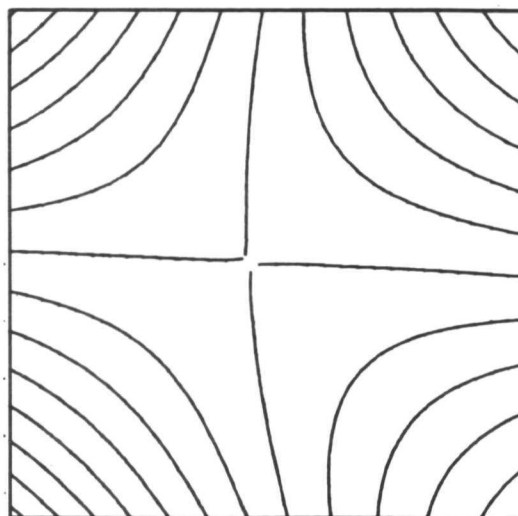


NH135
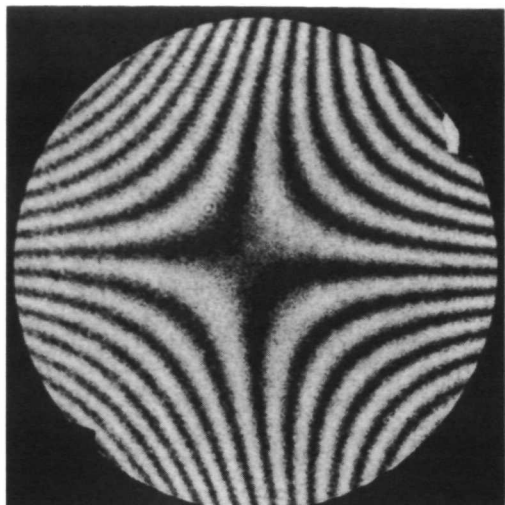
NH136
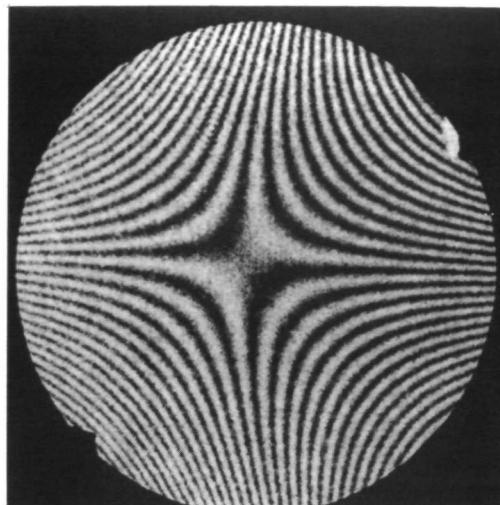


NH137
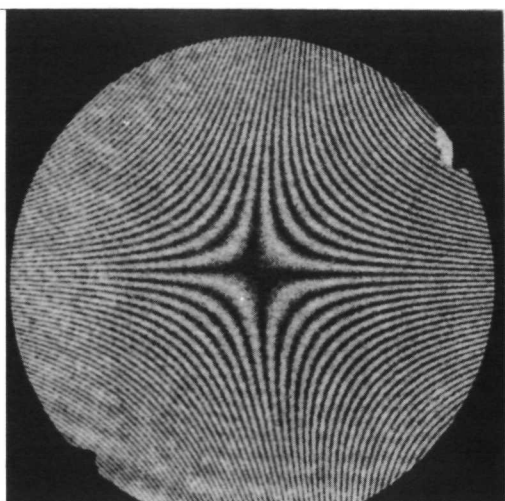


NH138
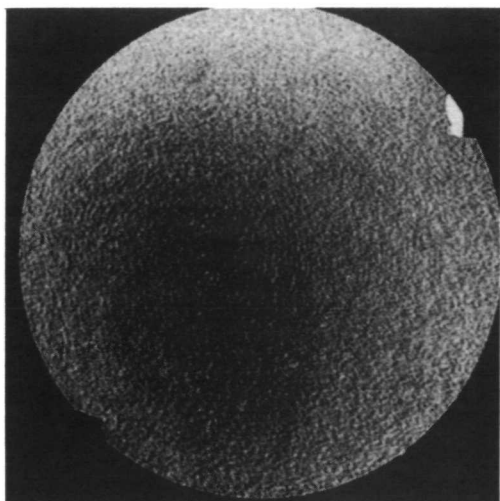


NH139
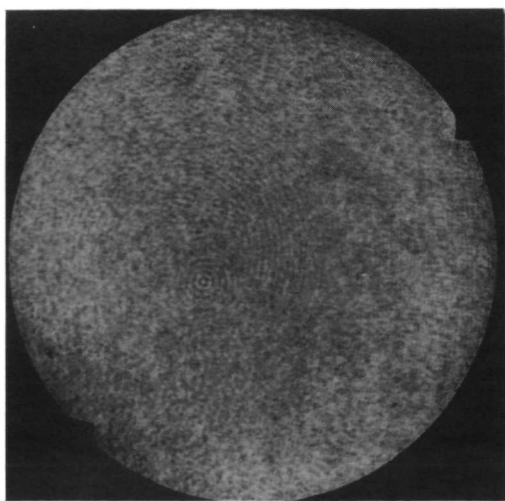


NH140
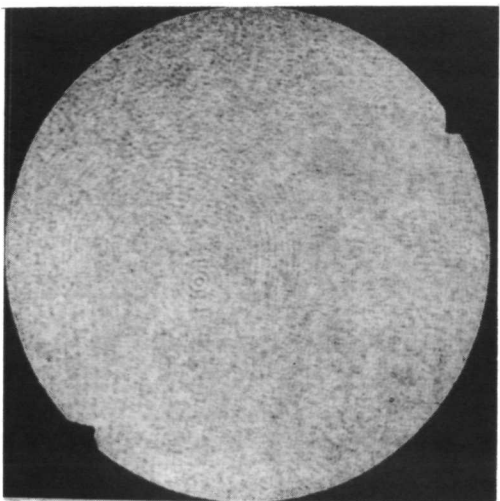


NH141
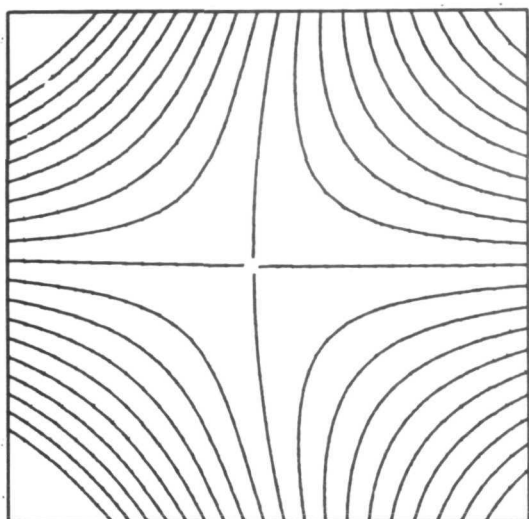
NHI36
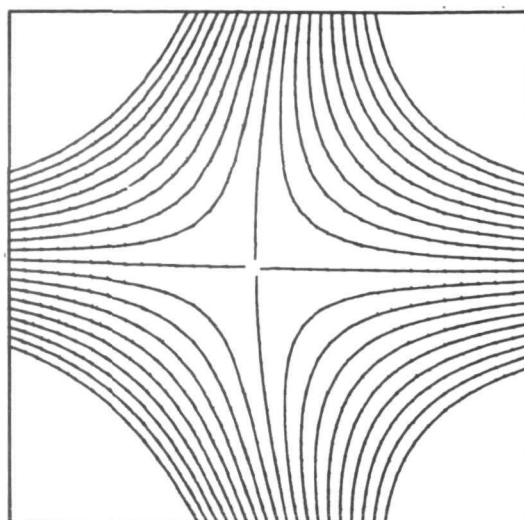

NHI37
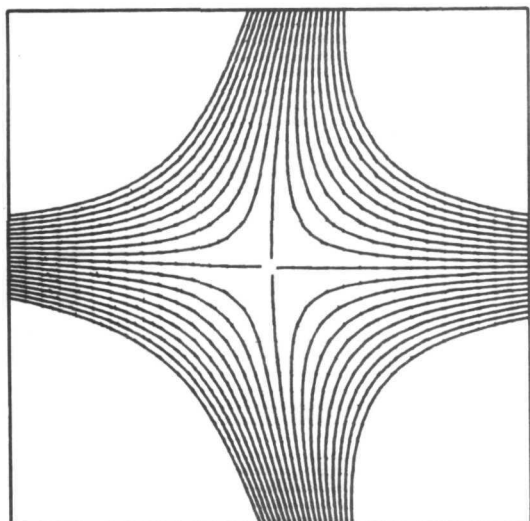

NHI38
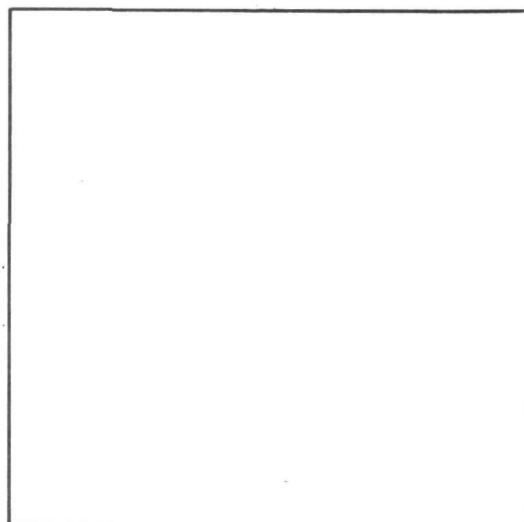

NHI39
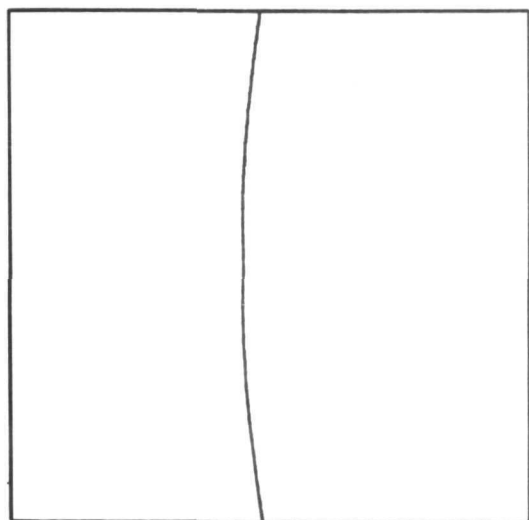

NHI40
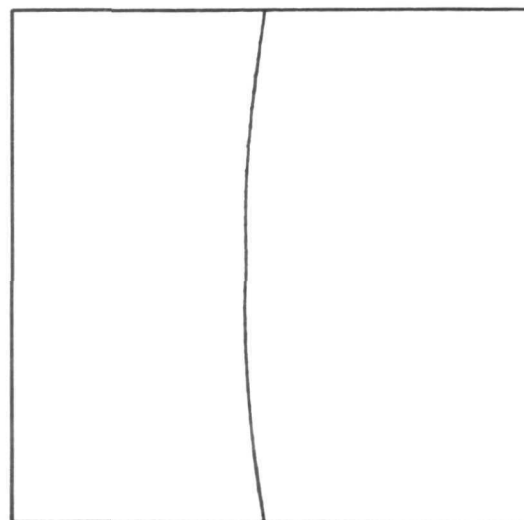

NHI41

NH142



NH143



NH144



NH145

A-25
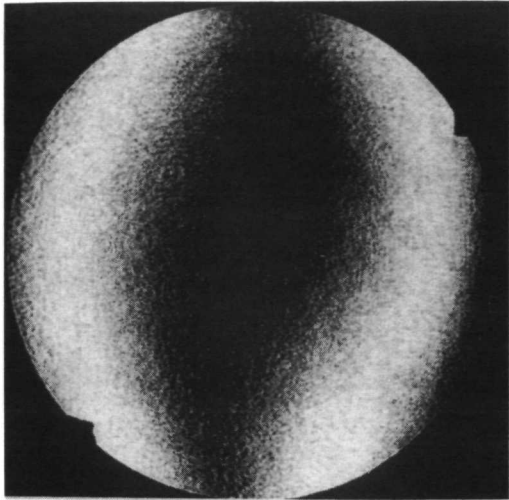
NH142
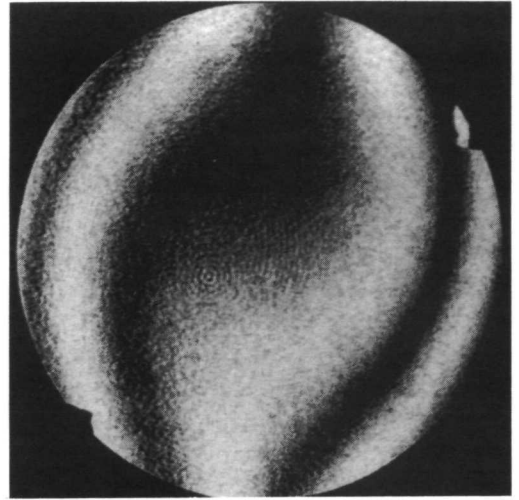
NH143
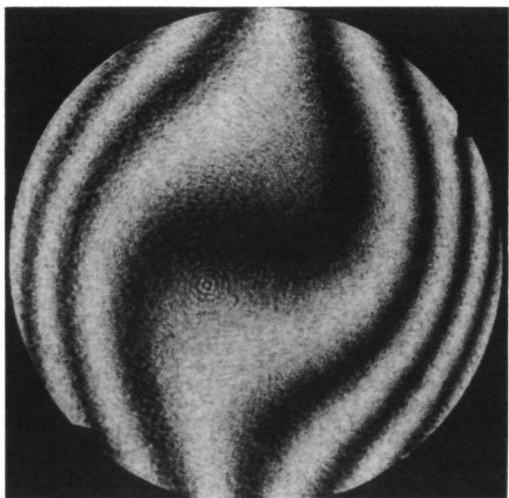
NH144
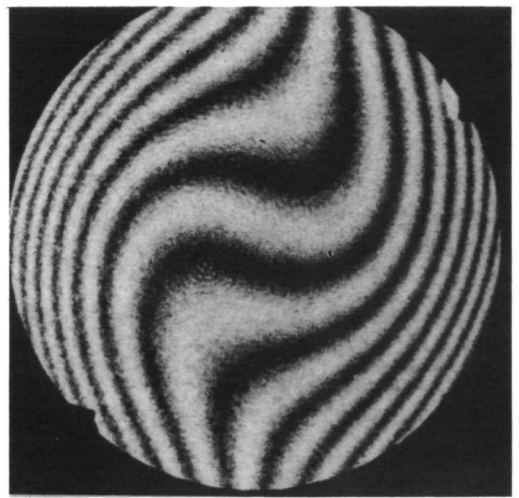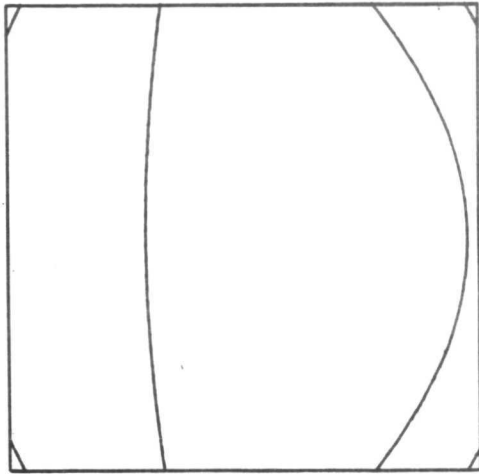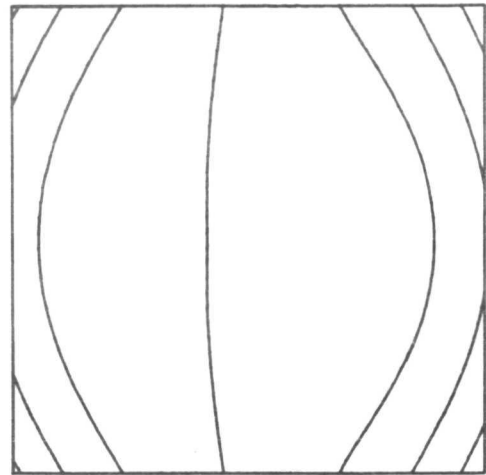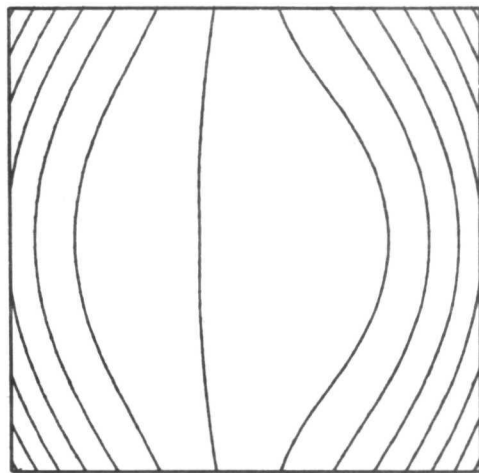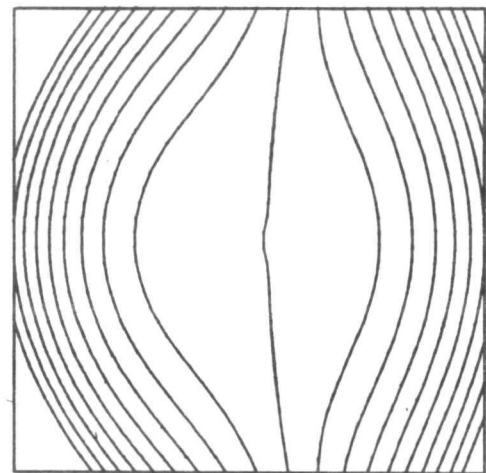
NH145

Group 3
Chromatic and Seidel Aberrations
Kodak HR Plate
$Q = 1$

The data presented in Group 3 combines both the chromatic and Seidel aberrations for the case $Q = 1$. Photographs NH146, 147, and 148 show the chromatic aberrations for $\lambda_c = 476.2$ nm in the usual way. We again determined the location of an object point that reduced the number of fringes by about one half and also found object coordinates that reduced to one wave the total residual aberration. These results are shown in photographs NH149, 150 and 151 and NH152 respectively. This was the only $\lambda_c$ for which we could obtain quantitative data. The results for Seidel aberrations are summarized in photographs NH153 to NH157 ($x_o$ - $z_o$ field) and in photographs NH158 to NH162 ($y_o$ - $z_o$ field). Photographs NH163 and NH164 are for large, uncalibrated, longitudinal displacements. The system for this case was relatively insensitive to axial position.

Since $R_R$ is infinite for $Q = 1$, changes in position of the reconstruction point with respect to the hologram are best given in terms of angular shifts. In order to obtain an infinite $R_R$, the reference point source was recollimated with an f/4 Super Baltar lens. Then to change the angular position of the reconstruction point, the micropositioner was used to move the reference point around in the back focal plane of the lens. The angular changes, which we call $\Delta\alpha_c$ and $\Delta\beta_c$, of the reconstruction point were calculated using the relations

$$\Delta\alpha_c = \frac{(x_c - x_R)}{F} \times 57.3°/\text{rad}$$

$$\Delta\beta_c = \frac{(y_c - y_R)}{F} \times 57.3°/\text{rad}$$

where F is the 9 inch effective focal length of the Super Baltar lens.

**HARRIS ELECTRO-OPTICS CENTER**

## Group 3

Kodak HR Plate (Seidel and Chromatic Aberrations)
$R_O$ = 15.7 in.  $\lambda_O$ = 482.5 nm  $\langle\theta\rangle$ = 29.°5
$R_R^O$ = ∞  $Q = °1$  $\langle\bar{K}\rangle$ = split bisector

| Photo | $\Delta x_i$ | $\Delta y_i$ | $\Delta z_i$ | $\Delta\alpha_c$ (°) | $\Delta\beta_c$ (°) | $\Delta z_c$ | $\lambda_c$ | $\Delta_x$ | $\Delta_y$ |
|---|---|---|---|---|---|---|---|---|---|
| 146 | .1098 | 0 | .2247 | 0 | 0 | 0 | 476.2 | 4 | 4 |
| 147 | .1103 | 0 | .2553 | 0 | 0 | 0 | 476.2 | 1 | 8 |
| 148 | .1098 | 0 | .1997 | 0 | 0 | 0 | 476.2 | 7 | 0 |
| 149 | .0602 | 0 | .1991 | -.179 | 0 | 0 | 476.2 | 2 | 1.5 |
| 150 | .0606 | 0 | .2254 | -.179 | 0 | 0 | 476.2 | 1 | 4 |
| 151 | .0599 | 0 | .2086 | -.179 | 0 | 0 | 476.2 | 3 | 0 |
| 152 | .0092 | 0 | .1994 | -.393 | 0 | 0 | 476.2 | 1 | 0 |
| 153 | .0279 | 0 | .0060 | .102 | 0 | 0 | 482.5 | 1 | 1 |
| 154 | .0557 | 0 | .0147 | .203 | 0 | 0 | 482.5 | 2 | 2 |
| 155 | .1114 | 0 | .0285 | .407 | 0 | 0 | 482.5 | 4 | 4 |
| 156 | .2226 | 0 | .0490 | .814 | 0 | 0 | 482.5 | 7 | 8 |
| 157 | .4446 | 0 | .0931 | 1.628 | 0 | 0 | 482.5 | 12 | 15 |
| 158 | 0 | .0282 | -.0018 | 0 | .102 | 0 | 482.5 | 1 | 1 |
| 159 | 0 | .0556 | -.0027 | 0 | .203 | 0 | 482.5 | 2 | 2 |
| 160 | 0 | .1014 | -.0050 | 0 | .407 | 0 | 482.5 | 4 | 4 |
| 161 | 0 | .2227 | -.0050 | 0 | .814 | 0 | 482.5 | 8 | 9 |
| 162 | 0 | .4456 | -.0050 | 0 | 1.628 | 0 | 482.5 | 12 | 24 |
| 163 | - | - | - | - | - | - | - | 1 | 0 |
| 164 | - | - | - | - | - | - | - | 2 | 1 |

A-28

GROUP 3 OPTIMIZED   KODAK H.R. PLATE

RO = 15.7 IN.        AO = 14.7 DEG.        LAMO = 482.5 NM.
RR = ∞               QR =-14.7 DEG.        Q = 1.0

| PHOTO | DXI | DYI | DZI | DAC | DBC | DRC | LAMC |
|-------|-----|-----|-----|-----|-----|-----|------|
| NH146 | 0.1097 | 0.0 | 0.2365 | 0.0 | 0.0 | 0.0 | 476.2 |
| NH147 | 0.1099 | 0.0 | 0.2684 | 0.0 | 0.0 | 0.0 | 476.2 |
| NH148 | 0.1095 | 0.0 | 0.2096 | 0.0 | 0.0 | 0.0 | 476.2 |
| NH149 | 0.0603 | 0.0 | 0.2176 | -0.1768 | 0.0 | 0.0 | 476.2 |
| NH150 | 0.0606 | 0.0 | 0.2378 | -0.1758 | 0.0 | 0.0 | 476.2 |
| NH151 | 0.0599 | 0.0 | 0.2070 | 0.0020 | 0.0 | 0.0 | 476.2 |
| NH152 | 0.0051 | 0.0 | 0.2092 | -0.3754 | 0.0 | 0.0 | 476.2 |
| NH153 | 0.0159 | 0.0 | 0.0039 | 0.0578 | 0.0 | 0.0 | 482.5 |
| NH154 | 0.0557 | 0.0 | 0.0146 | 0.2030 | 0.0 | 0.0 | 482.5 |
| NH155 | 0.1114 | 0.0 | 0.0287 | 0.4066 | 0.0 | 0.0 | 482.5 |
| NH156 | 0.2227 | 0.0 | 0.0567 | 0.8117 | 0.0 | 0.0 | 482.5 |
| NH157 | 0.3872 | 0.0 | 0.1031 | 1.4096 | 0.0 | 0.0 | 482.5 |
| NH158 | 0.0 | 0.0000 | -0.0000 | 0.0 | 0.0000 | 0.0 | 482.5 |
| NH159 | 0.0 | 0.0592 | 0.0019 | 0.0 | 0.2156 | 0.0 | 482.5 |
| NH160 | 0.0 | 0.1065 | -0.0004 | 0.0 | 0.3880 | 0.0 | 482.5 |
| NH161 | 0.0 | 0.2231 | -0.0103 | 0.0 | 0.8132 | 0.0 | 482.5 |
| NH162 | 0.0 | 0.4595 | -0.0465 | 0.0 | 1.6764 | 0.0 | 482.5 |

A-29

GROUP 3 OPTIMIZED KODAK H.R. PLATE

| PHOTO | SPHERICAL | COMA | ABERRATIONS ASTIGMATISM | RMS | TOTAL |
|-------|-----------|------|-------------------------|-----|-------|
| NH146 | 0.03697 | 1.44172 | 4.49137 | 1.09644 | 4.43146 |
| NH147 | 0.03696 | 1.44179 | 4.90582 | 1.70675 | 5.07997 |
| NH148 | 0.03697 | 1.44172 | 4.41491 | 1.44264 | 4.33908 |
| NH149 | 0.03271 | 0.99537 | 2.47379 | 0.64700 | 2.89949 |
| NH150 | 0.03273 | 0.99796 | 2.54438 | 0.85107 | 2.97685 |
| NH151 | 0.03268 | 0.99233 | 2.47914 | 0.85377 | 2.88589 |
| NH152 | 0.02797 | 0.49175 | 0.21095 | 0.06679 | 0.22564 |
| NH153 | 0.00159 | 0.14875 | 0.34492 | 0.16295 | 0.68164 |
| NH154 | 0.00549 | 0.52118 | 1.13095 | 0.56681 | 2.30191 |
| NH155 | 0.01070 | 1.04028 | 2.25097 | 1.13163 | 5.04889 |
| NH156 | 0.02019 | 2.06463 | 9.08772 | 2.21322 | 9.01311 |
| NH157 | 0.03216 | 3.55427 | 15.41161 | 3.84175 | 16.11147 |
| NH158 | 0.00033 | 0.00089 | 0.00343 | 0.00153 | 0.00343 |
| NH159 | 0.00585 | 0.39185 | 2.42636 | 0.59299 | 2.42634 |
| NH160 | 0.01053 | 0.70528 | 4.36753 | 1.05590 | 4.33376 |
| NH161 | 0.02209 | 1.47825 | 9.15670 | 2.23505 | 9.21887 |
| NH162 | 0.04567 | 3.04933 | 18.90269 | 4.87281 | 21.30141 |
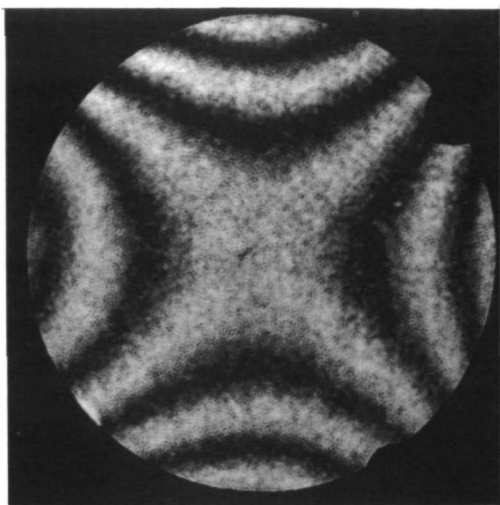
NH146
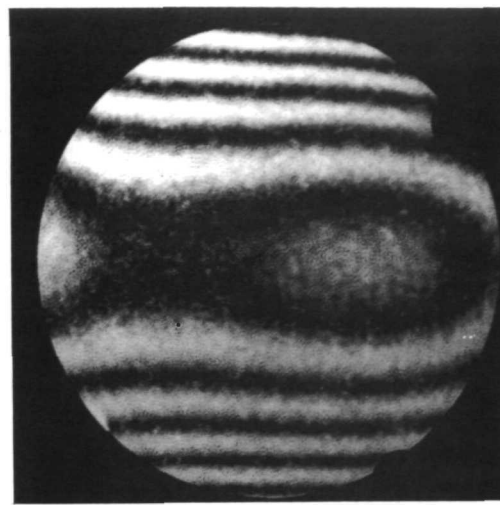


NH147
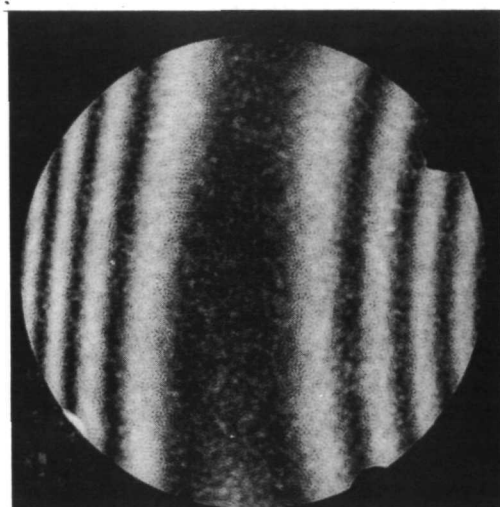


NH148
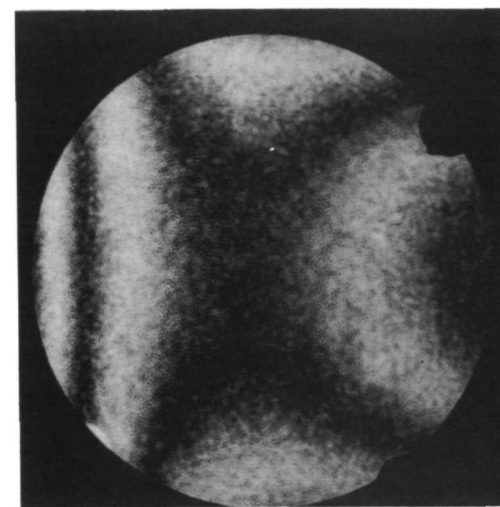


NH149
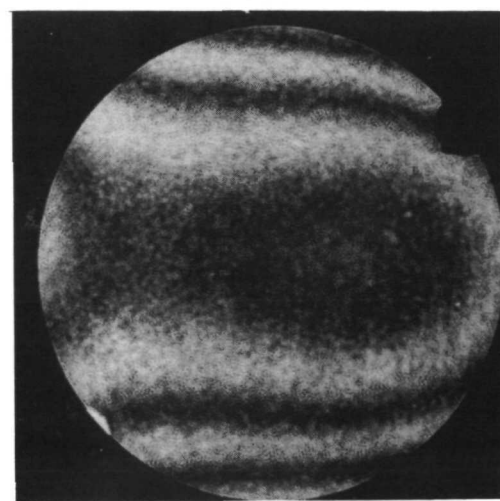


NH150
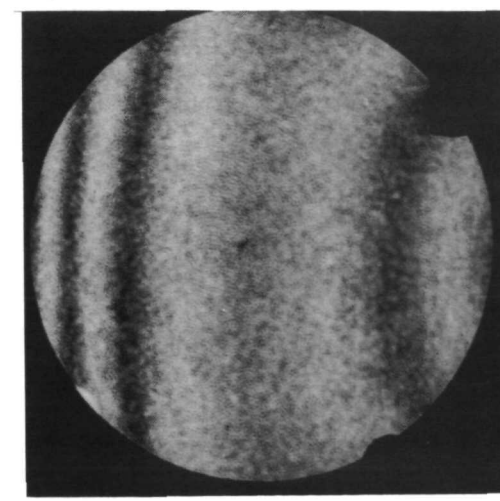


NH151
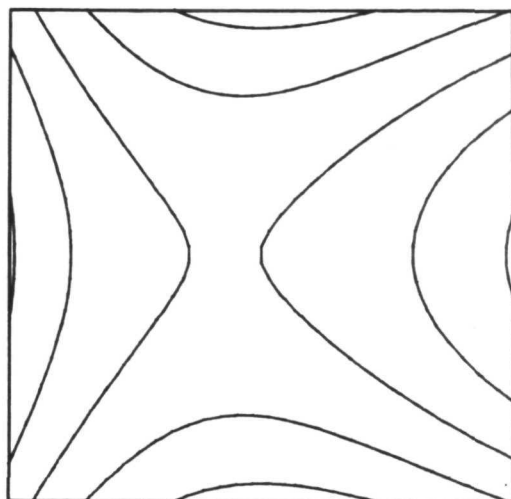
NHI46
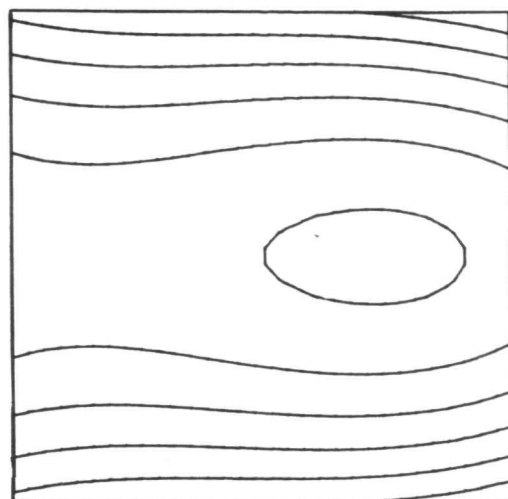


NHI47
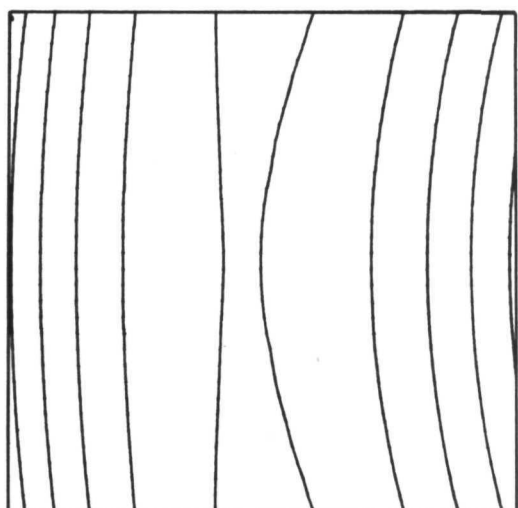


NHI48



NHI49



NHI50



NHI51

A-32
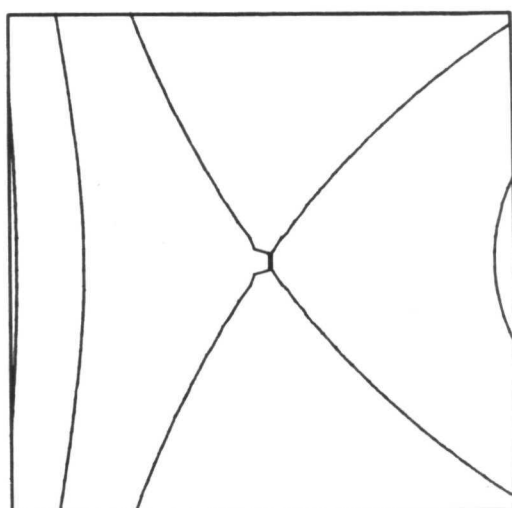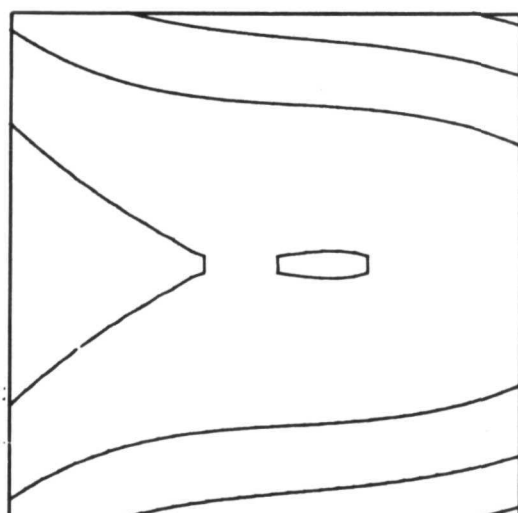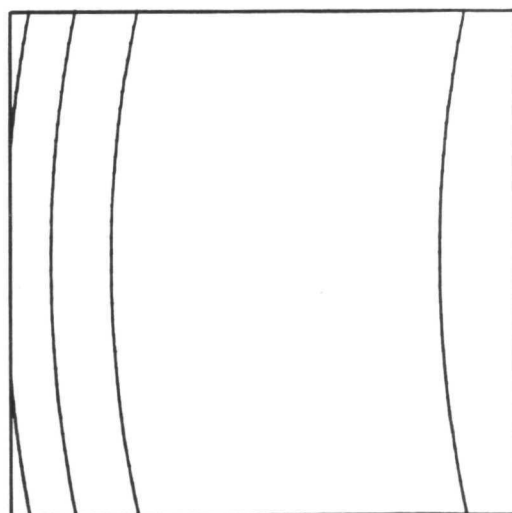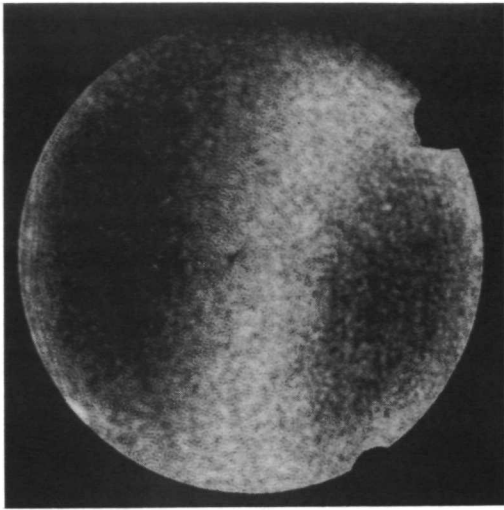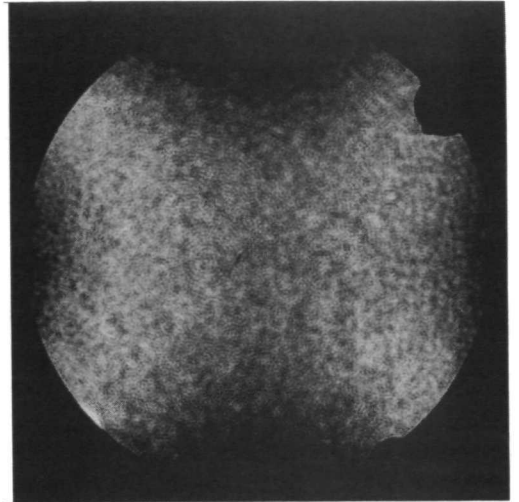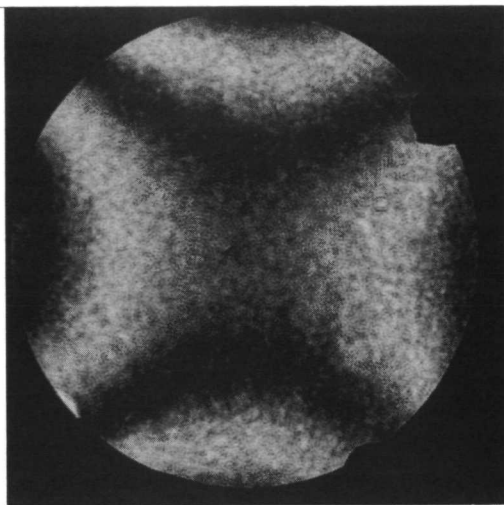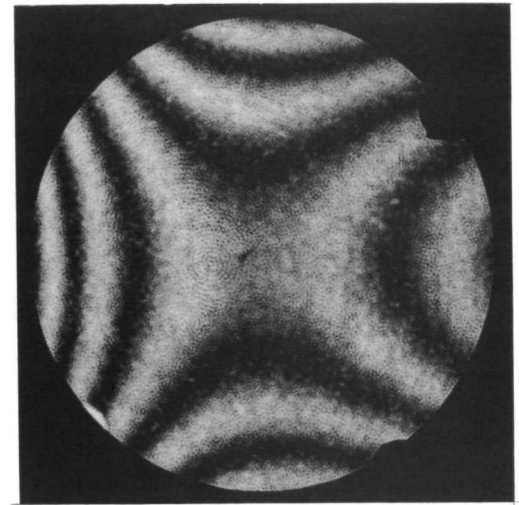
NH152
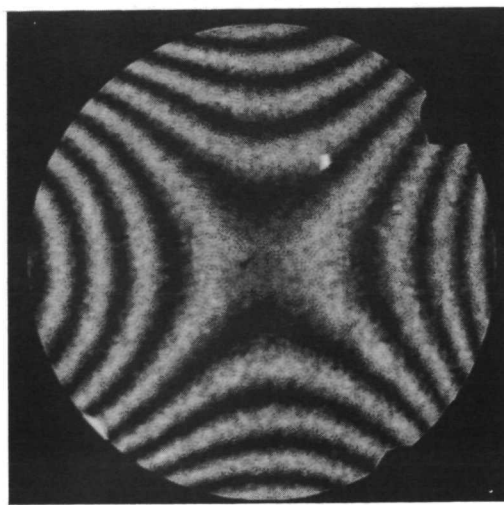


NH153
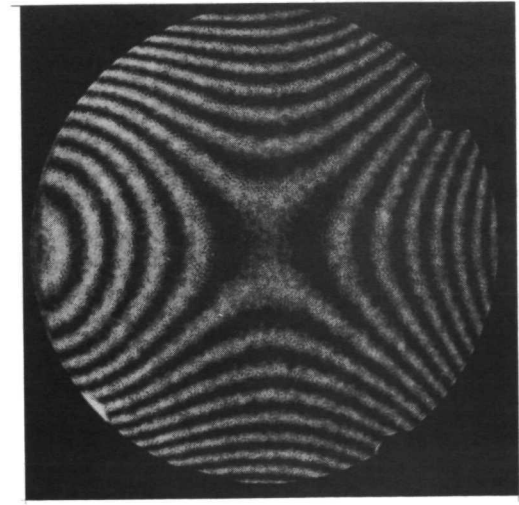


NH154
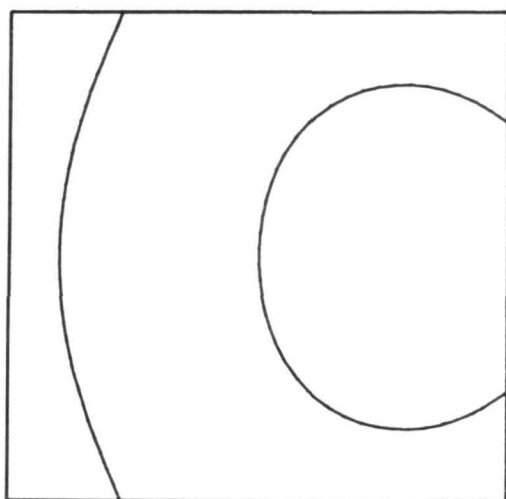


NH155



NH156



NH157

NH152
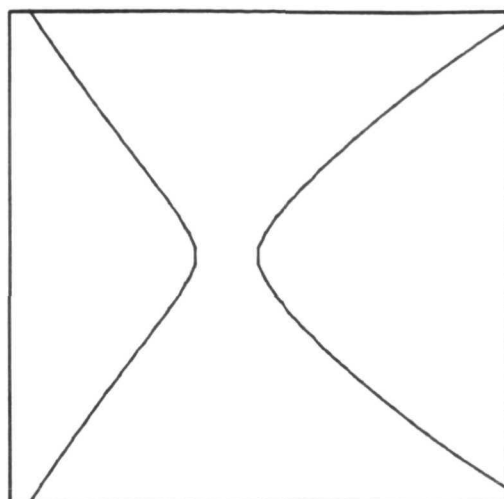
NH153
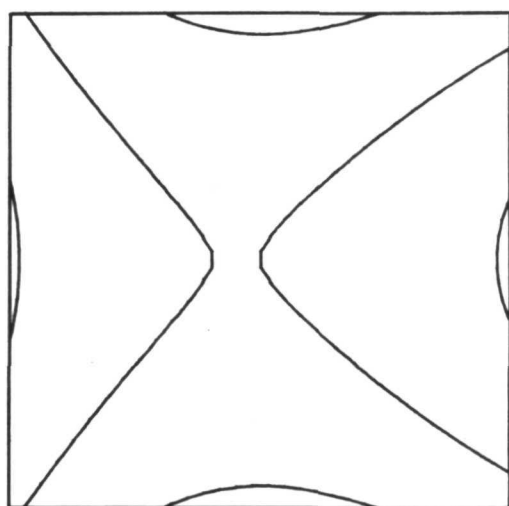
NH154
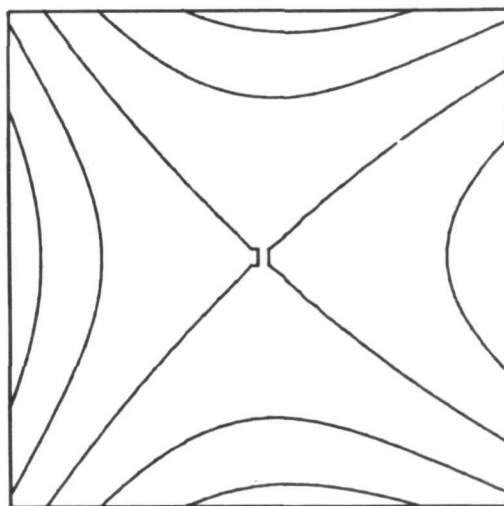
NH155
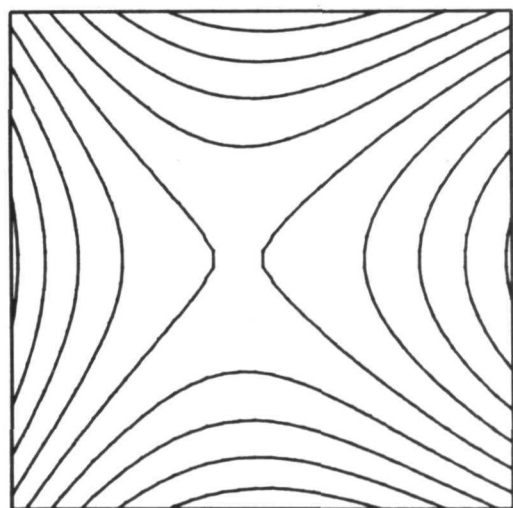
NH156
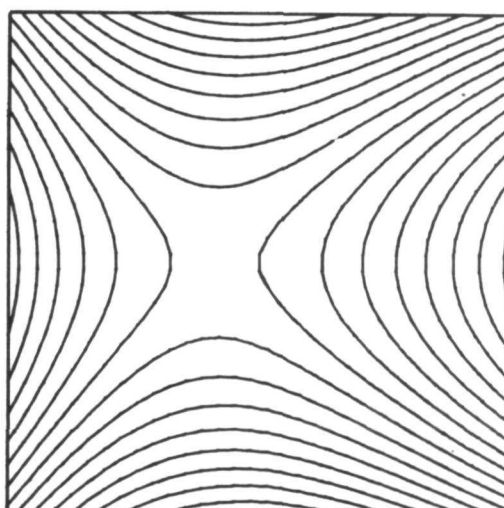
NH157
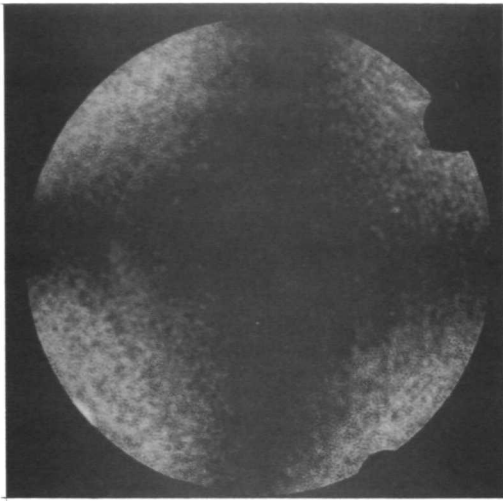
NH158
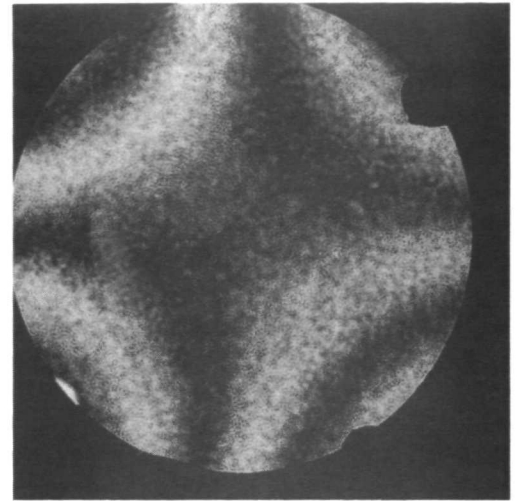


NH159
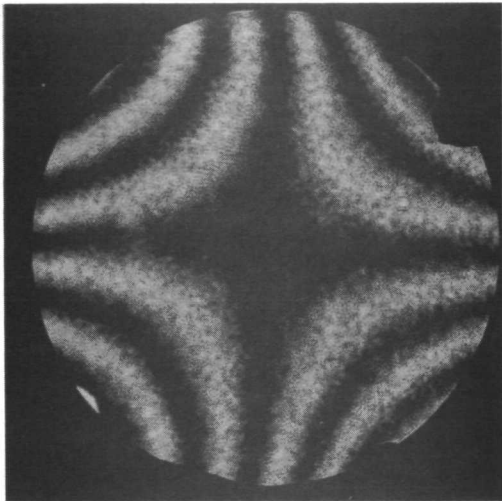


NH160
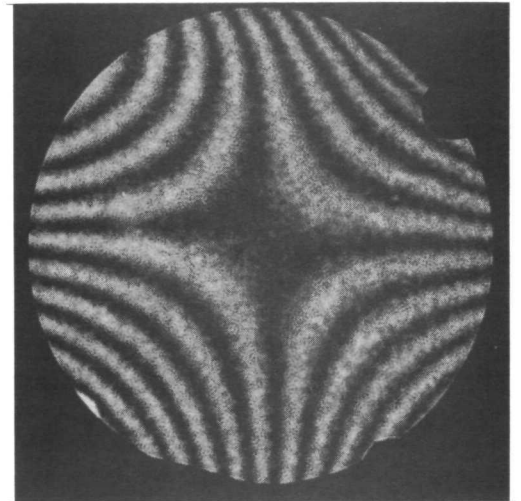


NH161



NH162



NH163

NHI58



NHI59



NHI60



NHI61



NHI62

A-36
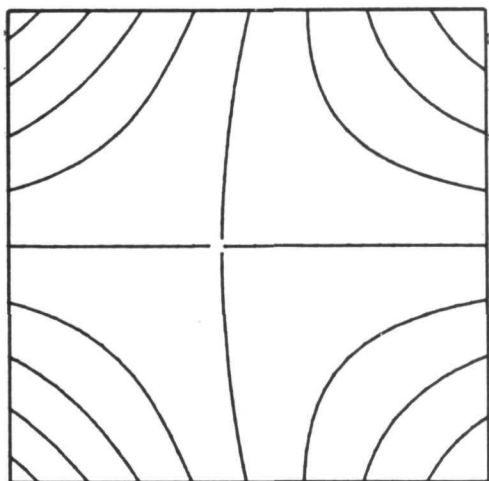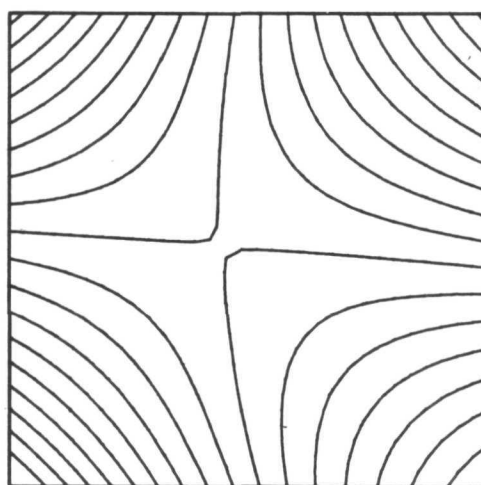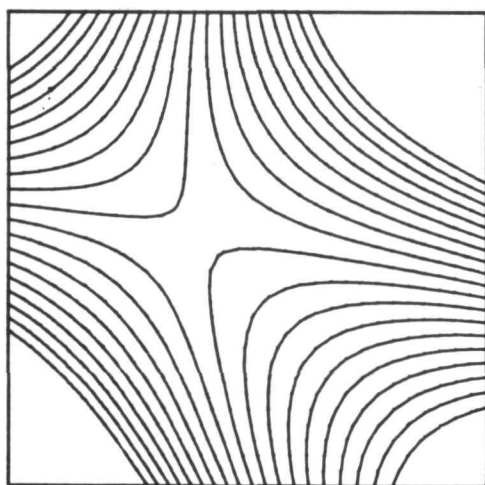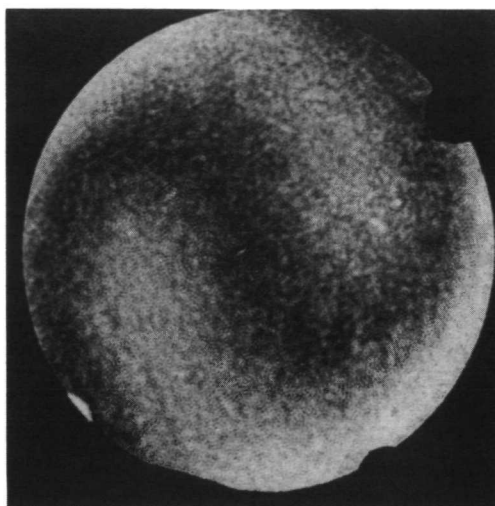
NH164

Page Intentionally Left Blank

Group 4
Chromatic and Seidel Aberrations
Kodak HR Plate
$Q = 2$

The data for chromatic and Seidel aberrations for $Q = 2$ are presented in this section. The chromatic aberrations are shown in photographs NH156 to NH171. For this case we were again able to obtain quantitative data for both $\lambda_c = 476.2$ nm and $\lambda_c = 520.8$. We did not, however, determine the coordinates required to achieve a 50 percent reduction in wavelengths of aberration. For $\lambda_c = 476.2$ nm photograph NH168 shows the residual aberration remaining after locating the optimum object point position. The interference patterns obtained for Seidel aberrations are shown in photographs NH172 to NH177 for the $(x_o - z_o)$ field and photographs NH178 and NH182 for the $(y_o - z_o)$ field. Photographs NH183 and NH184 show the interferograms obtained by moving the object point a relatively large, but still measurable, radial distance. It should be noted that this is a condition of minimum fringe count generated by axial translation of the object point that differs from that shown for Groups two and three.

HARRIS ELECTRO-OPTICS CENTER

## Group 4

Kodak HR Plate (Seidel and Chromatic Aberrations)
$R_o$ = 10.5 in.     $\lambda_o$ = 482.5 nm   $<\theta>$ = 29.°5
$R_R^o$ = 31.5 in.     $Q^o$= 2     $<\bar{K}>$ = split bisector

| Photo | $\Delta x_i$ | $\Delta y_i$ | $\Delta z_i$ | $\Delta x_c$ | $\Delta y_c$ | $\Delta z_c$ | $\lambda_c$ | $\Delta_x$ | $\Delta_y$ |
|---|---|---|---|---|---|---|---|---|---|
| 165 | .0728 | 0 | .1140 | 0 | 0 | 0 | 476.2 | 5.5 | 7 |
| 166 | .0728 | 0 | .1331 | 0 | 0 | 0 | 476.2 | 2.5 | 13 |
| 167 | .0728 | 0 | .0936 | 0 | 0 | 0 | 476.2 | 13 | 0 |
| 168 | .0223 | 0 | .0662 | -.1489 | 0 | -.2527 | 476.2 | .25 | 0 |
| 169 | -.4195 | 0 | -.6923 | 0 | 0 | 0 | 520.8 | 40 | 48 |
| 170 | -.4145 | 0 | -.8017 | 0 | 0 | 0 | 520.8 | 15 | 100 |
| 171 | -.4280 | 0 | -.5610 | 0 | 0 | 0 | 520.8 | 84 | 0 |
| 172 | .0054 | 0 | .0015 | .0160 | 0 | 0 | 482.5 | .5 | 1 |
| 173 | .0108 | 0 | .0042 | .0320 | 0 | 0 | 482.5 | 1.5 | 2 |
| 174 | .0216 | 0 | .0079 | .0640 | 0 | 0 | 482.5 | 2 | 2.5 |
| 175 | .0433 | 0 | .0154 | .1280 | 0 | 0 | 482.5 | 5 | 4 |
| 176 | .0863 | 0 | .0332 | .2560 | 0 | 0 | 482.5 | 9 | 11 |
| 177 | .1688 | 0 | .0594 | .5000 | 0 | 0 | 482.5 | 19 | 20 |
| 178 | 0 | .0107 | 0 | 0 | .0320 | 0 | 482.5 | 1 | 1 |
| 179 | 0 | .0215 | 0 | 0 | .0640 | 0 | 482.5 | 2 | 2 |
| 180 | 0 | .0432 | 0 | 0 | .1280 | 0 | 482.5 | 4 | 5 |
| 181 | 0 | .0863 | 0 | 0 | .2560 | 0 | 482.5 | 10 | 9 |
| 182 | 0 | .1602 | 0 | 0 | .4750 | 0 | 482.5 | 19 | 19 |
| 183 | 0 | 0 | -.3357 | 0 | 0 | * | 482.5 | 4 | 0 |
| 184 | 0 | 0 | -.4651 | 0 | 0 | * | 482.5 | 6.5 | 0 |

*Large, uncalibrated movements

GROUP 4 OPTIMIZED   KODAK H.R. PLATE

RO = 10.5 IN.    AO =  14.7 DEG.    LAMO = 482.5 NM.
RR = 31.5 IN.    AR = -14.7 DEG.    Q = 2.0

| PHOTO | DXI | DYI | DZI | DXC | DYC | DZC | LAMC |
|---|---|---|---|---|---|---|---|
| NH165 | 0.0733 | 0.0 | 0.1122 | 0.0 | 0.0 | 0.0 | 476.2 |
| NH166 | 0.0732 | 0.0 | 0.1294 | 0.0 | 0.0 | 0.0 | 476.2 |
| NH167 | 0.0730 | 0.0 | 0.0915 | 0.0 | 0.0 | 0.0 | 476.2 |
| NH168 | 0.0223 | 0.0 | 0.0662 | -0.1489 | 0.0 | -0.2410 | 476.2 |
| NH169 | -0.4135 | 0.0 | -0.6673 | 0.0 | 0.0 | 0.0 | 520.8 |
| NH170 | -0.4090 | 0.0 | -0.7760 | 0.0 | 0.0 | 0.0 | 520.8 |
| NH171 | -0.4203 | 0.0 | -0.5320 | 0.0 | 0.0 | 0.0 | 520.8 |
| NH172 | -0.0054 | 0.0 | 0.0015 | 0.0163 | 0.0 | 0.0315 | 482.5 |
| NH173 | 0.0108 | 0.0 | 0.0042 | 0.0324 | 0.0 | 0.0140 | 482.5 |
| NH174 | 0.0216 | 0.0 | 0.0079 | 0.0645 | 0.0 | -0.0035 | 482.5 |
| NH175 | 0.0433 | 0.0 | 0.0154 | 0.1294 | 0.0 | -0.0108 | 482.5 |
| NH176 | 0.0863 | 0.0 | 0.0332 | 0.2586 | 0.0 | 0.0162 | 482.5 |
| NH177 | 0.1688 | 0.0 | 0.0594 | 0.5054 | 0.0 | 0.0149 | 482.5 |
| NH178 | 0.0 | 0.0105 | -0.0000 | 0.0 | 0.0315 | -0.0064 | 482.5 |
| NH179 | 0.0 | 0.0305 | -0.0000 | 0.0 | 0.0910 | -0.0039 | 482.5 |
| NH180 | 0.0 | 0.0430 | -0.0000 | 0.0 | 0.1285 | -0.0118 | 482.5 |
| NH181 | 0.0 | 0.0865 | 0.0479 | 0.0 | 0.2607 | 0.4326 | 482.5 |
| NH182 | 0.0 | 0.1596 | 0.0000 | 0.0 | 0.4770 | 0.0143 | 482.5 |
| NH183 | 0.0 | 0.0 | -0.3357 | 0.0 | 0.0 | -2.8286 | 482.5 |
| NH184 | 0.0 | 0.0 | -0.4651 | 0.0 | 0.0 | -3.8324 | 482.5 |

GROUP 4 OPTIMIZED KODAK H.R. PLATE

| PHOTO | SPHERICAL | COMA | ABERRATIONS ASTIGMATISM | RMS | TOTAL |
|---|---|---|---|---|---|
| NH165 | 0.07294 | 2.46060 | 6.77437 | 1.68045 | 7.04723 |
| NH166 | 0.07294 | 2.45914 | 6.84181 | 2.34679 | 7.44612 |
| NH167 | 0.07298 | 2.45982 | 6.77089 | 2.27726 | 6.64493 |
| NH168 | 0.02213 | 0.39520 | 0.50312 | 0.12001 | 0.51567 |
| NH169 | 0.59169 | 16.04565 | 44.63689 | 11.02375 | 50.98547 |
| NH170 | 0.59202 | 16.04609 | 45.94746 | 16.10568 | 53.25447 |
| NH171 | 0.59022 | 16.05566 | 44.54240 | 14.73451 | 44.26226 |
| NH172 | 0.00757 | 0.23667 | 1.03281 | 0.37069 | 1.14000 |
| NH173 | 0.00833 | 0.36685 | 1.35764 | 0.33799 | 1.45312 |
| NH174 | 0.01252 | 0.66407 | 2.71555 | 0.66651 | 2.74186 |
| NH175 | 0.02655 | 1.36605 | 5.41567 | 1.31144 | 5.39164 |
| NH176 | 0.05100 | 2.70542 | 10.76830 | 2.61645 | 11.45177 |
| NH177 | 0.09273 | 5.21484 | 20.80062 | 5.03217 | 21.90989 |
| NH178 | 0.00576 | 0.22318 | 1.29611 | 0.31565 | 1.30615 |
| NH179 | 0.01661 | 0.64286 | 3.74246 | 0.90045 | 3.78120 |
| NH180 | 0.02349 | 0.90817 | 5.28741 | 1.27109 | 5.12966 |
| NH181 | 0.07175 | 2.38755 | 10.50134 | 2.53316 | 10.87241 |
| NH182 | 0.08699 | 3.36647 | 19.59650 | 4.72033 | 20.02352 |
| NH183 | 0.44967 | 6.83171 | 0.27392 | 1.05204 | 6.84013 |
| NH184 | 0.64245 | 9.68331 | 0.34078 | 1.49017 | 9.69252 |

NH165-



NH166



NH167



NH168



NH169



NH170

A-43
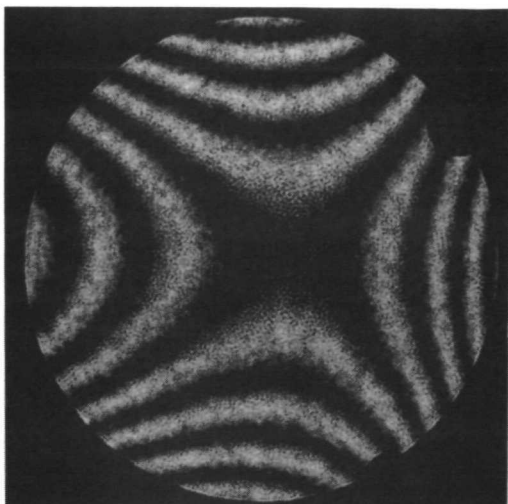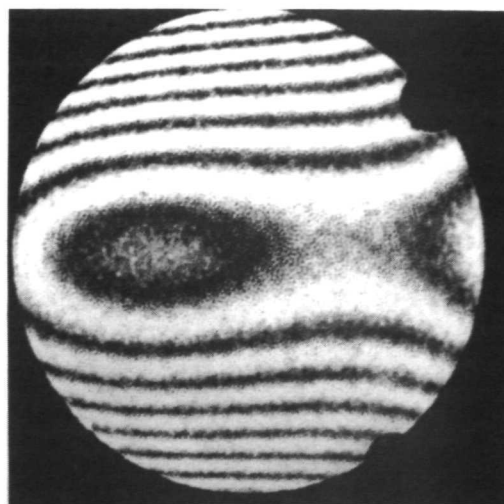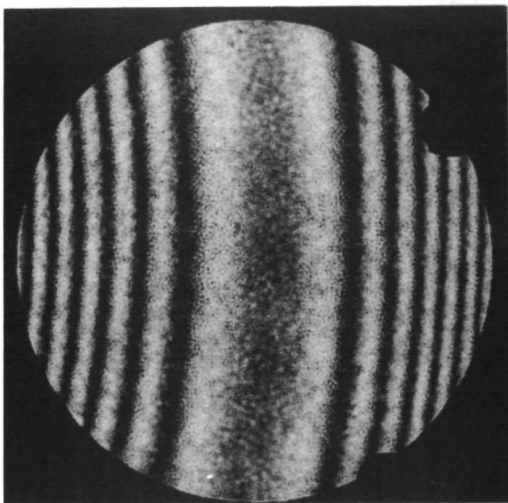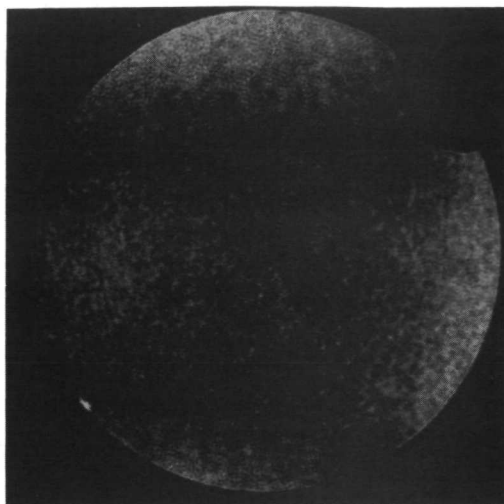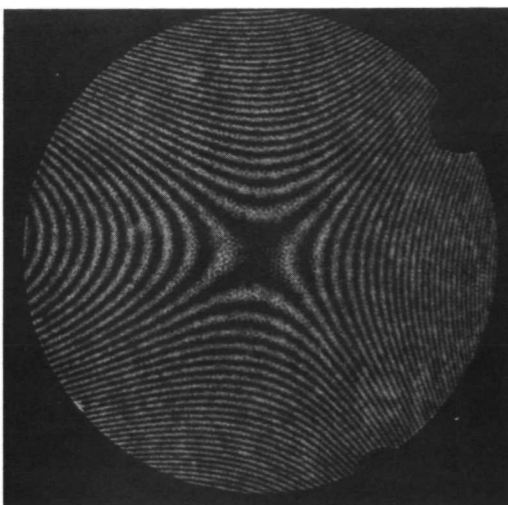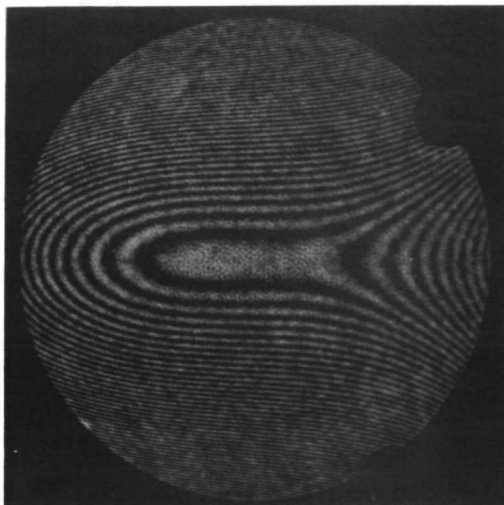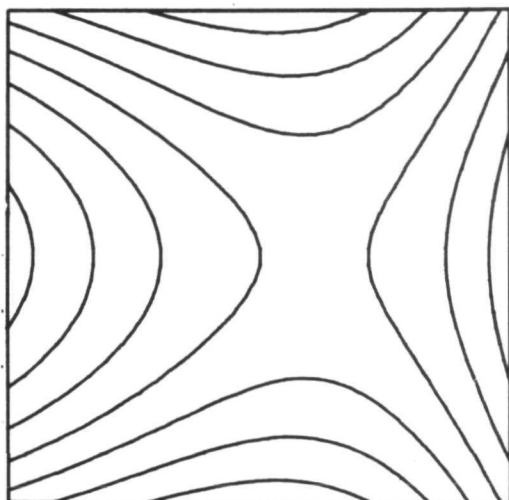
NH165
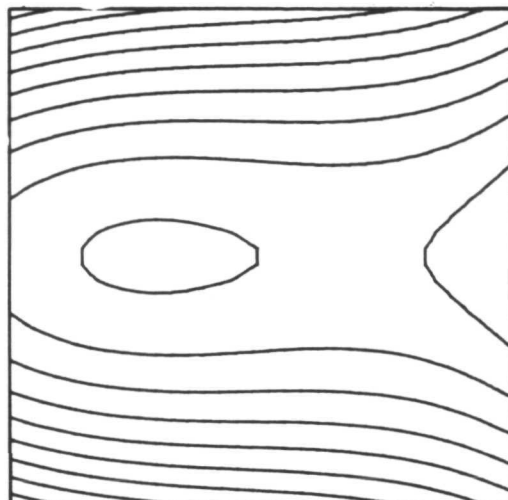


NH166
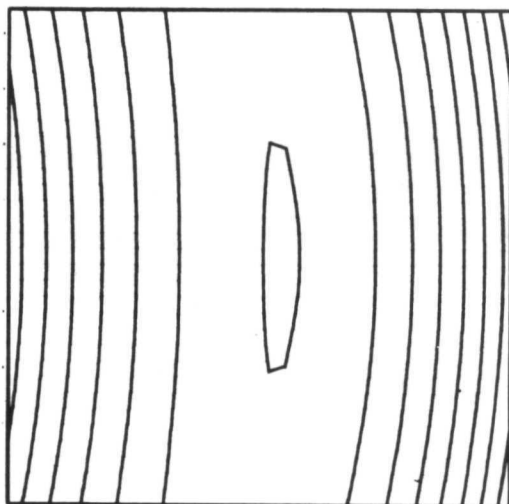


NH167
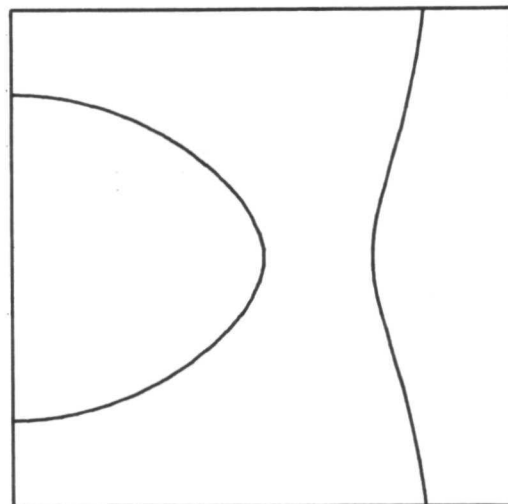


NH168
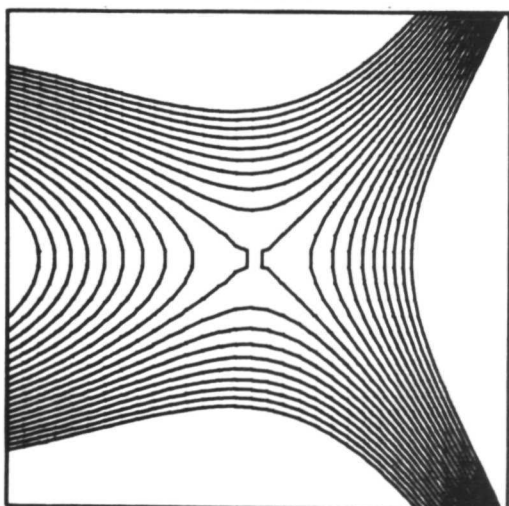


NH169
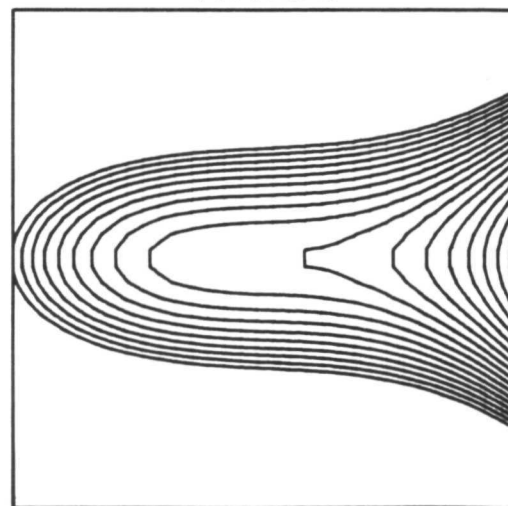


NH170
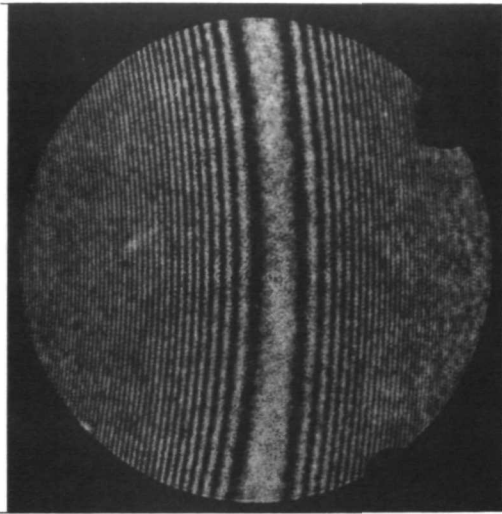
NH171
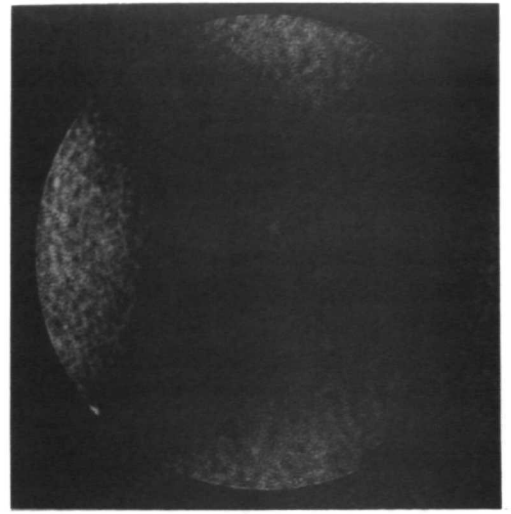


NH172
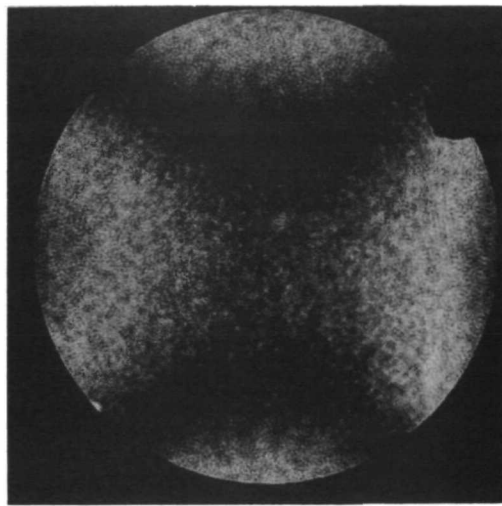


NH173
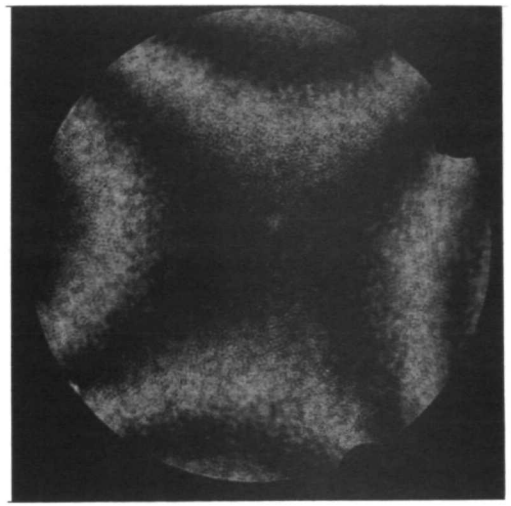


NH174



NH175



NH176

NHl7l



NHl72



NHl73



NHl74



NHl75
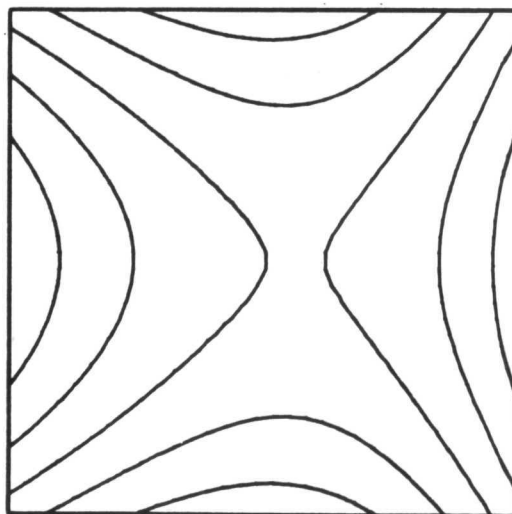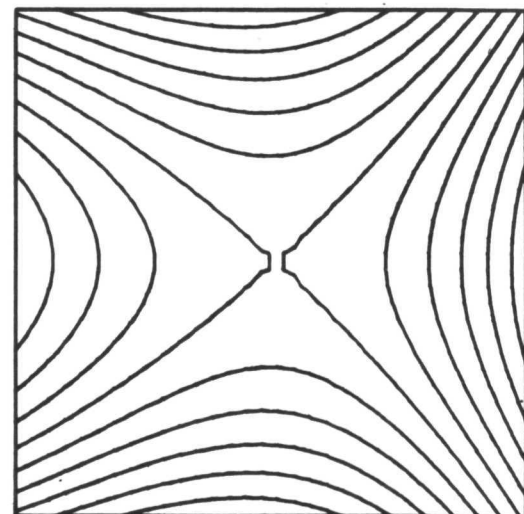


NHl76
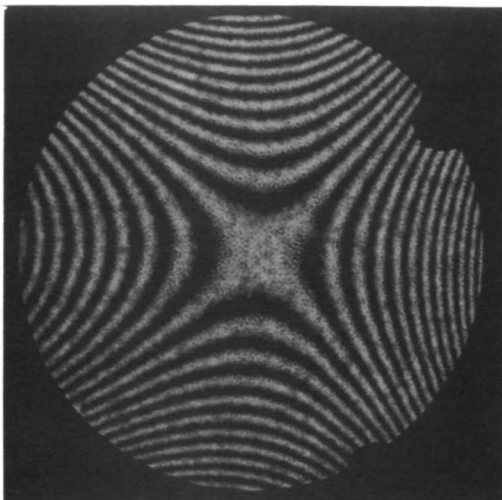
NH177
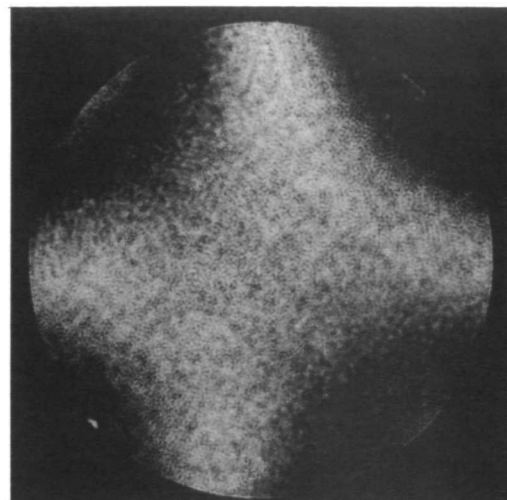


NH178
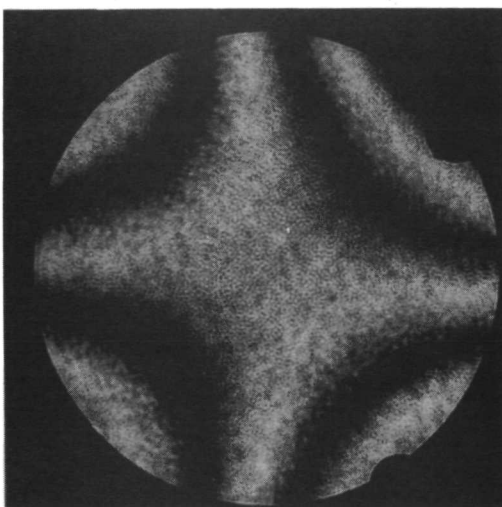


NH179
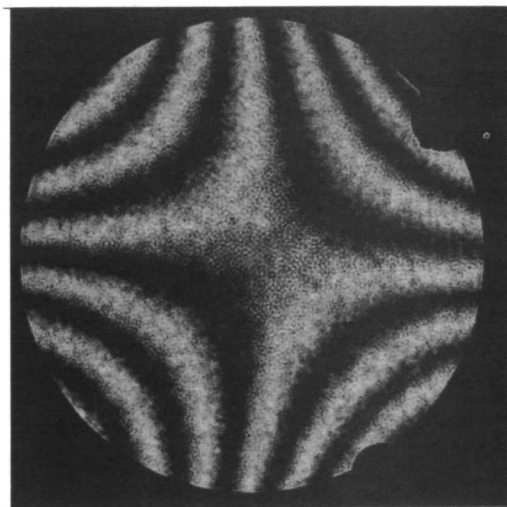


NH180
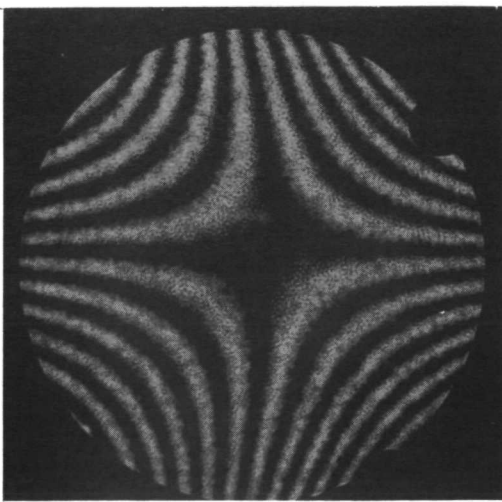


NH181
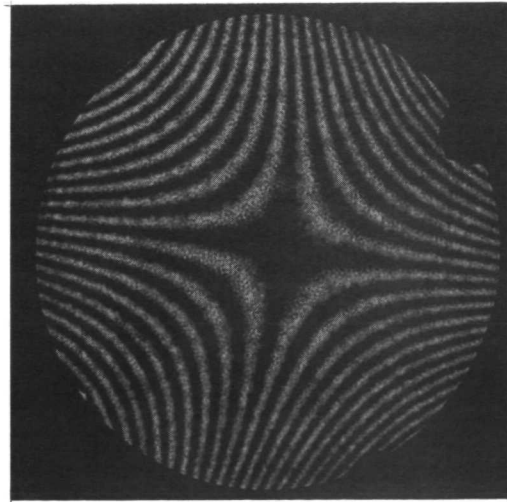


NH182
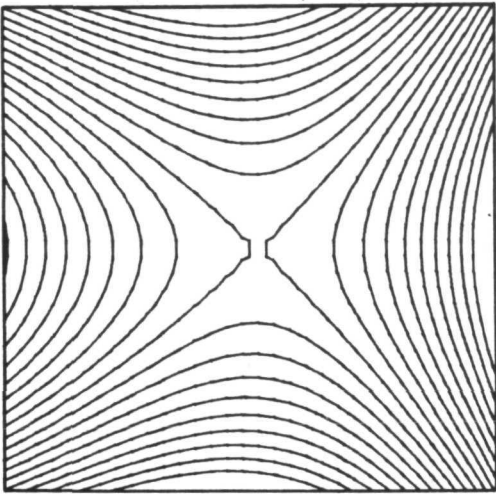
NHI77
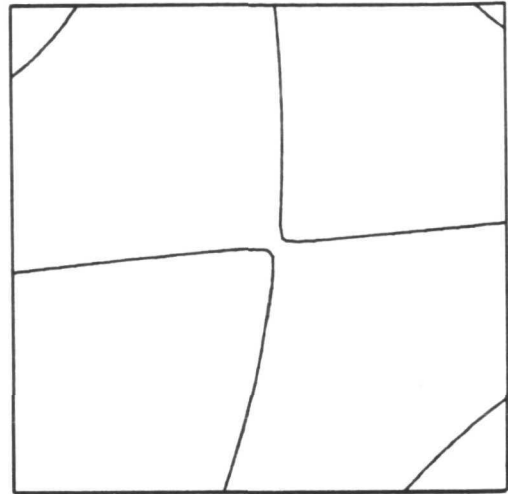


NHI78



NHI79



NHI80



NHI8I
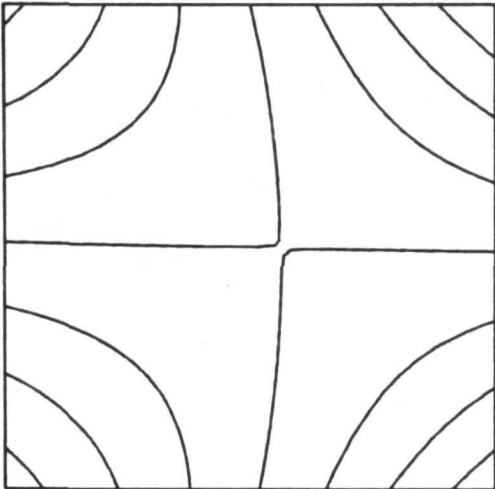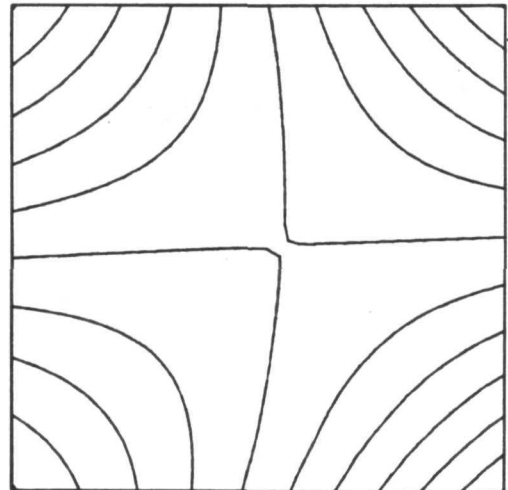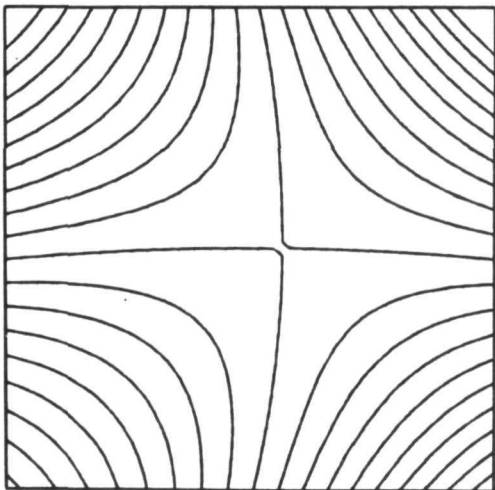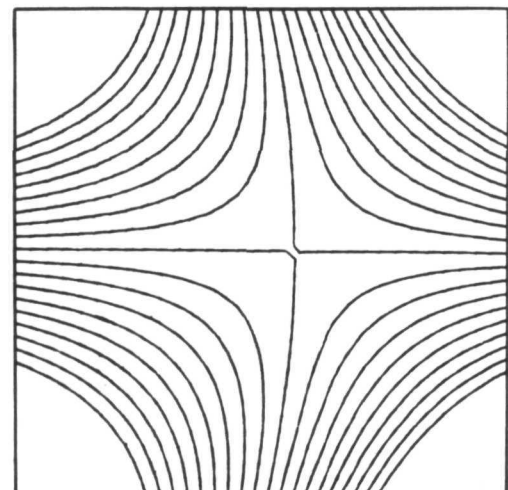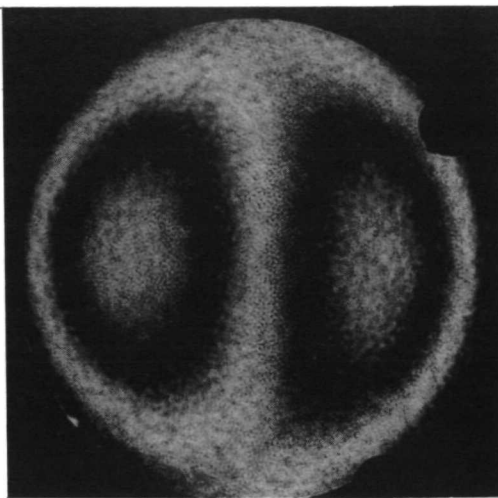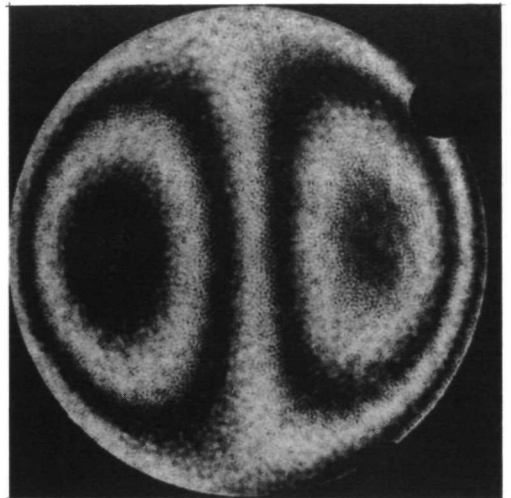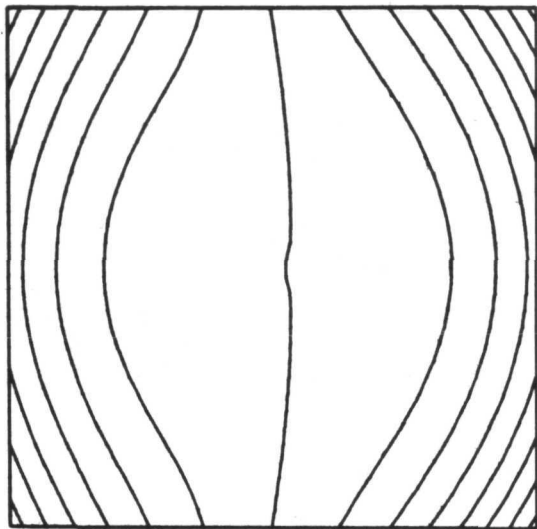


NHI82

NH183



NH184

NHI83
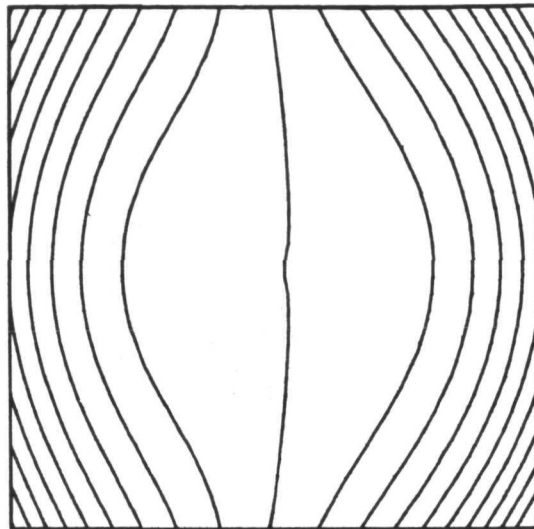


NHI84

A.3

Chromatic and Seidel Aberrations for

Phase Recording Materials

Groups 5 to 7

(Argon Laser Construction and Readout)

Group 5
Chromatic and Seidel Aberrations
Bleached Kodak HR Plate
Q = 4

Chromatic aberration data is shown in photographs NH185 to NH192 for bleached Kodak HR plates.  For $\lambda_c$ = 476.5 nm and 514.5 nm we photographed interference patterns corresponding to point image aberrations at the circle of least confusion, the tangential focus, and the sagittal focus.  These cases are illustrated in photographs NH185, 186, and 187 and NH189, 190, and 191.  Wavelength optimizations are shown in photographs NH188 and NH192 for $\lambda_c$ = 476.5 mm and 514.5 nm, respectively.  As before, we were able to locate a spatial position of the point object that reduced chromatic aberration to less than one wave.

In photographs NH193 to NH206 we present data on Seidel aberrations.  Lateral field aberrations were generated by translating a point object through calibrated x and y displacements; only the aberration patterns at the circle of least confusion are shown.  Photographs NH192 to NH198 are the interference patterns generated by x-axis translations while photographs NH199 to NH204 are created by y-axis displacements.  The field mapped out by these translations relative to a 400 mm focal length is about 1° (16 mrad).  Longitudinal field aberrations, caused by translating the object point axially, are illustrated in photographs NH205 to NH206.

HARRIS ELECTRO-OPTICS CENTER

## GROUP 5

Bleached HR Plate

$R_o$ = 6.32 in.  $\lambda_o$ = 488 nm  $\theta$ = 29.°5

$R_R$ = 10.5 in.  Q = 4  $\langle \bar{K} \rangle$ = split bisector

| Photo | $\Delta x_i$ | $\Delta y_i$ | $\Delta z_i$ | $\Delta x_c$ | $\Delta y_c$ | $\Delta z_c$ | $\lambda_c$ | $\Delta_x$ | $\Delta_y$ |
|---|---|---|---|---|---|---|---|---|---|
| 185 | .0799 | 0 | .0793 | 0 | 0 | 0 | 476.5 | 20 | 17 |
| 186 | .0799 | 0 | .1000 | 0 | 0 | 0 | 476.5 | 8 | 38 |
| 187 | .0799 | 0 | .0617 | 0 | 0 | 0 | 476.5 | 37 | 0 |
| 188 | .0298 | 0 | .0215 | -.0819 | 0 | -.1100 | 476.5 | 1 | .5 |
| 189 | -.1774 | 0 | -.1863 | 0 | 0 | 0 | 514.5 | 49 | 44 |
| 190 | -.1759 | 0 | -.2373 | 0 | 0 | 0 | 514.5 | 21 | 92 |
| 191 | -.1791 | 0 | -.1407 | 0 | 0 | 0 | 514.5 | 89 | 0 |
| 192 | -.0681 | 0 | -.0668 | .1948 | 0 | .2098 | 514.5 | 1 | .5 |
| 193 | -.0040 | 0 | 0 | -.0066 | 0 | .0048 | 488 | 1 | 2 |
| 194 | -.0080 | 0 | 0 | -.0134 | 0 | .0069 | 488 | 4 | 2.5 |
| 195 | -.0160 | 0 | 0 | -.0267 | 0 | .0157 | 488 | 7 | 5.5 |
| 196 | -.0320 | 0 | 0 | -.0535 | 0 | .0384 | 488 | 13 | 12 |
| 197 | -.0640 | 0 | 0 | -.1075 | 0 | .0783 | 488 | 24 | 27 |
| 198 | -.1280 | 0 | 0 | -.2157 | 0 | .1383 | 488 | 53 | 47 |
| 199 | 0 | .0040 | 0 | 0 | .0073 | 0 | 488 | 1.5 | 1.5 |
| 200 | 0 | .0080 | 0 | 0 | .0134 | 0 | 488 | 2 | 4 |
| 201 | 0 | .0160 | 0 | 0 | .0269 | 0 | 488 | 6 | 6 |
| 202 | 0 | .0320 | 0 | 0 | .0535 | 0 | 488 | 12.5 | 13 |
| 203 | 0 | .0640 | 0 | 0 | .1067 | 0 | 488 | 24 | 26 |
| 204 | 0 | .1280 | 0 | 0 | .2142 | 0 | 488 | 49 | 52 |
| 205 | 0 | 0 | -.1000 | .0002 | .0005 | -.2783 | 488 | 8 | 0 |
| 206 | 0 | 0 | -.1805 | .0003 | .0009 | -.4972 | 488 | 15 | 2 |

GROUP 5 OPTIMIZED   BLEACHED H.R. PLATE

RO = 6.3 IN.     AO = 14.7 DEG.     LAMO = 488.0 NM.
RR = 10.5 IN.    AR =-14.7 DEG.     Q = 4.0

| PHOTO | DXI | DYI | DZI | DXC | DYC | DZC | LAMC |
|---|---|---|---|---|---|---|---|
| NH185 | 0.0795 | 0.0 | 0.0771 | 0.0 | 0.0 | 0.0 | 476.5 |
| NH186 | 0.0795 | 0.0 | 0.0982 | 0.0 | 0.0 | 0.0 | 476.5 |
| NH187 | 0.0795 | 0.0 | 0.0599 | 0.0 | 0.0 | 0.0 | 476.5 |
| NH188 | 0.0298 | 0.0 | 0.0215 | -0.0799 | 0.0 | -0.1033 | 476.5 |
| NH189 | -0.1763 | 0.0 | -0.1815 | 0.0 | 0.0 | 0.0 | 514.5 |
| NH190 | -0.1748 | 0.0 | -0.2298 | 0.0 | 0.0 | 0.0 | 514.5 |
| NH191 | -0.1779 | 0.0 | -0.1362 | 0.0 | 0.0 | 0.0 | 514.5 |
| NH192 | -0.0664 | 0.0 | -0.0668 | 0.1926 | 0.0 | 0.1928 | 514.5 |
| NH193 | -0.0040 | 0.0 | -0.0000 | -0.0066 | 0.0 | 0.0055 | 488.0 |
| NH194 | -0.0079 | 0.0 | -0.0000 | -0.0131 | 0.0 | 0.0075 | 488.0 |
| NH195 | -0.0160 | 0.0 | -0.0000 | -0.0266 | 0.0 | 0.0150 | 488.0 |
| NH196 | -0.0320 | 0.0 | -0.0000 | -0.0531 | 0.0 | 0.0373 | 488.0 |
| NH197 | -0.0640 | 0.0 | -0.0000 | -0.1068 | 0.0 | 0.0747 | 488.0 |
| NH198 | -0.1280 | 0.0 | -0.0000 | -0.2141 | 0.0 | 0.1330 | 488.0 |
| NH199 | 0.0 | 0.0045 | -0.0000 | 0.0 | 0.0074 | -0.0000 | 488.0 |
| NH200 | 0.0 | 0.0080 | -0.0000 | 0.0 | 0.0133 | -0.0014 | 488.0 |
| NH201 | 0.0 | 0.0165 | -0.0000 | 0.0 | 0.0273 | -0.0010 | 488.0 |
| NH202 | 0.0 | 0.0331 | -0.0000 | 0.0 | 0.0548 | -0.0010 | 488.0 |
| NH203 | 0.0 | 0.0648 | -0.0000 | 0.0 | 0.1070 | 0.0007 | 488.0 |
| NH204 | 0.0 | 0.1305 | -0.0000 | 0.0 | 0.2167 | 0.0070 | 488.0 |
| NH205 | 0.0 | 0.0 | -0.1000 | 0.0002 | 0.0005 | -0.2703 | 488.0 |
| NH206 | 0.0 | 0.0 | -0.1805 | 0.0003 | 0.0009 | -0.4847 | 488.0 |

GROUP 5 OPTIMIZED BLEACHED H.R. PLATE

| PHOTO | SPHERICAL | COMA | ABERRATIONS ASTIGMATISM | RMS | TOTAL |
|---|---|---|---|---|---|
| NH185 | 0.23196 | 8.17721 | 20.11663 | 4.77679 | 20.79523 |
| NH186 | 0.23187 | 8.16920 | 20.04652 | 6.76424 | 23.82918 |
| NH187 | 0.23231 | 8.18396 | 20.17382 | 6.53633 | 19.27910 |
| NH188 | 0.24665 | 1.62228 | 0.14058 | 0.15865 | 0.63728 |
| NH189 | 0.75177 | 19.88319 | 48.63346 | 11.59654 | 53.74031 |
| NH190 | 0.75283 | 19.87688 | 48.64721 | 16.39674 | 58.06522 |
| NH191 | 0.74926 | 19.89693 | 48.65659 | 15.60037 | 48.52006 |
| NH192 | 0.44805 | 2.00674 | 0.15079 | 0.20005 | 0.75303 |
| NH193 | 0.00885 | 0.28452 | 1.66377 | 0.40678 | 1.63492 |
| NH194 | 0.01209 | 0.68763 | 3.28587 | 0.78639 | 3.21575 |
| NH195 | 0.02435 | 1.39781 | 6.66878 | 1.58912 | 6.71472 |
| NH196 | 0.06040 | 2.51807 | 13.30841 | 3.16024 | 12.90336 |
| NH197 | 0.12078 | 5.06466 | 26.72593 | 6.33731 | 27.10063 |
| NH198 | 0.21567 | 10.79433 | 53.62044 | 12.66976 | 53.81496 |
| NH199 | 0.01023 | 0.34845 | 1.81482 | 0.42575 | 1.72177 |
| NH200 | 0.01845 | 0.62785 | 3.26981 | 0.77622 | 3.11427 |
| NH201 | 0.03796 | 1.28985 | 6.72856 | 1.58166 | 7.21023 |
| NH202 | 0.07597 | 2.58694 | 13.48360 | 3.15456 | 13.52093 |
| NH203 | 0.14343 | 5.05576 | 26.33154 | 6.17751 | 25.02923 |
| NH204 | 0.29934 | 10.20933 | 53.25116 | 12.48105 | 55.86146 |
| NH205 | 0.97879 | 10.57756 | 0.59067 | 1.60443 | 8.91487 |
| NH206 | 1.82449 | 19.52186 | 0.93644 | 3.02988 | 16.94404 |
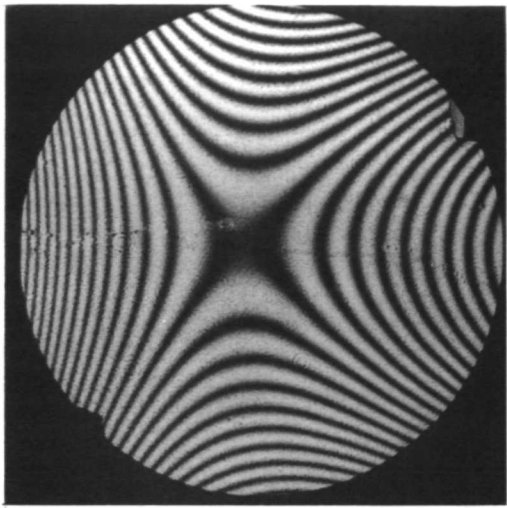
NH185
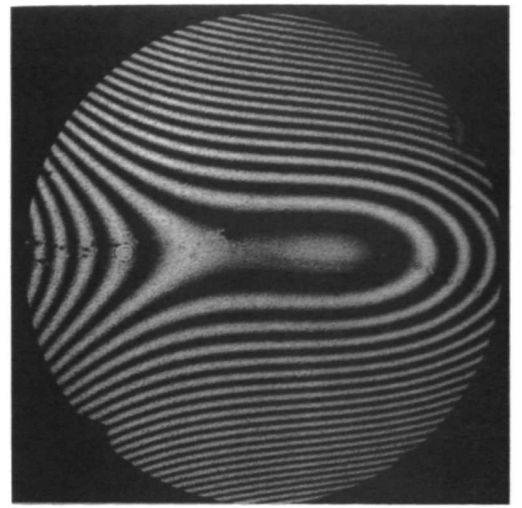


NH186
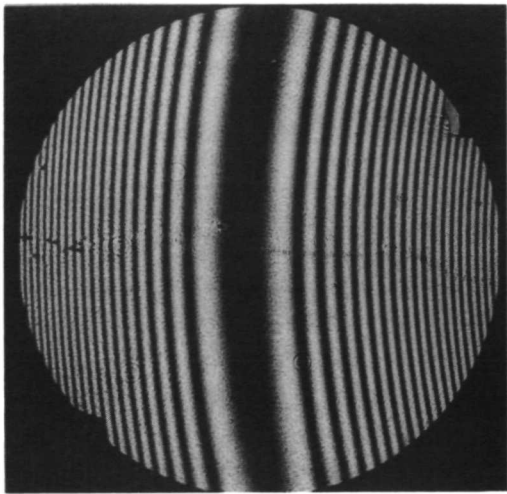


NH187
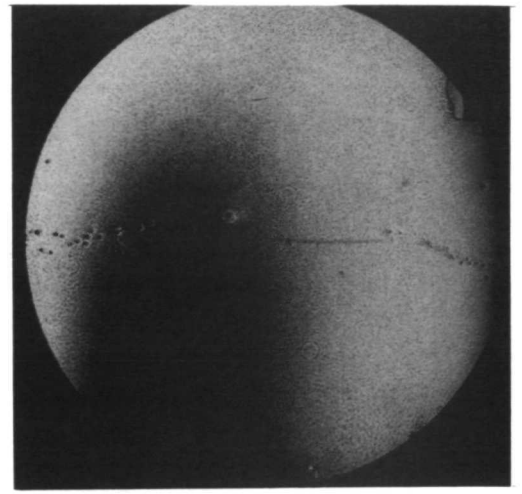


NH188
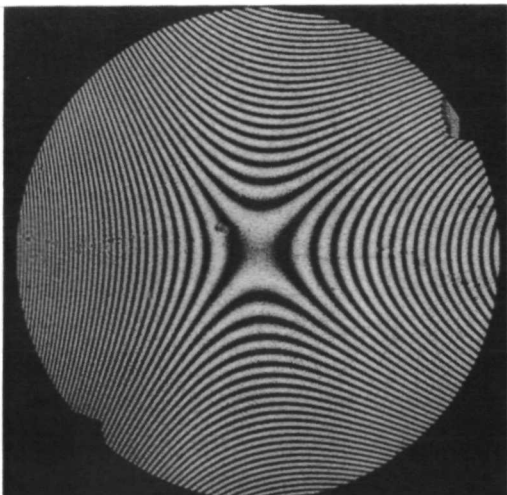


NH189
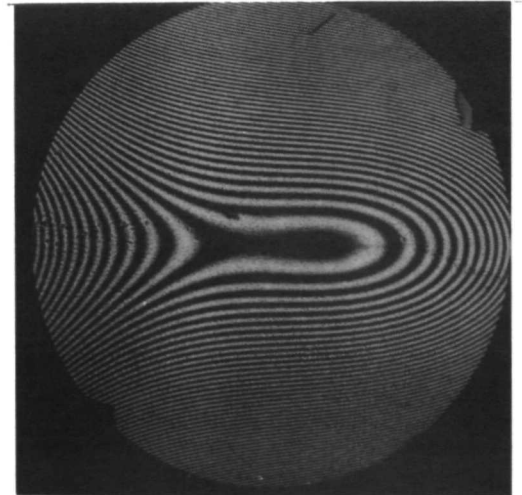


NH190
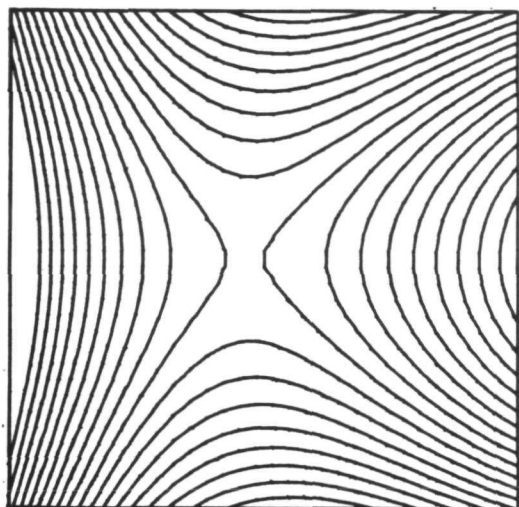
NHI85
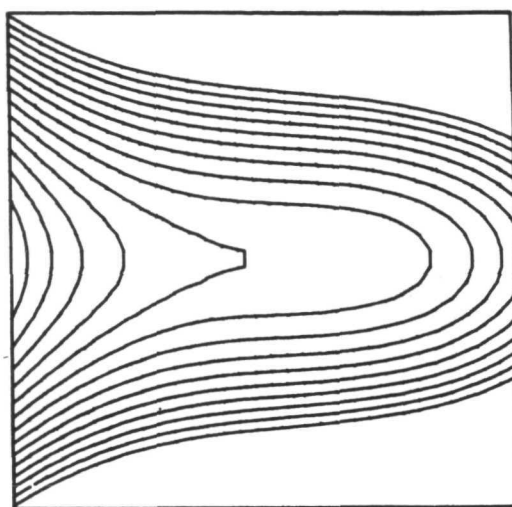


NHI86
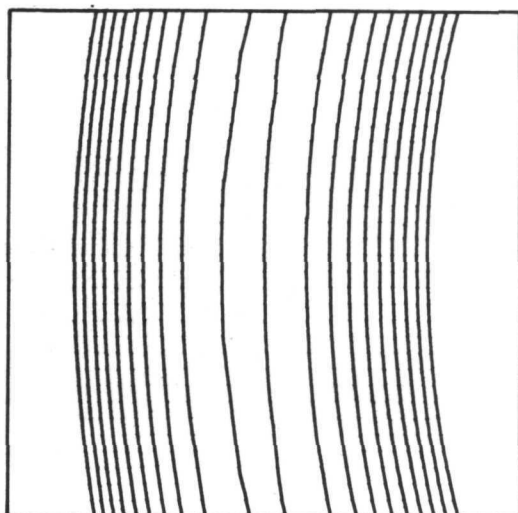


NHI87
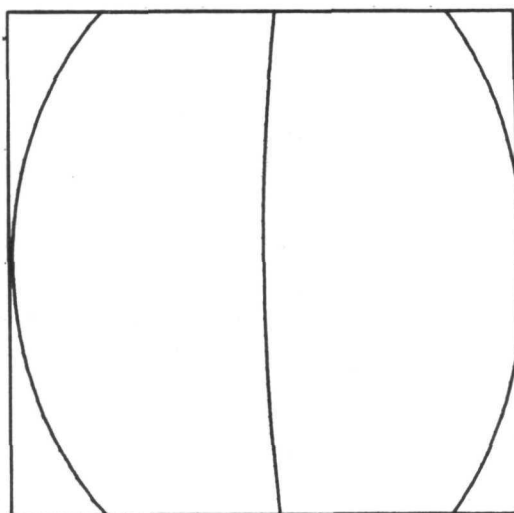


NHI88
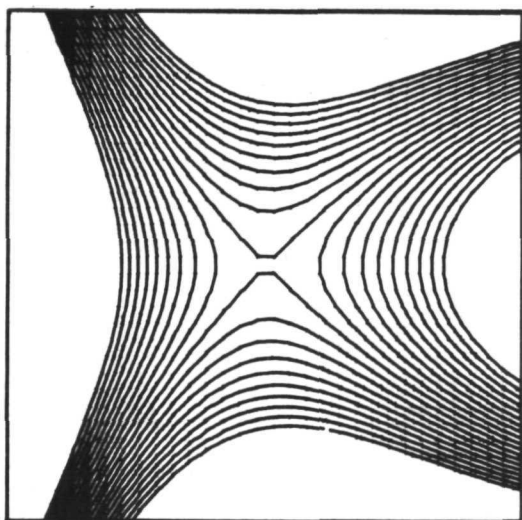


NHI89
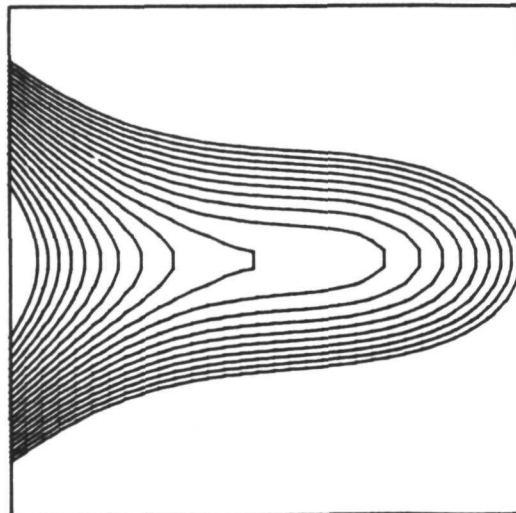


NHI90
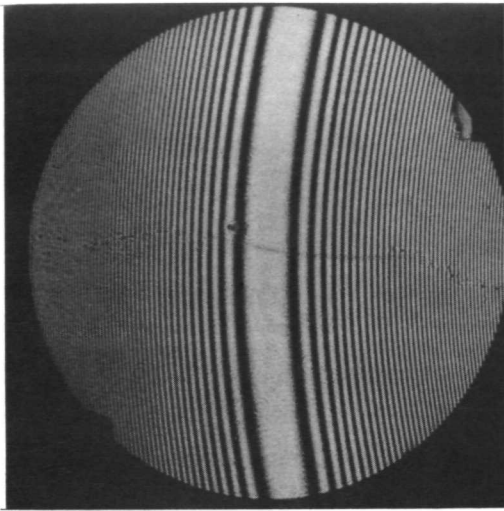
NH191
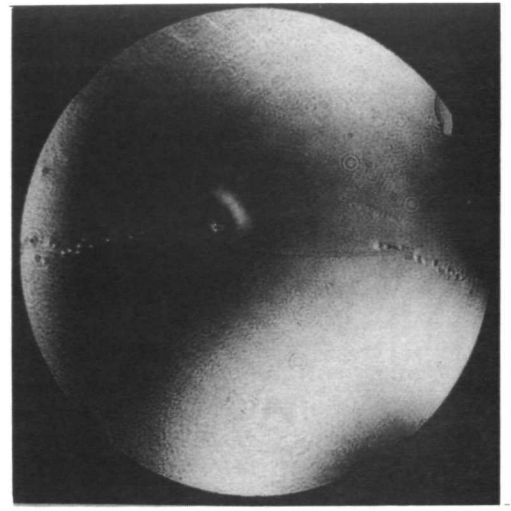


NH192
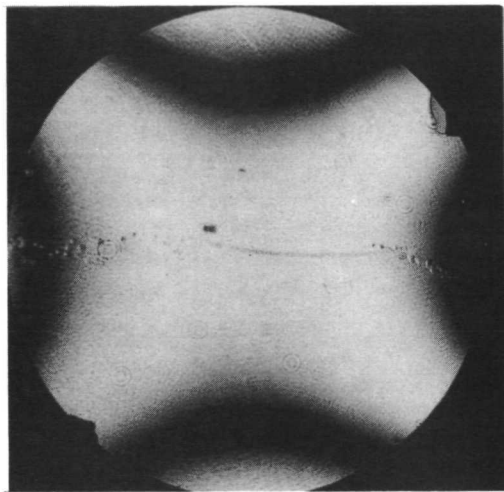


NH193
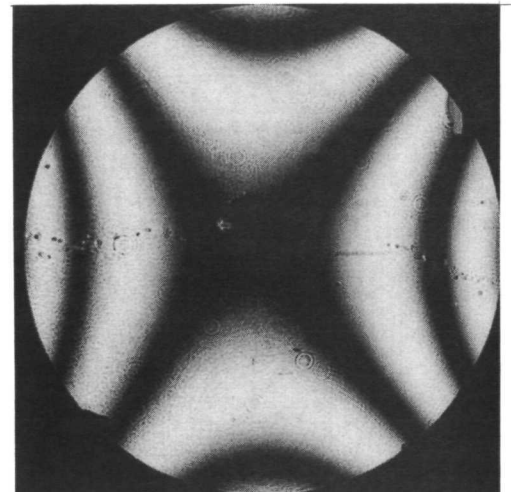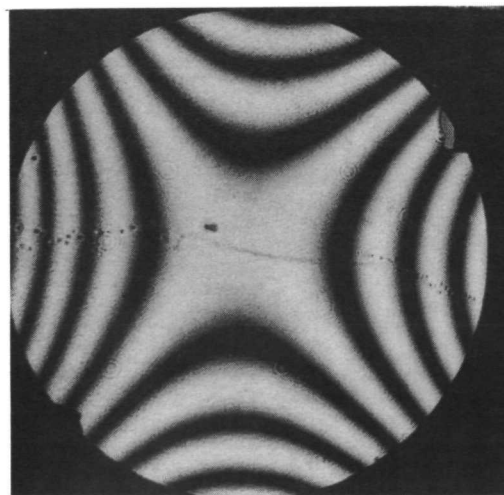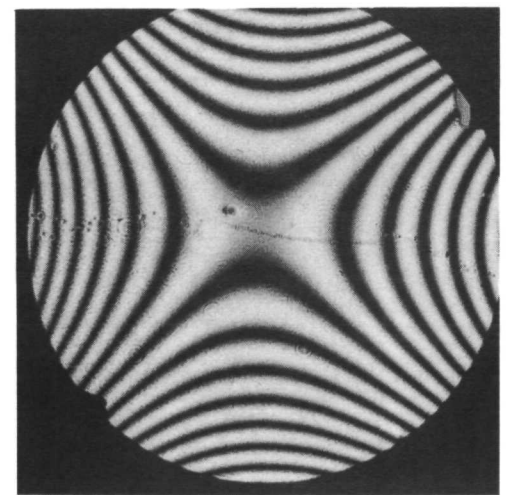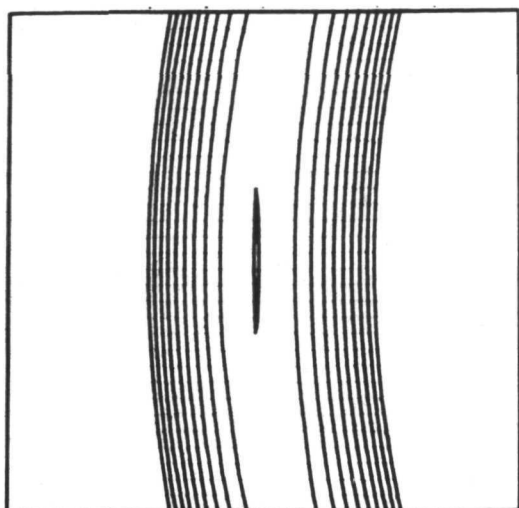


NH194



NH195



NH196

NH191
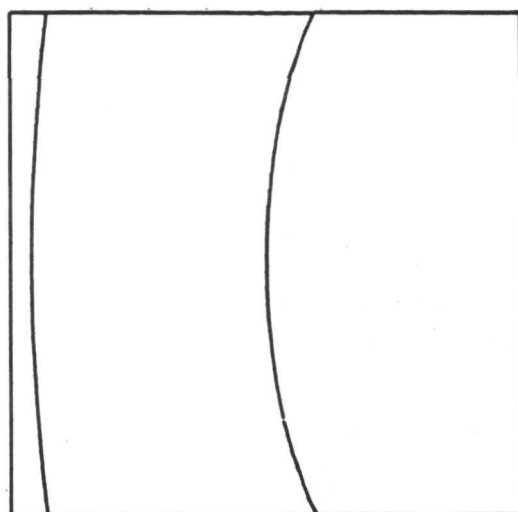
NH192
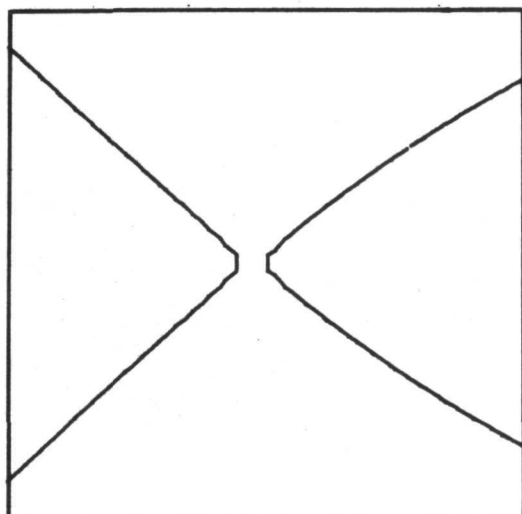
NH193
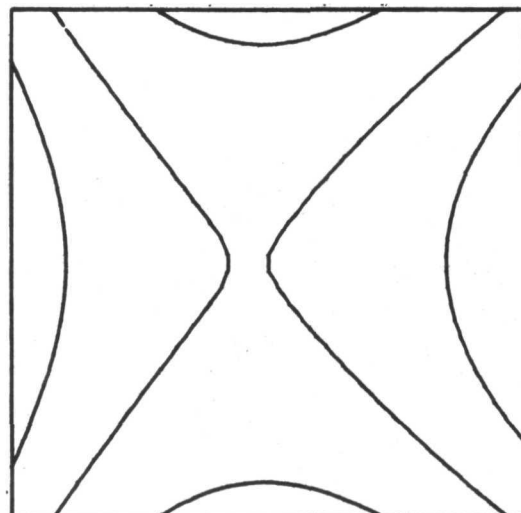
NH194
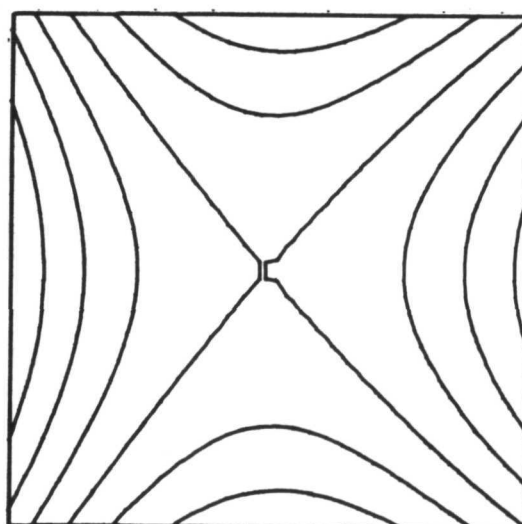
NH195
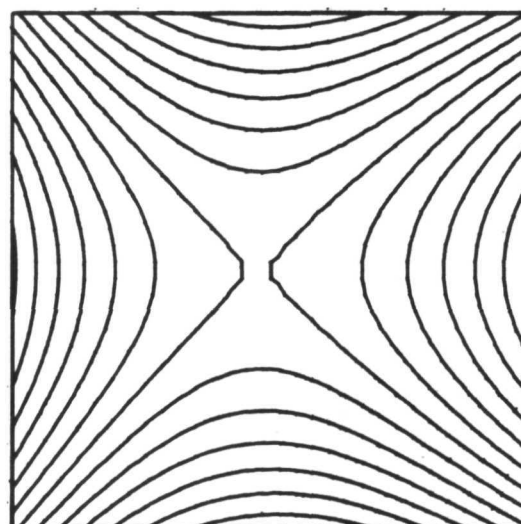
NH196
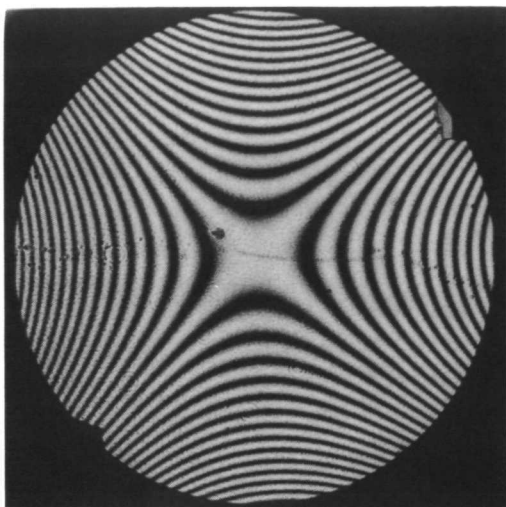
NH197
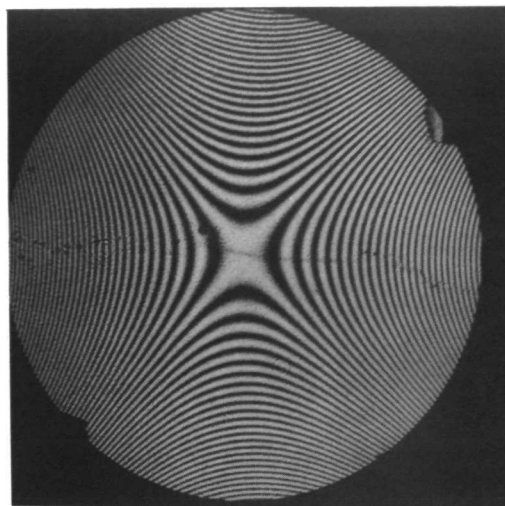
NH198
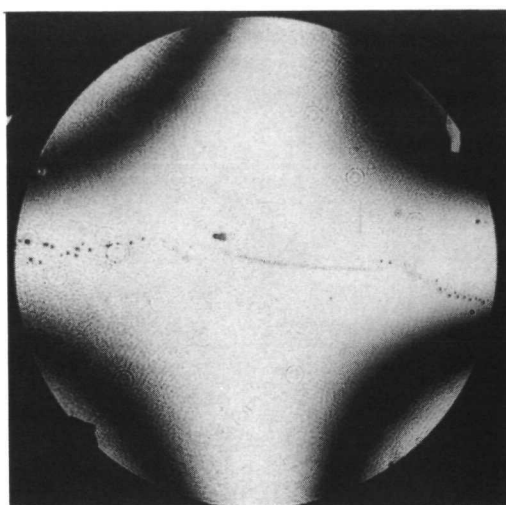
NH199
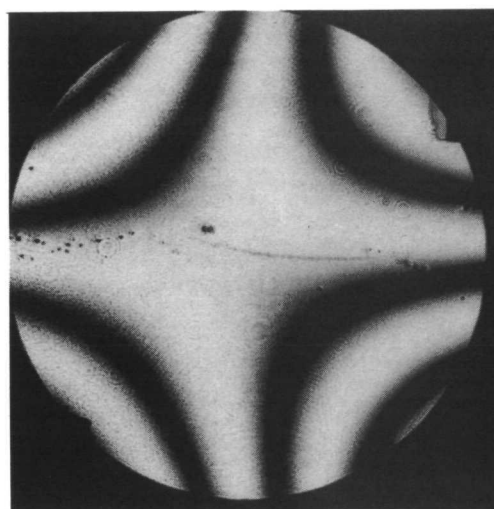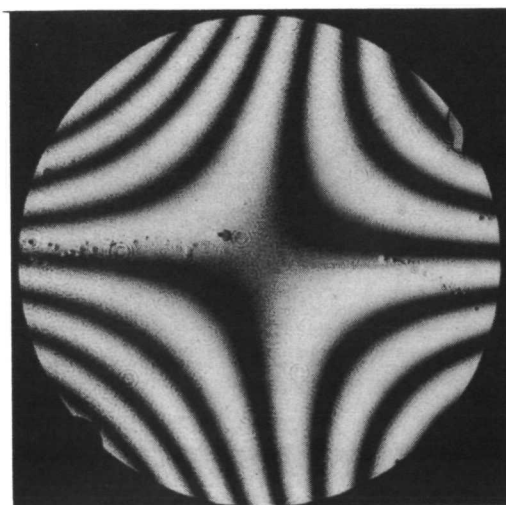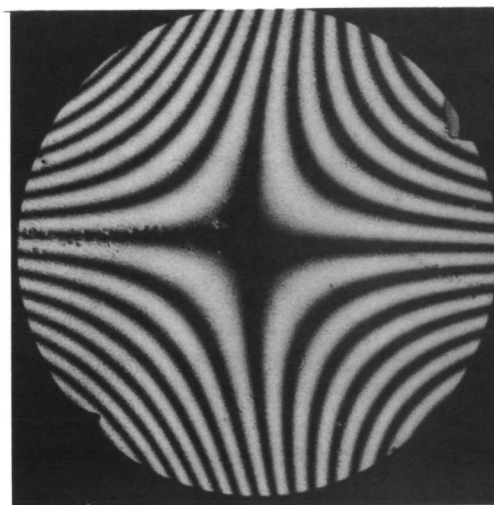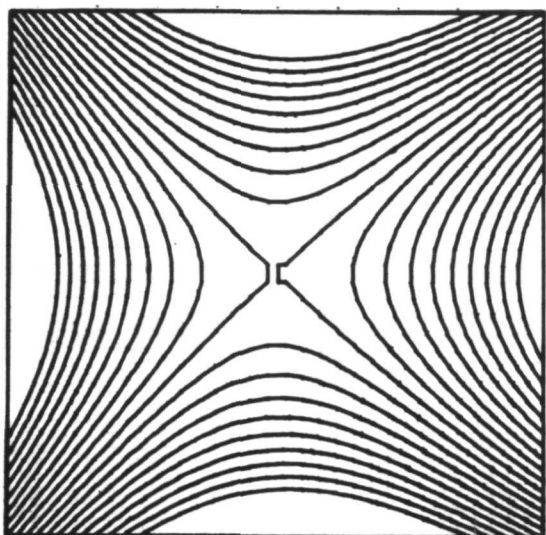
NH200

NH201

NH202

NH197
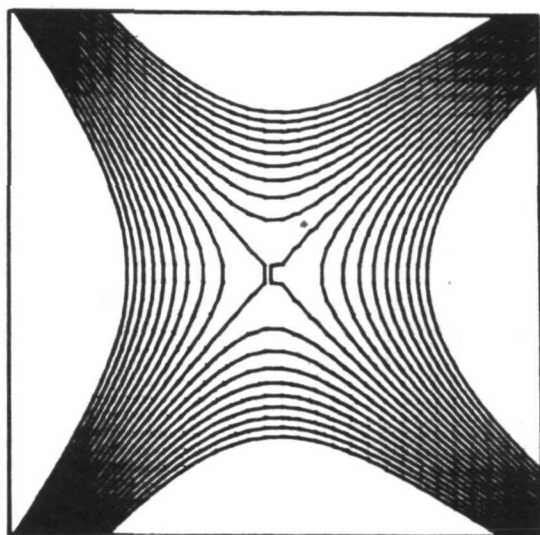


NH198
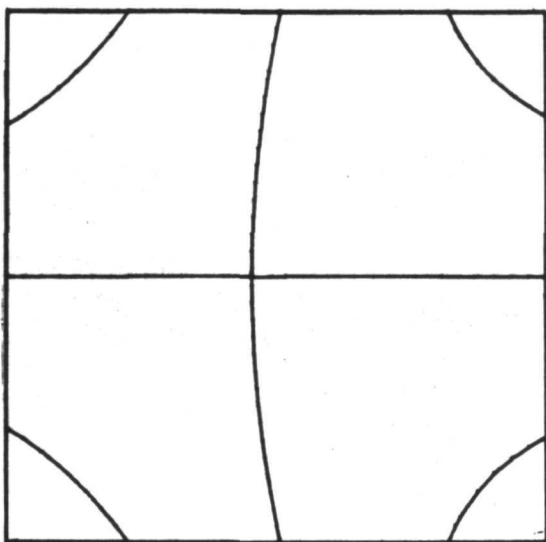


NH199
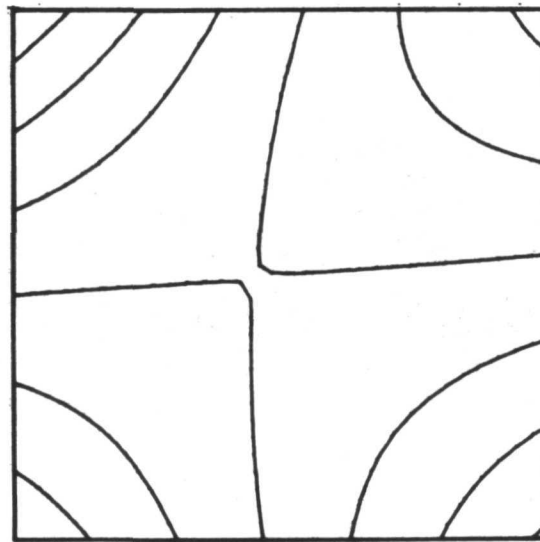


NH200
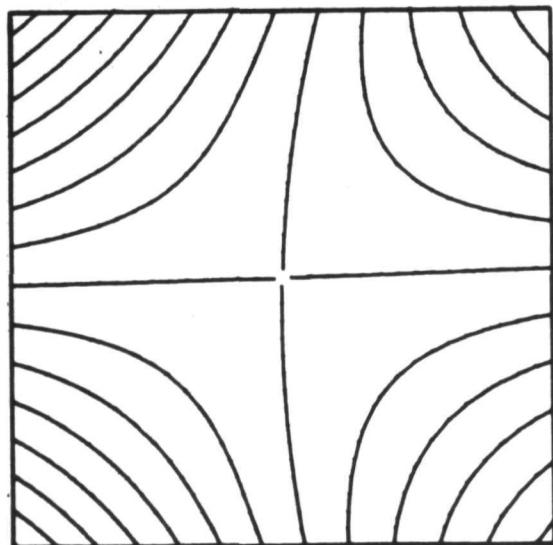


NH201
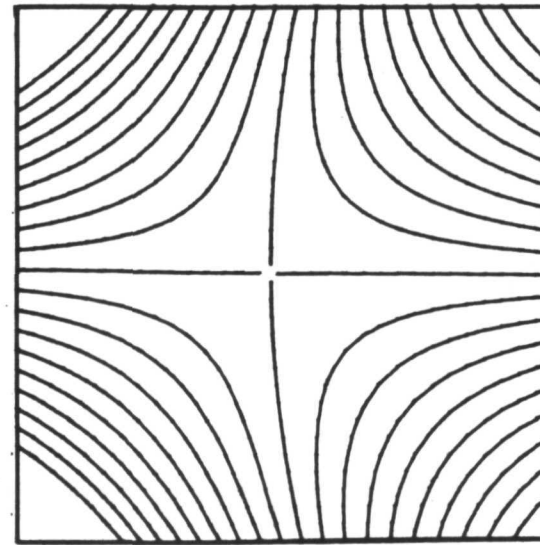


NH202
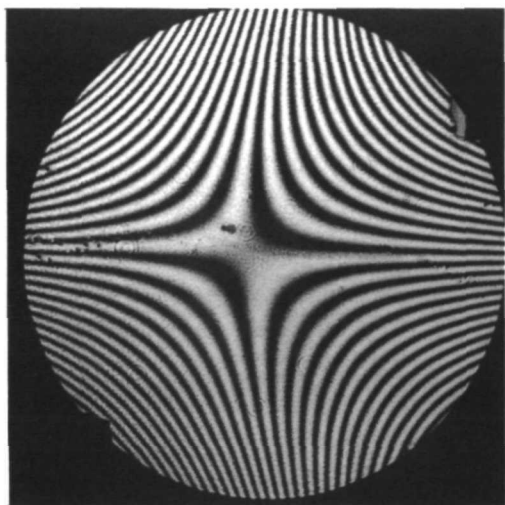
NH203
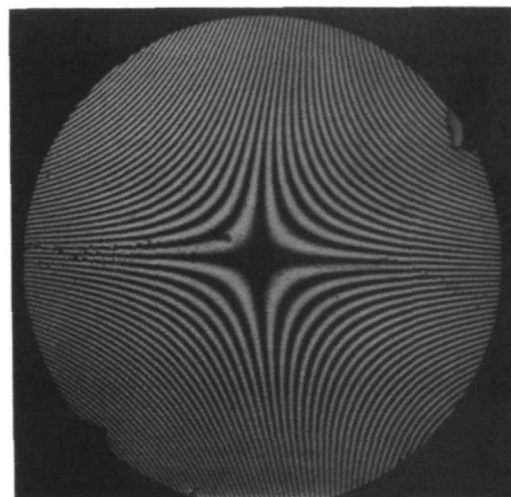


NH204
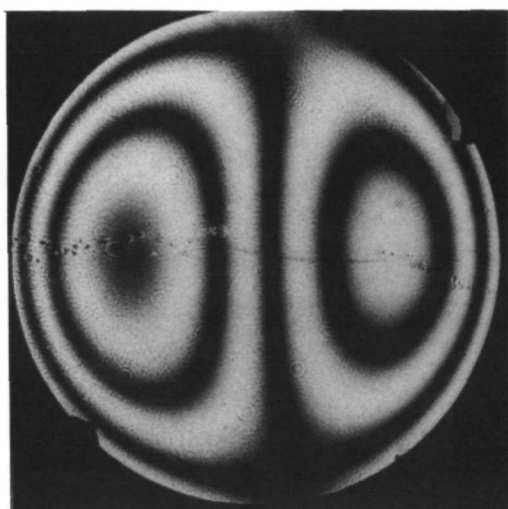


NH205
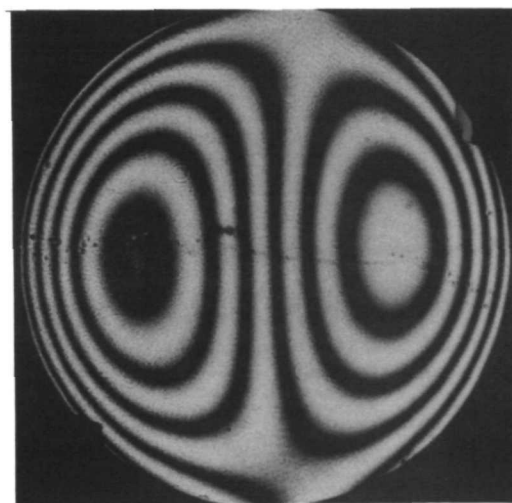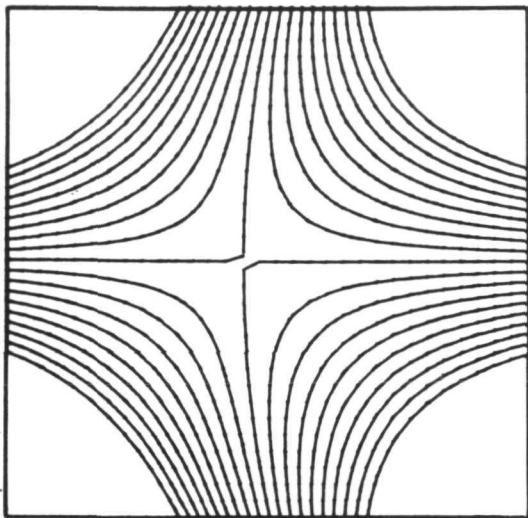


NH206

NH203
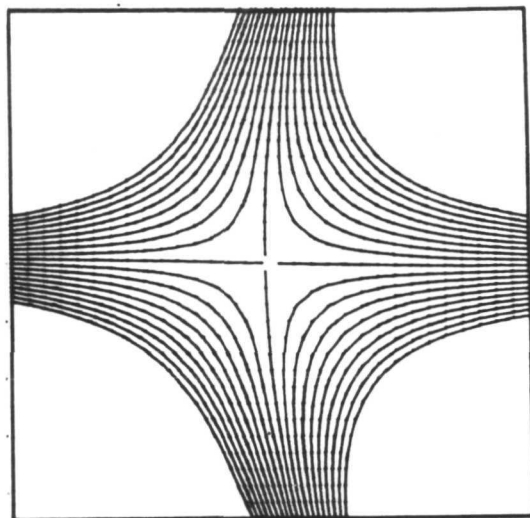


NH204
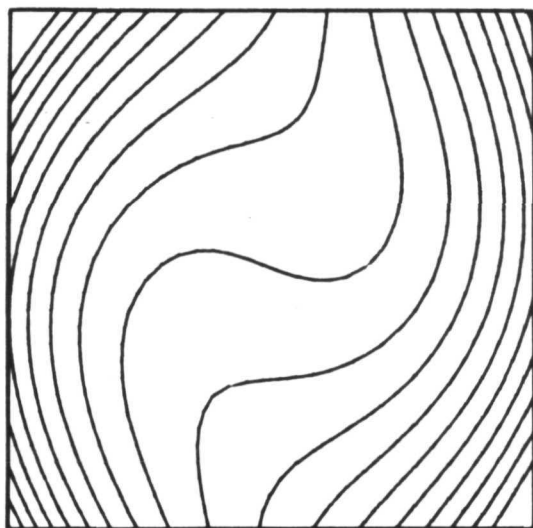


NH205
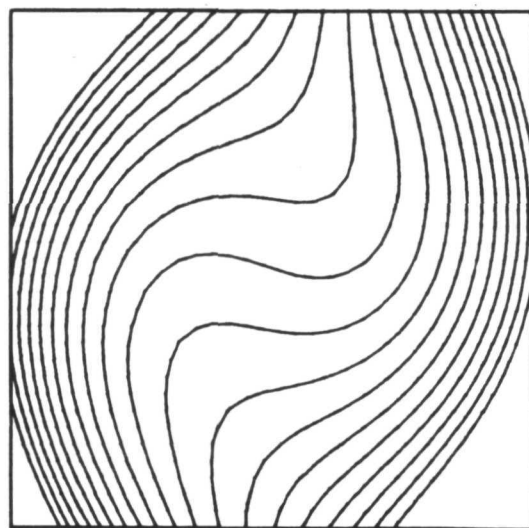


NH206

Group 6

Chromatic and Seidel Aberrations

Dichromated Gelatin

Q = 4

The data for chromatic and Seidel aberrations for dichromated gelatin are given in this section. The holographic elements fabricated on dichromated gelatin were of high quality with diffraction efficiencies of 70% or more and, in general, with very few cosmetic imperfections. The sample we selected for evaluation has a drying defect. However, we chose to evaluate this zone plate because of its high efficiency and to show how defects of this type influence aberration characteristics.

Chromatic aberrations are shown in photographs NH207, 208 and 209 and NH211, 212, and 213 for $\lambda_c$ = 476.5 nm and 514.5 nm. We again experimentally determined an object position that reduced residual chromatic aberration to less than one wave. Photographs NH210 and NH214 illustrate this condition for $\lambda_c$ = 476.5 nm and 514.5, respectively. It is interesting to note that although the surface defect interdicts the fringe pattern, it does not appear to appreciably alter the fringe contours.

The interference patterns obtained for the Seidel aberrations are shown in photographs NH215 to NH220 for the $(x_0 - z_0)$ field and in photographs NH221 to NH226 for the $(y_0 - z_0)$ field. The field angle covered is again about 1° in either dimension. Photographs NH227 and NH228 show the fringe contours generated by axial translation of the object point. The excellent fringe contrast obtained for the Seidel aberration data is due to the high diffraction efficiency of the optical element. The amplitude of the reconstructed point image is about equal to the amplitude of the point object; this yields a high degree of modulation and, hence, high fringe contrast.

GROUP 6

Dichromated Gelatin

$R_O$ = 6.32 in.                $\lambda_O$ = 488 nm          $\theta$ = 29.°5

$R_R$ = 10.5 in.               Q = 4              $<\bar{K}>$ = split bisector

| Photo | $\Delta x_i$ | $\Delta y_i$ | $\Delta z_i$ | $\Delta x_c$ | $\Delta y_c$ | $\Delta z_c$ | $\lambda_c$ | $\Delta_x$ | $\Delta_y$ |
|-------|------|------|------|------|------|------|------|------|------|
| 207 | .0803 | 0 | .0819 | 0 | 0 | 0 | 476.5 | 18.5 | 19.5 |
| 208 | .0803 | 0 | .1013 | 0 | 0 | 0 | 476.5 | 9 | 38 |
| 209 | .0803 | 0 | .0616 | 0 | 0 | 0 | 476.5 | 37 | .5 |
| 210 | .0300 | 0 | .0215 | -.0815 | 0 | -.1106 | 476.5 | .5 | 0 |
| 211 | -.1784 | 0 | -.1784 | 0 | 0 | 0 | 514.5 | 53 | 36 |
| 212 | -.1764 | 0 | -.2376 | 0 | 0 | 0 | 514.5 | 21 | 90 |
| 213 | -.1795 | 0 | -.1400 | 0 | 0 | 0 | 514.5 | 89 | 0 |
| 214 | -.0680 | 0 | -.0677 | .1950 | 0 | .2050 | 514.5 | .5 | .5 |
| 215 | -.0040 | 0 | 0 | -.0068 | 0 | .0040 | 488 | 1 | 1 |
| 216 | -.0080 | 0 | 0 | -.0136 | 0 | .0075 | 488 | 3.5 | 2 |
| 217 | -.0160 | 0 | 0 | -.0268 | 0 | .0183 | 488 | 6 | 6 |
| 218 | -.0320 | 0 | 0 | -.0536 | 0 | .0368 | 488 | 12 | 13.5 |
| 219 | -.0640 | 0 | 0 | -.1074 | 0 | .0671 | 488 | 26.5 | 23 |
| 220 | -.1280 | 0 | 0 | -.2156 | 0 | .1508 | 488 | 49 | 48 |
| 221 | 0 | .0040 | 0 | 0 | .0073 | 0 | 488 | 2 | 1.5 |
| 222 | 0 | .0080 | 0 | 0 | .0133 | 0 | 488 | 3 | 3 |
| 223 | 0 | .0160 | 0 | 0 | .0268 | 0 | 488 | 6 | 6.5 |
| 224 | 0 | .0320 | 0 | 0 | .0533 | 0 | 488 | 12 | 12 |
| 225 | 0 | .0640 | 0 | 0 | .1069 | 0 | 488 | 25 | 24 |
| 226 | 0 | .1280 | 0 | 0 | .2145 | 0 | 488 | 47 | 50 |
| 227 | 0 | 0 | -.1000 | 0 | 0 | -.2776 | 488 | 7.5 | 0 |
| 228 | 0 | 0 | -.1827 | 0 | 0 | -.5000 | 488 | 14 | 1 |

GROUP 6 OPTIMIZED    DICHROMATED GELATIN

RO =  6.3 IN.        AO =  14.7 DEG.        LAMO = 488.0 NM.
RR = 10.5 IN.        AR = -14.7 DEG.        Q = 4.0

| PHOTO | DXI | DYI | DZI | DXC | DYC | DZC | LAMC |
|-------|-----|-----|-----|-----|-----|-----|------|
| NH207 | 0.0795 | 0.0 | 0.0792 | 0.0 | 0.0 | 0.0 | 476.5 |
| NH208 | 0.0795 | 0.0 | 0.0975 | 0.0 | 0.0 | 0.0 | 476.5 |
| NH209 | 0.0796 | 0.0 | 0.0593 | 0.0 | 0.0 | 0.0 | 476.5 |
| NH210 | 0.0300 | 0.0 | 0.0215 | -0.0796 | 0.0 | -0.1035 | 476.5 |
| NH211 | -0.1768 | 0.0 | -0.1759 | 0.0 | 0.0 | 0.0 | 514.5 |
| NH212 | -0.1747 | 0.0 | -0.2284 | 0.0 | 0.0 | 0.0 | 514.5 |
| NH213 | -0.1778 | 0.0 | -0.1378 | 0.0 | 0.0 | 0.0 | 514.5 |
| NH214 | -0.0663 | 0.0 | -0.0677 | 0.1927 | 0.0 | 0.1901 | 514.5 |
| NH215 | -0.0040 | 0.0 | -0.0000 | -0.0066 | 0.0 | 0.0042 | 488.0 |
| NH216 | -0.0080 | 0.0 | -0.0000 | -0.0133 | 0.0 | 0.0064 | 488.0 |
| NH217 | -0.0160 | 0.0 | -0.0000 | -0.0265 | 0.0 | 0.0176 | 488.0 |
| NH218 | -0.0320 | 0.0 | -0.0000 | -0.0531 | 0.0 | 0.0373 | 488.0 |
| NH219 | -0.0640 | 0.0 | -0.0000 | -0.1065 | 0.0 | 0.0688 | 488.0 |
| NH220 | -0.1262 | 0.0 | -0.0004 | -0.2112 | 0.0 | 0.1467 | 488.0 |
| NH221 | 0.0 | 0.0046 | -0.0000 | 0.0 | 0.0076 | 0.0007 | 488.0 |
| NH222 | 0.0 | 0.0080 | -0.0000 | 0.0 | 0.0133 | -0.0002 | 488.0 |
| NH223 | 0.0 | 0.0153 | -0.0000 | 0.0 | 0.0254 | -0.0020 | 488.0 |
| NH224 | 0.0 | 0.0326 | 0.0001 | 0.0 | 0.0539 | -0.0001 | 488.0 |
| NH225 | 0.0 | 0.0667 | 0.0001 | 0.0 | 0.1104 | 0.0015 | 488.0 |
| NH226 | 0.0 | 0.1322 | 0.0001 | 0.0 | 0.2197 | 0.0060 | 488.0 |
| NH227 | 0.0 | 0.0 | -0.1000 | 0.0 | 0.0 | -0.2705 | 488.0 |
| NH228 | 0.0 | 0.0 | -0.1827 | 0.0 | 0.0 | -0.4901 | 488.0 |

A-66

GROUP 6 OPTIMIZED DICHROMATED GELATIN

|  | | | ABERRATIONS | | |
| PHOTO | SPHERICAL | COMA | ASTIGMATISM | RMS | TOTAL |
| --- | --- | --- | --- | --- | --- |
| NH207 | 0.23197 | 8.17737 | 20.10969 | 4.76783 | 20.83906 |
| NH208 | 0.23187 | 8.16885 | 20.04886 | 6.65563 | 23.36467 |
| NH209 | 0.23231 | 8.18597 | 20.18000 | 6.64748 | 20.06534 |
| NH210 | 0.24679 | 1.60693 | 0.18220 | 0.16024 | 0.64067 |
| NH211 | 0.75167 | 19.89425 | 48.63210 | 11.54818 | 51.18797 |
| NH212 | 0.75280 | 19.87523 | 48.64680 | 16.19697 | 58.32696 |
| NH213 | 0.74934 | 19.89439 | 48.62157 | 15.36691 | 48.74490 |
| NH214 | 0.44345 | 1.92132 | 0.15556 | 0.20924 | 0.77307 |
| NH215 | 0.06637 | 0.32966 | 1.66031 | 0.39524 | 1.63699 |
| NH216 | 0.01285 | 0.74191 | 3.33318 | 0.81146 | 3.33366 |
| NH217 | 0.02854 | 1.29539 | 6.64710 | 1.57553 | 6.41191 |
| NH218 | 0.06033 | 2.51751 | 13.29920 | 3.16141 | 12.82768 |
| NH219 | 0.11143 | 5.27584 | 26.69278 | 6.30777 | 26.44096 |
| NH220 | 0.23716 | 10.03951 | 52.75456 | 12.47037 | 51.99576 |
| NH221 | 0.01058 | 0.36060 | 1.87817 | 0.44436 | 1.78815 |
| NH222 | 0.01843 | 0.62754 | 3.26838 | 0.76706 | 3.10113 |
| NH223 | 0.03526 | 1.19865 | 6.24689 | 1.47055 | 6.26513 |
| NH224 | 0.07483 | 2.54366 | 13.27534 | 3.11238 | 12.68541 |
| NH225 | 0.15300 | 5.21092 | 27.15652 | 6.35298 | 26.96930 |
| NH226 | 0.30373 | 10.34864 | 53.99349 | 12.68247 | 58.02407 |
| NH227 | 0.97981 | 10.59539 | 0.50915 | 1.63594 | 10.60517 |
| NH228 | 1.84735 | 19.77181 | 0.94344 | 3.05373 | 19.79538 |
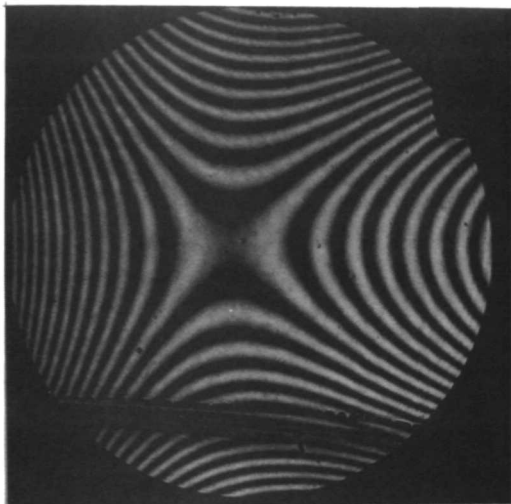
NH207
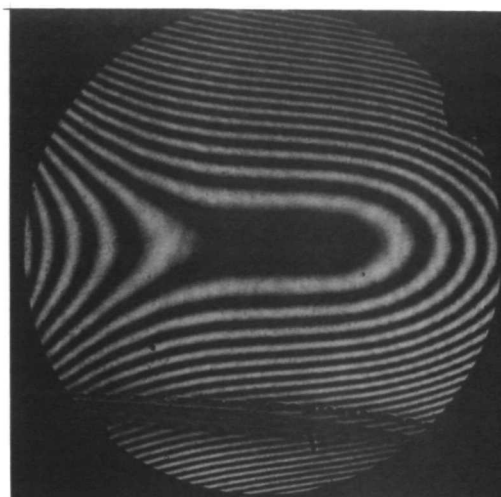


NH208
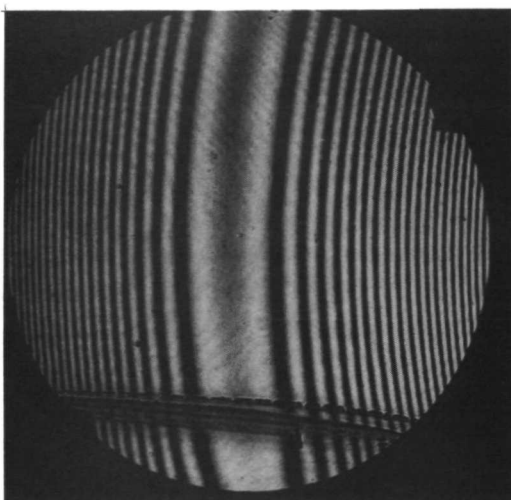


NH209
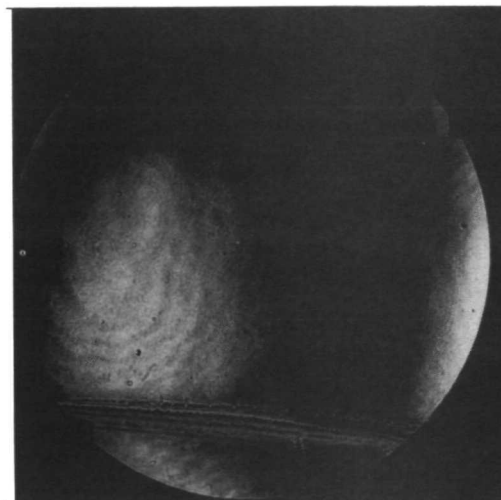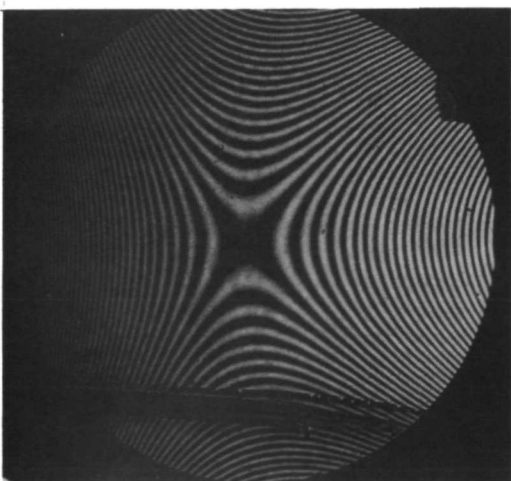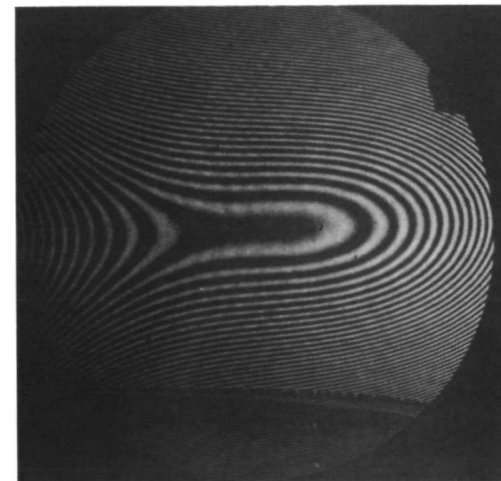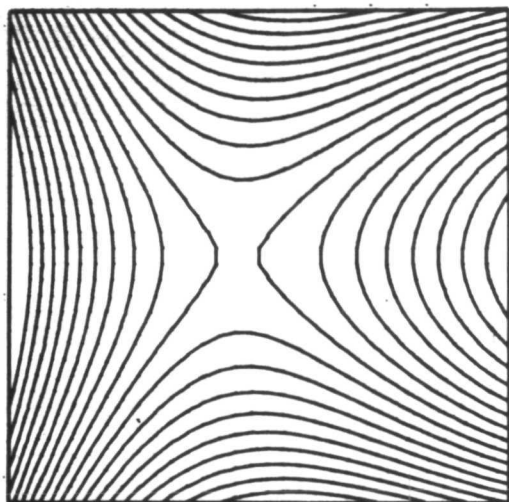


NH210



NH211



NH212

NH207
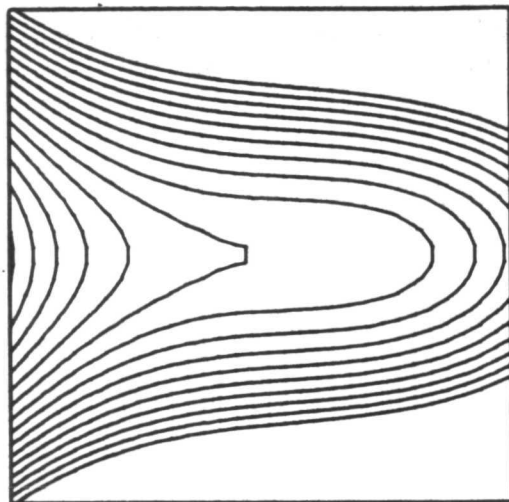


NH208
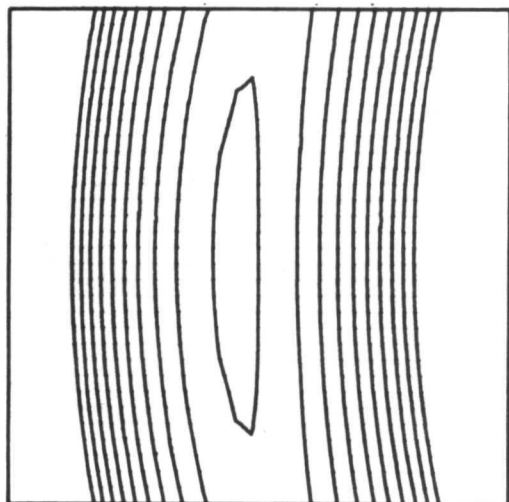


NH209
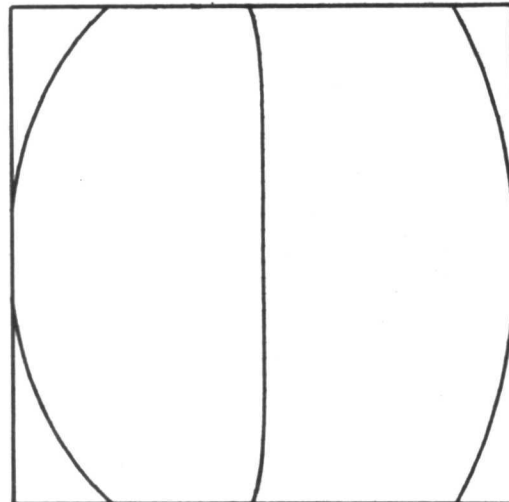


NH210
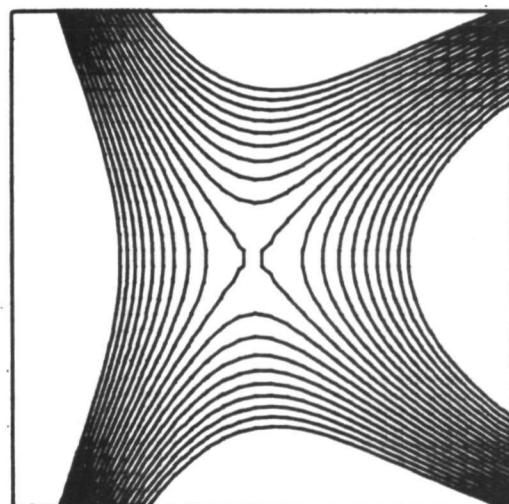


NH211
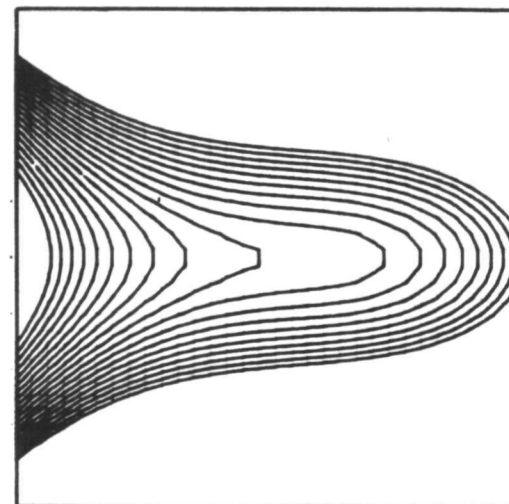


NH212
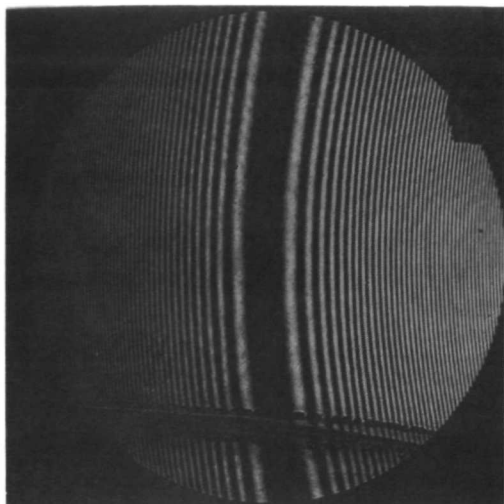
NH213
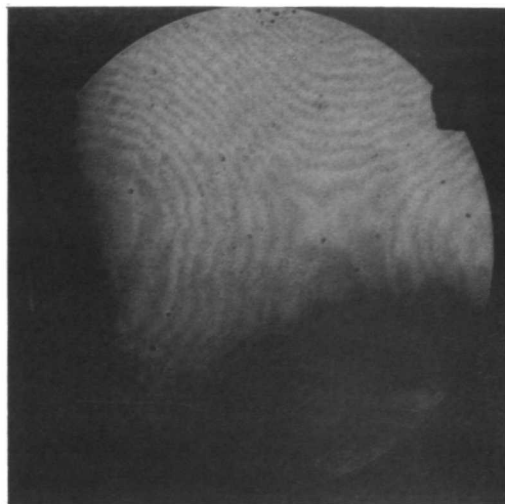


NH214
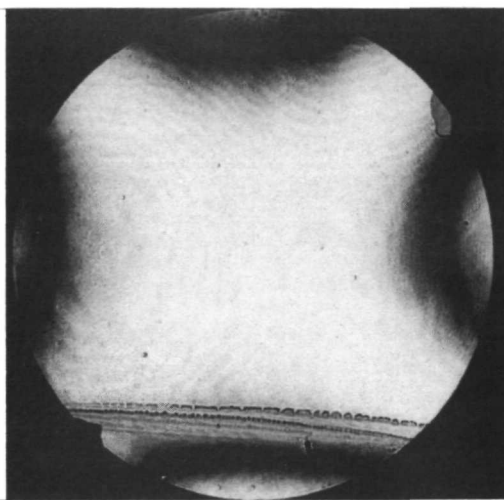


NH215
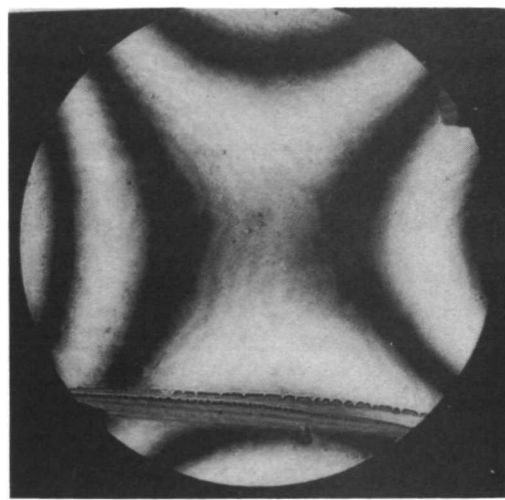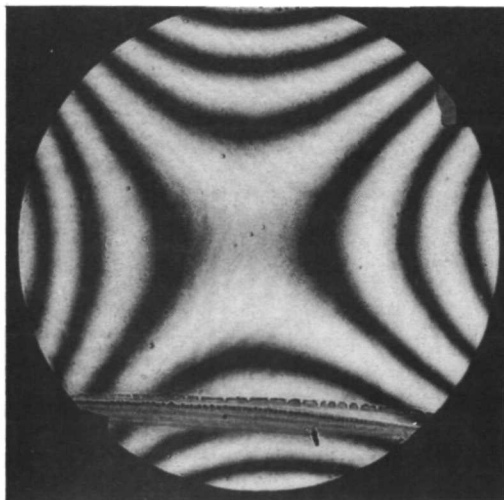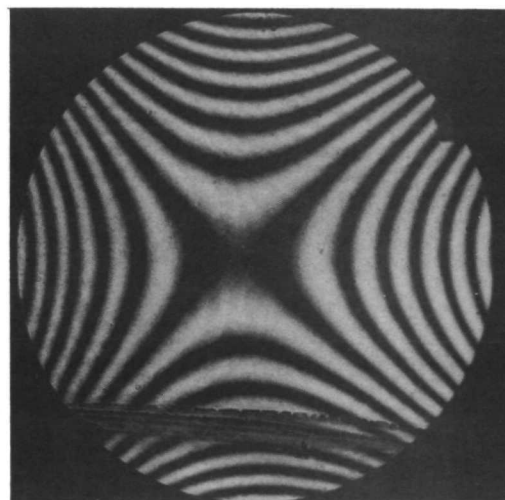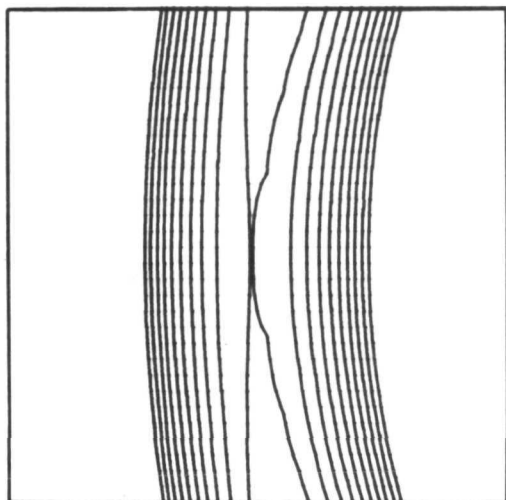


NH216



NH217



NH218

NH213
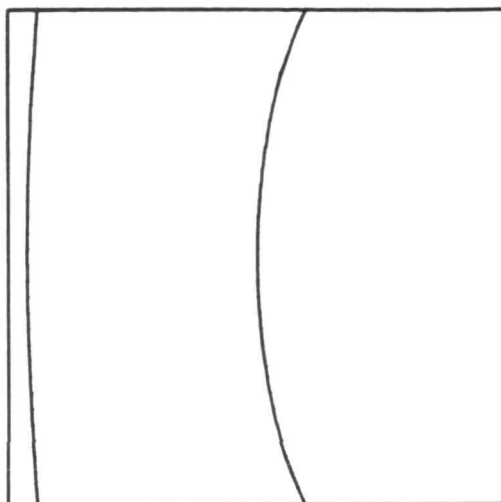
NH214
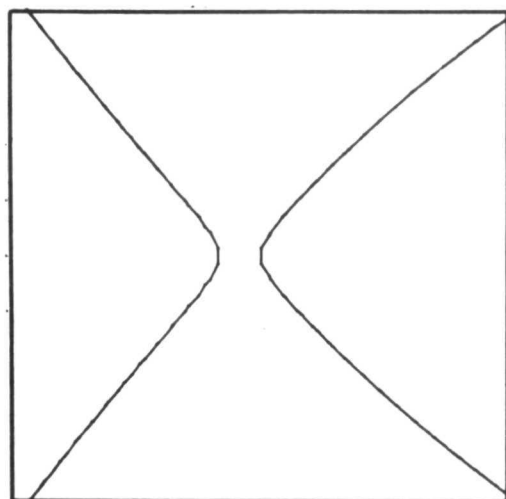
NH215
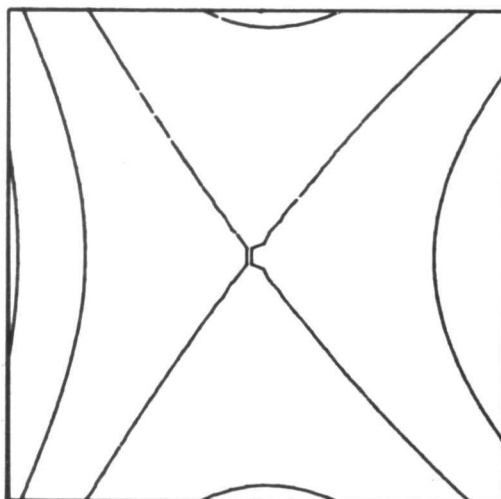
NH216
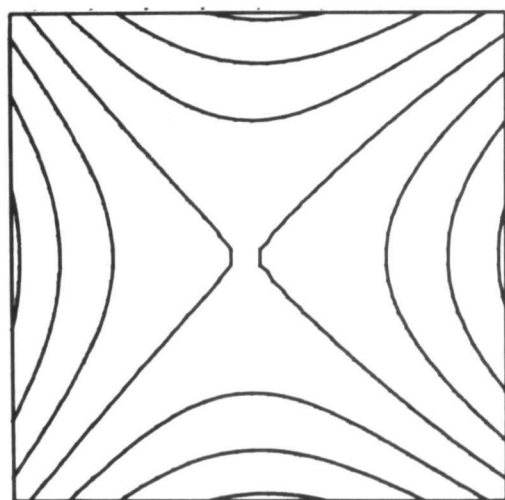
NH217
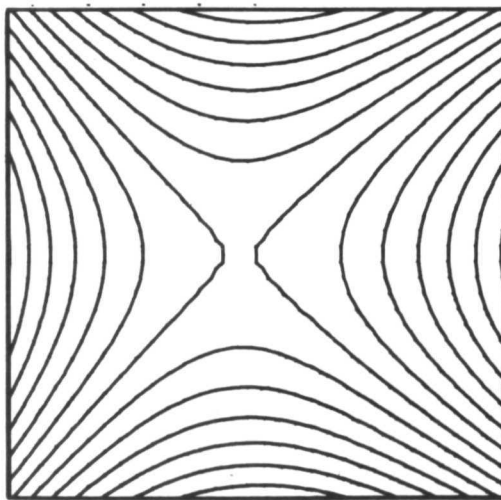
NH218
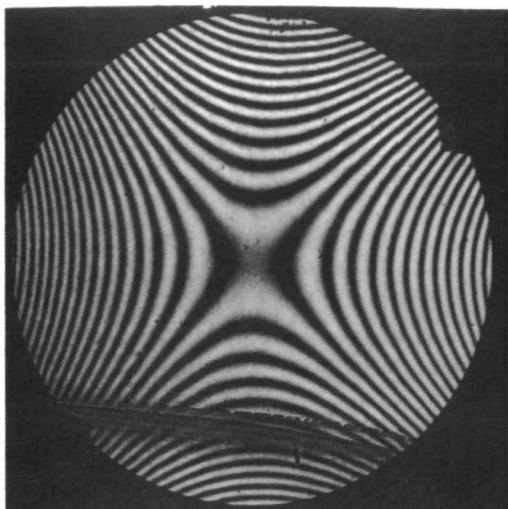
NH219
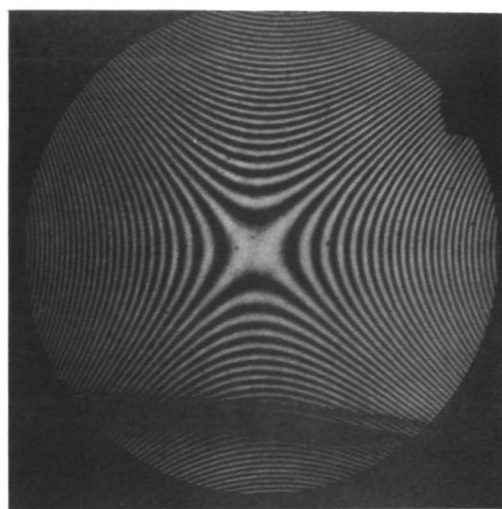
NH220
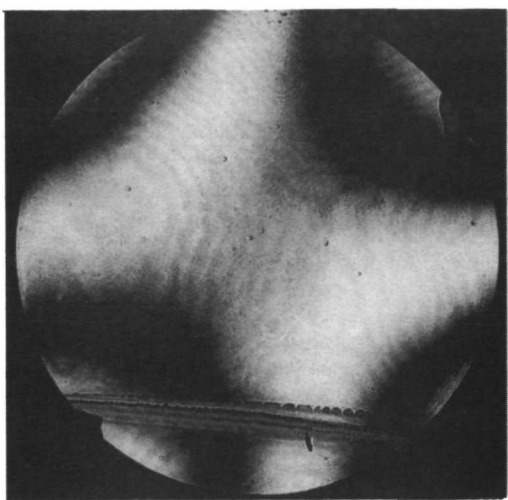
NH221
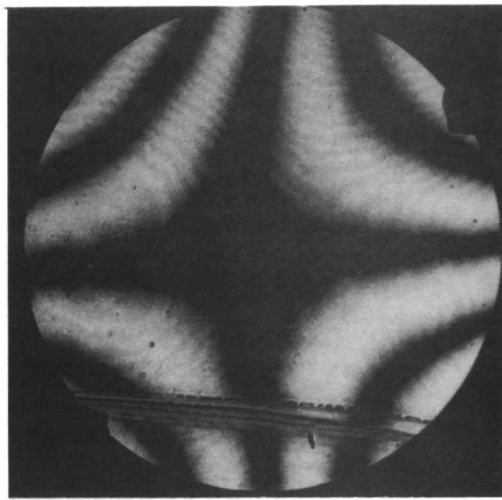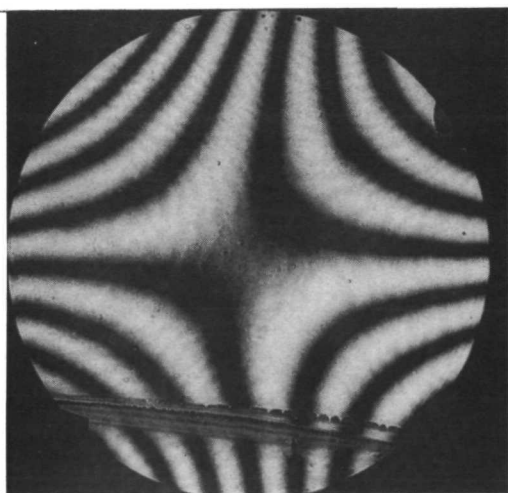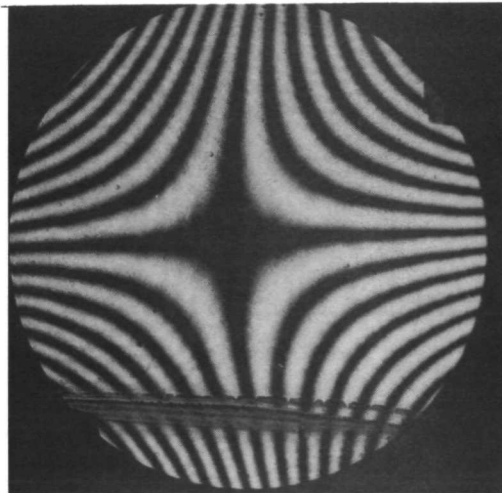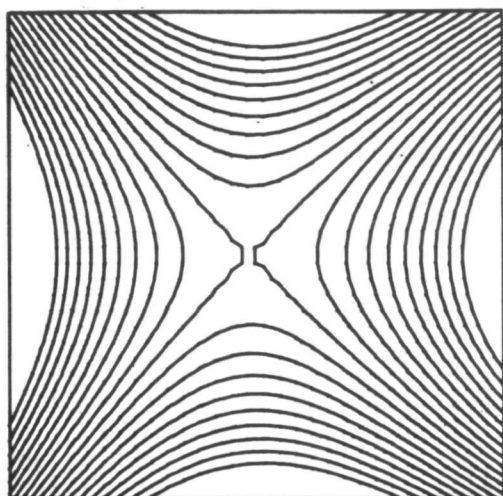
NH222

NH223

NH224

NH219
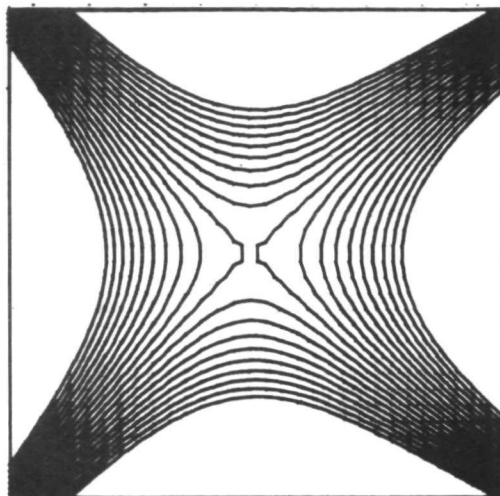


NH220
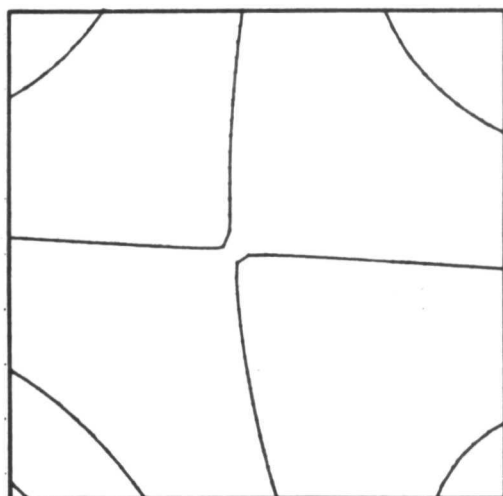


NH221
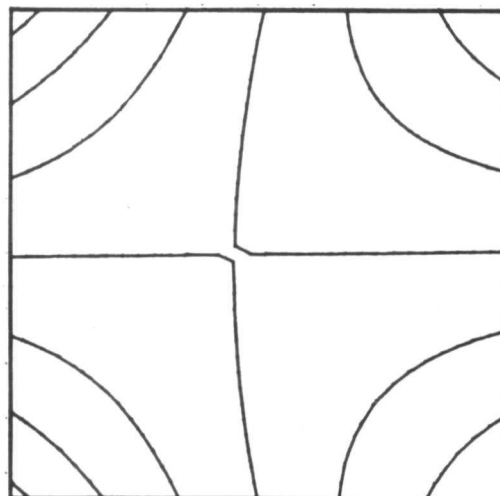


NH222
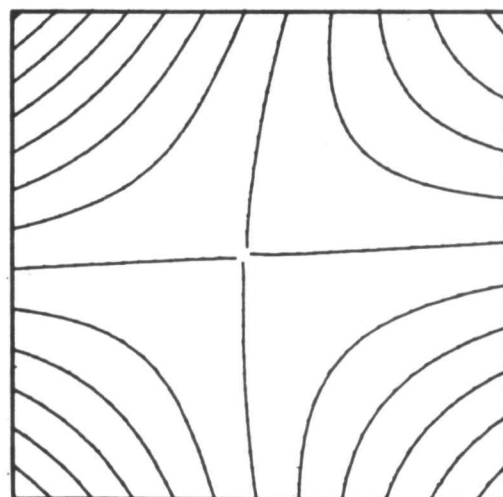


NH223
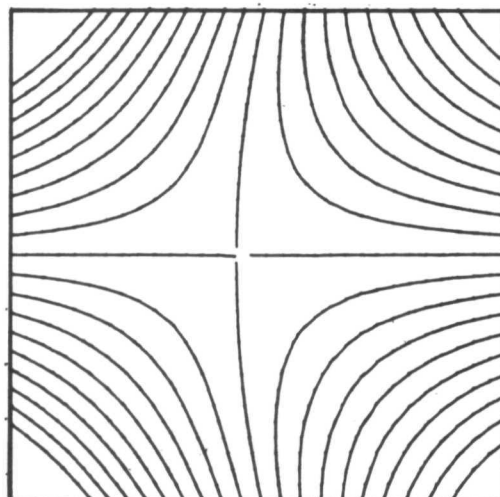


NH224
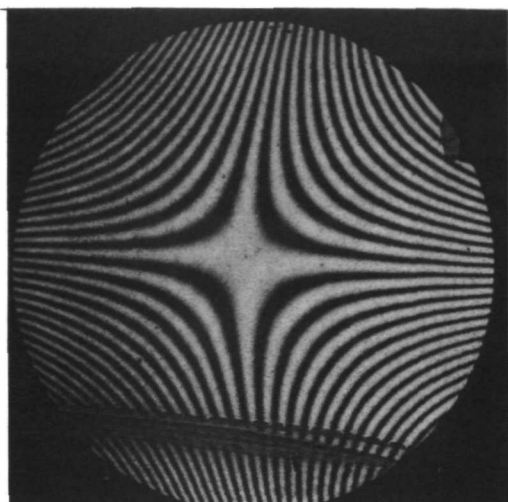
NH225
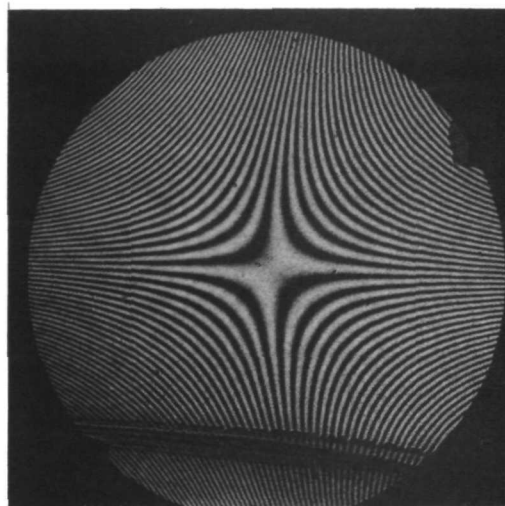


NH226
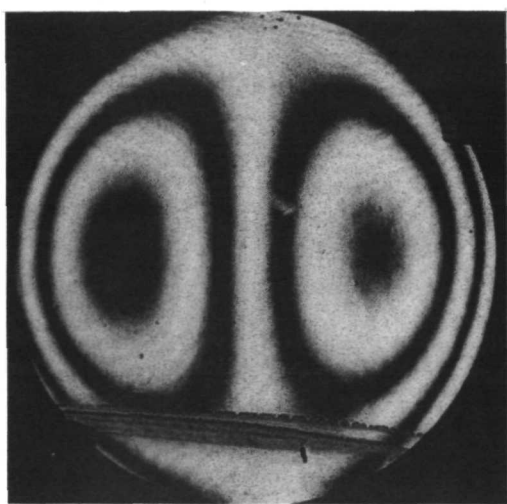


NH227
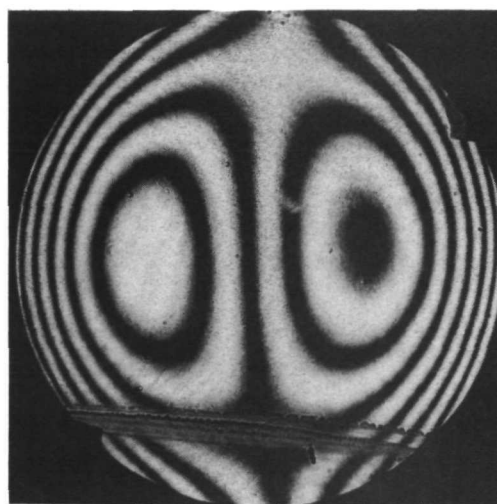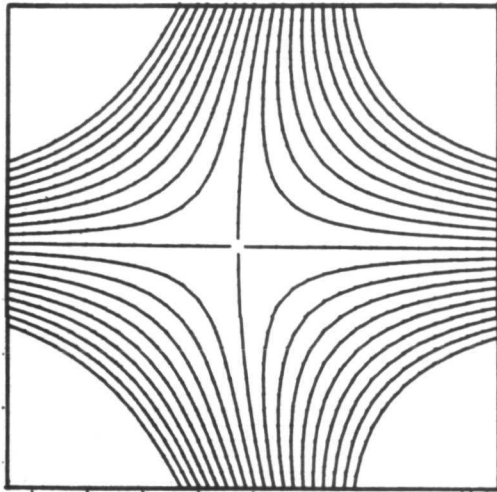


NH228

NH225
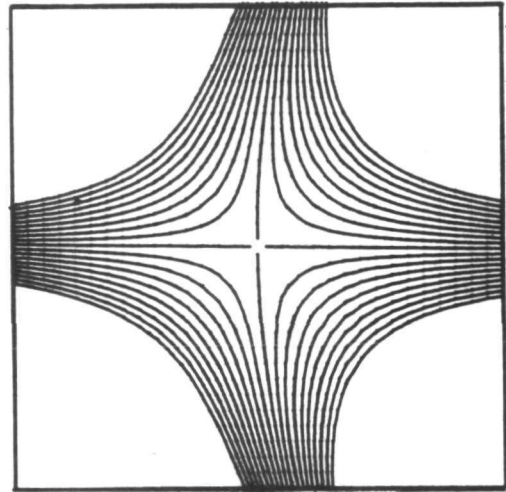


NH226
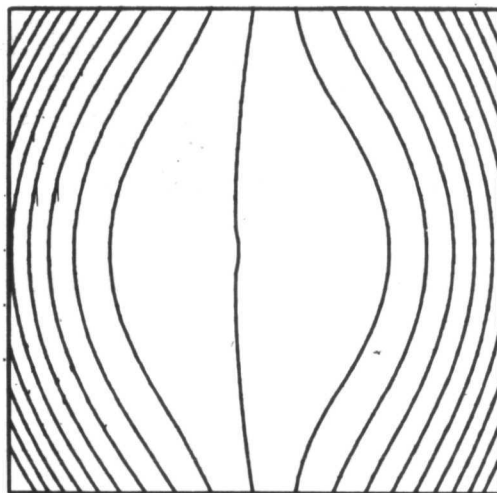


NH227
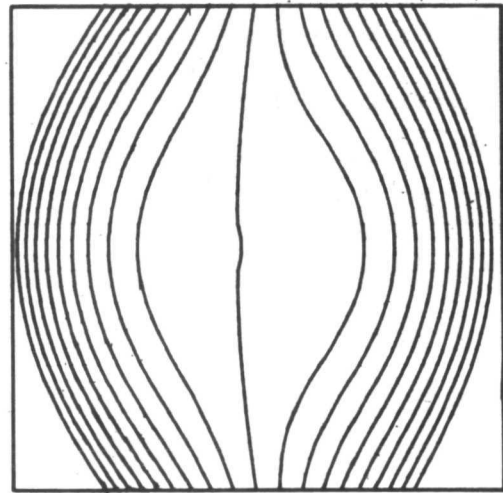


NH228

Group 7
Chromatic and Seidel Aberrations
Cellulose Acetate Butyrate
Q = 4


In this section we examine the aberrations of holographic optical elements recorded in a photodegradable polymer called cellulose acetate (55%) butyrate. The polymer layers were 750 μm thick; thus, Bragg effects were very strong. Hence, we anticipated one or more anamolous effects. However, as far as can be ascertained from a single experiment, no significant anomolous effects were observed. The main difficulties arose from the angular orientation sensitivity and wavelength selectivity of the hologram. These effects caused a rapid falloff in diffraction efficiency as a function of angular misalignment and wavelength shift. As a consequence, fringe contrast was significantly reduced even though we used attenuators to equalize the amplitudes of the reconstructed point image and the original object point. In fact, for a number of cases the contrast of the fringe patterns was markedly reduced by the low level of background light present on the experimental bench. Finally, in order to insure a uniform response, we reduced the clear aperture of the zone plate to 1.25 inches (32 mm). This was necessary because solution cast polymers set up with concave edges.

Our study of chromatic aberrations is shown in photographs NH229 to 234. For $\lambda_c$ = 476.5 nm we photographed the fringe patterns at the circle of least confusion and at the tangential and sagittal foci; these data are given in photographs NH229, 230 and 231. We then tuned the hologram to its Bragg angle for $\lambda_c$ = 476.5 nm and obtained the fringe patterns shown in photograph NH232. Note the single residual wave of aberration. This implies that for this case the Bragg condition coordinates are close to those required for wavelength optimization. For $\lambda_c$ = 514.5 nm, the diffracted wavefront was extinguished. We were, however, able to investigate two special cases. First we obtained a zero wave optimization; this is shown in photograph NH233.

Second, we determined the residual aberrations with the Bragg condition satisfied. The resulting fringe pattern is given in photograph NH234. The waves of residual aberration for the Bragg condition satisfied have increased substantially for $\lambda_c$ = 514.5 nm when compared to the results obtained for $\lambda_c$ = 476.5.

The Seidel aberrations generated by exploring the $(x_0 - z_0)$ plane are shown in photographs NH235 to 238; similar data for the $(y_0 - z_0)$ plane are shown in photographs NH239 to 243. As usual, we also displaced the object point axially to obtain a measure of the longitudinal field aberrations. Our results are shown in photographs NH244 and 245; they do not differ in form from previous results obtained for this case.

HARRIS ELECTRO-OPTICS CENTER

GROUP 7

Thick Plastics (CAB)

$R_o$ = 6.32 in.          $\lambda_o$ = 488 nm          $\theta$ = 29.°5

$R_R$ = 10.5 in.          Q = 4          $\langle \bar{K} \rangle$ = split bisector

| Photo | $\Delta x_i$ | $\Delta y_i$ | $\Delta z_i$ | $\Delta x_c$ | $\Delta y_c$ | $\Delta z_c$ | $\lambda_c$ | $\Delta_x$ | $\Delta_y$ |
|---|---|---|---|---|---|---|---|---|---|
| 229 | .0800 | 0 | .0806 | 0 | 0 | 0 | 476.5 | 10 | 10 |
| 230 | .0800 | 0 | .1048 | 0 | 0 | 0 | 476.5 | 4 | 23 |
| 231 | .0800 | 0 | .0610 | 0 | 0 | 0 | 476.5 | 20 | 0 |
| * 232 | .0347 | 0 | .0215 | -.0738 | 0 | -.1146 | 476.5 | 1 | 0 |
| ** 233 | -.0679 | 0 | -.0668 | .1958 | 0 | .2100 | 514.5 | 0 | 0 |
| * 234 | -.0963 | 0 | -.1083 | .1442 | 0 | .1253 | 514.5 | 7 | 7.5 |
| 235 | -.0080 | 0 | 0 | -.0134 | 0 | .0102 | 488 | 1.5 | 1.5 |
| 236 | -.0160 | 0 | 0 | -.0267 | 0 | .0215 | 488 | 3 | 4 |
| 237 | -.0640 | 0 | 0 | -.1075 | 0 | .0767 | 488 | 7 | 6.5 |
| 238 | -.0320 | 0 | 0 | -.0537 | 0 | .0369 | 488 | 13 | 14 |
| 239 | 0 | .0080 | 0 | 0 | .0140 | 0 | 488 | 1.5 | 1.5 |
| 240 | 0 | .0160 | 0 | 0 | .0275 | 0 | 488 | 4 | 4 |
| 241 | 0 | .0320 | 0 | 0 | .0545 | 0 | 488 | 6.5 | 7 |
| 242 | 0 | .0640 | 0 | 0 | .1082 | 0 | 488 | 13.5 | 14 |
| 243 | 0 | .1280 | 0 | 0 | .2160 | 0 | 488 | 29 | 27 |
| 244 | 0 | 0 | -.1000 | 0 | 0 | -.2778 | 488 | 3.5 | 1 |
| 245 | 0 | 0 | -.1815 | 0 | 0 | -.5000 | 488 | 5.5 | 1 |

* Bragg condition
** Wavelength optimization

GROUP 7 OPTIMIZED   THICK PLASTIC

RO = 6.3 IN.   AO = 14.7 DEG.   LAMO = 488.0 NM.
RR = 10.5 IN.   AR = -14.7 DEG.   Q = 4.0

| PHOTO | DXI | DYI | DZI | DXC | DYC | DZC | LAMC |
|---|---|---|---|---|---|---|---|
| NH229 | 0.0797 | 0.0 | 0.0791 | 0.0 | 0.0 | 0.0 | 476.5 |
| NH230 | 0.0799 | 0.0 | 0.1064 | 0.0 | 0.0 | 0.0 | 476.5 |
| NH231 | 0.0796 | 0.0 | 0.0589 | 0.0 | 0.0 | 0.0 | 476.5 |
| NH232 | 0.0347 | 0.0 | 0.0199 | -0.0719 | 0.0 | -0.1076 | 476.5 |
| NH233 | -0.0662 | 0.0 | -0.0668 | 0.1930 | 0.0 | 0.1929 | 514.5 |
| NH234 | -0.0947 | 0.0 | -0.1052 | 0.1427 | 0.0 | 0.1200 | 514.5 |
| NH235 | -0.0080 | 0.0 | -0.0000 | -0.0134 | 0.0 | 0.0094 | 488.0 |
| NH236 | -0.0160 | 0.0 | -0.0000 | -0.0267 | 0.0 | 0.0218 | 488.0 |
| NH237 | -0.0320 | 0.0 | -0.0000 | -0.0530 | 0.0 | 0.0360 | 488.0 |
| NH238 | -0.0640 | 0.0 | -0.0000 | -0.1064 | 0.0 | 0.0751 | 488.0 |
| NH239 | 0.0 | 0.0091 | -0.0063 | 0.0 | 0.0151 | -0.0177 | 488.0 |
| NH240 | 0.0 | 0.0182 | -0.0000 | 0.0 | 0.0301 | 0.0026 | 488.0 |
| NH241 | 0.0 | 0.0346 | 0.0063 | 0.0 | 0.0574 | 0.0170 | 488.0 |
| NH242 | 0.0 | 0.0688 | 0.0142 | 0.0 | 0.1143 | 0.0393 | 488.0 |
| NH243 | 0.0 | 0.1372 | -0.0002 | 0.0 | 0.2281 | 0.0040 | 488.0 |
| NH244 | 0.0 | 0.0 | -0.1000 | 0.0 | 0.0 | -0.2718 | 488.0 |
| NH245 | 0.0 | 0.0 | -0.1815 | 0.0 | 0.0 | -0.4892 | 488.0 |

GROUP 7 OPTIMIZED THICK PLASTIC
IMAGE POINT FOUND BY RAY TRACING PROGRAM

| PHOTO | SPHERICAL | COMA | ABERRATIONS ASTIGMATISM | RMS | TOTAL |
|-------|-----------|------|------------|-----|-------|
| NH229 | 0.05862 | 2.98640 | 10.20711 | 2.46785 | 11.12586 |
| NH230 | 0.05862 | 2.98640 | 10.20711 | 2.46785 | 11.12586 |
| NH231 | 0.05862 | 2.98640 | 10.20711 | 2.46785 | 11.12586 |
| NH232 | 0.06248 | 0.43674 | 1.07137 | 0.26226 | 1.25404 |
| NH233 | 0.11328 | 0.74522 | 0.07096 | 0.11695 | 0.73334 |
| NH234 | 0.05328 | 1.57286 | 6.10678 | 1.45502 | 6.44827 |
| NH235 | 0.00401 | 0.23060 | 1.69883 | 0.40755 | 1.72486 |
| NH236 | 0.00927 | 0.41914 | 3.38949 | 0.81280 | 3.42100 |
| NH237 | 0.01531 | 0.93366 | 6.73251 | 1.61447 | 6.83969 |
| NH238 | 0.03192 | 1.83553 | 13.51027 | 3.23749 | 13.69261 |
| NH239 | 0.01444 | 0.42307 | 1.88299 | 0.44894 | 1.98591 |
| NH240 | 0.01063 | 0.51061 | 3.74345 | 0.88937 | 3.94756 |
| NH241 | 0.02095 | 1.09038 | 7.11104 | 1.68988 | 7.49905 |
| NH242 | 0.04424 | 2.21650 | 14.12428 | 3.35698 | 14.89566 |
| NH243 | 0.08066 | 3.86114 | 28.33757 | 6.73215 | 29.88104 |
| NH244 | 0.24833 | 3.89391 | 0.00278 | 0.58254 | 3.80370 |
| NH245 | 0.46487 | 7.21776 | 0.00535 | 1.07994 | 7.05125 |
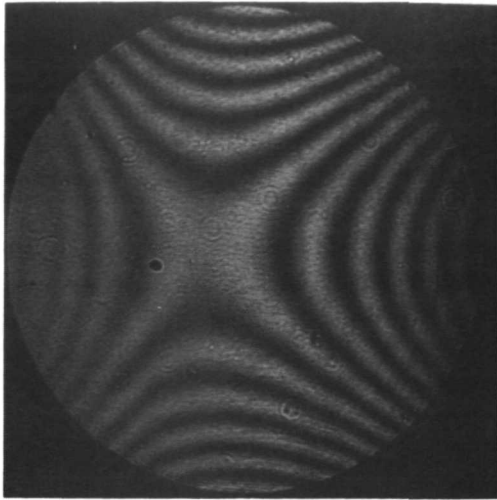
NH229
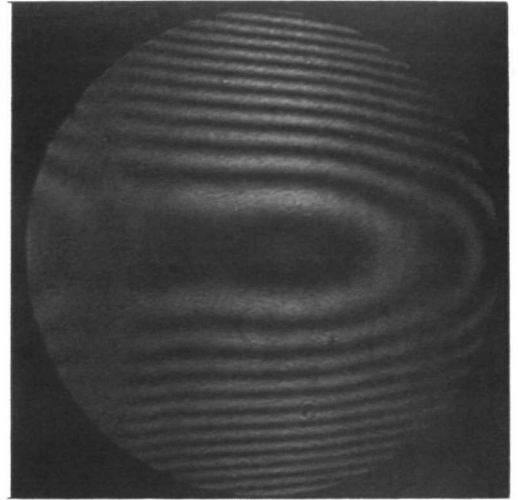


NH230
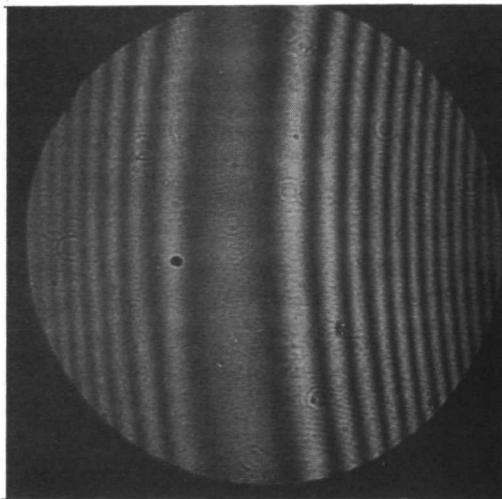


NH231
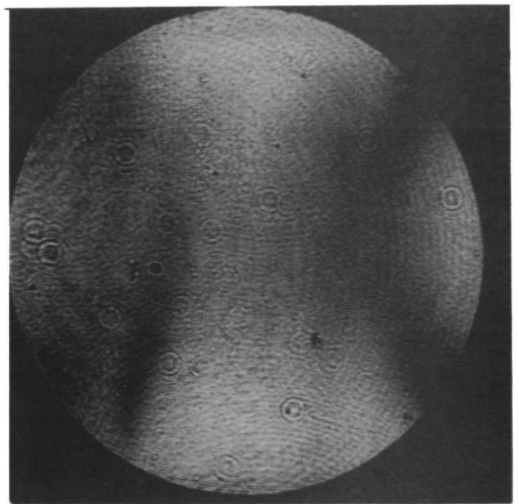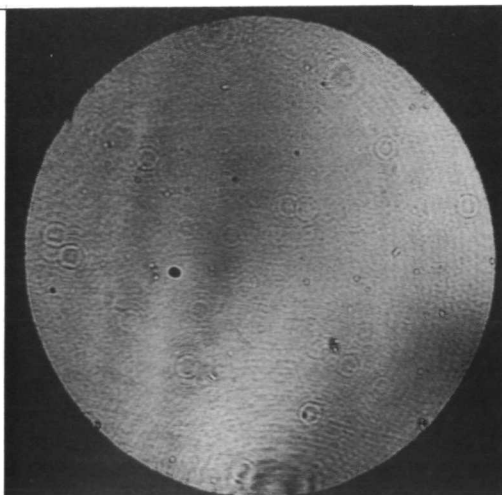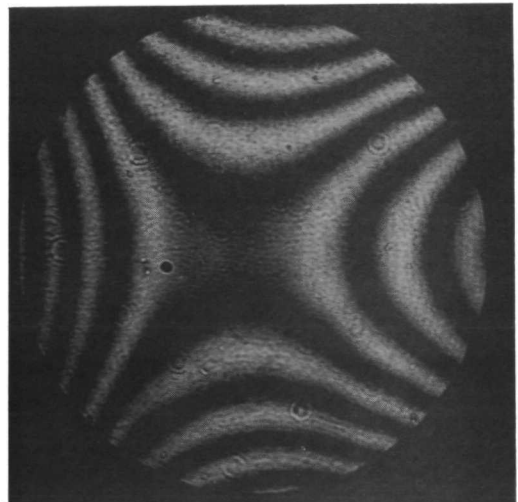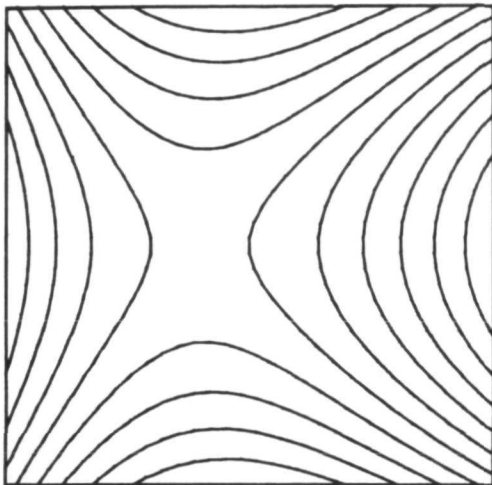


NH232



NH233



NH234

NH229
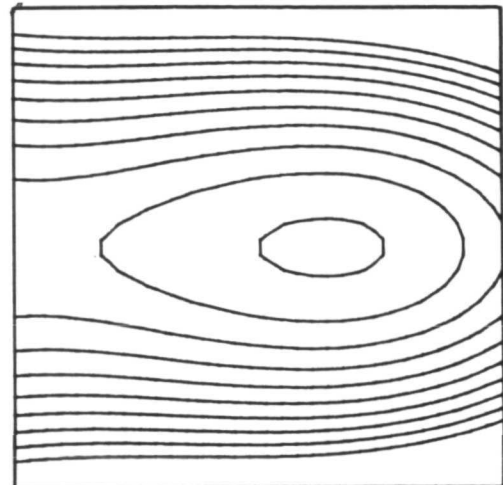


NH230
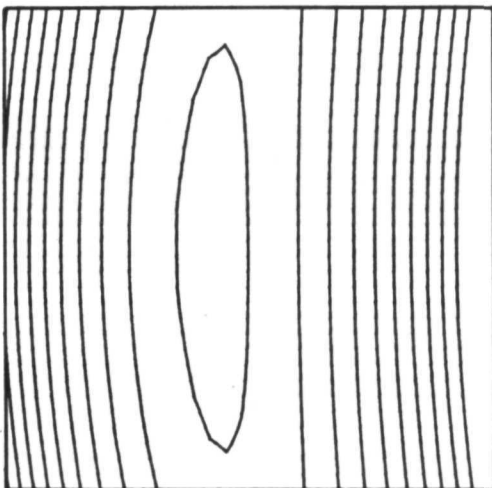


NH231
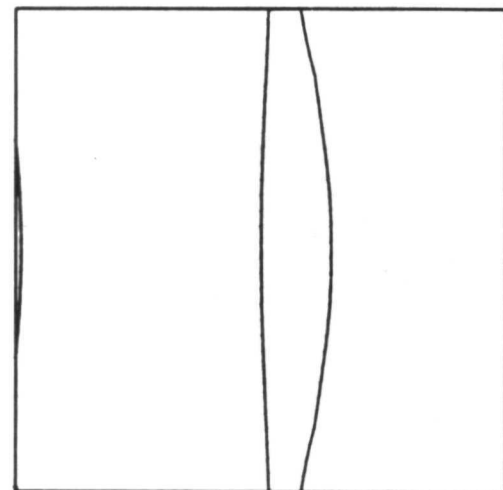


NH232
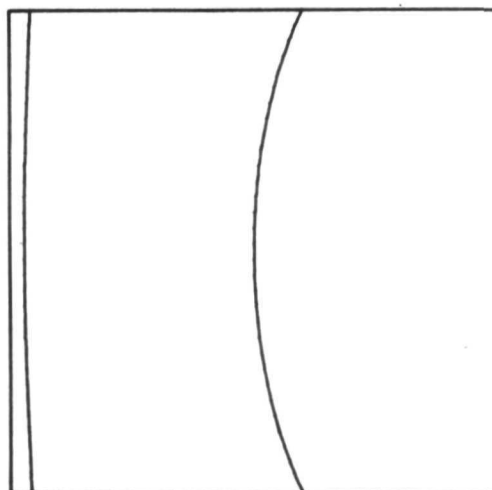


NH233
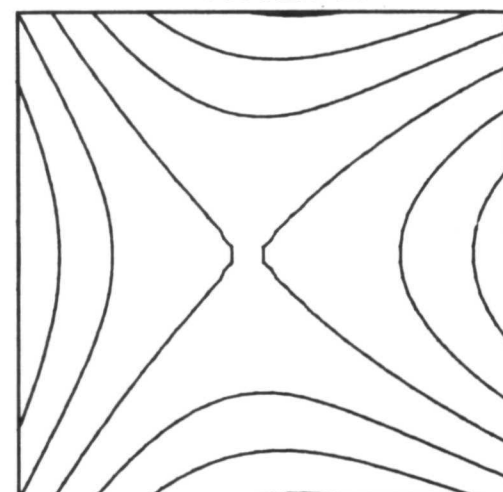


NH234
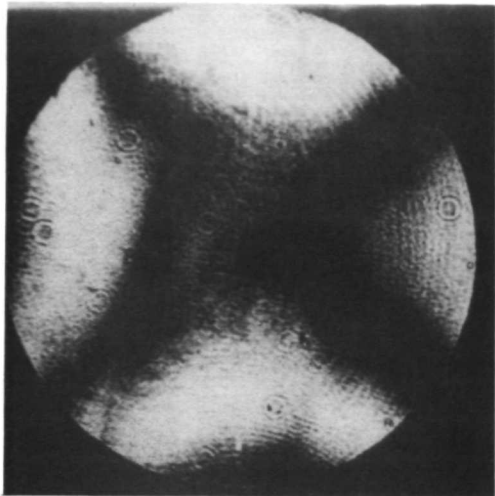
NH235
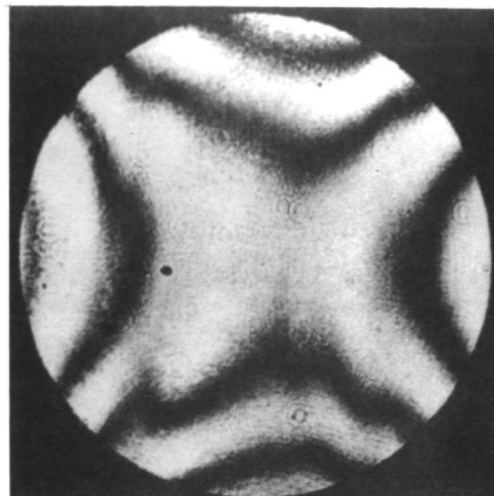


NH236
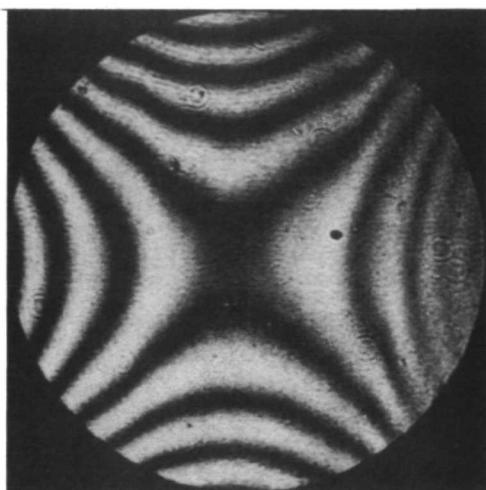


NH237
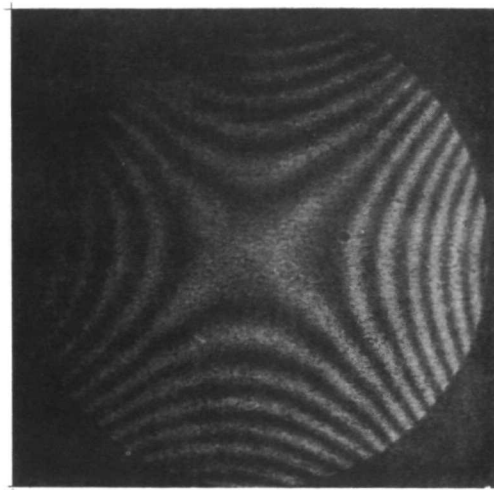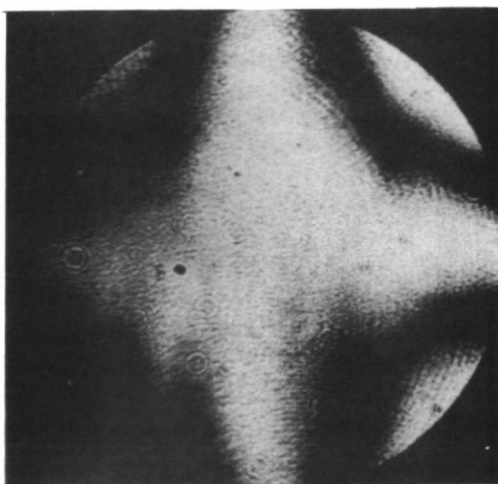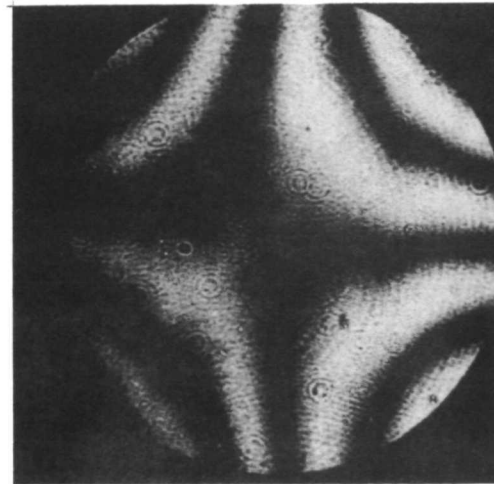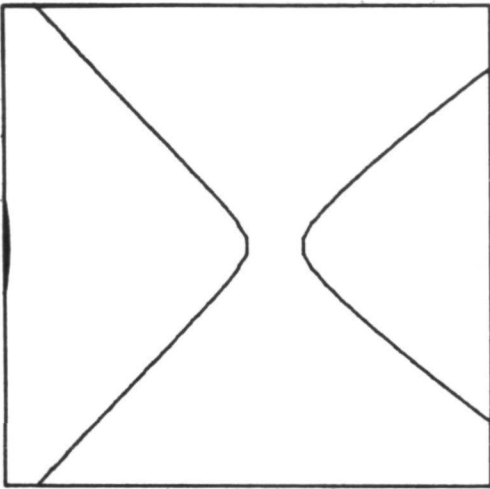


NH238



NH239



NH240

NH235
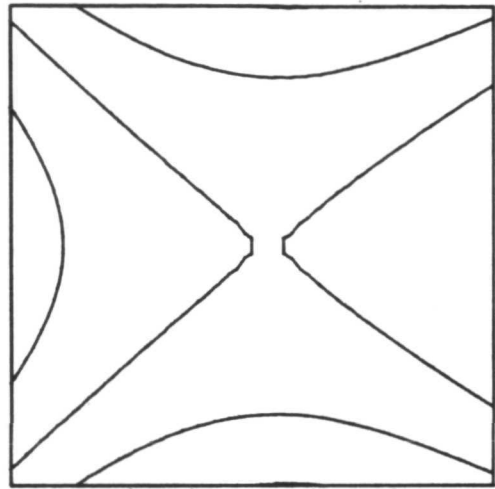


NH236
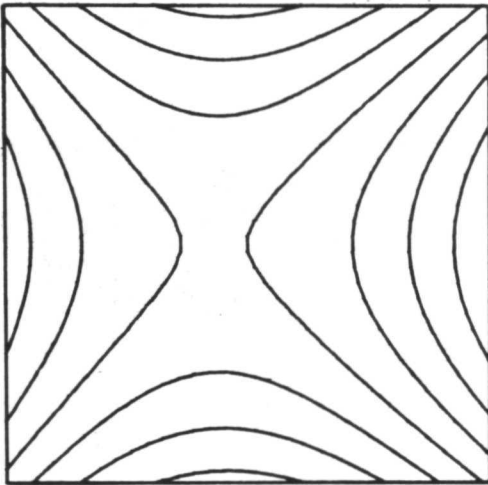


NH237
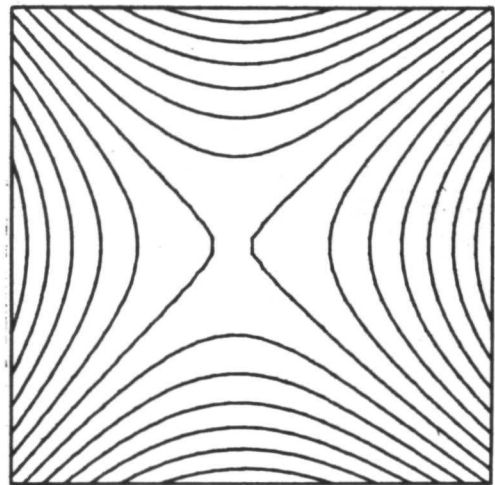


NH238
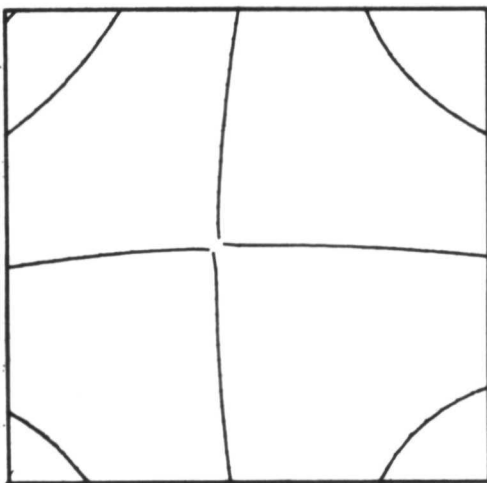


NH239
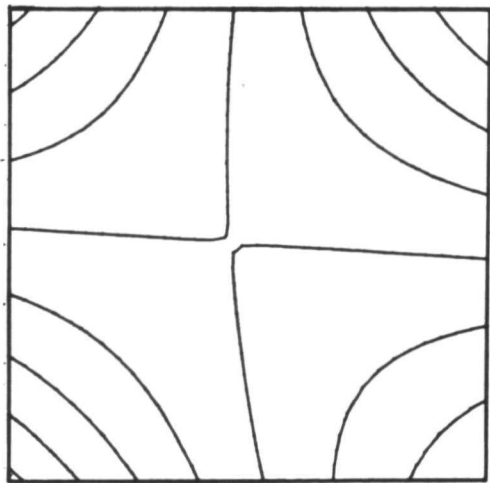


NH240
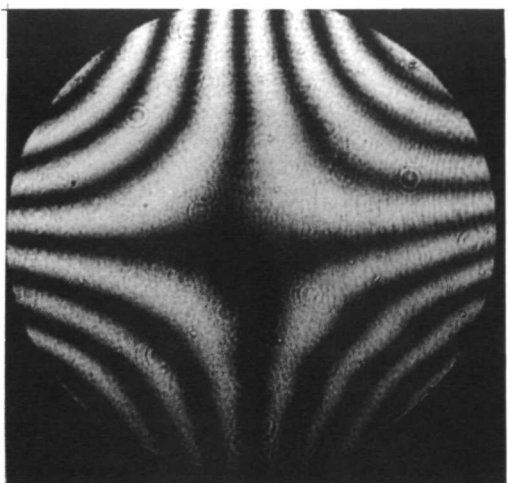
NH241
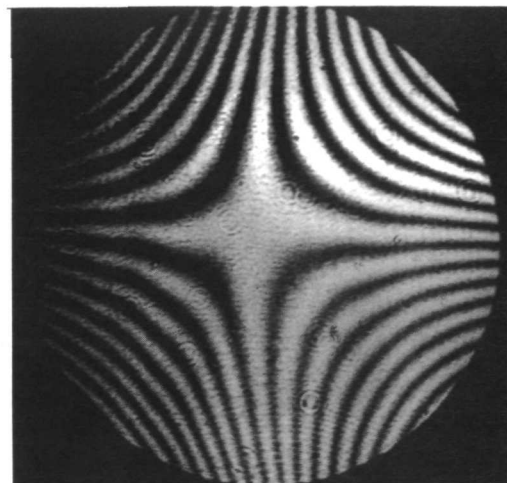


NH242
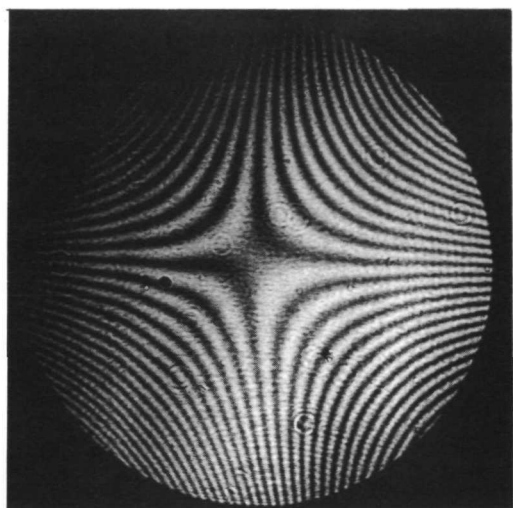


NH243
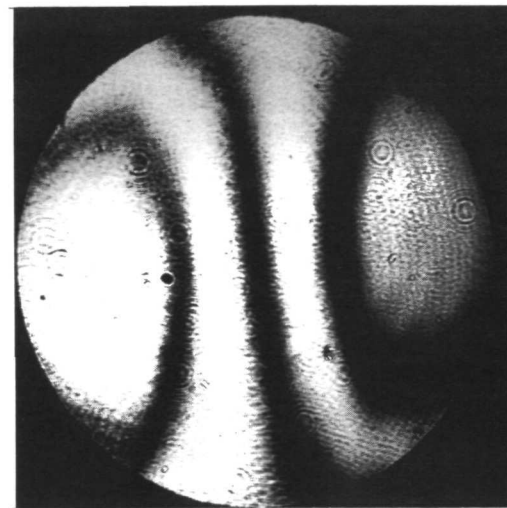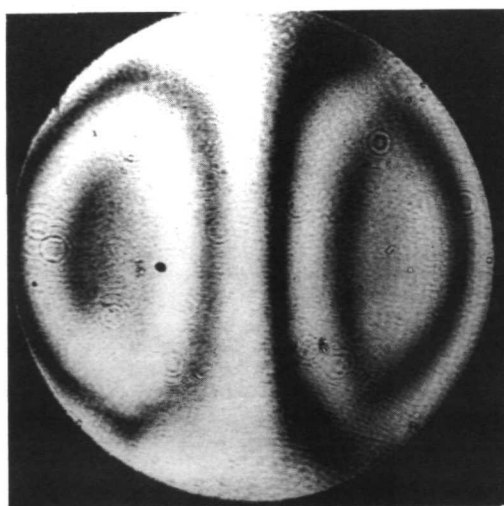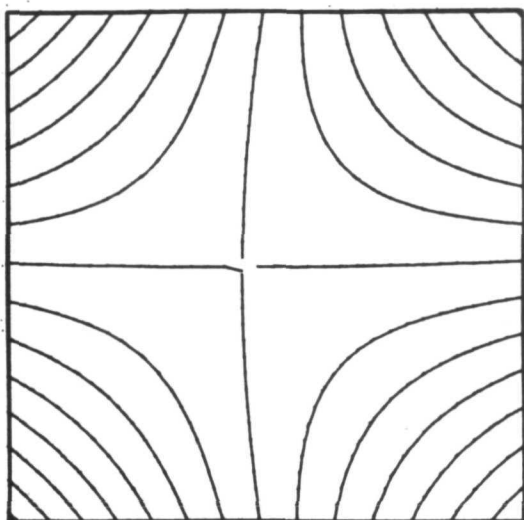


NH244



NH245

NH241
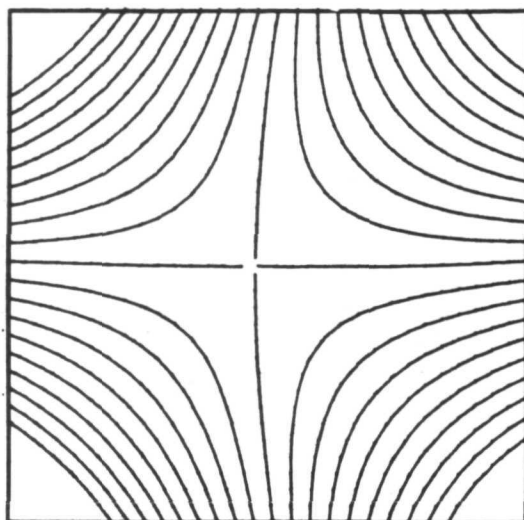


NH242
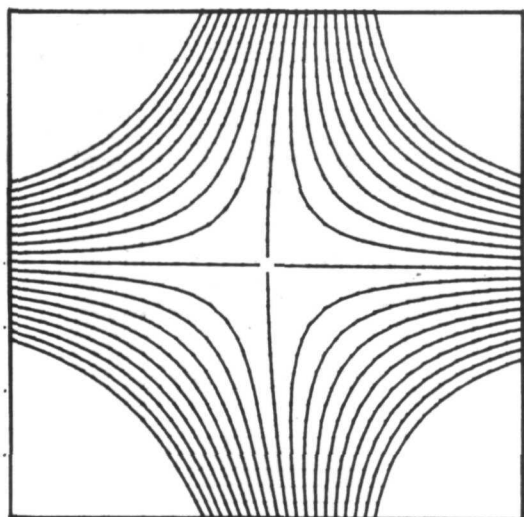


NH243
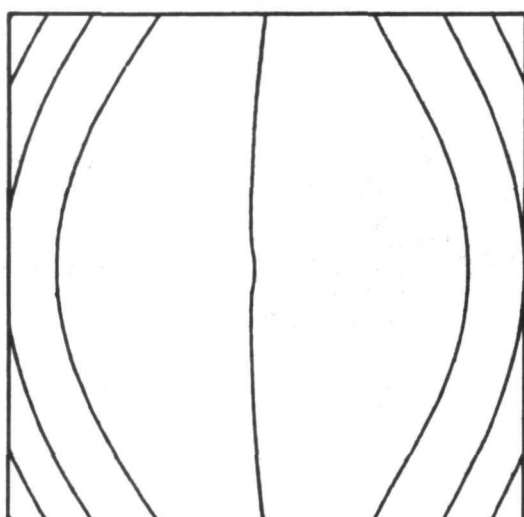


NH244
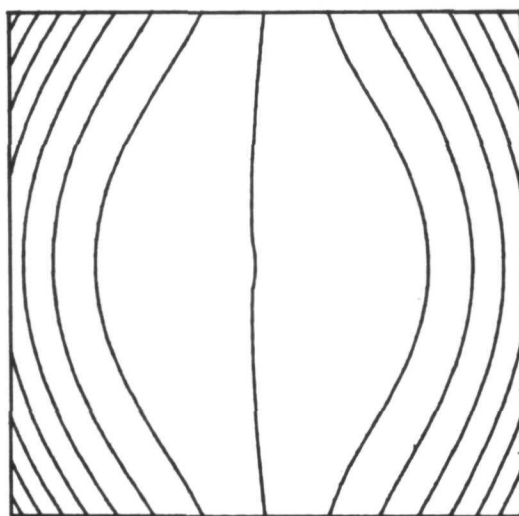


NH245

## APPENDIX B

Related Applications

B.1   Lenslet Arrays

B.2   Large Gratings

## B.1  Lenslet Arrays

A number of lenslet arrays were constructed using holographic techniques in a preliminary effort to provide uniform, efficient illumination for an optical mass memory application.  Each element of the lenslet arrays was a holographic zone plate recorded on dichromated gelatin.  Dichromated gelatin was selected for its good cosmetic quality and high diffraction efficiency capability.  The recording parameters selected were a bending factor $Q = 1$ (plano-convex lens) together with a prescribed offset angle $<\theta>$ of 60°.  One lenslet array contained 25 elements in a 5 x 5 matrix.  The lenslets were on 5.5 mm centers and had a focal length of 12.5 mm with a 5 mm diameter.  A 20 x 20 array was constructed with each element on a 1.5 mm center and with a focal length of 3 mm and a diameter of 1.5 mm.  Overall efficiency of the lenslet arrays was about 60 percent.

To fabricate the lenslet arrays we used the experimental setup shown in Figure B-1.  An argon laser beam was divided into two parts to form a typical holographic interferometer.  The reference beam was expanded into a uniform, well-collimated plane wave while the signal beam was first collimated and then converged with a Bausch and Lomb f/2 (100 mm) Super Baltar Lens to form an approximately ideal point source.  The interference of reference and signal waves subsequently formed a zone plate when used to expose a dichromated gelatin plate.  A limiting aperture fixed the size of each zone plate and prevented unwanted exposure in neighboring areas.  The dichromated gelatin plate was transported between exposures an exact distance by means of indexed translation stages.  To prevent back scatter and reflections due to air/glass index of refraction mismatch, a layer of removable optical black lacquer was painted on the glass substrate of the gelatin layer after dichromation.
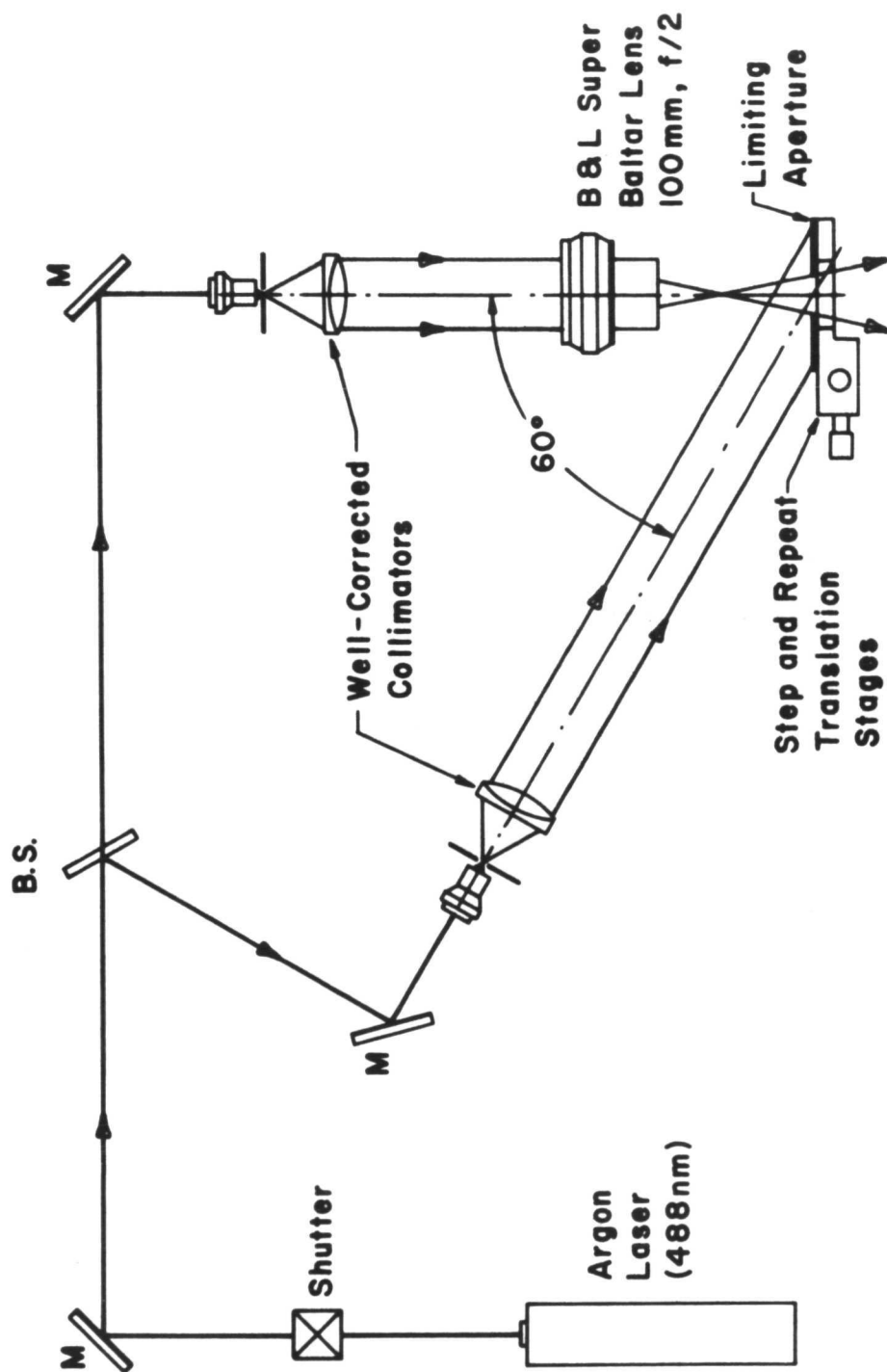
FIGURE B-1. Recording geometry for lenslet array construction.

The lenslet arrays were fabricated from gelatin layers sensitized with ammonium dichromate. The procedure used to prepare and process the dichromated gelatin was given in Section 4. Recall that the gelatin layer is obtained by removing the silver salts from Kodak 649F spectrascopic emulsions. Considerable care must be exercised in both the preparation and processing of dichromated gelatin in order to obtain satisfactory holograms. Primary advantages of the procedures outlined in Section 4 are consistency of results obtained for holographic reconstruction parameters and good cosmetic quality. An obvious disadvantage in the time required for preparation. After drying the processed gelatin layer at room temperature and humidity, it was protected from damage with a glass cover plate cemented in place with an optical lens bond.

Dichromated gelatin layers are volume phase media that exhibit a net increase in thickness after processing. Typically, there is a thickness increase on the order of 10 to 20 percent. The practical effect of the layer swelling is to generate Bragg angle mismatch and aberrations. The reason is that the swelling modifies the actual recording parameters due to fringe rotation. As a consequence, the average reference and signal beam angles appear changed, as does the recording wavelength. To compensate for this effect the hologram must be repositioned to satisfy the apparent Bragg condition. This restores maximum diffraction efficiency, but creates significant aberrations over the reconstructed wavefront. In addition, the original construction geometry is not recovered, which in the present case is of primary importance.

The cause of the swelling is not well understood. A reasonable hypothesis is that the naturally hygroscopic gelatin entraps a small amount of water (highly polar substance) by means of vanderWaal forces. The residual water is apparently in excess of that removed by the final alcohol rinse. Other unknown factors may also be involved.

Regardless of cause, it appears that post baking may provide a solution to this problem. In future work we propose to study Bragg angle mismatch as a function of postbaking time in order to determine the optimum conditioning process. The procedure is to record a zone plate at maximum efficiency, and then to reposition interferometrically. The zone plate is then rotated to determine the apparent Bragg angle. The angular rotation is a measure of the amount of layer swelling. The sample is then baked for a fixed time and the Bragg angle change is remeasured. By repeating this procedure a number of times we expect to determine the amount of post baking required for minimum layer swelling.

Further study of dichromated gelatin is recommended for a number of reasons. First, dichromated gelatin holograms can be nearly 100 percent efficient. Second, since there are no scattering centers and no absorption in the visible spectrum, dichromated gelatin holograms have low noise and excellent cosmetic quality. Finally, dichromated gelatin layers are relatively thin and hence, angular orientation sensitivity is low enough to provide a reasonable working field. This is important, for example, when a laser beam must be directed over a small angular field to provide uniform illumination of approximately constant irradiance. Although dichromated gelatin holograms are effected by extremes in relative humidity, this problem can be solved by protective overcoating techniques.

## B.2 Large Gratings

Large area gratings were fabricated on the Horizons Research LH57 photo-resist described in Section 4.2.1. By using the methodology outlined there, we prepared six 50 mm x 75 mm coatings on glass substrates. Each coating was cosmetically flawless when viewed both with the unaided eye and also when viewed with various levels of magnification. To insure uniform, low noise wavefronts and at the same time to produce linear fringes, we used a lensless-Fourier transform geometry with $R_R = R_O = 1$ meter to record the gratings. Other recording parameters were an average exposure of 4 mJ/cm$^2$ (at 488 nm), a K-ratio of 2, and a spatial frequency of 250 cycles/mm. After exposure, the gratings were dry-processed.

The results obtained for each grating were impressive both in terms of cosmetic quality and efficiency. First order efficiency was on the order of 30 percent, which is close to the theoretical maximum for thin phase gratings. A magnified cross-section (dark field illumination) of a randomly selected grating is shown in Figure B-2. Note the high-contrast and the uniformity of the fringes. It is of interest to note that a grating could be completly fabricated in less than 5 minutes; i.e., coating and drying, 2.5 minutes; exposure, 2 seconds; heat processing 1.5 minutes.

We are currently studying problems related to the preparation of high quality coated substrates 250 mm or larger in diameter. Our intention is to develop a capability for constructing large aperture holographic optical elements. It appears that the Horizons photoresist is well suited for this task, and promises to enhance the practical utility of holographic optical elements.

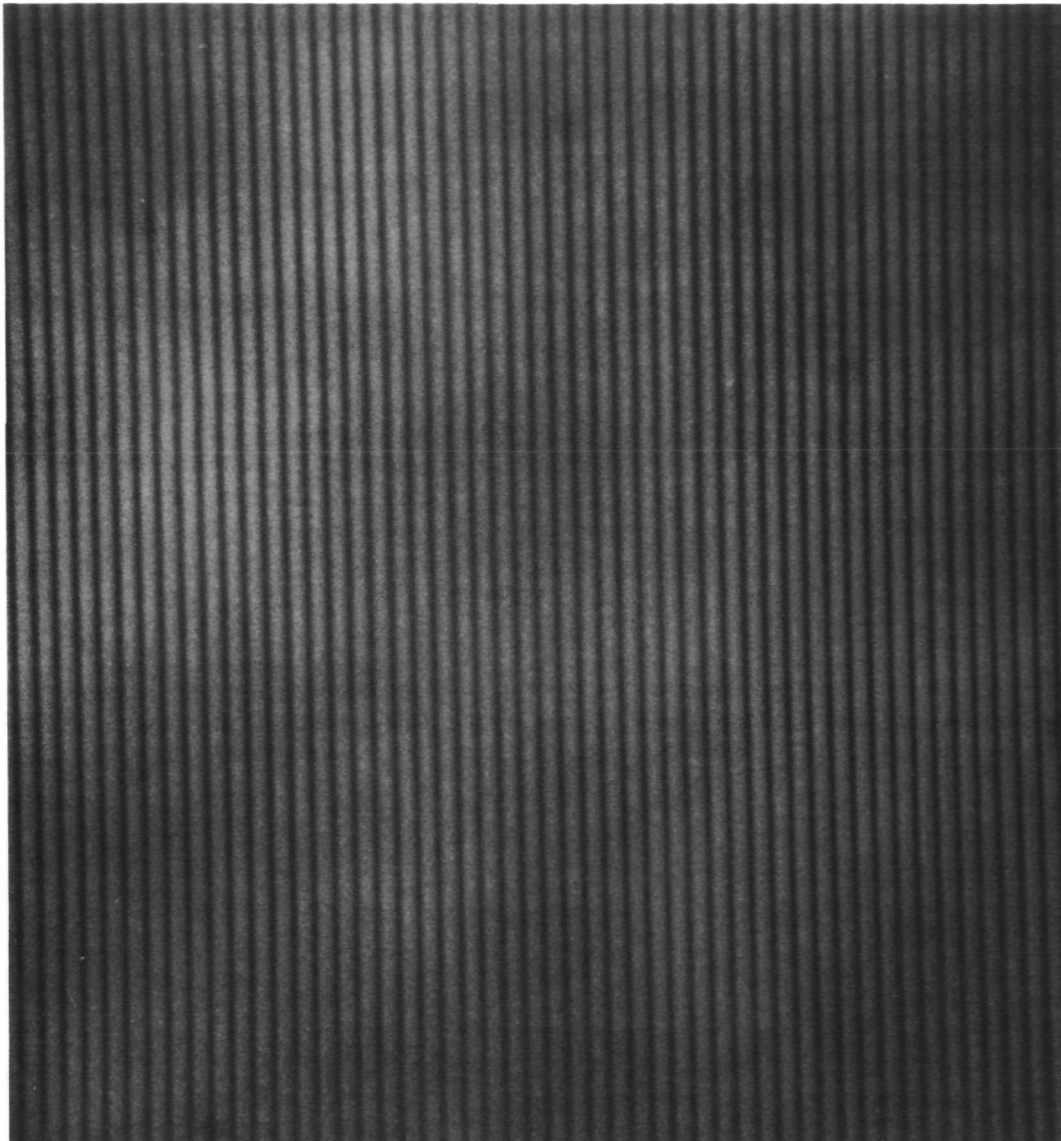**HARRIS ELECTRO-OPTICS CENTER**

FIGURE B-2.   Photomicrograph of a holographic grating recorded on
              Horizons Research LHS7 photoresist.